Ion Beam Handling by an Einzel Lens Chopper for the KEK Digital Accelerator

LEO KWEE WAH

DOCTOR OF PHILOSOPHY

Department of Accelerator Science

School of High Energy Accelerator Science

The Graduate University for Advanced Studies

2012

Acknowledgements

The opportunity of working with the KEK-DA group has been a very memorable time, in which the experiences are gained technically and practically. Without the KEK-DA members' contribution, my work would not be completed successfully.

I would like to express my deepest appreciation to my academic advisor, Prof. Toshikazu Adachi for all the time and effort that he has spent with me. I have benefited from his excellent teaching, guidance, suggestion, and advice. Also, he always gives me a hand if I have confronted with any problem in our daily life. In particular, I would like to express my gratitude to Prof. Ken Takayama for his kind support, helpful advice, excellent suggestion and valuable discussion and as well as his help in our personal life.

I would also like to express my special thanks to Mr. Okazaki and Mr. Arai, their generous help and guidance for the installation, development and experimental preparation works. Also I appreciate the graduate student Mr. Tanaka and Mr. Liu for their support.

Not forgotten, I would like to express my thanks to Dr. John Flanagan to lend us some apparatuses for our emittance measurement. Also, I like to express my gratitude to Dr. Olli Tarvainen for his valuable suggestions.

Special thanks to Mrs. Kyoko Kitazawa for her help in our daily life. I would also like to express my special appreciation to Mrs. Kyoko Takayama, Miss Nurul Amal and Miss Nurul Hawa for their support and help during my wife hospitalization.

Finally, I would like to express my deeply and heartfelt thanks to my loving wife Chow, for her sacrifice to leave the homeland and confronted with a strange and different culture environment. Besides, her efforts to provide a "relaxing environment" at home helped me to rest leisurely and without thinking of my work.

Last but not least, I would like to state that my study was financially supported by the Malaysian Ministry of Science, Technology and Innovation (MOSTI).

Abstract

The KEK-Digital Accelerator (DA) has been constructed, and it is in commission now. This accelerator is a rapid cycle synchrotron. Its acceleration principle is based on the induction synchrotron (IS) concept which was demonstrated in 2006 using the existing KEK 12 GeV proton synchrotron. Even before this demonstration, the small IS not employing any large scale injector had been proposed as All Ion Accelerator, which has the capability to accelerate all kinds of ions with their possible charge-state. Similarly, there is no large-scale injector in the KEK-DA. For KEK- DA, an ion beam is extracted from an ion source, chopped, post-accelerated and immediately guided to be injected to the DA ring. Presently, a permanent magnet type of Electron Resonance Ion Source (ECRIS) is utilized as the ion source for the KEK-DA. In order to mitigate the space charge effect and closed orbit distortion caused by a remanent field in the ring, the ion beam must be accelerated after extraction. Therefore, the KEK-DA ECRIS is embedded inside a 200 kV High Voltage Platform (HVP).

In order to accelerate an ion beam in a synchrotron, a beam pulse length must be less than revolution time period in the ring. Since the typical revolution time is ~10 μs in our case, a ms ion beam which is produced from an ECRIS must be chopped before injection into the ring. For such purpose, a novel chopper device has been developed after our examination and consideration of various chopping systems. The novel chopper, so-called Einzel lens chopper, has been developed and demonstrated. Its principle is rather simple: by modulating a voltage applied to the middle electrode of the Einzel lens, it is worked as a longitudinal gating device as well as the focusing device. This performance can be realized by introducing a Marx generator to provide a pulse voltage in a desired duration time. The Marx generator used in the present studies has the fast response of rising and falling times with the solid-state switching device.

For this implementation, the functionality and performance of the Marx generator have been confirmed by measurement and simulation. At first, in order to obtain a voltage for beam blocking and another voltage for beam optics matching of the Einzle lens, a beam

blocking experiment was carried out by using the helium and nitrogen ion beams. In addition, a simulation was also performed by using the IGUN code. The chopping performances with different chopping timings and time durations have been investigated by observing time profiles of the chopped beam at a Faraday cup. The results were further confirmed and explained by using the circuit model of the Faraday cup. Reconstruction of a beam profile from the observed signal, which is modified by the Faraday cup response, is important to investigate a chopper performance. By solving the inverse problem, the beam profile was reconstructed successfully

A chopped beam is transported through a transport line and injected into the ring. In order to avoid a beam loss during transportation, it is important to know a beam emittance. Therefore, a beam emittance measurement was carried out by using a pepper pot emittance monitor. Through this experiment, the measurement and analysis procedures have been established. The optimization of the LEBT parameter was performed to reduce the beam losses.

For further investigation of the transient beam behavior from the Einzel lens to the DA ring, a simple code was developed. By using the simulation result, we can identify the intrinsic characteristic of the Einzel lens chopper. Such an intrinsic nature is that the bunch head is retarded and bunch tail is moving forward. This source is originated from the transient time region of the Einzel lens chopper voltage, which modulates a momentum at the bunch head and tail. This phenomenon, which is called as “drift compression”, has been confirmed by comparing the bunch profile at the entrance and exit of transportation line. For the beam motion in the ring, beam diffusion or spread is also observed in the experimental and simulation results. For a long distance beam motion in the ring, the space charge effect is clearly seen: the particles are diffused from the bunch in time. The experimental results for the longitudinal motion can be quantitatively reproduced by using our simulation code.

Presently, the Einzel lens chopper has been operating successfully with its stable and reliable performances and without causing any trouble during the KEK-DA beam commissioning.

Table of Contents

1. Introduction

The KEK-Digital Accelerator (DA) has been constructed. This accelerator is a rapid cycle synchrotron. Its acceleration principle is based on the induction synchrotron (IS) concept [1, 2], which was demonstrated in 2006 using the existing KEK 12 GeV proton synchrotron [3, 4]. Even before this demonstration, the small IS not employing any large scale injector had been proposed as All Ion Accelerator [5], which has the capability to accelerate all kinds of ions with their possible charge-state. The KEK-DA [6], which is under beam commissioning [7, 8], is expected to deliver ion beams for a wide range of applications, such as laboratory space science using virtual cosmic rays for the development of radiation-hard LSI and bio science to confirm an origin of life in space [9].

In the KEK-DA without any large-scale injector, ions are extracted from an ion source, and injected to the DA ring, after being further accelerated by a simple electrostatic potential gap instead of injector accelerator.

A permanent magnet type of Electron Cyclotron Resonance Ion Source (ECRIS) is used as the ion source for the KEK-DA. The KEK-DA has novel properties that are distinguished from the conventional synchrotron. A pre-injector is not required but an ion beam itself must be accelerated before injection in order to mitigate space-charge effects and closed orbit distortion caused by a remnant field in the DA ring. For this purpose, electrostatic acceleration is used because it is quite stable and maintenance-free. Thus, the ECRIS is installed on the 200 kV High Voltage Platform (HVP).
As the injection scheme, 1-turn injection method is employed for the simplicity. The injection device is an electrostatic kicker, the voltage of which is turned off before the head of injected beam arrives at the injection point.

Major constraints on the ECRIS for the KEK-DA are listed here.
(1) It is embedded inside the 200 kV HVP.
(2) It is operated at 10 Hz, since a repetition rate of the DA ring is 10 Hz.

(3) A beam pulse length must be less than 1 revolution time period in the ring, ~10 μs as a typical revolution time.

Constraint (1) requires a compact ECRIS so that the required electric power is minimized. In addition, introduction of cooling water into the HVP is undesired. Constraint (2) tells us the necessity of pulse mode operation. To meet Constraint (1), an x-band permanent magnet ECRIS, where required asymmetric mirror fields are generated by permanent ring magnets, has been developed at KEK [11, 12]. To avoid water cooling of the plasma chamber of the ECRIS, driving microwaves must be injected into their interaction region through a waveguide in a pulse mode. Namely, the ECRIS is operated in a pulse mode at the same repetition rate as the ring. Constraint (3) demands any method of pulse length control. Since it takes ms long to build up plasma in an ECRIS at a sufficient saturated level, the pulse length of an extracted beam from the ECRIS must be chopped in a desired pulse length. For this purpose, the novel Einzel lens longitudinal chopper has been developed [13, 14, 15]. It is a type of longitudinal chopper. This was the first demonstration in the world. Now its capability is attracting world-wide interests from ion beam society. Its idea is rather simple. Voltage of the middle electrode of the Einzel lens is manipulated in the desired pulse mode. Details will be discussed later.

A μs-long ion pulse delivered from the HVP is guided through the Lowe Energy Beam Transport Line (LEBT) consisting of three bending magnets including a momentum and charge-state selector, 7 quadrupole magnets, steering magnets, and diagnostic devices up to the injection point. After careful optimization of the injection condition, it has been confirmed that a well-chopped beam pulse with a rectangular profile in the longitudinal direction is injected and trapped with barrier voltage pulses and accelerated with a long induction pulse voltage as expected.

The organization of this thesis is as follows. The principle of the IS and the KEK-DA as an accelerator complex are described in the Chapter 2. An over-all outline of the KEK-DA ECRIS, such as principle, set up, permanent magnet system, microwave system, ion

extraction device, and its pulse mode operation is described in Chapter 3. Chapter 4, which is devoted to description of the longitudinal chopper, solid-state Marx generator to drive the chopper and its operational performance, is one of highlights of this Thesis. In this chapter, other chopping methods including a conventional transverse chopper are compared with the Einzel lens chopper. A chopped ion beam is dispatched from the ECRIS region, which is embedded in a High Voltage Platform (HVP) of 200 kV, and its charge-state is selected by an analyzer magnet, and then guided downstream through the LEBT. The beam propagation process through the LEBT is described together with beam optics information of the LEBT in Chapter 5. A beam tracking code has been developed to evaluate transient effects in the longitudinal ion beam motion caused by the Einzel lens chopper. The outline of the simulation code and its predictions are given in Chapter 6. Qualities of an un-chopped beam and chopped beam have been measured using beam diagnostic devices, such as luminescence target and pepper-pot type emittance measurement tool. Those measurement results are presented in Chapter 7. Eventually the chopped beam was injected into the DA ring and subject to beam commissioning in the ring. Chapter 8 is devoted to describe how the chopped beam behaves in the ring by comparison the measurement results with the simulation results. Thesis is summarized in Chapter 9.

References

[1] K. Takayama, and J. Kishiro, “Induction Synchrotron”, *Nucl. Inst. Meth. Phys. Res.* A **451**, 304 (2000).

[2] K. Takayama and R. J. Briggs (Eds), “Induction Accelerators”, (Springer, 2010).

[3] K. Takayama *et al.*, “Observation of the Acceleration of a Single Bunch by Using the Induction Device in the KEK Proton Synchrotron”, *Phys. Rev. Lett.* **94**, 144801 (2005).

[4] K. Takayama, Y. Arakida, T. Dixit, T. Iwashita, T. Kono, E. Nakamura, K. Otsuka, Y. Shimosaki, K. Torikai, and M. Wake, "Experimental Demonstration of the Induction Synchrotron" , *Phys. Rev. Lett*. **98**, 054801-4 (2007).

[5] K. Takayama, Y. Arakida, T. Iwashita, Y. Shimosaki, and K. Torikai, and T. Dixit, "All-Ion Accelerators: An Injector-free Synchrotron", *J. of Appl. Phys.* **101**, 063304 (2007).

[6] T. Iwashita, T. Adachi, K. Takayama, T. Arai, Y. Arakida, M. Hashimoto, E. Kadokura, M. Kawai, T. Kawakubo, Tomio Kubo, K. Koyama, H. Nakanishi, K. Okazaki, K. Okamura, H. Someya, A. Takagi, A. Tokuchi, **K. W. Leo**, and M. Wake, "KEK Digital Accelerator", *Phys. Rev. AB-ST* **14**, 071301 (2011).

[7] K. Takayama, T. Adachi, T. Arai, Y. Arakida, M. Hashimoto, T. Iwashita, E. Kadokura, T. Kawakubo, T. Kubo, H. Nakanishi, K. Okamura, H. Someya, A. Takagi, and M. Wake, "KEK Digital Accelerator and its Beam Commissioning", *Proceedings of IPAC2011*, San Sebastian, Spain, WEOBA02 (2011).

[8] K. Takayama, "All-ion Accelerators", School for Accelerator Technology and Applications", 30th Jan.-3rd February 2012, IIT Bombay. (http://www.phy.iitb.ac.in/~Accelerator-School/index_files/Presentations/day4/Ken_Takayama_AccelSchool.pdf)

[9] KEK Workshop, "Exploration of Laboratory Space Science using Virtual Cosmic Rays", August 14-15 (2011).

[10] Bernhard Wolf (Eds), Handbook of Ion Sources, CRC Press (1995) ISBN 0849325021.

[11] H. Suzuki, Y. Arakida, T. Iwashita, M. Kawai, T. Kono, K. Takayama, K. Okazaki, and S. Inagaki, "ECR Ion Source for the KEK All-ion Accelerator", *Proceeding of EPAC08*, Pg. 442 (2008).

[12] **Leo Kwee Wah**, K. Takayama, T. Arai, K. Okazaki, A. Takagi, T. Adachi, K.Koyama, M. Wake, and Y. Arakida, "Permanent Magnet ECRIS for the KEK Digital Accelerator", *Proceeding of ECRIS2010*, August 23rd -26th, 2010 Grenoble, France, Pg. 150(2010).

[13] T. Adachi, T. Arai, **K. W. Leo**, K. Takayama, and A. Tokuchi , "A Solid-State Marx Generator Driven Einzel Lens Chopper", *Rev. Sci. Instrum.* **82**, 083305 (2011).

[14] **K. W. Leo**, T. Adachi, K. Okazaki, T. Arai, A. Tokuchi, and K. Takayama, " A Permanent Magnet ECRIS with a Solid-state Marx Generator Driven Chopper for

the KEK Digital Accelerator", *Proceedings of the 14th International Conference on Ion Source*, Giardini-Naxos, Sicily, Italy, September (2011).

[15] **K. W. Leo**, T. Adachi, T. Arai, and K. Takayama, "Einzel Lens Chopper and Behavior of the Chopped Beam in the KEK Digital Accelerator", submitted to *Phys. Rev. AB-ST (2012).*

2. KEK-Digital Accelerator

2.1 Induction Synchrotron

The concept of the induction synchrotron (IS) was proposed by Takayama and Kishiro in 2000 [1] to overcome the following principle limitations posed by RF acceleration.

(1) A band-width limitation

Usually resonant frequency of a resonant cavity and RF amplifier is changed by order of single-digit but not beyond that.

(2) Limited acceleration phase

In principle, the acceleration phase is a region of positive voltage growing in value over time.

(3) Localized higher line density

An essential aspect of the phase stability tends to increase the local beam intensity around the bunch center.

The principle of the IS is based on the acceleration and confinement of particles, which are independently achieved by using two transformers instead of the resonant cavity employed in a conventional RF synchrotron. The rectangular-shaped voltage pulses are obtained from a one-to-one transformer, so-called induction cell. It is energized by a switching power supply, which is fired by triggering solid-state switching elements (power MOSFET).Trigger signal is generated in a digital signal processor (DSP), synchronizing with the detected signals. Consequently, acceleration and confinement are synchronized automatically with respect to the beam revolution [2]. The principle is described in Fig. 2.1a, in contrast with the conventional RF synchrotron.

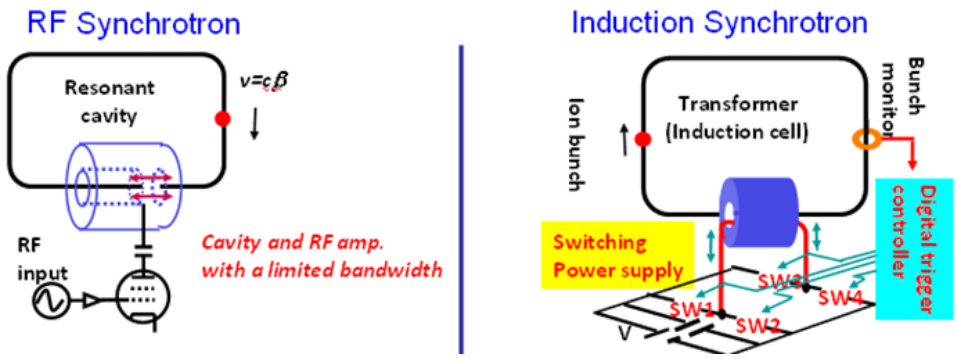

Figure 2.1a: Schematic of the conventional RF synchrotron and induction synchrotron

This characteristic allows any ions to be accelerated with their possible charge state from an extremely low energy to high energy in a single ring. Thus an injector-free synchrotron is realized as shown in Fig. 2.1b [2].

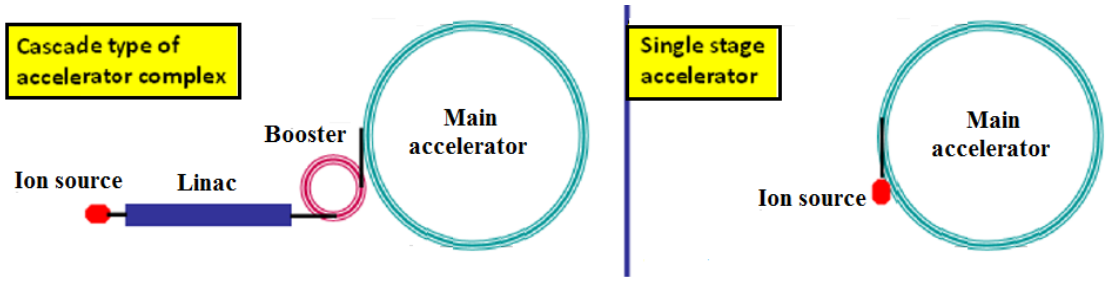

Figure 2.1b: Accelerator complex configuration (Left: Cascade type accelerator complex based on the RF synchrotron, Right: Single stage accelerator complex based on the induction synchrotron)

The acceleration and longitudinal confinement of particles are independently carried out with pulse-voltages rather than a sinusoidal voltage as shown in Fig. 2.1c. A long pulse voltage generated in the induction acceleration cells provides the acceleration voltage. A pair of pulse voltages with opposite sign generated in other induction cells is used to providing the longitudinal focusing forces for beam confinement [2, 3]. This characteristic allows us to increase the particle number by expanding the bunch length, while the stable region is limited in the conventional RF accelerator.

Figure 2.1c: Voltage profile in the conventional RF synchrotron and induction synchrotron

The equivalent circuit of the induction acceleration system is shown in Fig. 2.1d. A power supply (DC-PS) energizes the switching power supply, and the high-voltage pulses are transferred into the induction cell through a 120Ω transmission line. A matching resistor (*Z*) is connected in parallel to the induction cell so that voltage reflection is reduced. *R* is resistance corresponding to core loss and eddy current loss, *L* is the inductance of magnetic material and *C* is the stray capacitance, which is determined from the cell structure and acceleration gap. This induction cell is operated as a one-to-one transformer. The beams are exerted by the same voltage as that supplied by the DC-PS [2].

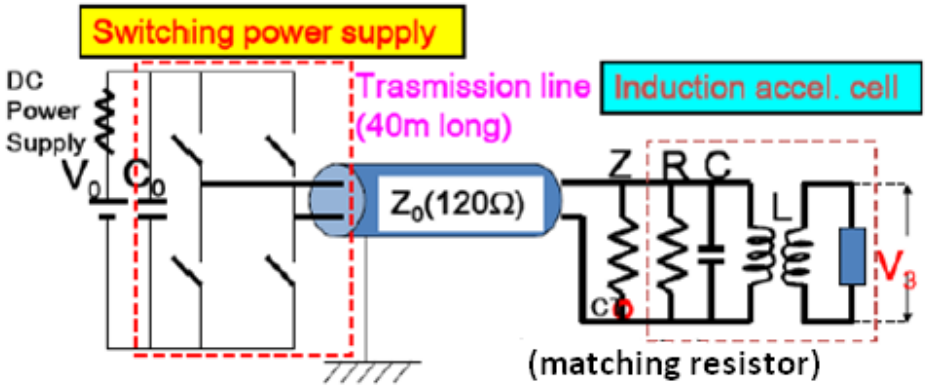

Figure 2.1d: Equivalent circuit of the induction acceleration system

2.2 Digital Accelerator Complex

The digital accelerator (DA) [2, 4] complex has been renovated from the former KEK 500 MeV booster, which was shut down in March 2006 after 35 years of operation as the

injector of the KEK 12-GeV proton synchrotron. The lattice parameters are summarized in Table 2.1 [2].

Table 2.1: DA ring lattice parameters

Parameters	
Lattice (1 period)	FDFO
Super period	8
Average radius	6 [m]
Bending radius	3.3 [m]
Magnet length	2.5918 [m]
Length of the drift space	2.1206 [m/period]
Q_X (injection-ext)	2.17–2.09
Q_Y (injection-ext)	2.30–2.40
β_X(max/ min)	3.8/1.5 [m]
β_y (max/ min)	8.2/1.5 [m]
Chromaticity (ξ_x/ξ_y)	-1.06/- 5.73
Momentum compaction, α	0.197
Transition gamma, γ_T	2.25
Dispersion function, η_{max}	1.43 [m]

Main components of the KEK-DA complex are listed below, and the layout is shown in Fig. 2.2a.

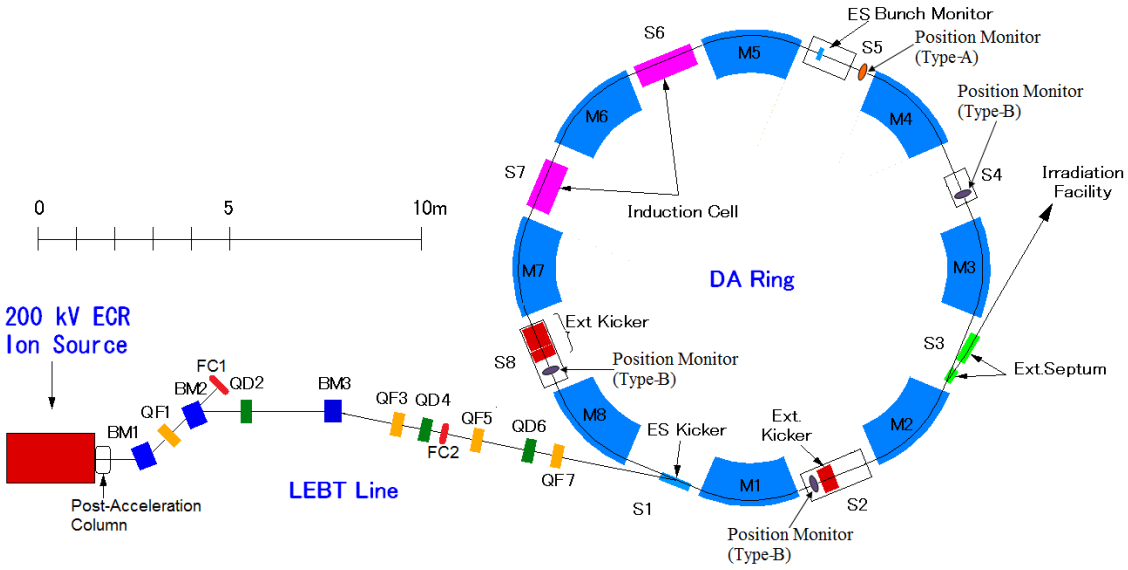

Figure 2.2a: Layout of the KEK digital accelerator

2.2.1 Ion Source

Expecting the stability and capability to produce various ion beams with higher charge state, an electron cyclotron resonance ion source (ECRIS) has been developed as an ion source for the KEK-DA [5, 6, 7]. It is embedded inside the high voltage platform (HVP). The details will be described in chapter 3. The KEK-DA ECRIS is operated in a pulse mode, a 5 ms-long ion pulse is generated at a repetition rate of 10 Hz [6]. An Einzel lens chopper located just after the extraction electrode is used to take optics matching in the transverse direction and chop the beam into a fractional beam with a desired pulse length [7, 8].

2.2.2 Low Energy Beam Transport Line (LEBT)

An ion beam propagating from the Einzel region is accelerated to 200 kV through the post acceleration gap of the HVP and transported to the DA ring through the LEBT of 16 meter long. It consists of 3 bending magnets, 7 quadrupole magnets [5], and 6 steering magnets. In addition, two Faraday cups, FC1 and FC2, are installed to measure a beam current, as shown in Fig. 2.2a. The result of current measurement will be compared with a simulation in Chapter 6.

2.2.3 Digital Accelerator Ring

The KEK-DA is basically a rapid cycle synchrotron. The main components such as the vacuum and magnet system of the booster ring are used as they are. The existing RF cavities were replaced by the induction cells and the power supply for energizing those induction cells, which had been used in the first demonstration of induction synchrotron, were reconnected there [2].

2.2.3.1 Lattice

The DA ring consist of eight FDF type combined function magnets with the lattice parameters as shown in Table 2.1 and beta functions and dispersion function are shown in Fig. 2.2.3.1a.

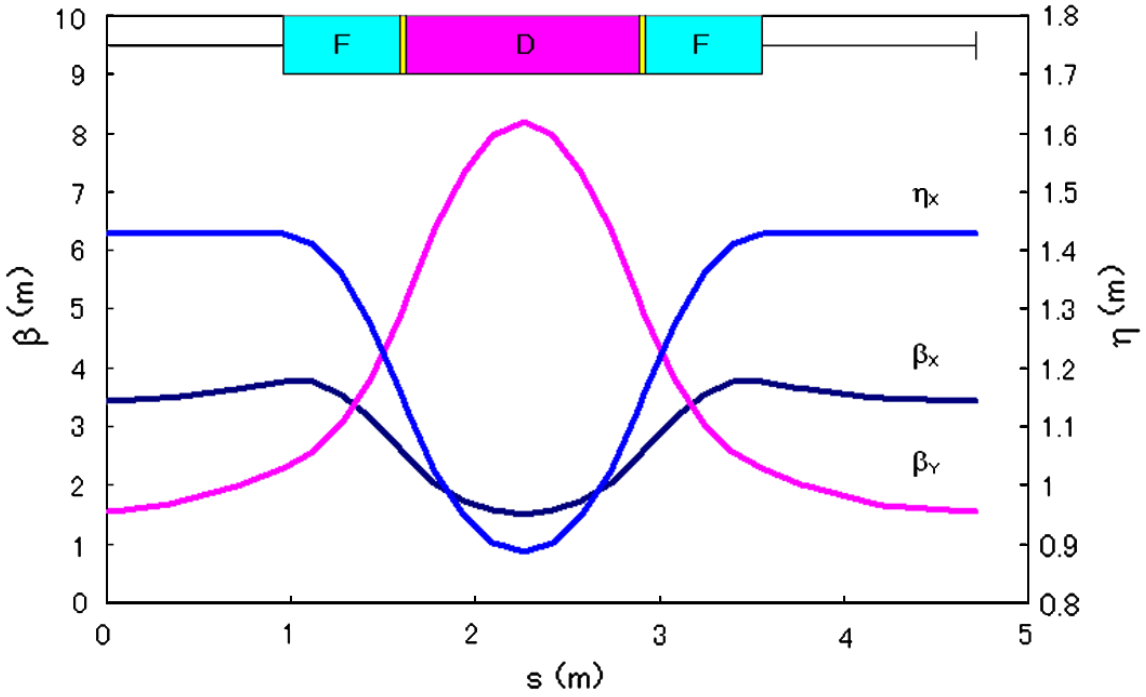

Figure 2.2.3.1a: Beta functions and dispersion function [2]

2.2.3.2 Main magnet

The main magnets as shown in Fig. 2.2.3.2a have an FDF structure, in which a D sector is sandwiched between F sectors [2]. The D sector and the F sectors are connected by a T sector, which has a transient structure. All sectors are fabricated by using an oriented low-carbon, low silicon steel of 0.35 mm thickness [2].

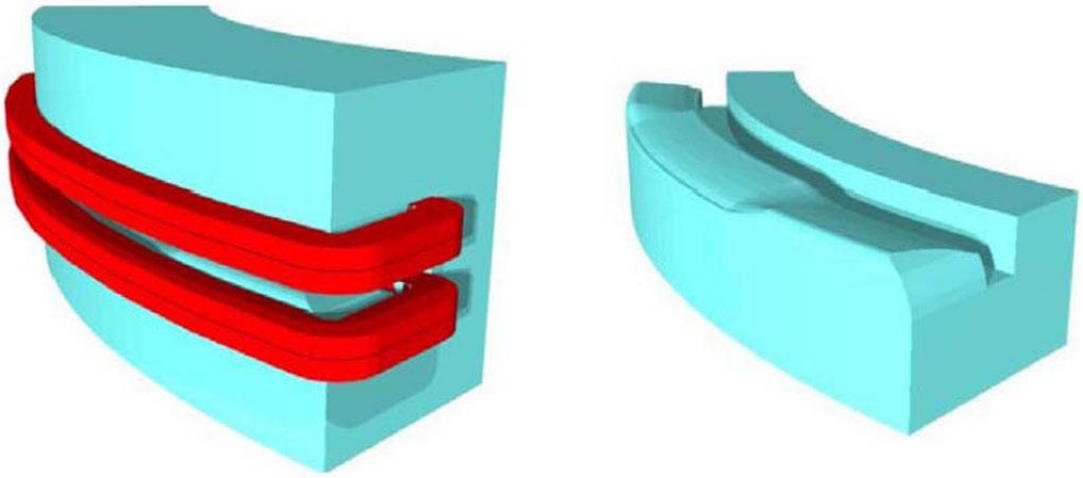

Figure 2.2.3.2a: Left: Schematic view of the main magnet and Right: Its lower half magnet core [2]

2.2.3.3 Power supply

Eight magnets are installed inside the DA ring and one monitor magnet is placed in the power supply building. All of them are excited at a repetition rate of 10 Hz in a resonant network circuit as shown in Fig. 2.2.3.3a [2]. The resonant network comprises three meshes, each of which contains a series inductance of three magnets and a parallel circuit consisting of a resonant capacitor and an inductance from a secondary winding of a choke transformer. The primary winding and all secondary windings of the choke have a common iron core, so that close coupling of each resonant mesh is realized. A DC power supply (DCPS) is connected to the choke transformer secondary windings in one mesh and feeds a bias current to all magnets. An AC power supply is connected to the choke's primary winding and provides AC power which is dissipated in the resonant circuit [2].

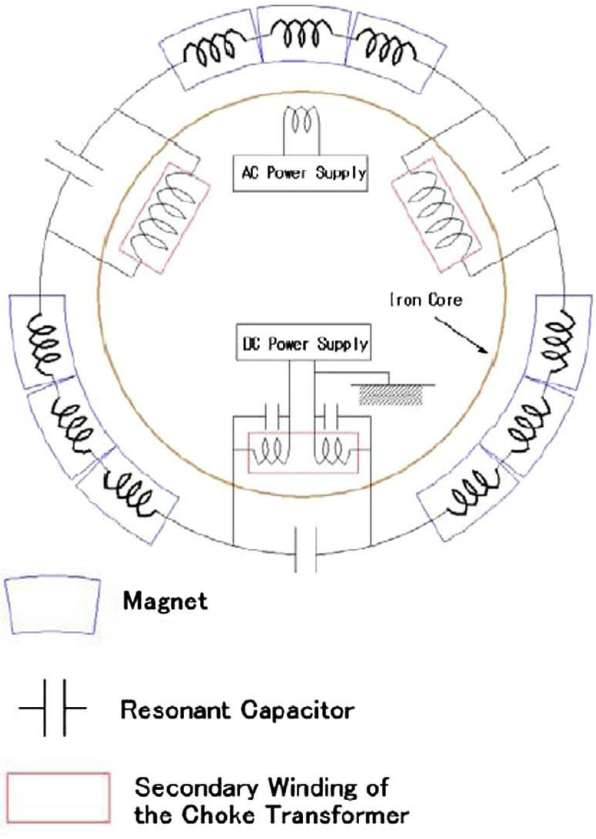

Figure 2.2.3.3a: Resonant network for excitation of the KEK-DA main ring [2]

2.2.4 Acceleration System

2.2.4.1 Induction cell

Presently, 9 induction cells in total have been installed in the KEK-DA ring. The magnetic material of the induction cell is the Finemet® FT-3M. It is a nano crystalline alloy of very high relative permeability, $\mu \sim 10^4$. The magnetic core is cooled by silicon oil. Each induction cell consists of 6 Finemet® bobbins as shown in Fig. 2.2.4.1a [2].

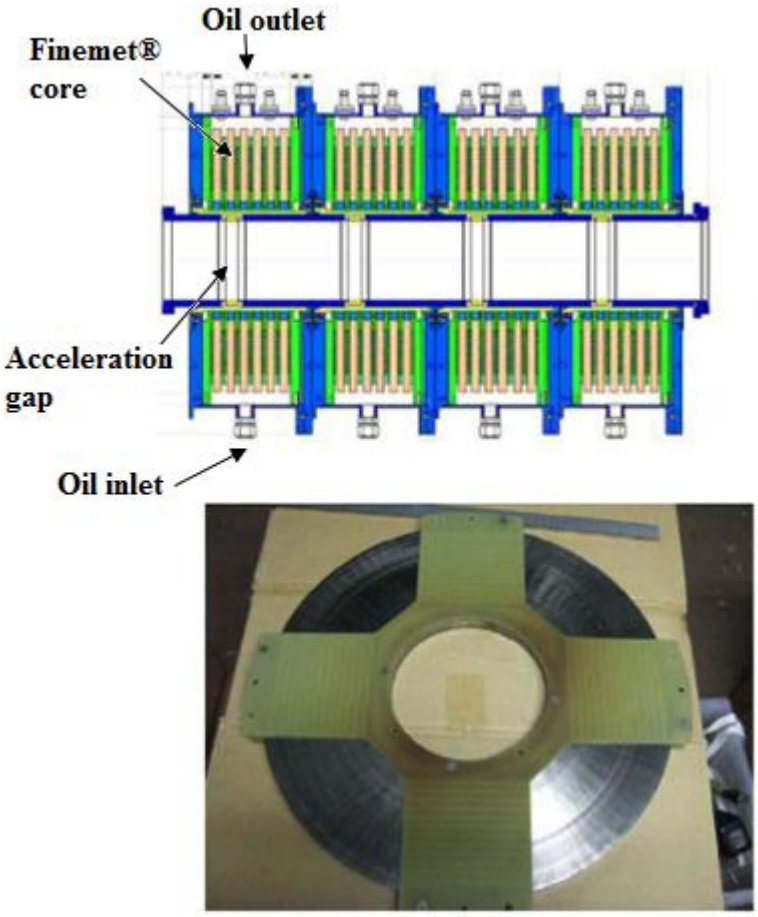

Figure 2.2.4.1a: Cross-section view of the Induction cell (upper) and magnetic core bobbin and G-spacer with oil flow channels (bottom) [2]

2.2.4.2 Switching power supply (SPS)

One of the key components of KEK-DA is a switching power supply for induction acceleration. The SPS, which modulates a voltage of a capacitor charged up by the DC power supply, is operated in a full bridge circuit. The single switching arm shown in Fig. 2.2.4.2a consists of seven power MOSFETs which are connected in series. Its switching frequency capability is~1 MHz with an output voltage of 2.5 kV and peak current of 20 A. In this setup, the seven MOSFETs sharing the high voltage must be individually isolated from the ground. The gates of these MOSFETs are turned on and off by gate signals, which are generated in the control system and delivered through optical fibers. The power for the MOSFET driving circuit is provided through a DC-DC converter with an extremely low capacitance, because the source-drain voltage balance between individual MOSFETs is strongly dependent on the effective capacitance in the circuit [1].

Fig. 2.2.4.2a: A photo of the SPS with seven MOSFETS in a single arm

2.2.5 Injection System

An electrostatic kicker as shown in Fig. 2.2.5a was developed to deflect an ion beam into the DA ring orbit. The electrostatic kicker deflects the beam horizontally. Three subsidi-

ary electrodes are inserted symmetrically between the high-voltage electrode and the ground electrode. These electrodes are connected to each other by voltage dividing resistors to obtain a linear voltage drop, which ensures field uniformity throughout beam passage [2, 9]. In addition, the kicker must be turned off within the single revolution time just after the injection to prevent the remained field from disturbing the circulating beam. As shown in Fig. 2.2.5b, the fast falling time and charge up within the acceleration cycle (100 ms) are realized. The kicker voltage timing is synchronized with the operation of KEK-DA at 10 Hz repetition rate.

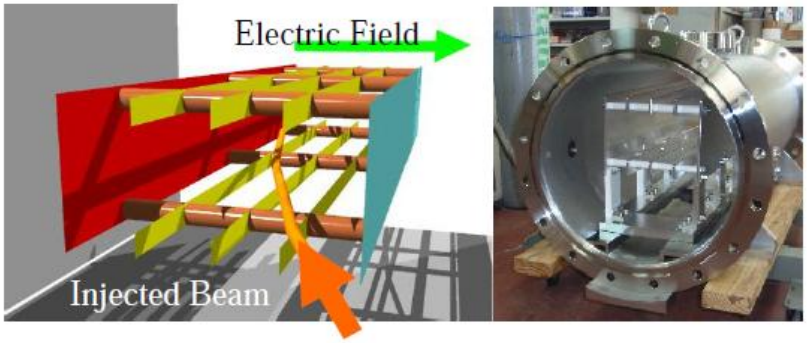

Fig. 2.2.5a: Schematic and photograph of the electrostatic kicker for KEK-DA [8]

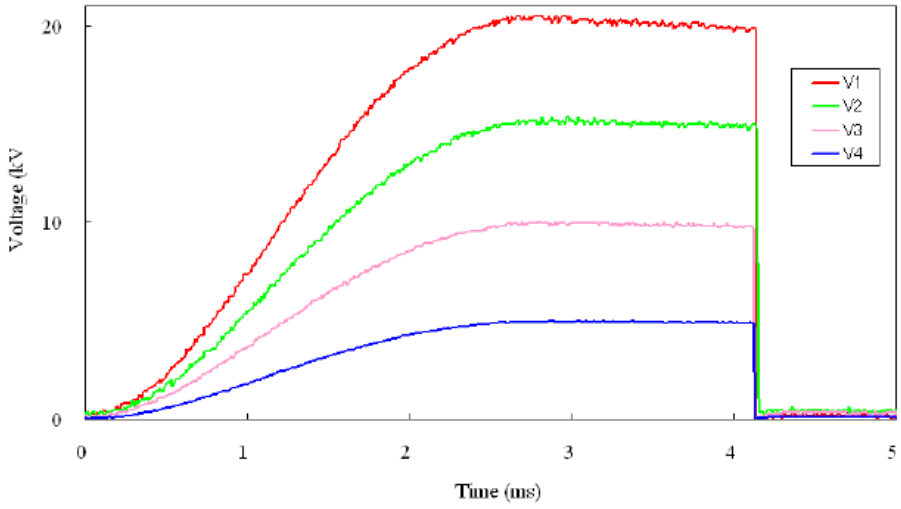

Fig. 2.2.5b: Voltage waveform measured at the kicker electrode [2]

2.2.6 Extraction System

The extraction system consists of four kicker magnets and two septum magnets, which had been used for the KEK 500 MeV booster synchrotron [2]. The excited kicker magnets kick the beam into the core gap of the septum magnets. Thus, a beam can be extracted from the DA ring with a further aid of septum magnets. Figure 2.2.6a shows the extraction system and beam envelope in the corresponding region [2].

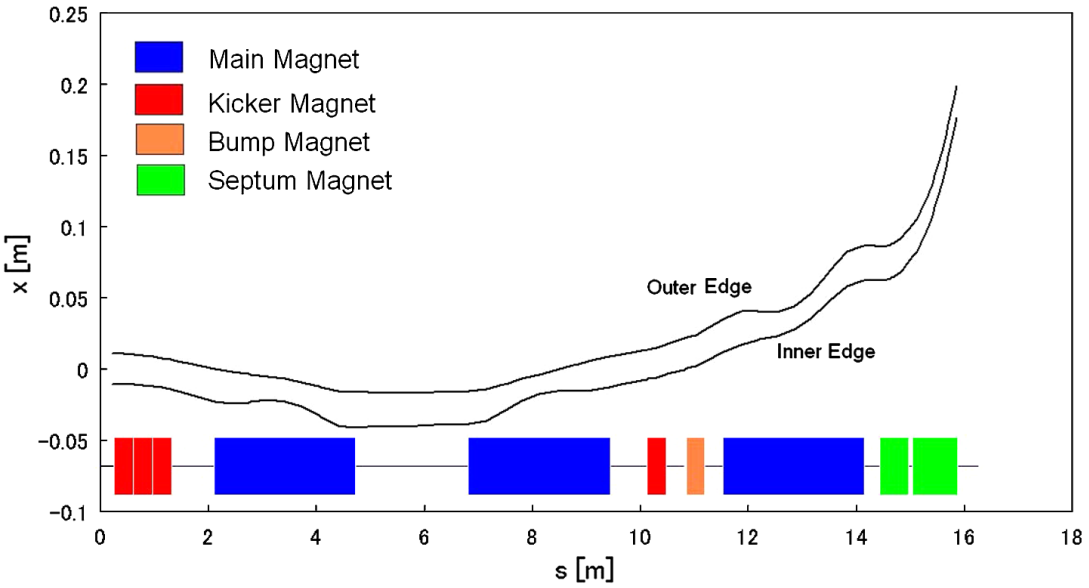

Fig. 2.2.6a: Extraction system and the beam envelope [2]

The septum magnets were modified, which is removed from the vacuum chamber and excited in air. This reduces outgas from magnet cores and excitation coils and reduces the total out gassing area [2]. New vacuum ducts have been developed and inserted inside the pole gap which is shown in Fig. 2.2.6b.

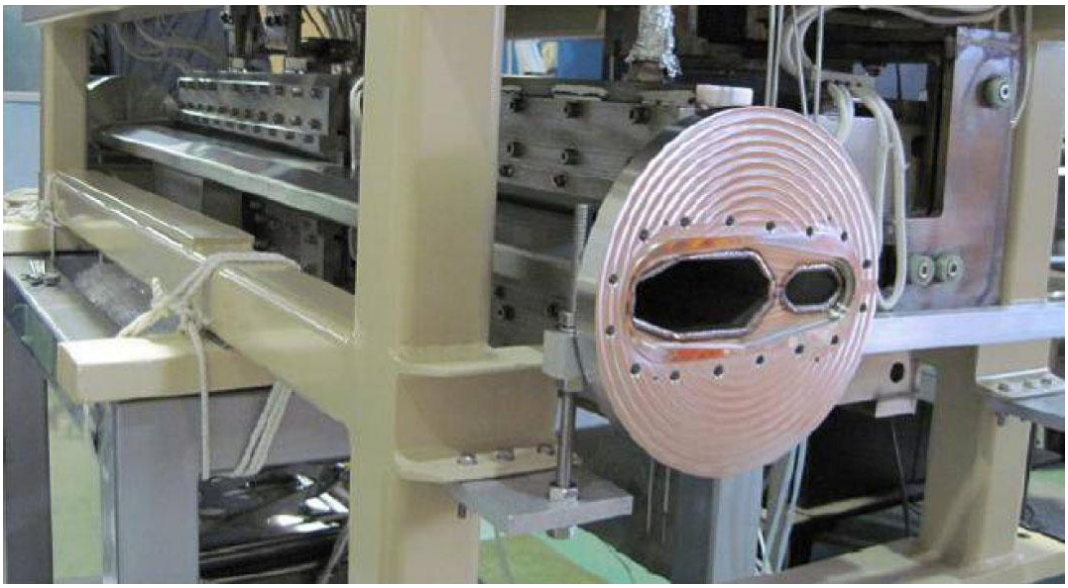

Fig. 2.2.6b: Septum magnet and new vacuum ducts (The left duct is for the circulating beam and the right duct is for the extracted beam) [2]

2.2.7 Diagnostic System

In the KEK-DA ring several diagnostic devices, such as an electrostatic bunch monitor and four position monitors are installed. The electrostatic bunch monitor is simply a cylindrical electrode, in which the signal is induced when a pulse beam is passing through the electrode. The induced signal is amplified and transmitted into the control room. Two types of position monitors have been installed into the KEK-DA ring. Those position monitors consist of four plates but with different plate shape. They are shown in Fig. 2.2.7a and Fig. 2.2.7b, respectively. The position monitor is utilized to measure the transverse beam position. The induced signal is also transmitted into the control room after amplification.

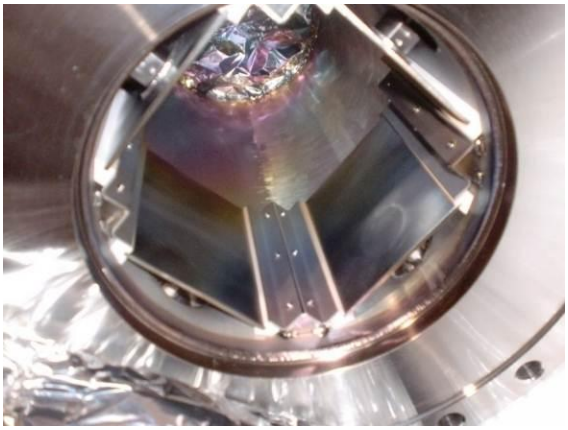

Figure 2.2.7a: Position monitor (Type-A)

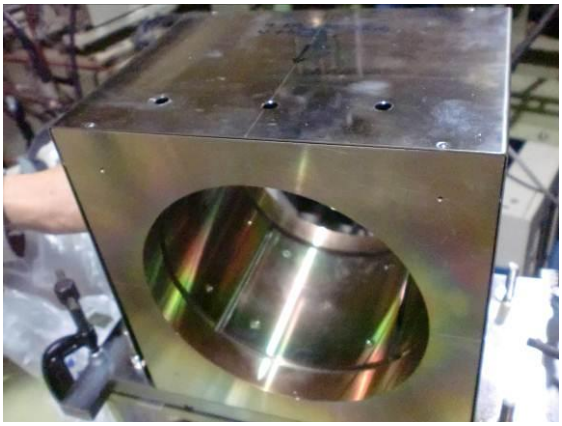

Figure 2.2.7b: Position monitor (Type-B)

References

[1] K. Takayama, and J. Kishiro, "Induction Synchrotron", *Nucl. Inst. Meth. A***451**, 304 (2000).

[2] T. Iwashita, T. Adachi, K. Takayama, T. Arai, Y. Arakida, M. Hashimoto, E. Kadokura, M. Kawai, T. Kawakubo, Tomio Kubo, K. Koyama, H. Nakanishi, K. Okazaki, K. Okamura, H. Someya, A. Takagi, A. Tokuchi, **K. W. Leo**, and M. Wake, "KEK Digital Accelerator", *Phys. Rev. AB-ST* **14**, 071301(2011).

[3] K. Takayama and R. Briggs (*Eds.*), Induction Accelerators, Springer, ISBN 9783642139161.

[4] K. Takayama, Y. Arakida, T. Iwashita, Y. Shimosaki, T. Dixit, and K. Torikai, "All-Ion Accelerators: An Injector-Free Synchrotron", *J. Appl. Phys.* 101 (2007) p. 063304.

[5] K. Takayama, T. Adachi. T. Arai. A. Takagi, **Leo Kwee Wah**, T. Kikuchi, K. Okazaki, and Zhang Kaizhi, "Ion Source and Low Energy Beam Transport for KEK Digital Accelerator", *Proceeding of IPAC10*, May 23rd-28th, 2010 Kyoto, Japan, Pg. 579 (2010).

[6] **Leo Kwee Wah**, K. Takayama, T. Arai, K. Okazaki, A. Takagi, T. Adachi, K. Koyama, M. Wake, and Y. Arakida, "Permanent Magnet ECRIS for the KEK Digital Accelerator", *Proceedings of 19th International workshop on ECR Ion Sources* , August 23rd -26th, 2010 Grenoble, France, Pg. 150 (2010).

[7] **K. W. Leo**, T. Adachi, K. Okazaki, T. Arai, A. Tokuchi, and K. Takayama, " A Permanent Magnet ECRIS with a Solid-state Marx Generator Driven Chopper for the KEK Digital Accelerator", *Proceedings of the 14th International Conference on Ion Source*, Giardini-Naxos, Sicily, Italy, September (2011).

[8] **K. W. Leo**, T. Adachi, T. Arai, and K. Takayama, "Einzel Lens Chopper and Behavior of the Chopped Beam in the KEK Digital Accelerator", submitted to *Phys. Rev. AB-ST (2012).*

[9] T. Adachi, T. Kawakubo, and T. Yoshii, "Injection and Extraction System for the KEK Digital Accelerator", *Proceeding of IPAC10*, May 23rd-28th, 2010 Kyoto, Japan, Pg. 570 (2010).

3. KEK-DA ECRIS

3.1 Introduction

As reviewed in Appendix 1, various ion sources are available in the world. Individual ion sources, they have their own advantages and disadvantages as summarized in Table 1 (Appendix 1). Our requirements to the ion source are: stable production of multi-charged ions, good beam quantity (higher beam current) and quality (small beam emittance), low repetition rate with μs-pulse length, compact size to be embedded into a high voltage platform with low power consumption. With the comparison among those ion sources, EBIS/EBIT and ECRIS are the compatible ion sources which fulfil the requirement of the KEK-DA ion source. But within the cost and simplicity construction factors consideration, ECRIS is much cheaper and with much simple construction compared with EBIS/EBIT. In addition, the related x-band microwave components are available in the group. Therefore, an ECRIS has been selected presently as an ion source for the KEK-DA.

KEK-DA ECRIS was designed and constructed at 2008 [1]. The performance of the KEK-DA ECRIS has been optimized and the ion data record can be referred to Ref. [2]. The schematic view of the KEK-DA ECRIS and its specification [3, 4] are shown in Fig. 3.1a and Table 3.1. Record values of the beam current for various ion species are summarized in Table 3.2.

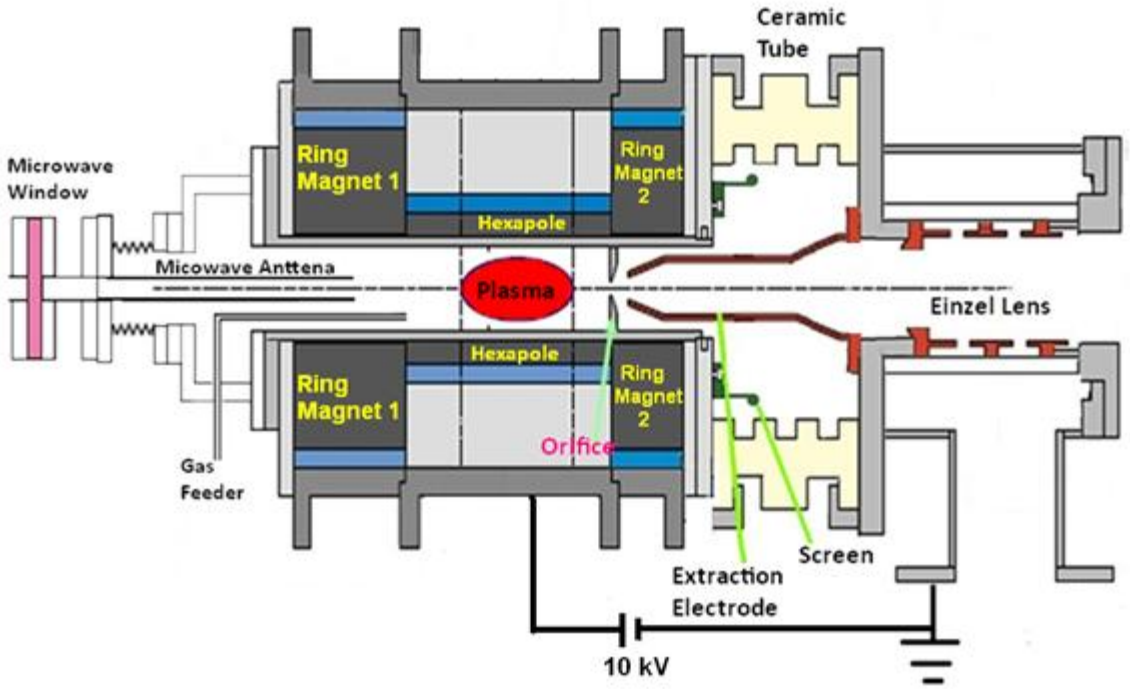

Figure 3.1a: Overview of the KEK-DA ECRIS

Table 3.1: Parameters of the KEK-DA ECRIS

Parameter	Figure
Frequency, f_{RF}	~9.35 GHz
Plasma chamber diameter, Φ_P	30 mm
Hexapole length, l	148 mm
Plasma volume, V_p	0.1 liter
Resonance magnetic flux density, B_{ECR}	0.334 T
Axial magnetic flux density at the injection side, B_{Inj}	0.710 T
Axial magnetic flux density at the extraction side, B_{Ext}	0.565 T
Axial magnetic flux density at minimum, B_{Min}	0.178 T
Radial magnetic flux density on surface of plasma chamber, B_{Rad}	0.597 T
Mirror ratio, $R=B_{Inj}/B_{ECR}$	2.13
Orifice diameter, Φ_{Ori}	2 mm

Table 3.2: Record currents for various ion beams provided by the KEK-DA ECRIS

Charge state	H	He	O	Ne
1	> 100	300	118	142
2		4	72	54
3			18	4.8
4			1.25	0.24
5				<0.1
6			0.08	<0.1
7				
8			0.25	
9				~0.1
10				~0.1

3.1.1 Microwave System

An x-band traveling wave tube (TWT) amplifier is utilized in the KEK-DA ECRIS with the operation frequency of 9.15-9.65 GHz and the maximum power of 800 W. A rectangular waveguide is used to couple with the TWT amplifier to the plasma chamber. In addition, a DC-cut device is installed between the waveguide and the plasma chamber to insulate the TWT from the chamber-side high-voltage. A ceramic window as a good microwave power transmitter is used to keep the plasma chamber in the vacuum condition. The KEK-DA ECRIS is operated at repetition rate of 10 Hz, this pulse mode operation can be realized by introducing a PIN diode as described in the next section.

3.1.1.1 Pulse mode operation

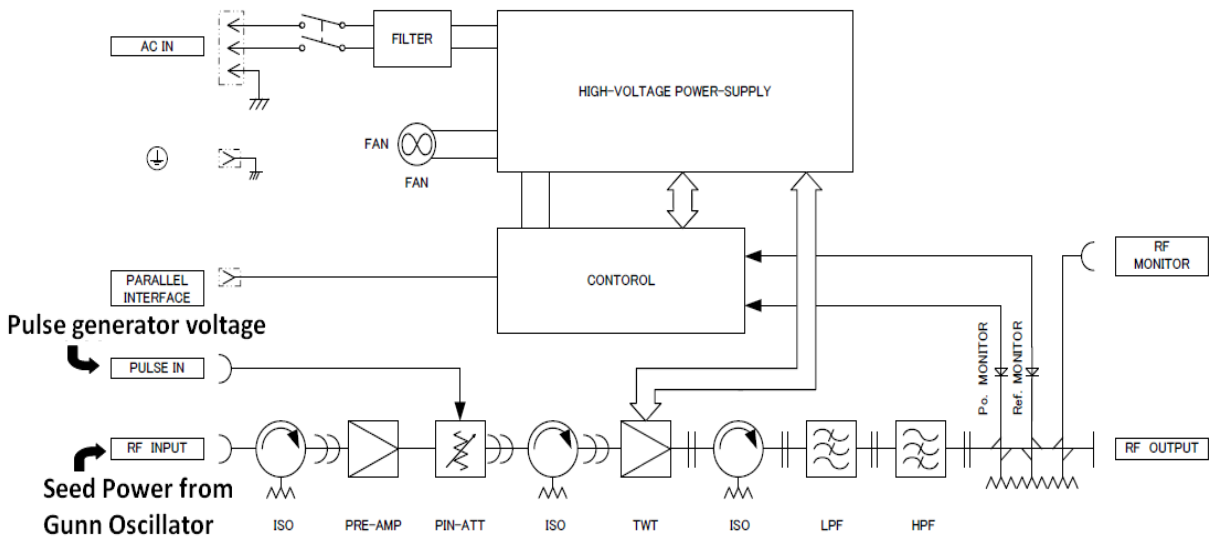

Figure 3.1.1.1a: Schematic diagram of TWT device (Pulse mode operation: Controlled by the pulse generator)

A seed power is transmitted from a Gunn Oscillator with a range of ~ few tens μwatt into the TWT for amplification. In addition, a pulse generator is used to control the amplifier gain in the PRE-AMP by controlling the PIN diode shown in Fig. 3.1.1.1a. Pulse voltage from the pulse generator is applied to this PIN diode. Namely resistance against microwaves of concern is changed by controlling bias current of the PIN diode, which is a function of an applied pulse voltage. This mechanism realizes a variable attenuator. Therefore by controlling the amplitude, pulse length and frequency of the pulse generator, the microwave power, beam length and repetition rate are adjusted simultaneously. The setup of the microwave system of the KEK-DA ECRIS is shown in Fig. 3.1.1.1b.

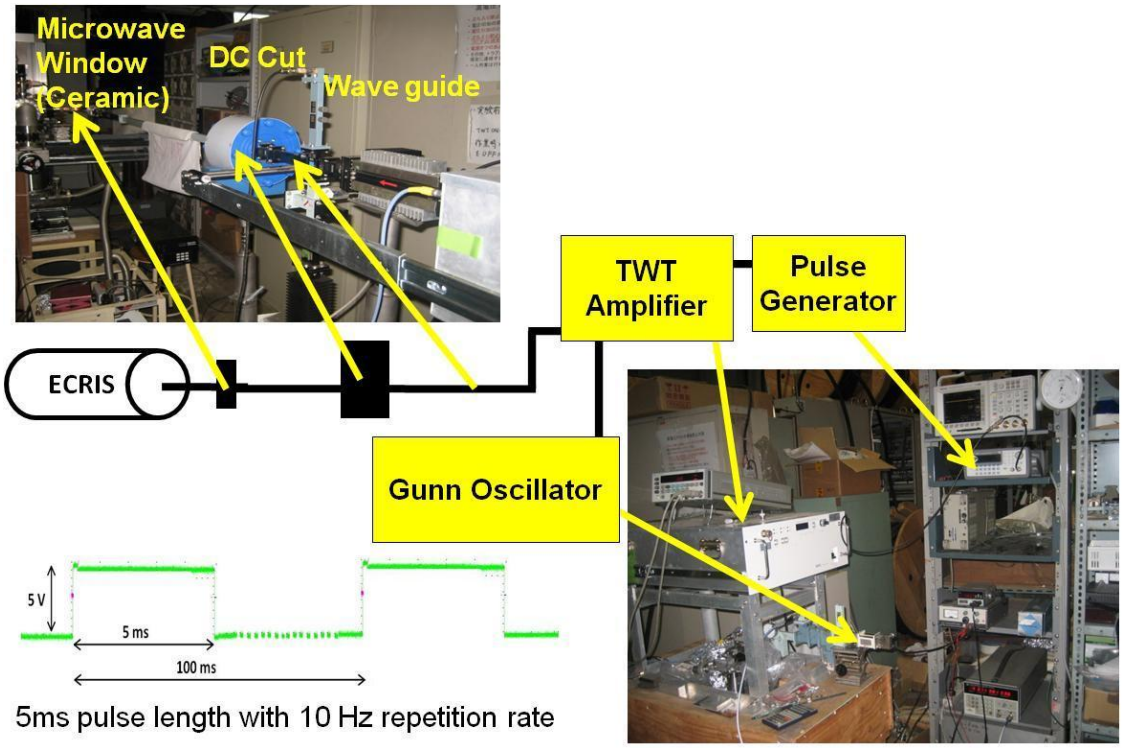

Figure 3.1.1.1b: Microwave system setup of the KEK-DA ECRIS

For the fundamental ionization mechanism of ECRIS, it takes few hundred μs for highly charged state ions to build up and around few ms to achieve a stable and saturated condition as shown in 3.1.1.1c. This time duration is 1000 times longer than the required pulse length of ~10 μs in KEK-DA, where so-called 1-turn injection method is employed. Thus, 1/1000 ion beam pulse extracted from the ECRIS must be chopped. In addition, typical duration to obtain higher beam intensity is ~ 5 ms. Therefore, our ECRIS is operated in the 5 ms pulse length and 10 Hz repetition rate.

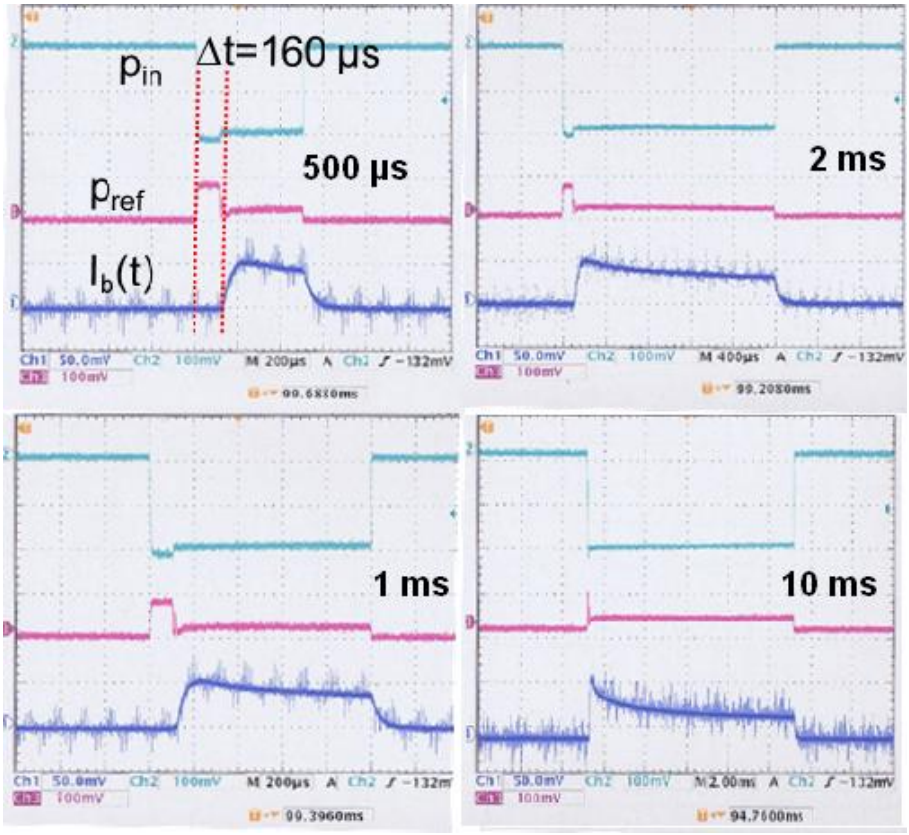

Figure 3.1.1.1c: Typical plasma built up time with various durations (Green line=Injected microwave power, Pink line=Reflected microwave power, Dark blue=Ion beam current)

3.1.2 Magnet System

For the KEK-DA, a permanent magnet fabricated by the NdFeB material (NEOMAX) was adopted for the ring and hexapole magnets due to the simplicity of the magnet installation, in which the cooling system and magnet power supply are excluded. Superposition of the axial and radial fields generated by the ring magnet and hexapole magnet is used for the plasma confinement as described in Appendix 2.

3.1.2.1 Axial magnetic field

The ring magnets for axial magnetic fields are assembled into both ends of the plasma chamber as shown in Fig. 3.1.2.1a. The axial magnetic field distribution was independently measured by the manufacturer (the Hitachi Metal Ltd) and at KEK. The result is plotted by the red line in Fig. 3.1.2.1b. By using the POISON/PANDIRA code [5], an

axial magnetic field distribution was also simulated. Both results of field distribution are plotted by the blue line in the Fig. 3.1.2.1b and the flux lines are shown in Fig. 3.1.2.1c.

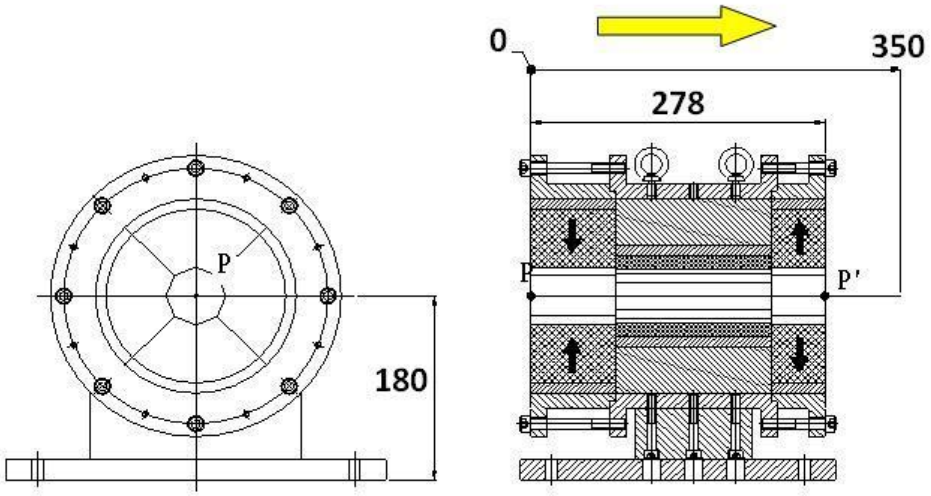

Figure 3.1.2.1a: Axial field distribution measurement through the KEK-DA ECRIS

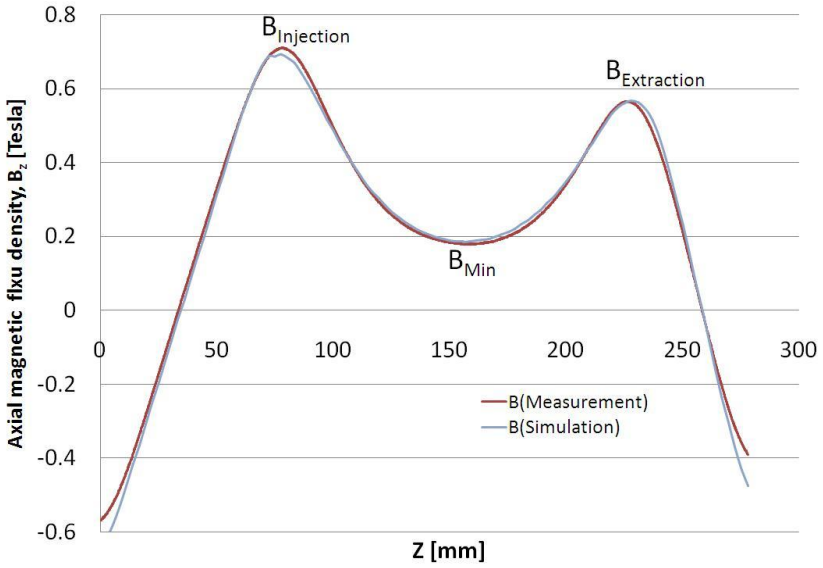

Figure 3.1.2.1b: Axial field distribution through the KEK-DA ECRIS. $B_{Injection}$=0.710 Tesla , $B_{Extraction}$=0.565 Tesla, B_{min}=0.178 Tesla

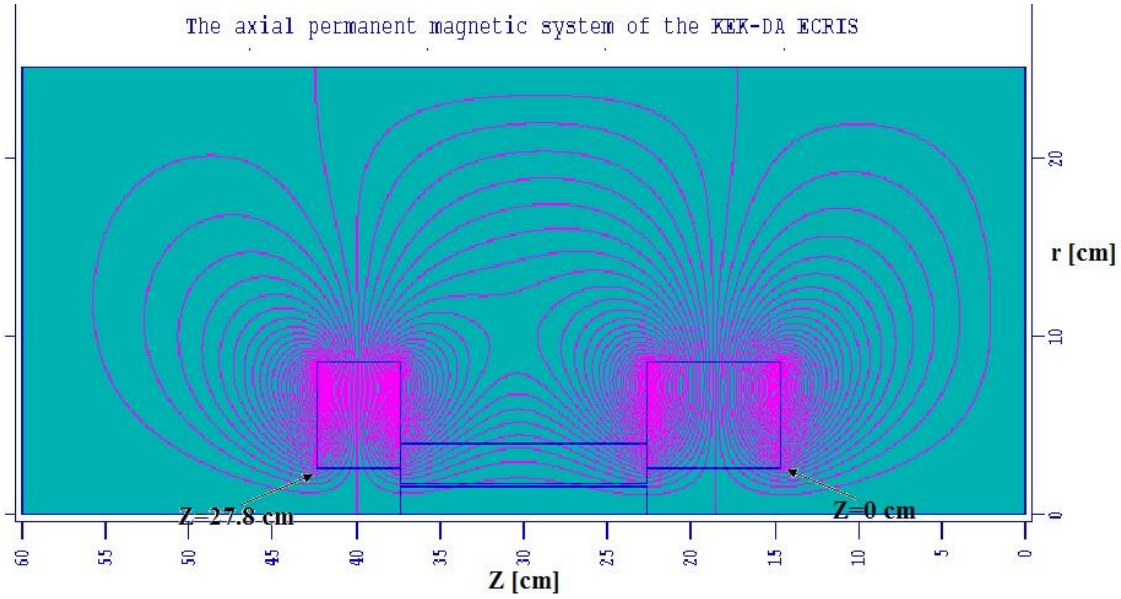

Figure 3.1.2.1 c: Flux lines of the axial magnet by Poisson/Pandira code

3.1.2.2 Radial magnetic field

The mechanical schematic view of the hexapole magnet for the KEK-DA is shown in Fig. 3.1.2.2a. In order to improve the performance of the ECRIS, an additional hexapole was inserted into the existing hexapole. In fact, this work had increased the radial magnetic field at the plasma chamber wall by ~58% improvement as shown in Table 3.2. The radial magnetic field distribution measured by the Hitachi Metal Ltd. is plotted by the red line in Fig. 3.1.2.2b. By using the POISON/PANDIRA code [5], a radial magnetic field distribution was simulated. The result is also plotted by the green line in the Fig. 3.1.2.2b and the flux lines are shown in Fig. 3.1.2.2c.

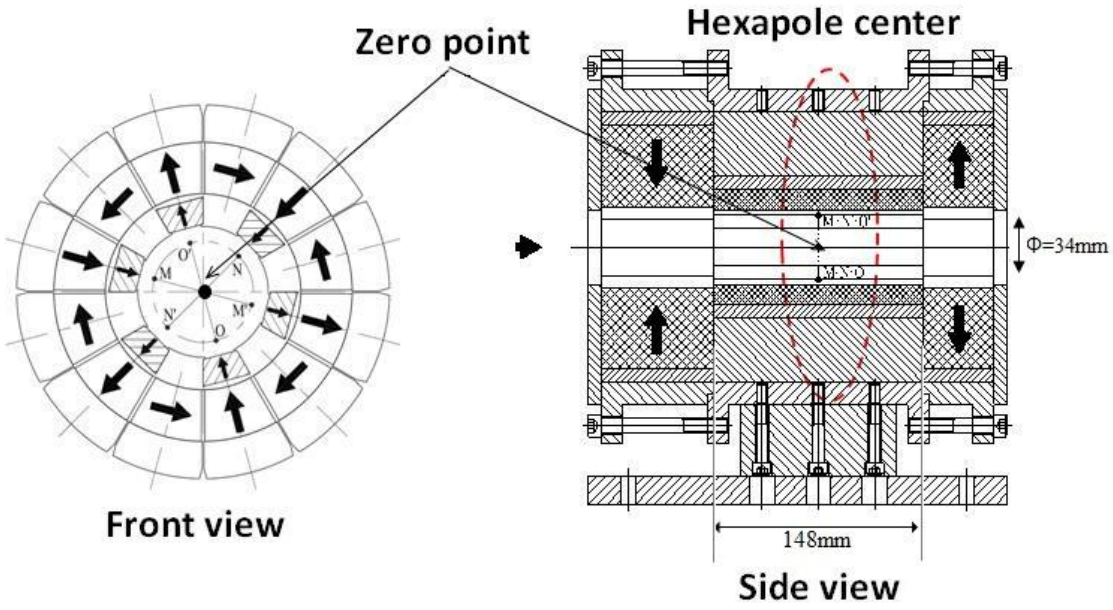

Figure 3.1.2.2a: Schematic view of the hexapole magnet for the KEK-DA ECRIS

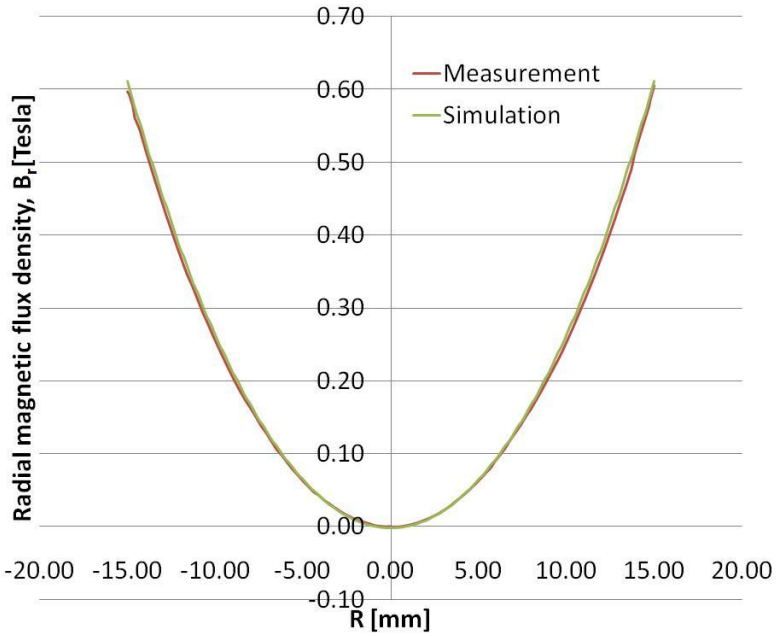

Figure 3.1.2.2b: Radial field distribution at center of the KEK-DA ECRIS

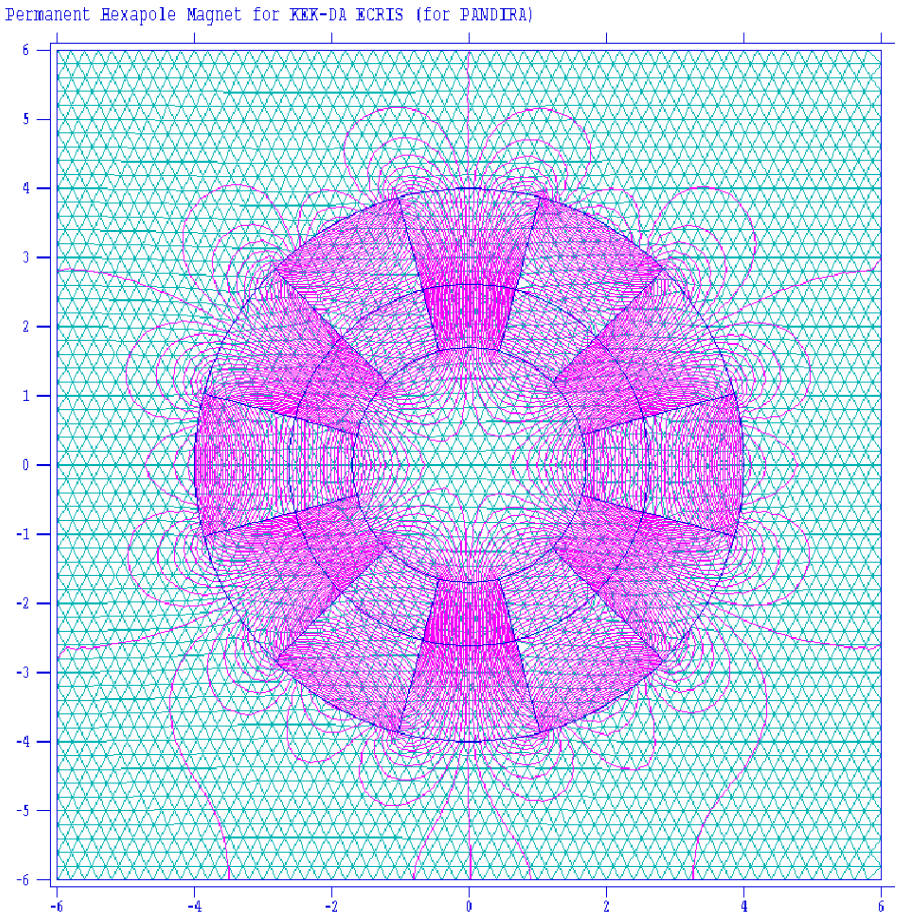

Figure 3.1.2.2c: Cross section and flux lines of the hexapole magnet by Poisson/Pandira code

3.1.3 Plasma Chamber

Originally, the plasma chamber of KEK-DA ECRIS is made of stainless steel, which has an inner diameter of 40 mm. For the KEK-DA ECRIS improvement, the stainless steel plasma chamber was replaced by the aluminum chamber expecting the higher secondary electron emission coefficient as discussed in Appendix 1. The chamber is usually cooled by water to prevent the permanent magnets from demagnetization due to heat conduction. Since the KEK-DA is operated with a repetition rate of 10 Hz, the ion beams are generated from the ECRIS fired with 5 ms-pulse length [2]. In such pulse operation, water cooling is not required. Consequently, the leaving space of the extra hexapole magnet [2] can be occupied with an aluminum plasma chamber of 30 mm in diameter.

3.1.4 Extraction System

The extraction system is a critical component to extract an ion beam from the ECRIS. Therefore, the design of the extraction geometry must be optimized precisely. In the present setup, the orifice of 2 mm diameter was installed into the plasma chamber with the extraction gap 10 mm and aperture of 7 mm diameter as shown in Fig. 3.1.4a. The extraction electrode was made of stainless steel.

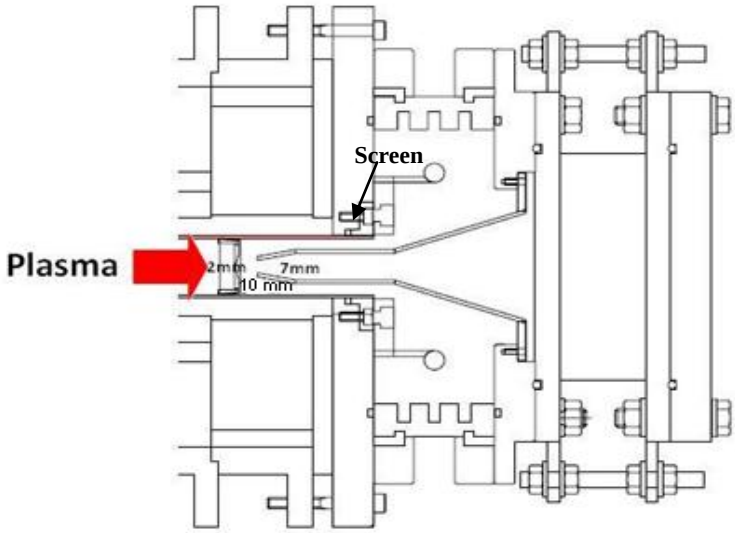

Figure 3.1.4a: Extraction system of the KEK-DA ECRIS

3.1.4.1 Screen protection

In addition, a screen was installed between the cathode and anode as shown in Fig. 3.1.4a. The purpose of the screen is to avoid sputtering effects that the inner surface of the ceramic might be coated with metal. In fact, this screen works very well to avoid the surface coating. Recently, our ECRIS has been operated for more than 1 year without being anxious about such effects. Fig. 3.1.4.1a shows metal coating on the ceramic surface before screen installation.

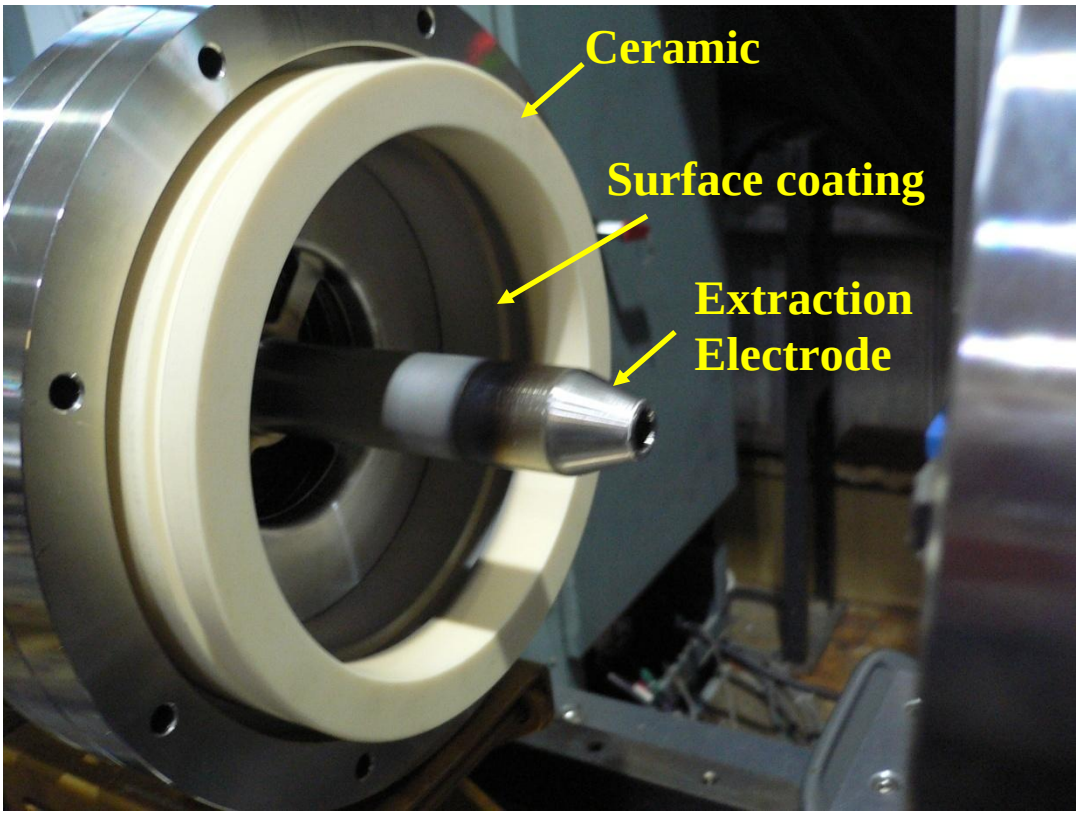

Figure 3.1.4.1a: Surface coating without screen protection

References

[1] H. Suzuki, Y. Arakida, T. Iwashita, M. Kawai, T. Kono, K. Takayama, K. Okazaki, and S. Inagaki, "ECR Ion Source for the KEK All-ion Accelerator", *Proceeding of EPAC08*, Pg. 442 (2008).

[2] T. Iwashita, T. Adachi, K. Takayama, T. Arai, Y. Arakida, M. Hashimoto, E. Kadokura, M. Kawai, T. Kawakubo, Tomio Kubo, K. Koyama, H. Nakanishi, K. Okazaki, K. Okamura, H. Someya, A. Takagi, A. Tokuchi, **K. W. Leo**, and M. Wake, "KEK Digital Accelerator", *Phys. Rev. AB-ST* **14**, 071301 (2011).

[3] **K. W. Leo**, T. Adachi, K. Okazaki, T. Arai, A. Tokuchi, and K. Takayama, " A Permanent Magnet ECRIS with a Solid-state Marx Generator Driven Chopper for the KEK Digital Accelerator", *Proceedings of the 14th International Conference on Ion Source*, Giardini-Naxos, Sicily, Italy, September (2011) .

[4] **K. W. Leo**, T. Adachi, T. Arai, and K. Takayama, "Einzel Lens Chopper and Behavior of the Chopped Beam in the KEK Digital Accelerator", submitted to *Phys. Rev. AB-ST (2012).*

[5] M. T. Menzel and H.K. Stokes, Use's Guide for the POISSON/SUPERFISH Group of codes, LA-UR-87-115, Loa Alamos (1987).

4. Einzel Lens Chopper

4.1 Background of the Einzel Lens Chopper Development

As mentioned in the early chapter, an ion beam extracted from the ion source must be chopped before injection into the KEK-DA ring. In the KEK-DA, an ECRIS is embedded on the 200 kV-HVP. The ion beam is extracted from the ECRIS and post-accelerated, then guided through the LEBT and injected into the ring.

The beam transport region may be divided into two regions: low energy region (< 200 kV) and high energy region (=200 kV). If a chopping device is installed somewhere downstream of the post-acceleration column, it must handle a beam of 200 kV. On the other hand, the chopping device being placed upstream handles the beam of lower extraction voltage from the ECRIS. For the convenience of discussion in this sub-section, we call the former region as high energy region and the latter as low energy region [1]. For each region, the chopper can be categorized into two types of transverse and longitudinal chopper as shown in Table 4.1

Table 4.1: Classification of the possible choppers

	High energy region	Low energy region
Transverse chopper	A	C
Longitudinal chopper	B	D

Figure of merits and demerits of these possible chopping schemes will be examined below.

4.1.1 Chopper in the High Energy Region

4.1.1.1 Transverse chopper (A)

In this scheme, a transverse electrostatic chopper [2] which is the same as the electrostatic injection kicker in the DA ring can be installed in the LEBT as shown in Fig. 4.1.1.1a. Its structure is shown in Fig. 2.2.5a in Chapter 2.

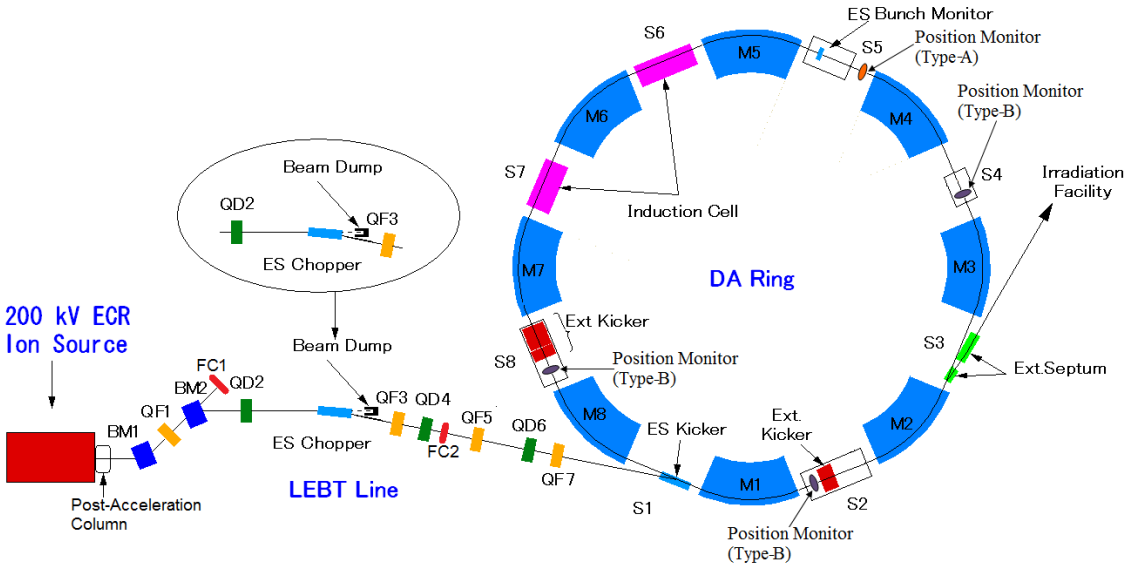

Fig. 4.1.1.1a: Schematic view of KEK-DA complex with ES chopper and kicker locations [2]

Although the electrostatic chopper and kicker have the same structure, their operation conditions must be different.

The chopper generates pulsed fields to deflect a small fraction of the incident beam pulse, while the kicker holds fields until the beam pulse tail finishes to be injected [2]. In the chopper operation, the beam is deflected and guided to the ring only for the pulse voltage duration (~ 5 μs). For the other time period (~ 5 ms) the beam is not deflected and guided to the beam dump. Voltage profiles for excitation of the chopper and kicker are shown in Fig. 4.1.1.1b.

Table 4.2: Characteristics of the chopper

Parameter	Figure
Deflection Angle	11.25 deg
Length	800 mm
Maximum Voltage	20 kV
Aperture (W x H)	200 x 100 mm^2

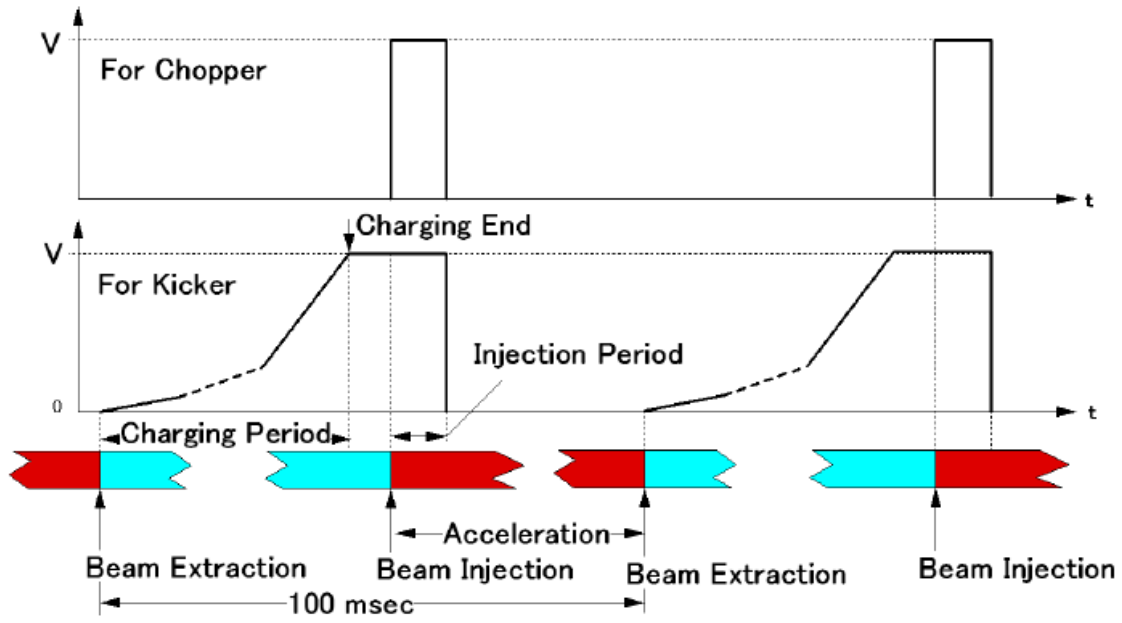

Fig. 4.1.1.1b: Voltage profiles for chopper and kicker [2]

In order to realize the chopper performance, two major components must be developed and other issues must be considered as:

a) Pulse voltage generator
   - Must provide μs-pulse voltage pulses with sharp rising and falling time at a repetition of 10 Hz.

b) Chopper head
   - Is newly fabricated with the same specification as that of the injection kicker component. And a large vacuum chamber must be also fabricated.

c) Beam dump
   - Is required to make loss of un-deflected beam localized, so that activation of various components of the LEBT by irradiation of high energy beam is avoided.

d) Radiation shielding
   - Is required to shield X-ray induced by some fraction of the chopped beam, which-passes through the chopper at transient time regions of the pulse voltage.

4.1.1.2 Longitudinal Chopper (B)

In this region, a high energy beam travels with a large velocity and the chopping device is required to produce a longitudinal gating voltage in a very fast transient time. For instance, the velocity of He^{1+} accelerated by 200 kV is ~$3.1x10^6$ m/s and the gating voltage must be 200 kV. Therefore, this type of chopper is eliminated from our consideration, since a high voltage pulse generator with a very short falling and rising times must be developed.

4.1.2 Chopper in the Low Energy Region

4.1.2.1 Transverse chopper (C)

A chopping device shown in Fig. 4.1.2.1a can be utilized as a transverse chopper. It is noted that this type of chopper is rather popular in the accelerator society. In this setup, a metal electrode or screen with an aperture hole for collimation is located just after the deflection plate which is driven by an RF pulse generator [1]. A fraction of the ion beam, which is not deflected or deflected within the screen hole, can propagate downstream. On the other hand, a largely deflected beam fraction hits the screen and cannot propagate downstream. For this setup, some space is needed within the low energy region and the possible location is just after the Einzel region and before the post-acceleration column. Even though the kinetic energy of a hitting particle is low, some of particles in the beam pulse hit the post-acceleration electrode directly and the resultant secondary electrons might trigger breakdown of the high voltage and also produce X-ray. Therefore, this chopper has been also eliminated from our consideration.

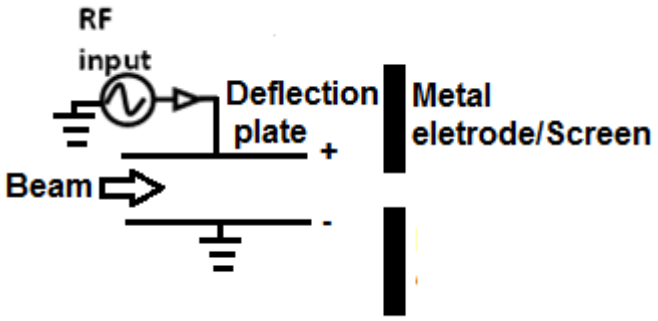

Fig. 4.1.2.1a: Transverse chopper at the low energy beam handling region and driven by an RF voltage

4.1.2.2 Longitudinal chopper (D)

There are two schemes for a chopper in the low energy region, as indicated by red circles in Fig. 4.1.2.2a [1]. The first is an extraction electrode system and the second is the Einzel lens. The idea by using the extraction electrode is closed to the novel ion bunching technique originated in Ref. 3 by S. C. Jeong and his collaborators, where ion pulse bunching has been demonstrated by introducing an additional bunching electrode between the orifice and extraction electrode [3]. Since in our case there is no space to insert an additional electrode working as a chopper electrode, the extraction electrode may be used.

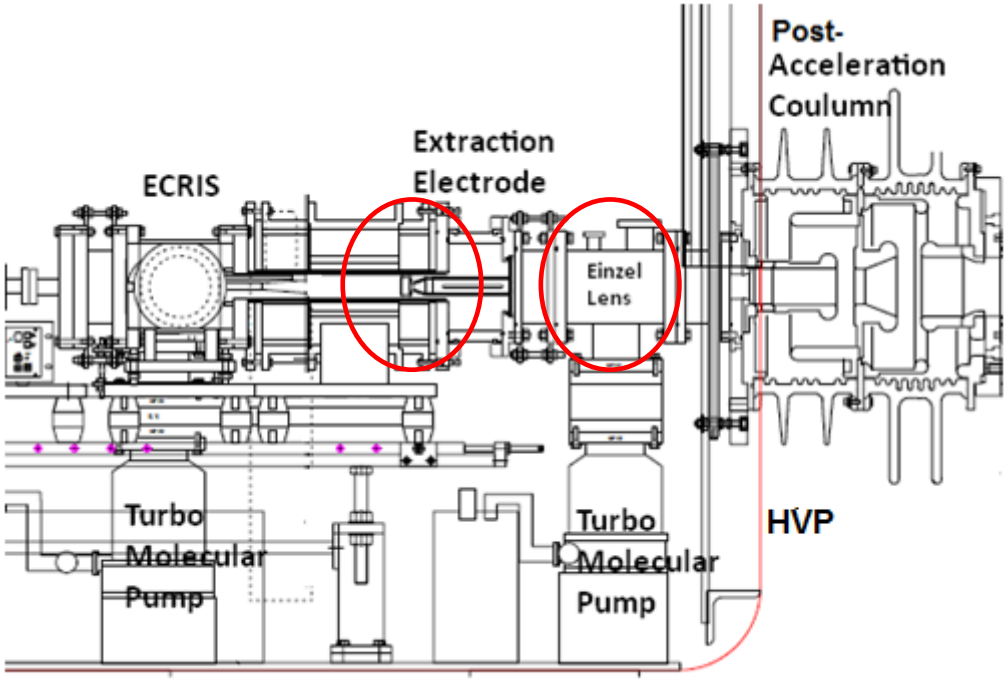

Fig. 4.1.2.2a: Possible candidates for chopper system

From the beam dynamic point of view, a beam matching condition must be optimized in the delicate balance between the extraction, Einzel lens and post-acceleration column voltages. Suppose an acceleration voltage of the post-acceleration column is constant

and the voltages for extraction electrode and Einzel lens are V_0 and V_1. If the voltages of those electrodes are modulated in time, the chopper performance can be realized as describe below:

a) Full modulation of extraction voltage
   i. V_0 is parameter, while V_1 = optimized constant voltage.
   ii. If $V_0 = 0$, the ion beam cannot be extracted from the ion source. While if V_0 = optimized extraction voltage for a time duration of τ, the ion beam is extracted from ion source with a well-defined beam size through the post-acceleration column and the LEBT during τ.

b) Small modulation of extraction voltage
   i. V_0 is parameter, while V_1 = optimized constant voltage.
   ii. If V_0 < optimized extraction voltage, an ion beam might be blown up due to the unmatched beam optics.
   iii. The unmatched beam hits the vacuum chamber. It might propagate to the post-acceleration column, but does not propagate downstream of the LEBT due to the unmatched condition of analyzer magnet.
   iv. On the other hand, if a positive voltage pulse ΔV is superposed over the fixed extraction electrode voltage for a time duration of τ to obtain V_0 = optimized extraction voltage , an ion beam can propagate with a well-defined beam size through the post-acceleration column and the LEBT during τ.

c) Einzel lens
   i. V_1 is parameter, while V_0 = optimized constant voltage.
   ii. If $V_1 > V_0$, an ion beam is blocked due to potential barrier of the Einzel lens and cannot propagate to the downstream.
   iii. If a negative voltage pulse ΔV is superposed over the middle electrode of an Einzel lens voltage for time duration of τ to obtain V_1 =optimized Einzel lens voltage, an ion beam can propagate with a well-defined beam size through the post acceleration column and the LEBT during τ.

In those cases, we need to prepare only a pulse voltage generator, while a new chopping device is not needed to be fabricated.

Since we require a width of a chopped beam to be a few μs, rising and falling time of the chopping voltage must be less than a hundred ns. Fast response of the extraction electrode is not expected due to a large stray capacitance which a whole system integrating the ion source has. Therefore the case a) has been eliminated from our consideration. In the case b), this section is close to the ECR plasma and the rejected beam could affect the ECR plasma by beam-plasma interaction. Thus, the decreasing of beam current might occur. Another possibility, an unmatched ion beam might propagate to the post-acceleration column and directly hit the high voltage electrode due to the large beam size. This bombardment causes a serious damage to the post-acceleration column with a high voltage supply, leading to high voltage breakdown. Therefore, an open space is required with more stable and fast response of chopping operation. Consequently, "Einzel lens" chopper should be a solution for the KEK digital accelerator and has been selected [1].

4.1.3 Summary

After elimination of the "extraction electrode", two possible candidates, which are transverse electrostatic (ES) chopper and Einzel lens chopper, are examined as our chopping device. Their characteristics are summarized in Table 4.3 as:

Table 4.3: Characteristics of possible choppers

Chopper	Cost	Vacuum deterioration	Radiation production	Required voltage of pulse generator
Transverse ES	●	●	●	●
Einzel lens	▲	▲	▲	◦

Remarks:

▲ = Low ◦ = Moderate ● = High

In the comparison between two possible choppers, it is very clear that the Einzel lens chopper has more figures of merit compared with the transverse ES chopper. Therefore,

an Einzel lens chopper has been developed and presently work as the beam chopper for KEK-DA with reliable and stable performances.

4.2 Overview of an Einzel Lens Chopper

An Einzel lens is a device commonly used to focus a low energy beam in the transverse direction. As shown in Fig. 4.2a, it comprises three cylindrical electrodes aligned coaxially, where the voltage is applied at the middle electrode and the other electrodes are grounded. In an ECRIS, the Einzel lens is usually equipped just after the extraction electrode [4, 5]. Such a construction is also similar to the KEK-DA ECRIS [4].

As mentioned above, the KEK-DA ring requires a short pulse beam with duration of a few μs, while the ECRIS cannot supply the beam with duration shorter than a few ms to assure its stable operation. Therefore, the extracted beam from the ECRIS must be chopped into the required pulse duration before injection to the ring. For its purpose, we have modified the voltage supplying circuit for the Einzel lens by introducing a Marx generator, so that a function of a longitudinal chopper is added to the Einzel lens. The details will be discussed in the following sections.

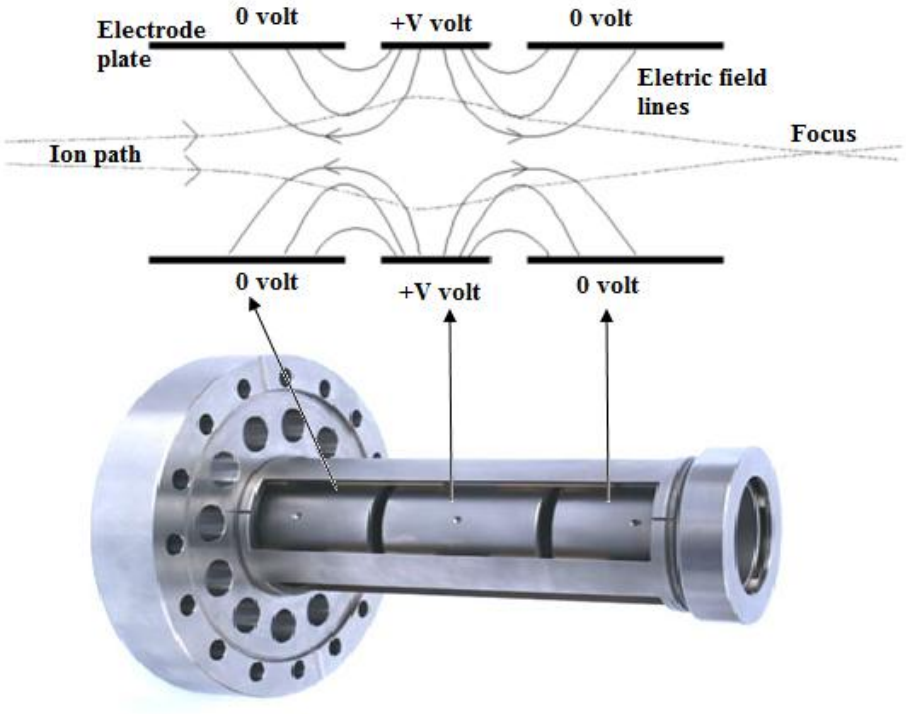

Figure 4.2a: Schematic view of an Einzel lens

4.2.1 Transverse Focusing Mechanism of an Einzel Lens

As mentioned above, an Einzel lens consists of three cylindrical electrodes. Both end-sides of electrode are grounded and the middle electrode is biased at a potential V. The equation of motions of a particle with mass, $m\ (=Am_N)$, and charge, $q\ (=Ze)$, in the axial symmetric electric field are given as:

$$m\frac{d^2r}{dt^2} = qE_r \tag{4.1}$$

$$m\frac{d^2z}{dt^2} = qE_z \tag{4.2}$$

Here, E_r and E_z are electric fields in the radial direction and the longitudinal direction, respectively.

Supposing that v_z » v_r, the Eq. (4.1) describes a transverse focusing effect and the Eq. (4.2) describes an acceleration effect. Let's introduce a path length, *s*, instead of the time,

t, as a reference to describe the beam motion. The first and the second derivatives with respect to t are converted to the following formula:

$$s \equiv vt\,, \qquad \frac{dr}{dt} = \frac{dr}{ds}v, \qquad \frac{d^2r}{dt^2} = \frac{d^2r}{ds^2}v^2 + \frac{dr}{ds}\frac{dv}{ds}v \tag{4.3}$$

By substituting the Eq. (4.3) into (4.1), the equation becomes:

$$\frac{dr'}{ds} + \frac{1}{v}\frac{dv}{ds} = \frac{qE_r}{mv^2} \; where \; r' = \frac{dr}{ds} \tag{4.4}$$

According to the energy conservation law, the particle velocity and its derivative are given as:

$$v = \sqrt{{v_0}^2 - \frac{2q}{m}V}$$

$$v = \sqrt{\frac{2q}{m}(V_0 - V)} \tag{4.5}$$

$$\frac{dv}{ds} = -\frac{q}{m\sqrt{\frac{2q}{m}(V_0 - V)}}\frac{dV}{ds} \tag{4.6}$$

$$= -\frac{q}{m\sqrt{\frac{2q}{m}(V_0 - V)}}\left(\frac{\partial V}{\partial r}r' + \frac{\partial V}{\partial z}\frac{dz}{ds}\right)$$

$$= -\frac{q}{\sqrt{2qm(V_0 - V)}}\left(\frac{\partial V}{\partial r}r' + \frac{\partial V}{\partial z}\frac{dz}{ds}\right)$$

Here, v_0 is an initial particle velocity and V_0=Extraction voltage.

By assuming that the s-direction is nearly equal to the z-direction, i.e. dz/ds~1, substitution of Eq. (4.6) into (4.4) gives the following equation.

$$\frac{d^2r}{ds^2} - \frac{r'}{2(V_0 - V)}\left(\frac{\partial V}{\partial r}r' + \frac{\partial V}{\partial s}\right) = \frac{E_r}{2(V_0 - V)} \tag{4.7}$$

Near the central axis, the transverse electric field is given approximately as:

$$E_r \approx -\frac{r}{2}\left(\frac{\partial E_z}{\partial z}\right)_{r=0} = \frac{r}{2}\left(\frac{\partial^2 V}{\partial z^2}\right)_{r=0} \tag{4.8}$$

By substituting Eq. (4.8) into (4.7), we obtain

$$\frac{d^2r}{ds^2} - \frac{r'}{2(V_0 - V)}\left(\frac{\partial V}{\partial r}r' + \frac{\partial V}{\partial s}\right) = \frac{1}{2(V_0 - V)}\frac{r}{2}\left(\frac{\partial^2 V}{\partial s^2}\right)_{r=0} \tag{4.9}$$

And rearrangement of Eq. (4.9) is done as follows:

$$\frac{d^2r}{ds^2} - \frac{r}{4(V_0 - V)}\left(1 + r'^2\right)\left(\frac{\partial^2 V}{\partial s^2}\right)_{r=0} = \frac{1}{2(V_0 - V)}\frac{\partial V}{\partial s}r' \tag{4.10}$$

Here, the following relation is used.

$$\frac{\partial V}{\partial r} = -E_r \approx \frac{r}{2}\left(\frac{\partial^2 V}{\partial s^2}\right)_{r=0} \tag{4.11}$$

If the 2nd order term, r'^2 is omitted, the resultant equation becomes the Hill's equation.

$$\frac{d^2r}{ds^2} + Kr = pertubation\ term \tag{4.12}$$

Here,

$$K \equiv -\frac{1}{4(V_0 - V)}\left(\frac{\partial^2 V}{\partial s^2}\right)_{r=0} \quad and \tag{4.13}$$

$$pertubation\ term = \frac{1}{2(V_0 - V)}\frac{\partial V}{\partial s}r' \tag{4.14}$$

As shown in the Eq. (4.13), the focusing action is proportional to the second order derivative of the electric potential along the central axis. An example of the potential distribution along the z-axis and its second derivative in the Einzel lens region is shown in Fig. 4.2.1a.

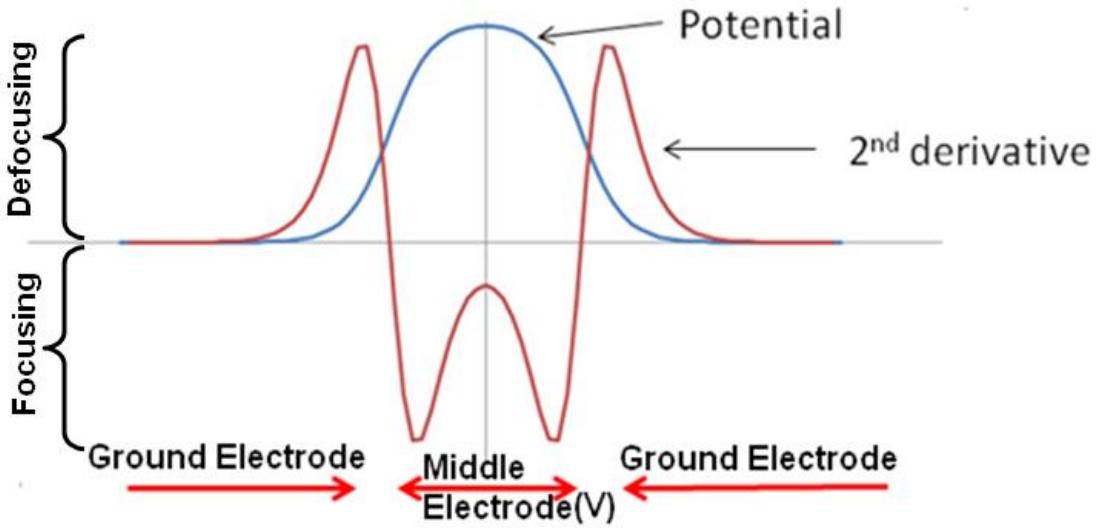

Figure 4.2.1a: Potential distribution and its second derivative in the Einzel lens region

The focusing/defocusing action is dominates at the edge of the electrodes as shown in the figure; a positive charged particle is defocused at the both edges of the ground electrodes and focused at the edges of the middle electrode. In addition, the Eq. (4.13) implies that the focusing effect is enhanced as the potential becomes higher. Hence, the Einzel lens is expected to give a net focusing effect.

4.3 Principle of an Einzel Lens Chopper

As mentioned above, the focusing action of an Einzel lens is controlled by a potential applied to the middle electrode. When the potential is kept at V_0 higher than the extraction voltage of the ECRIS, an ion beam is blocked at the entrance of the middle electrode. If a negative voltage pulse ΔV ($V_0+\Delta V < V_0$) is superposed into the middle electrode for a duration τ, the net voltage of the middle electrode is reduced. Hence, the ion beam can propagate beyond the Einzel lens region during τ. This is the essential performance of the Einzel lens chopper, which may be called as “longitudinal gating”. As shown in Fig. 4.3a, the whole system of the ECRIS and the Einzel Lens is embedded in the HVP with a total voltage of 200 kV [1, 6].

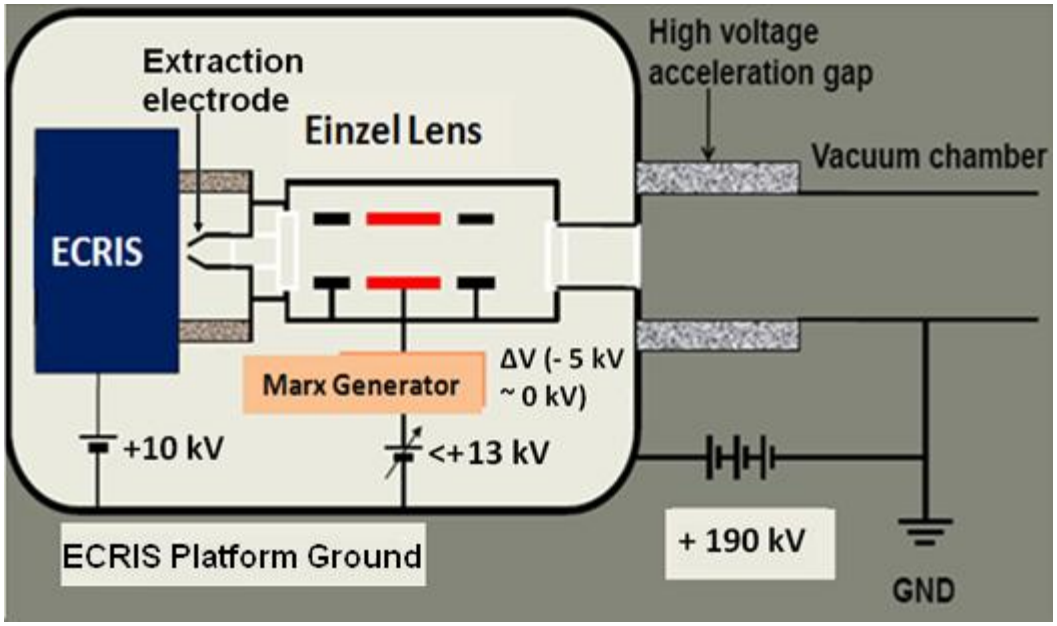

Figure 4.3a: ECRIS and the Einzel lens in the HVP [1]

4.4 Voltage Modulation System for an Einzel Lens Chopper

A voltage of the Einzel lens is modulated between a blocking voltage and the optimum focusing voltage. For this purpose, a Marx generator with a solid-state switching device has been developed. The details will be discussed as in the following sub sections.

4.4.1 Principle of a Marx Generator

A Marx generator is widely used as a pulse power device [7]. Originally, this device was developed by Erwin Marx in the 1920s [8] as a fast charging system and simple low impedance voltage source. A schematic view of a basic construction of the Marx generator is shown in Fig. 4.4.1a. By using this figure, performance of the Marx generator is described below.

When switches (S) are turned off, capacitors (C) are connected in parallel and charged up by a voltage source (V_{DC}). When the switches (S) are turned on, the capacitors are connected in series. As the result, individual voltages shared by the capacitors are summed up to generate a high voltage pulse. The pulse duration is uniquely determined by an on-time period of the switches.

In the KEK-DA, a solid-state switching device such as MOSFET has been employed owing to its fast response. Therefore, a voltage pulse with rising/falling time of 10-200 ns can be provided. As shown in Fig. 4.4.1b, our Marx generator consists of 4 units which are connected to a -1.25 kV DC power supply, and supplies a high voltage up to -5 kV [4].

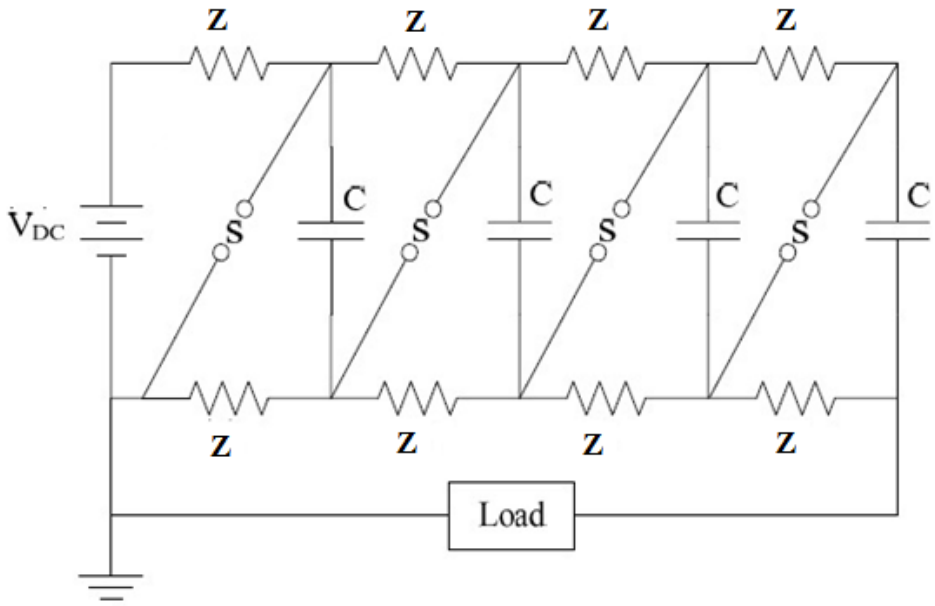

Figure 4.4.1a: Schematic view of the Marx generator

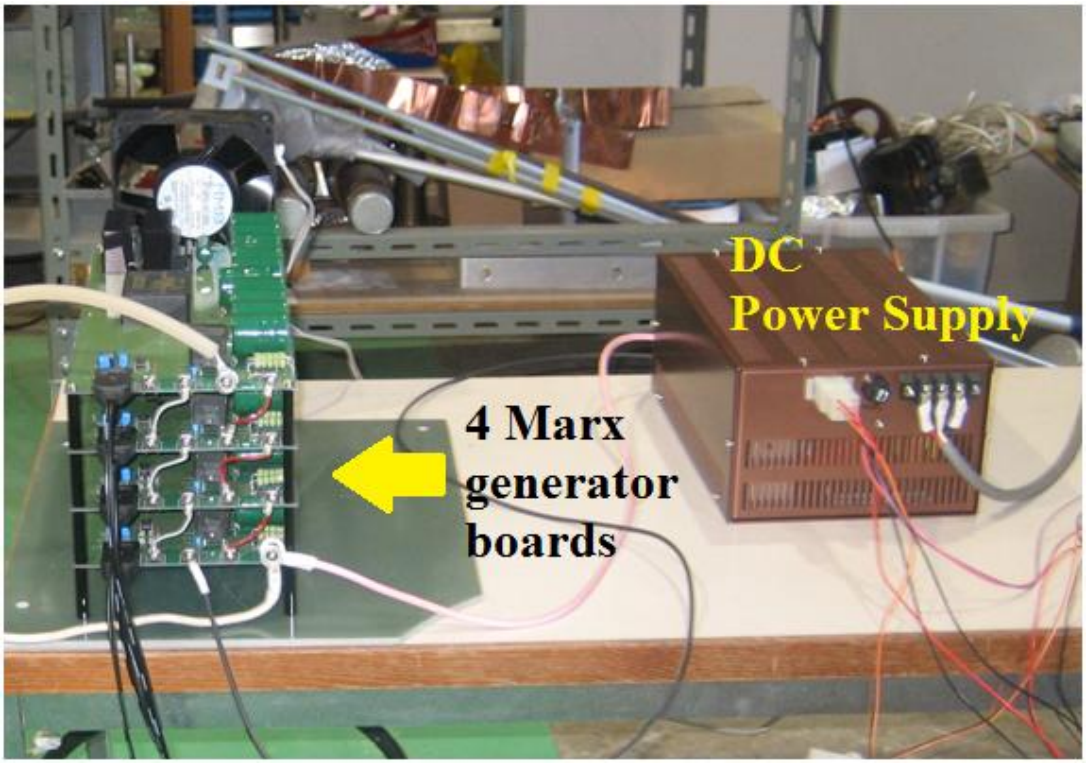

Figure 4.4.1b: Marx generator for the KEK-DA

4.4.2 Simulation and Experimental Results of the Marx Generator

The circuit performance of our Marx generator is simulated by using the LT Spice circuit analysis software [9]. Figure 4.4.2a shows the schematic of the equivalent circuit of our system. The V1 (negative voltage) is fed to capacitors (from C1 to C4) connected in parallel when the switches (from S1 to S4) are turned off. While the switches are kept to be on by a pulse source (V2) for some duration, the capacitors are connected in series. Then, voltages of 4 capacitors are summed up and supplied to the Einzel lens. Within such a duration, the beam propagates through the Einzel lens since the blocking voltage (V3=13 kV) is reduced by the output voltage of the Marx generator (-5 kV). Comparisons of the simulated voltage waveform by the LT Spice with the measured one for various pulse durations of 2, 3 and 5 μs are shown in Fig. 4.4.2b. It turns out that the measured voltage waveform is consistent with the simulated one.

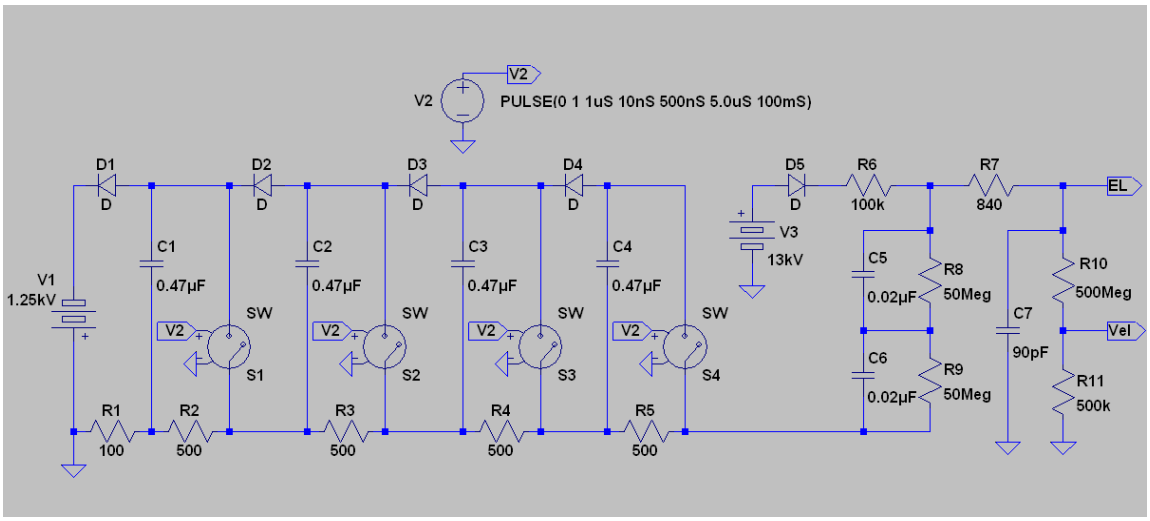

Figure 4.4.2a: Equivalent circuit of the Marx generator

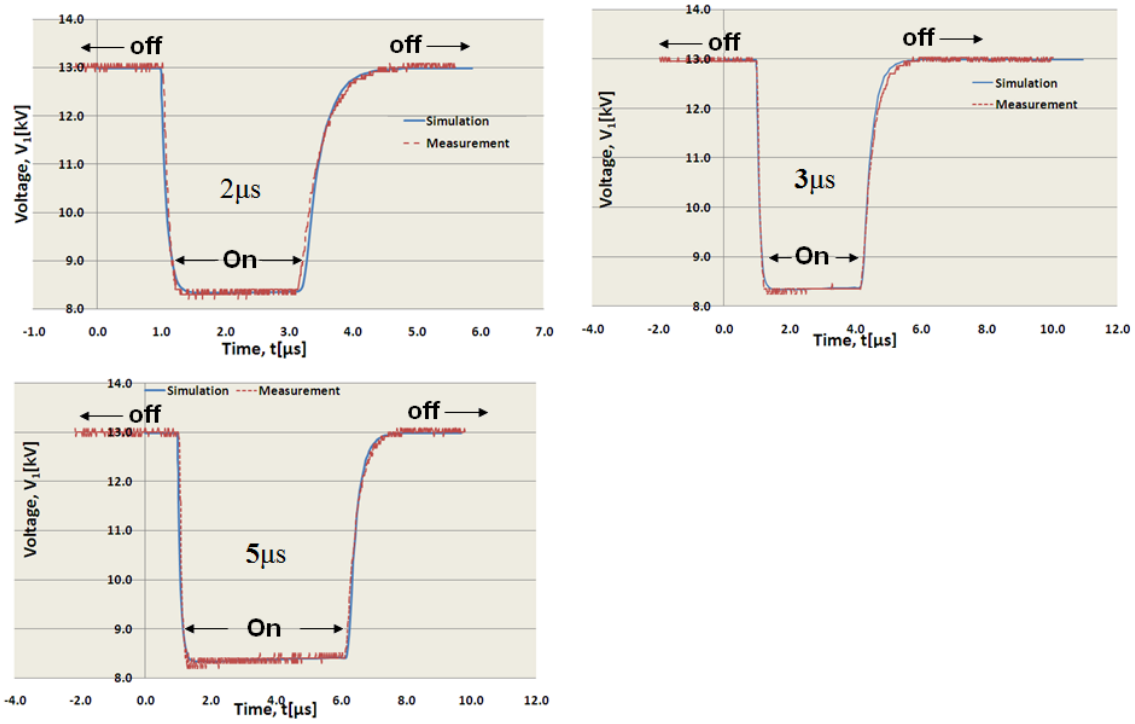

Figure 4.4.2b: Comparison of the simulated voltage waveform with the measured one for pulse durations of 2 µs, 3 µs and 5 µs (On=Chopping is operated, off=Chopping is un-operated)

A droop of ~2% /5µs in the flat pulse region is found in our system. Such a droop causes additional energy spread in an ion beam. Fortunately, the ion beam is accelerated by a DC voltage of 200 kV just after the Einzel lens. Therefore, we can expect that effective

energy droop can be reduced to ~0.1%/5μs. Thus, such a small energy droop can be accepted in our setup. In addition, the falling and rising times are few hundred ns which is negligibly small for a μs pulse which can be accepted too.

4.5 Experimental Setup

In order to test the performance of the Einzel lens chopper, a test bench was constructed at the LEBT. The upstream of the LEBT consists of two vertical steering magnets, a separation magnet of BM1 and BM2 (deflects to downstream). During the experiments, the BM 2 is switched off and the beam is guided to the test bench, where a Faraday cup (FC) with bias voltage (-250V) is installed and the beam current is measured [10].

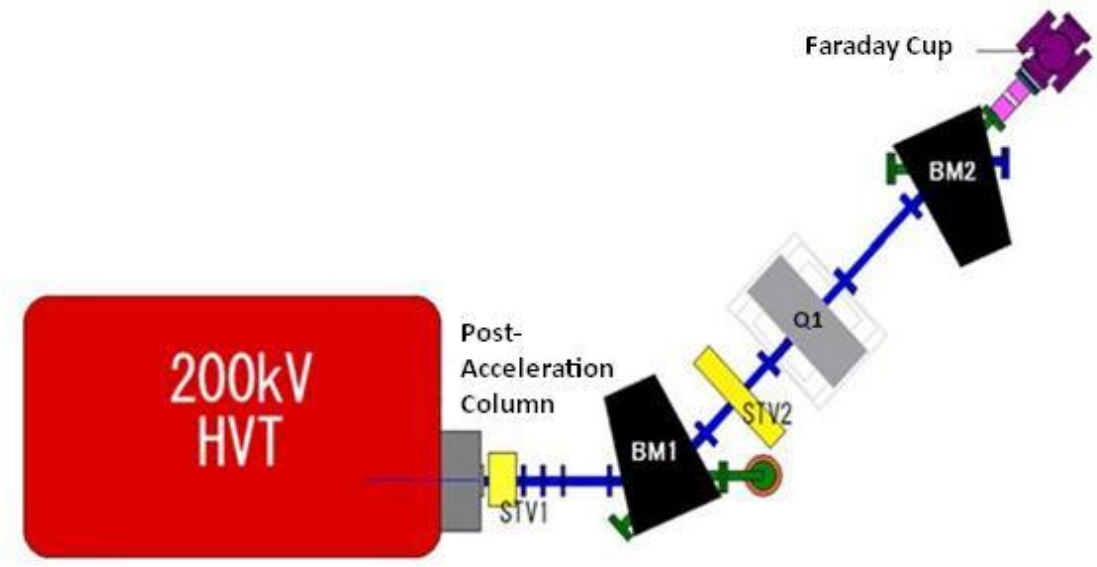

Figure 4.5a: Layout of the experimental setup (BM1, 2: Bending Magnet, STV1, 2: Steering Magnet) [10]

4.5.1 Simulation and Experimental Results to Block the Beam

The IGUN code [11] is used to simulate the beam orbits from the orifice in the plasma chamber to the exit of the Einzel lens by changing the Einzel lens voltage. Here, the extraction voltage from the plasma chamber is fixed to be 10 kV and He^{1+} is assumed. IGUN code gives the beam parameters (beam current, phase space parameters) at the entrance of bending magnet BM1. By using this information, the beam is transported

from the entrance of BM1 to the Faraday cup by a transfer matrix. Fig 4.5.1a shows the voltage dependence of the beam current at the Faraday cup. As shown in this figure, the Einzel lens voltage for beam focusing is optimized to be ~8 kV. Beam trajectories for five cases of the Einzel lens voltage V_1, which are 5, 6, 8, 12 and 13 kV, are shown in Fig. 4.5.1b. At the lower voltages of V_1=5 kV and 6 kV, the beam is not focused. Even at V_1=12 kV, a fraction of the beam can still propagate through the Einzel lens region. At V_1=13 kV, all ions are reflected to upstream and never propagate to downstream. Therefore, the voltage higher than 13 kV is at least needed to block a beam accelerated by the extraction voltage of 10 kV.

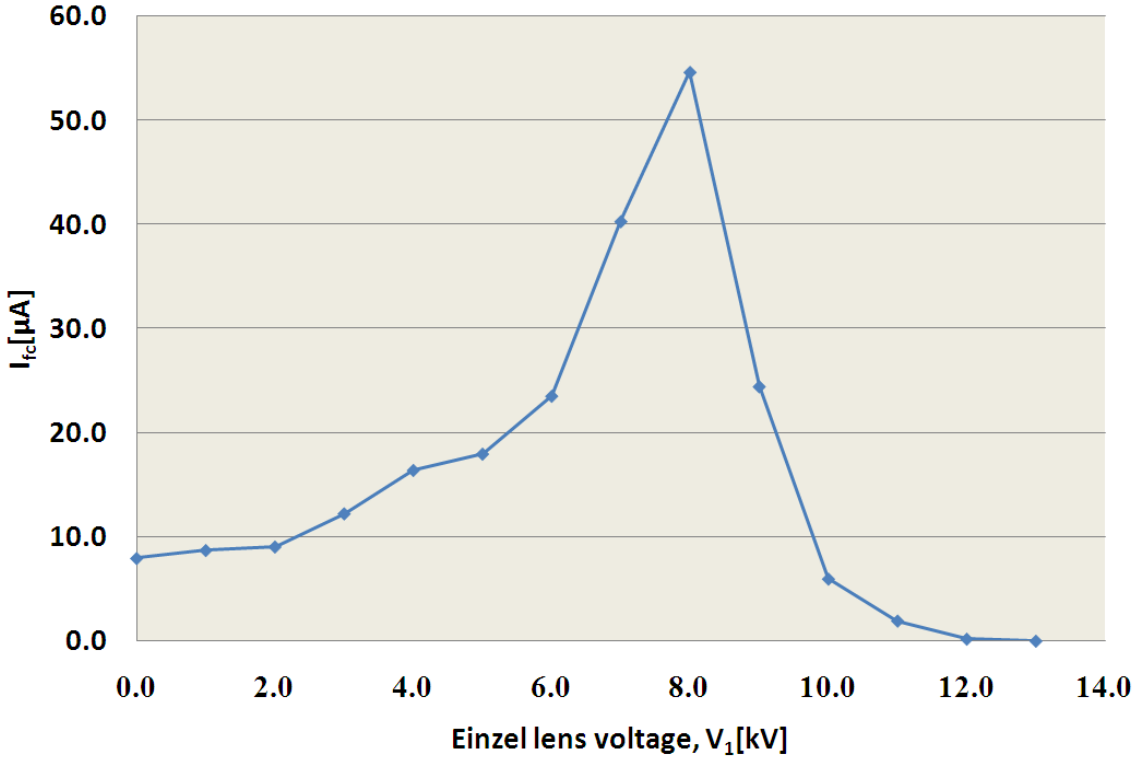

Figure 4.5.1a: V_1 dependence of the He^{1+} beam currents simulated by IGUN and transfer matrix

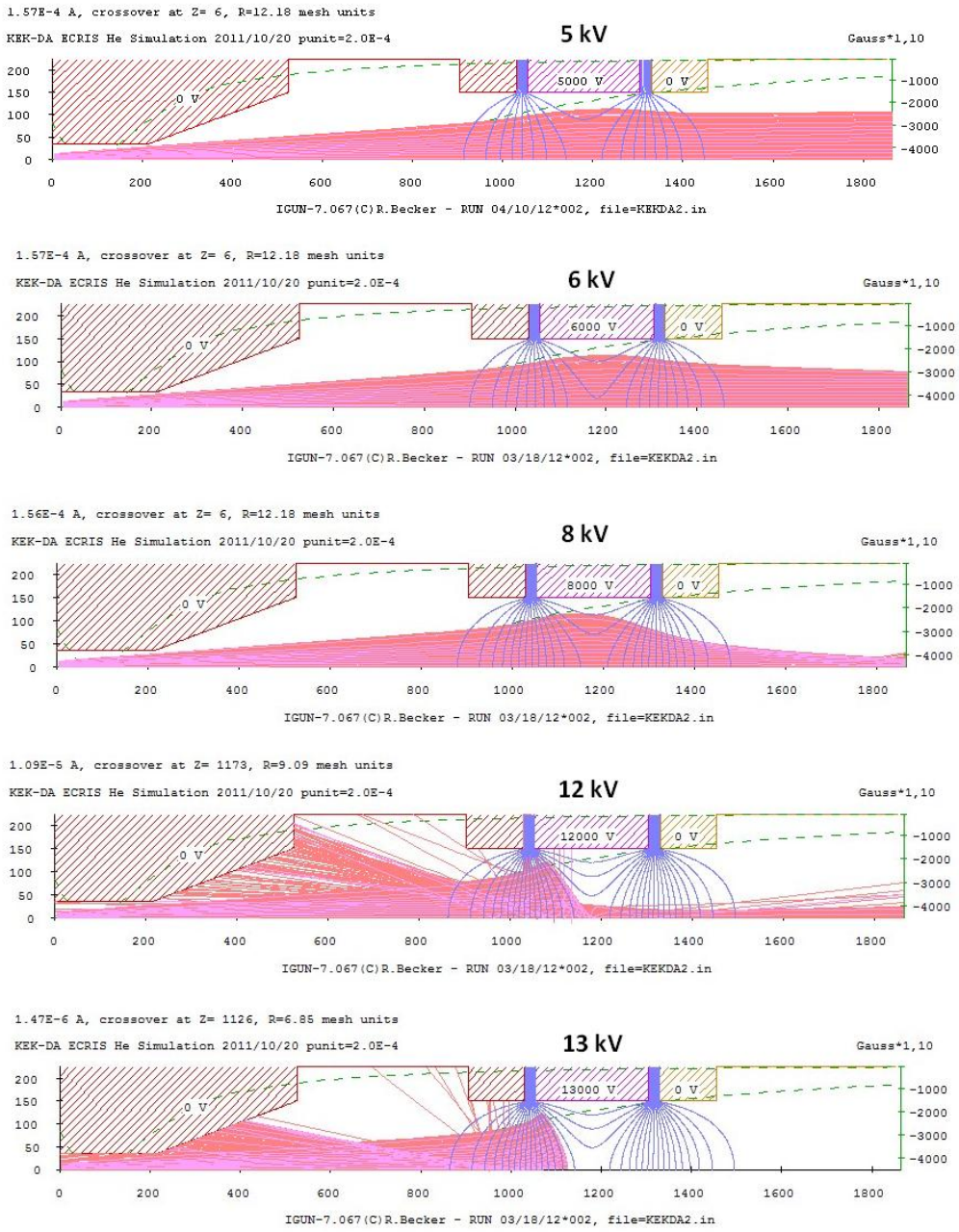

Figure 4.5.1b: Simulation results of He^{1+} for various Einzel lens voltages

In the beam blocking experiment, the extraction voltage is fixed at 10 kV similar to the simulation. The voltage (V_1) at the middle electrode of the Einzel lens was varied from 0

to 13 kV and the post-acceleration column voltage was fixed as 190 kV (V_2). Two ion species of $He^{1+}$and N^{1+} were used in this experiment.

4.5.1.1 Blocking experiment of helium and nitrogen ion beams

By scanning the voltage V_1, the ion current of He^{1+} and N^{1+} were measured by the FC. V_1 dependence of the observed beam current of each ion species is shown in Fig. 4.5.1.1a. Both results have a sharp peak at V_1=8 kV and the beam current is drastically reduced on both sides. This can be qualitatively explained by taking account of the simulation result. Below V_1=8 kV, the Einzel lens voltage is not enough to focus the beam and beam size exceeds the FC effective area and some beam fraction may be lost during transportation. Beyond 8kV, the beam is also blown up due to over focus and finally blocked when the voltage exceeds the blocking voltage. The experimental result also shows that the beam is completely blocked beyond 13 kV.

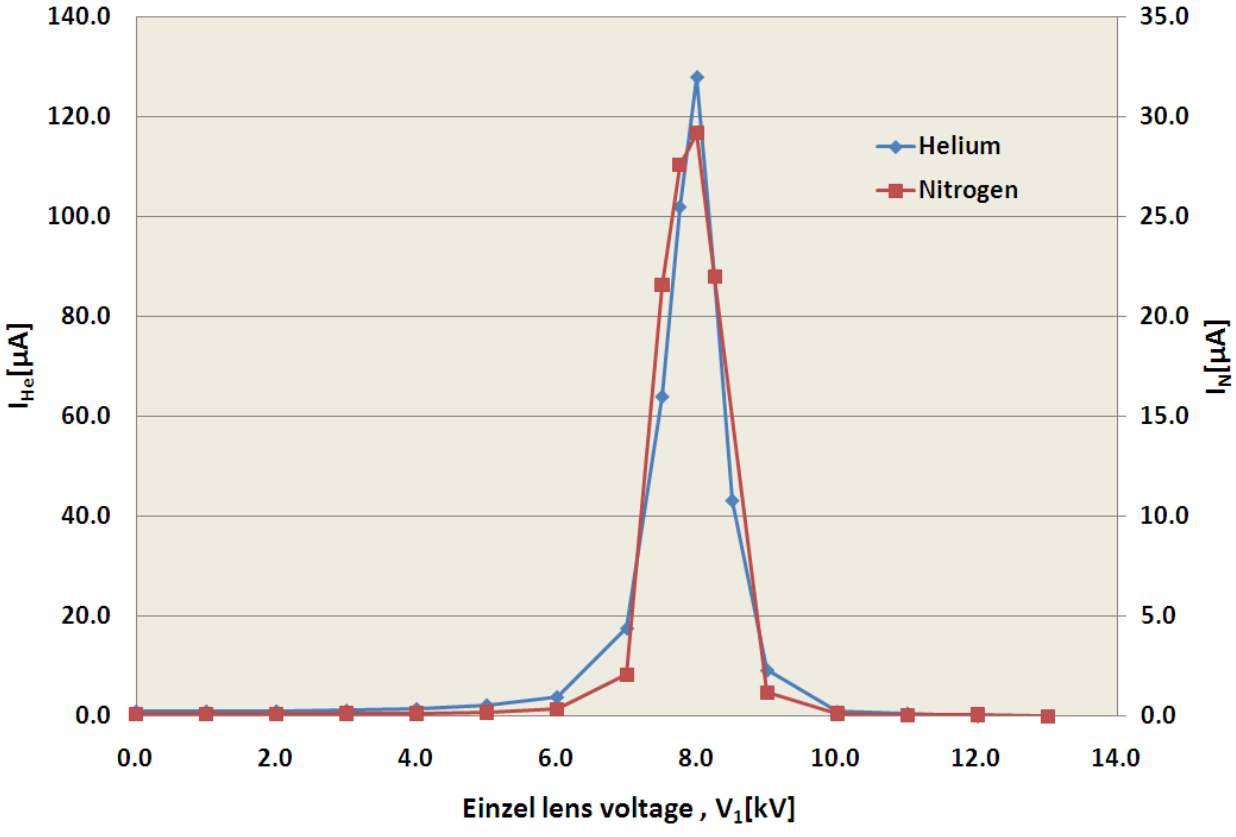

Figure 4.5.1.1a: V_1dependence of the $He^{1+}$and N^{1+} beam currents

For both cases, the experimental results imply that the optimum focusing voltage applied to the middle electrode of the Einzel lens is 8 kV in the present configuration where the extraction voltage is 10 kV and the post-acceleration column voltage is 190 kV. In addition, the voltage of V_1= 8 kV is optimized by taking account of the matching condition of the post-acceleration column voltage of 190 kV as well. About blocking and optimum focusing voltages, both simulation and experimental results are consistent. Thus, it can show the response of our beam optics. On the other hand, the simulation result of the voltage dependence of the beam current is rather broad by comparing the experimental result. Such a difference may occur due to a lack of information for transverse aperture and transverse space charge effect.

4.6 Beam Chopping Experiment with Einzel Lens Chopper

Performance of the Einzel lens chopper have been studied by using ion beams of $He^{1+}$and He^{2+}. The extraction voltage from the ECRIS and the static Einzel lens voltage to secure complete blocking of beam propagation were fixed at 8 kV and 13 kV, respectively. Since the Einzel lens voltage has been already optimized to be 8 kV from stand point of the beam optics, a pulse voltage of -5 kV with 5 μs duration is superposed on the DC bias voltage of 13 kV at the middle electrode of the Einzel lens. The current of the chopped beam was measured by the Faraday cup.

4.6.1 Chop of Helium Ion Beam

4.6.1.1 Chop at different timings

For this experiment, a He^{1+} ion was selected by the BM1. A microwave power with 5 ms duration is injected into the plasma chamber and 5 ms beam pulse with was measured by the Faraday cup. The result is shown in 4.6.1.1a.

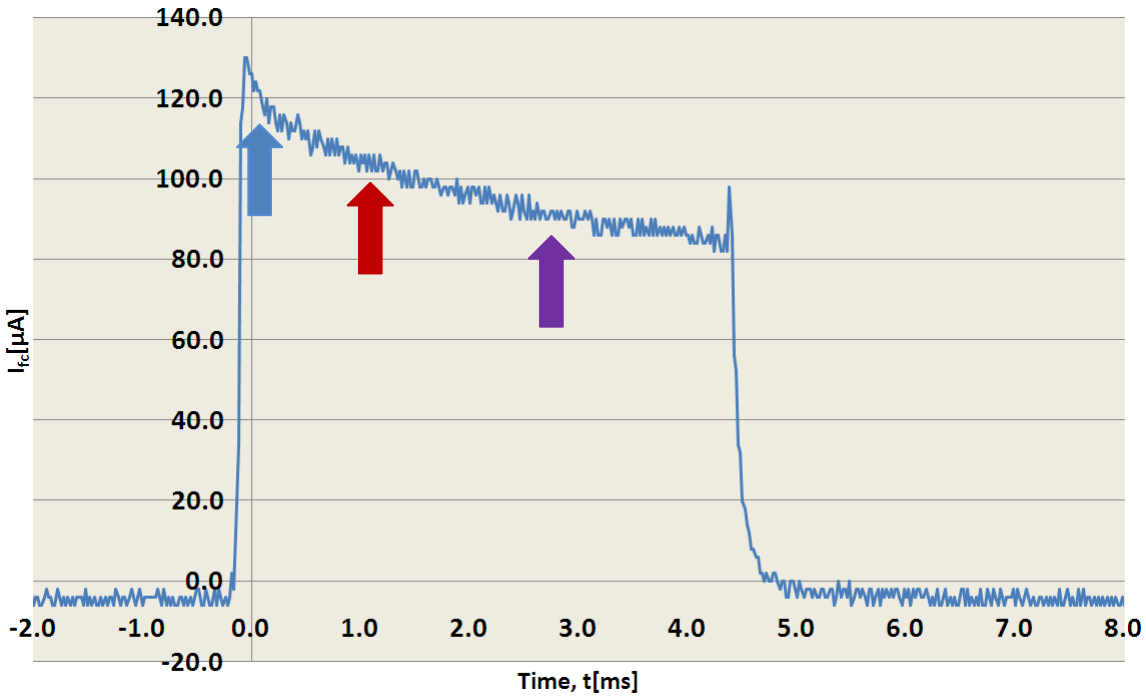

Figure 4.6.1.1a: He^{1+} ion beam pulse with duration of 5 ms measured by the Faraday cup (With different timings from the pulse head of 5 ms, detail as described below)

In order to investigate the chopper performance which can be utilized to control the required ion beam current, the following experiment was performed. The 5 ms beam pulse is chopped into a fractional beam pulse with duration of 5 μs at various timings after the TWT is activated. Those timings are indicated by the blue arrow (0.6 ms), the red arrow (1.0 ms) and purple arrow (3.0 ms) in the figure. Corresponding chopped beam profiles are shown in Fig. 4.6.1.1b.

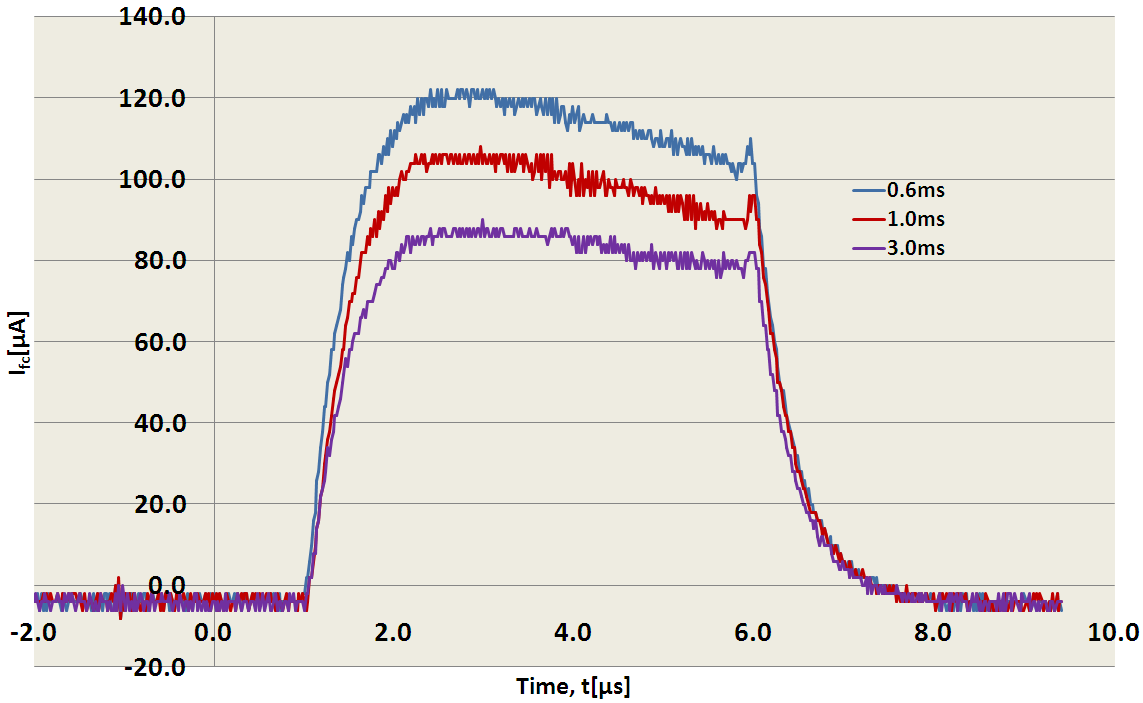

Figure 4.6.1.1b: Profiles of chopped beam of He^{1+} at different timings

The expected results have been obtained, where the intensity of beam chopped earlier is much higher than the beam chopped later as shown in Fig. 4.6.1.1a and Fig. 4.6.1.1b. Thus we can state that chopping timing is well controlled. For further investigation, chopping experiments with different time durations have been performed and will be described in the next subsection.

4.6.1.2 Chop with different time durations

For this experiment, the He^{2+} ion beam was utilized. A beam profile before chopping is shown in Fig. 4.6.1.2a. The ion beam is chopped at the timing of 1 ms, which is indicated by the red arrow, with various durations. The results are shown in Fig. 4.6.1.2b. Few μs beams have been successfully demonstrated in this experiment, this is an urgent task and strong demand of the KEK-DA which must be fulfilled by this novel chopper. In order to clarify the chopper performances, a beam reconstruction technique by using a Faraday cup response model has been developed which will be discussed in the following section.

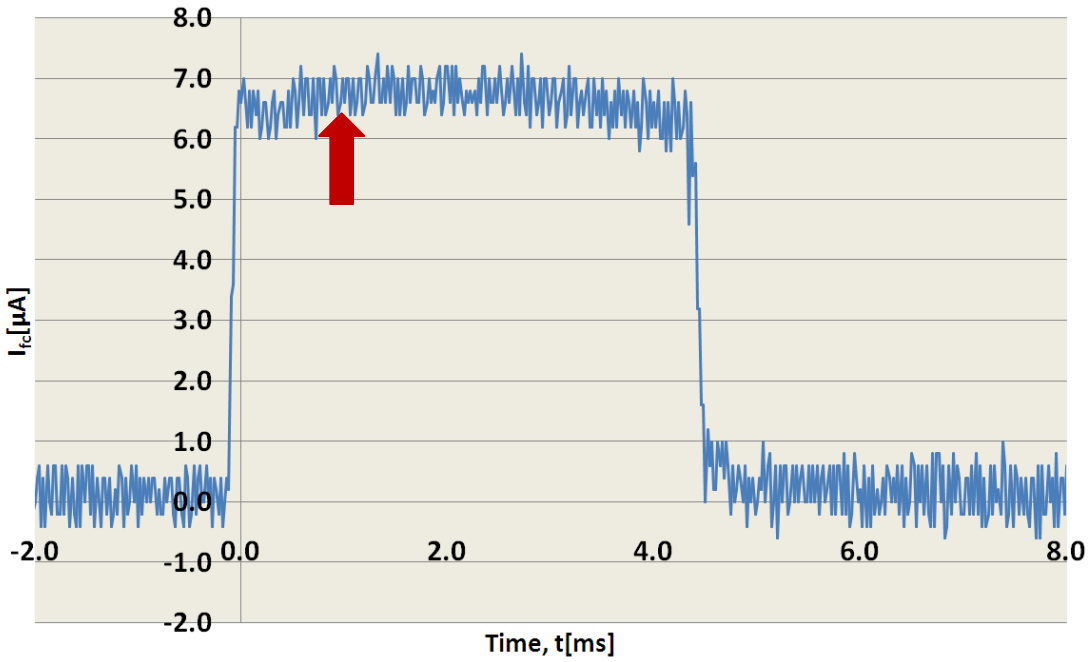

Figure 4.6.1.2a: He^{2+} Ion beam pulse with duration of 5 ms measured by the Faraday cup

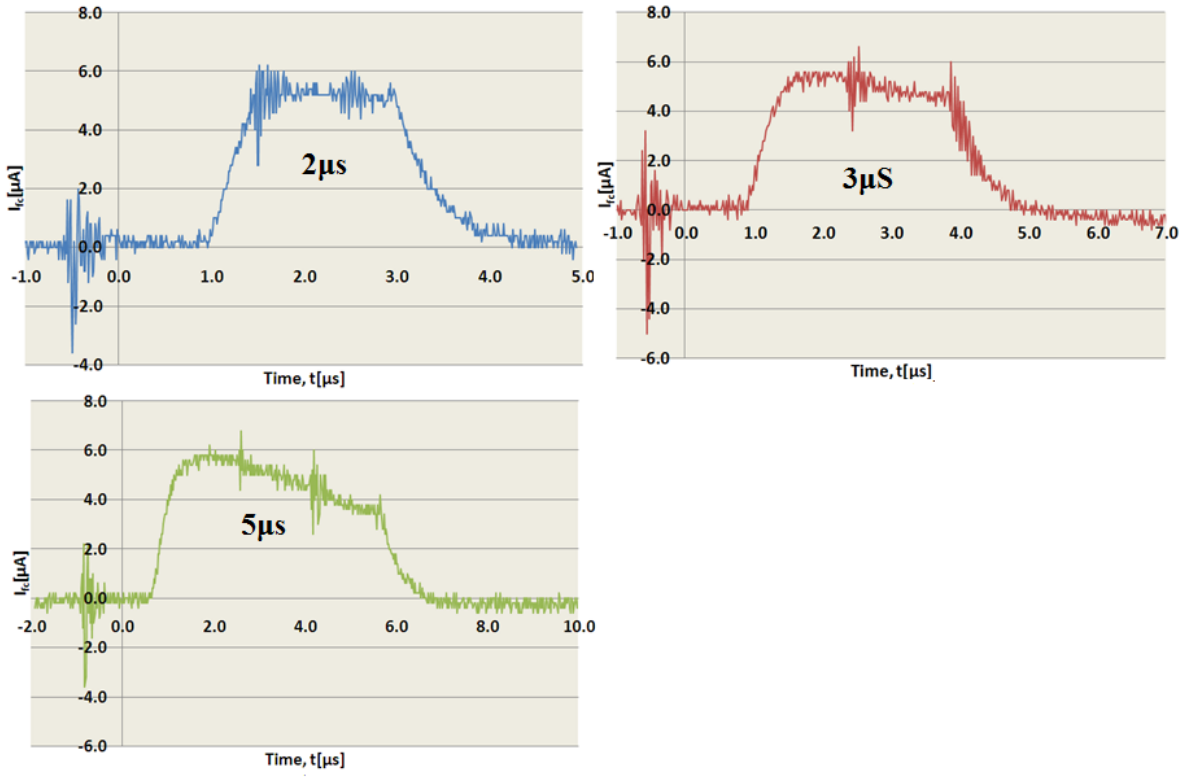

Figure 4.6.1.2b: Profiles of chopped beam of He^{2+}chopped with durations of 2 μs, 3 μs and 5 μs

The chopping experiments have been also performed by using N^{1+} and N^{2+} ion beams and expected results have been obtained.

4.7 Faraday Cup Response and Beam Reconstruction

Through the chopped beam experiments for He^{1+}, He^{2+}, N^{1+} and N^{2+}, we have successfully demonstrated the performance of the Einzel lens chopper. During those experiments, the chopped beam was measured by a Faraday cup.

The response of the Faraday cup can be described by the equivalent circuit shown in Fig. 4.7a. From the Appendix (3), the beam current observed by the Faraday cup (i_R) can be expressed as:

$$i_R = \left\{ \int_0^t \frac{i_b}{RC} \left(e^{t'/RC} \right) dt' \right\} \left\{ e^{-t/RC} \right\} \tag{4.15}$$

Here, i_b is the beam current (Unknown parameter), C the stray capacitance and R the readout resistance. The stray capacitance was measured to be 173 pF and the resistance of 1000 Ω was used.

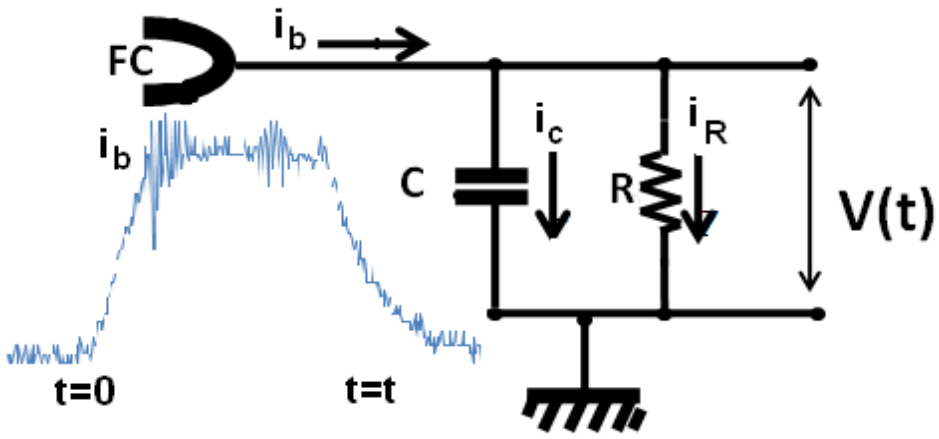

Figure 4.7a: Equivalent circuit of a Faraday cup

By solving the Eq. (4.15) as an inverse problem, the beam waveform can be reconstructed. The reconstruction procedure is described below.

As shown in Fig. 4.7b, reconstruction procedure is divided three parts: beam measurement by the FC, solving the inverse problem and check of the result.

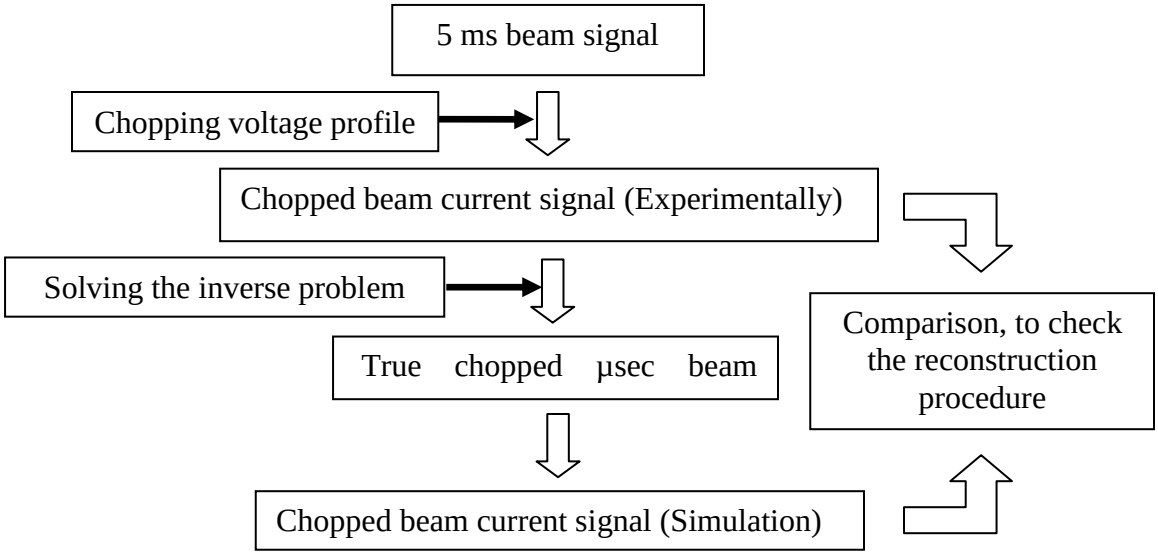

Figure 4.7b: Flow chart of the beam reconstruction procedure

In the followings, the formula to solve the inverse problem is derived. Suppose that the Faraday cup signal is obtained by sampling the signal successively with the sampling time of Δt. By using numerical integration (trapezoidal rule), i-th sample of the Faraday cup signal is given as:

$$i_R(t_i) \approx \left\{ \frac{\Delta t}{2RC} \sum_{k=1}^{i} \left(i_b(t_k)\, e^{t_k/RC} + i_b(t_{k-1}) e^{t_{k-1}/RC} \right) \right\} e^{-t_i/RC}, i = 1 \rightarrow N \tag{4.16}$$

Explicit forms for the first three sampling data are given as:

$$i_R(t_1) \approx \frac{\Delta t}{2RC} \left(i_{b1} + i_{b0} e^{-\Delta t/RC} \right) \tag{4.17}$$

$$i_R(t_2) \approx \frac{\Delta t}{2RC} \left(i_{b2} + 2 i_{b1} e^{-\Delta t/RC} + i_{b0} e^{-2\Delta t/RC} \right)$$

$$i_R(t_3) \approx \frac{\Delta t}{2RC}\left(i_{b3} + 2i_{b2}e^{-\Delta t/RC} + 2i_{b1}e^{-2\Delta t/RC} + i_{b0}e^{-3\Delta t/RC}\right)$$

and .....

Here,

$$i_{bk} \equiv i_b(t_k), \quad t_k = k\Delta t \tag{4.18}$$

By assuming $i_{b0}=0$, the above equation can be solved successively with respect to i_{bk}. Hence, the results are:

$$i_{b0} = 0\ ; (Definition)$$

$$i_{b1} = \frac{2RC}{\Delta t} i_R(t_1) \ldots\ldots$$

$$i_{bk} = \frac{2RC}{\Delta t} i_R(t_k) - 2\sum_{j=1}^{k-1} i_{bk-j}\, e^{-j\Delta t/RC} \tag{4.19}$$

Since a noise is enhanced in this procedure, the Faraday cup signal is smoothed before evaluation by using Eq. (4.19). The results for the beam pulses with duration of 2, 3 and 5 μs are shown in Fig. 4.7b, 4.7c and 4.7d, where the inverted voltage profile to chop the beam is also plotted. Somehow, waveforms of reconstructed beam profile are not in good agreement with the chopping voltage profile especially for 5 μs chopped beam. This difference can be explained by using the blocking experiment as described in section 4.8.

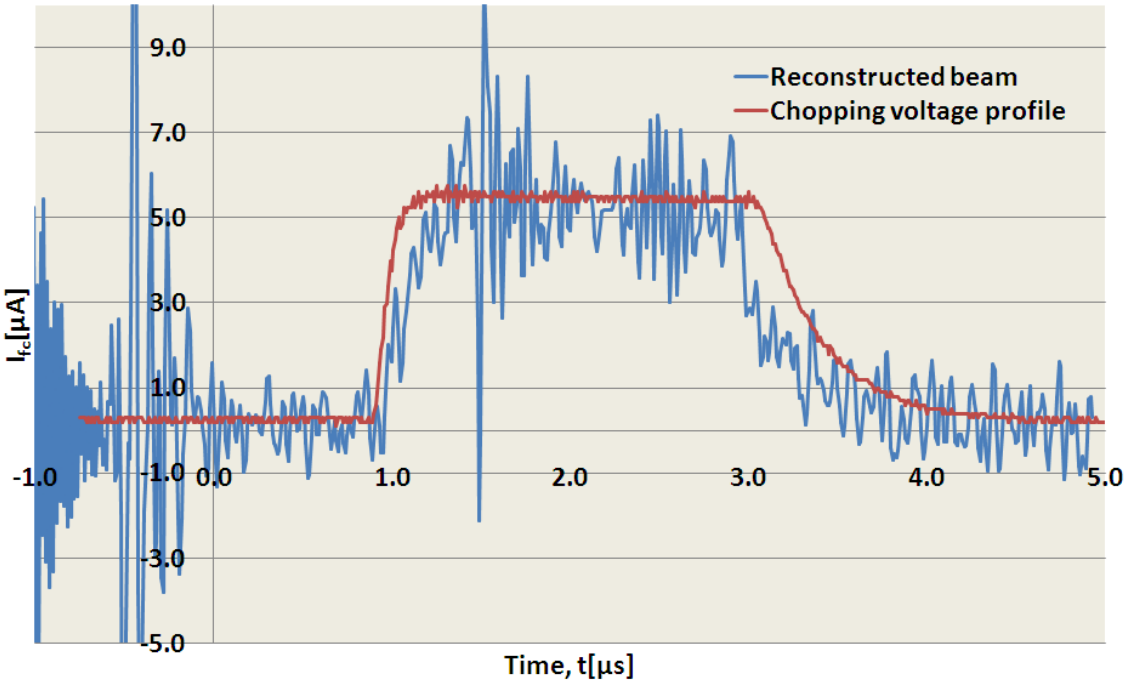

Figure 4.7b: Reconstructed He^{2+} beam pulse with 2 μs duration and the chopping voltage profile

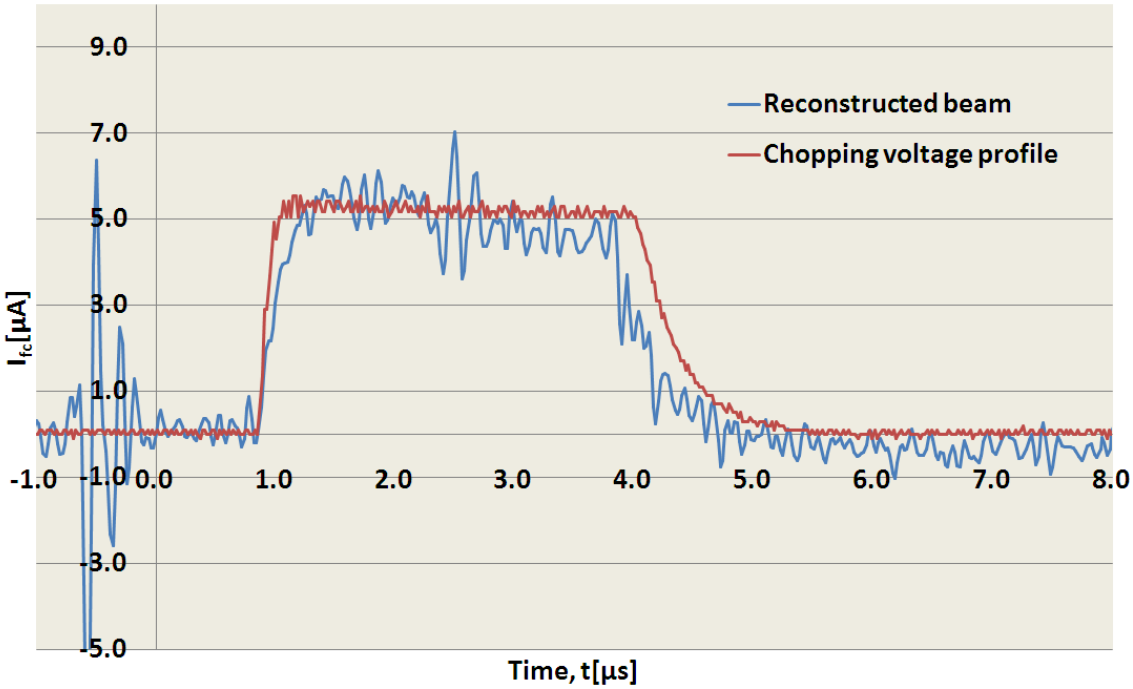

Figure 4.7c: Reconstructed He^{2+} beam pulse with 3 μs duration and the chopping voltage profile

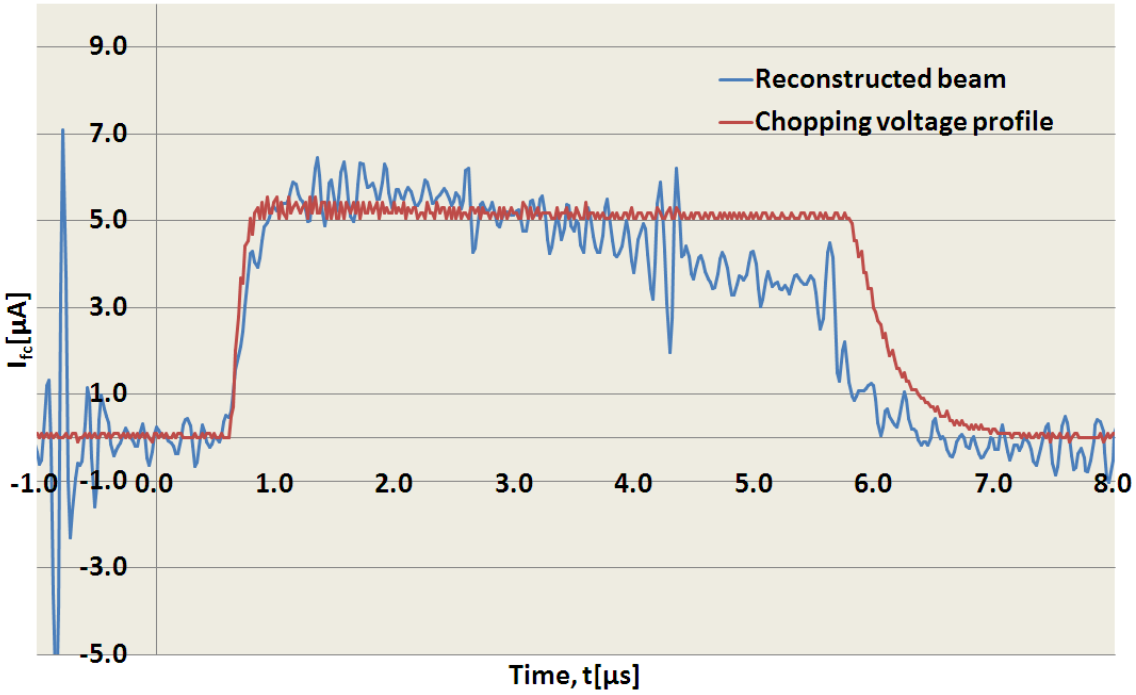

Figure 4.7d: Reconstructed He^{2+} beam pulse with 5 μs duration and the chopping voltage profile

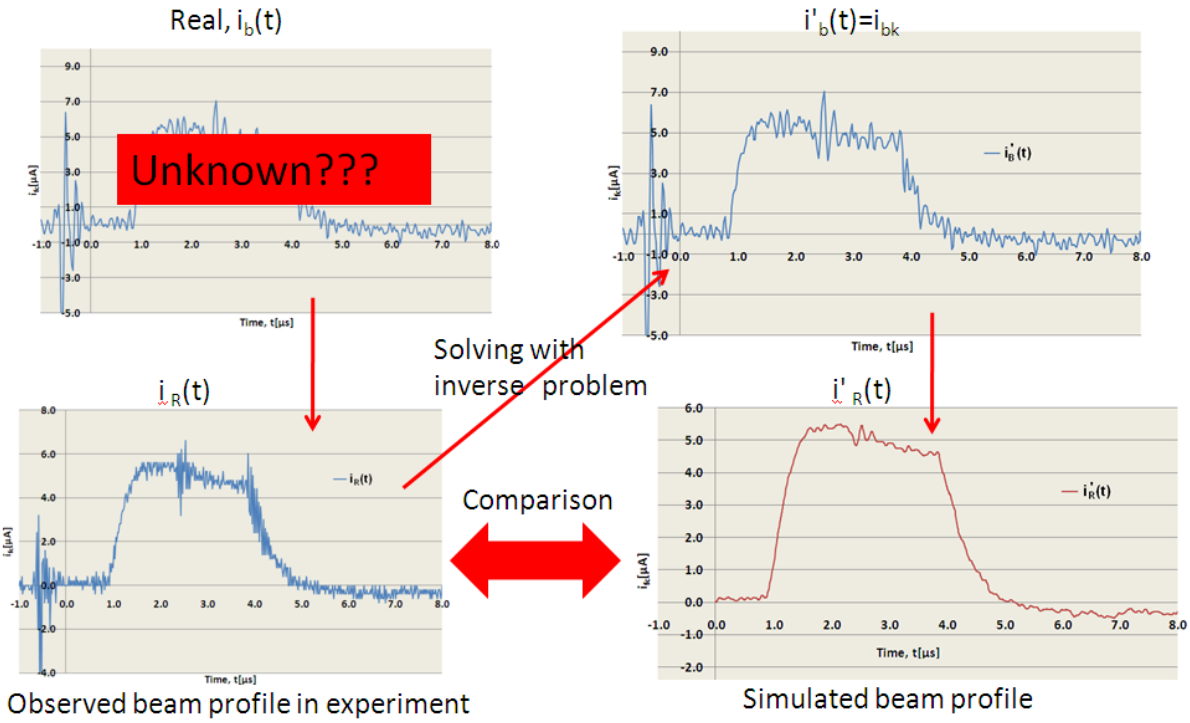

Figure 4.7e: Validation process of the beam reconstruction

In order to check the validity of the beam reconstruction procedure, the Faraday cup signal (i_R) is simulated by using the reconstructed beam current (i_b) by LT Spice. According to our validation process as shown in Fig. 4.7e, the true chopped beam signal with μs pulse width is unknown, since it cannot be observed directly by our measurement. By solving the inverse problem with respect to the observed beam signal, the candidate of the actual beam signal can be evaluated. From the LT spice circuit analysis software, the observed beam can be simulated by using the candidate of the beam signal as the input parameter. Those simulated beam signal results are all consistent with the measurements. One of the results for 3 μs case is shown in Fig. 4.7f.

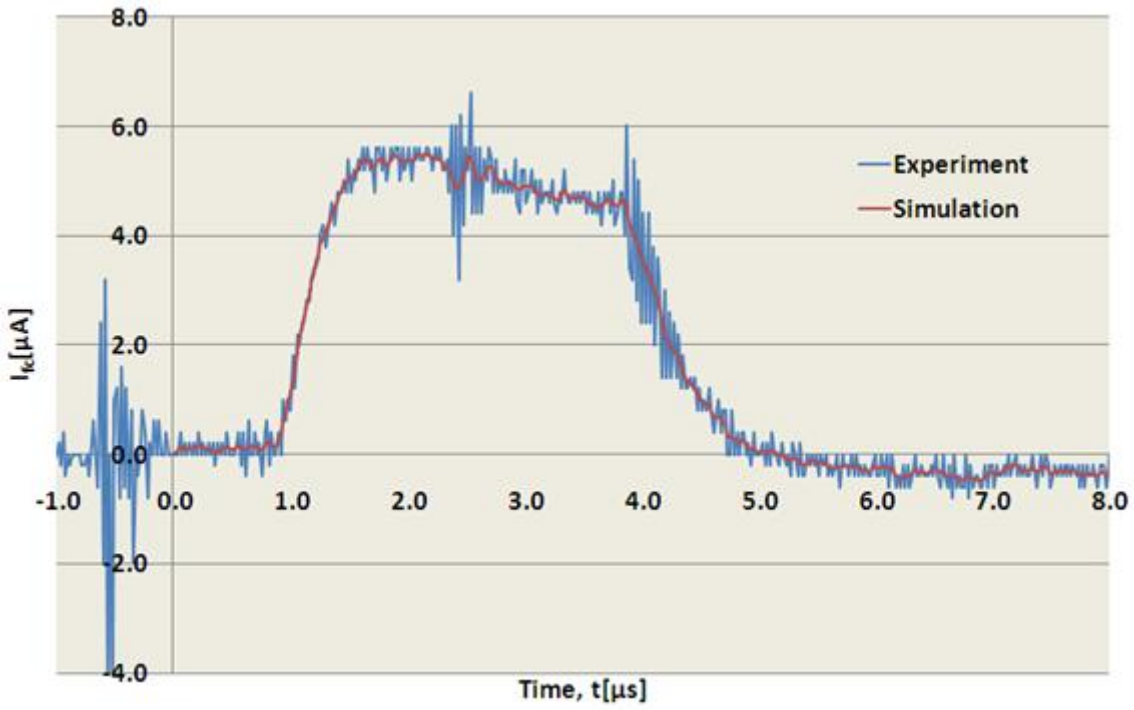

Figure 4.7f: Comparison of the 3 μs FC signal with the simulation by the LT Spice

4.8 Discussion

The beam chopping experiments have been performed by using the helium and nitrogen ion beams. In the experiments, chop at different timings and chop with different time durations have been performed and the expected performance of the Einzel chopper is confirmed. By using the equivalent circuit of the Faraday cup, a waveform of a chopped

beam is reconstructed successfully. However, the resultant waveform is a bit different from the waveform of the chopped beam voltage applied to the Einzel lens in the case of 5 μs. It can be explained by using the results of the blocking experiment, where the beam current is sensitively dependent on the Einzel lens voltage. Therefore, the chopping voltage profile cannot be directly compared with the chopped beam profile. In order to compare with the beam profile, the beam profile is predicted by taking account of the voltage dependence of the FC current, which is shown in Fig. 4.8a together with the fitting result by using a Lorentzian function.

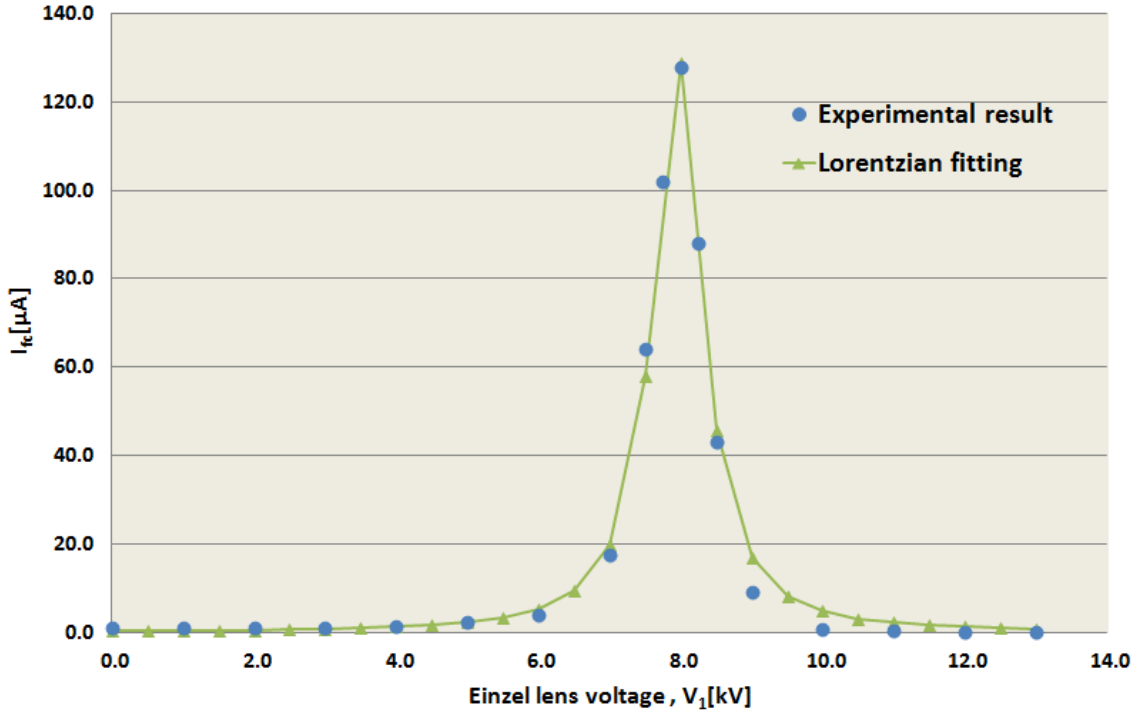

Figure 4.8a: V_1 dependence of the He^{1+} beam current and the fitting curve

Fitting results are obtained as:

$$I_{fc}(V_1) = \frac{1}{V_{peak}}\left[\frac{a}{1+(\frac{V_1-b}{c})^2}\right] \tag{4.20}$$

Here,

$a = 1.306 \times 10^{-4}$, $b = 7.951 \times 10^{3}$, $c = 4.029 \times 10^{2}$

$$and\ V_{peak} = 128.69\mu A$$

Thus , by substituting the time dependent chopping voltage profile of $V_1(t) = V_1$ into Eq. (4.20), the predicted beam signal can be obtained as shown in Fig. 4.8b with the comparison between reconstructed beam profile.

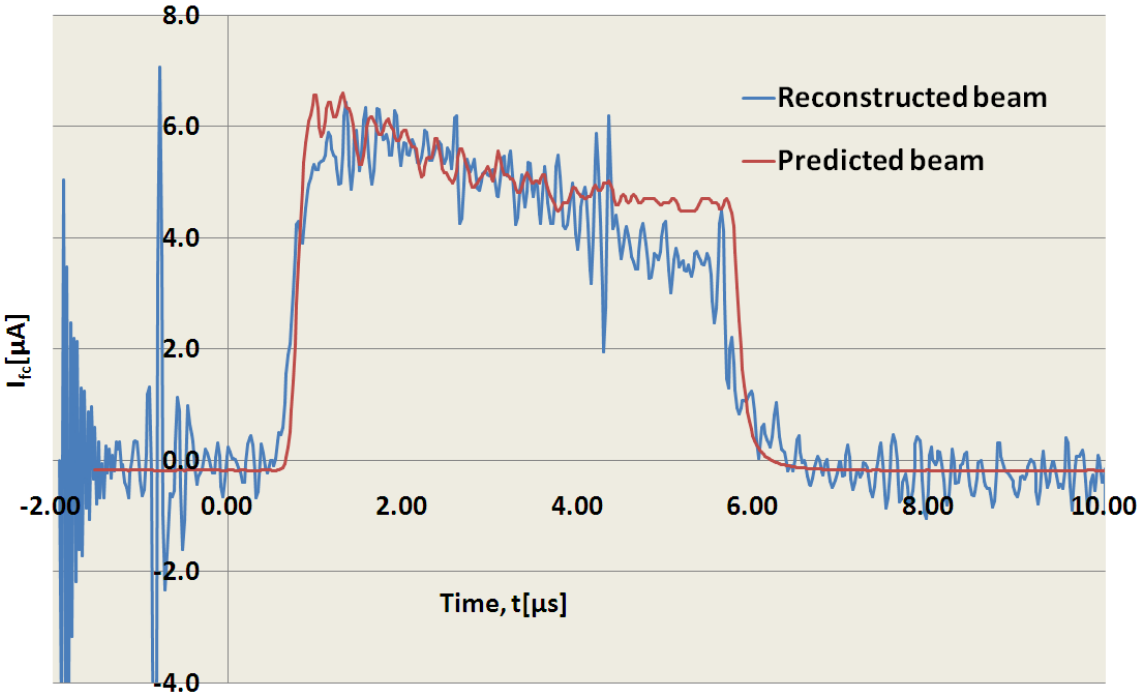

Figure 4.8b: Comparison of the reconstructed He^{2+} beam pulse with the reconstructed chopping voltage profile

From the Fig. 4.8b, the droop for both curves is consistent with each other. Thus, the different between the beam profile and the voltage profile can be compensated by taking account the effect of the voltage dependence of the observed current at FC. With the newly developed Einzel lens chopper, the beam is chopped and injected into the KEK-DA ring without any failure and trouble.

References

[1] **K. W. Leo**, T. Adachi, T. Arai, and K. Takayama, "Einzel Lens Chopper and Behavior of the Chopped Beam in the KEK Digital Accelerator", submitted to *Phys. Rev. AB-ST (2012).*

[2] T. Adachi, T. Kawakubo, and T. Yoshii, *Proceeding of IPAC10*, May 23rd-28th, 2010 Kyoto, Japan, MOPEC050 (2010).

[3] S. C. Jeong, M. Oyaizu, H. Kawakami, Y. Shirakabe, N. Ikeda, and T. Nomura, "Beam-bunching in an ECR Ion Source by the Pulsed Gating-Potential Method", *Nucl. Instrum. Methods* B **114, 1**54 (1996).

[4] D. Yuan, K. Jayamanna, M. Dombsky, D. Louie, S. Kadantsev *et al*. "Design of an Electron Cyclotron Resonance for the Isotope Separator and Accelerator at TRIUMF", *Rev. Sci. Instrum.***71**, 643, (2000).

[5] M. Dubois, P. Jardin, O. Bajeat, C. Barue, C. Canet, M. Dupuis, J. L. Flambard, R. Frigot, C. Leboucher, N. Lecesne, P. Lecomte, P. Leherissier, F. Lemagnen, L. Maunoury, B. Osmond, J.Y. Pacquet, and A. Pichard, "MONOBOB II: Latest Results of Monocharged Ions Source for SPIRAL2 Project", *Proceedings of 19th International workshop on ECR Ion Sources*, August 23rd -26th, 2010 Grenoble, France, Pg. 64 (2010).

[6] **K. W. Leo**, T. Adachi, K. Okazaki, T. Arai, A. Tokuchi, and K. Takayama, " A Permanent Magnet ECRIS with a Solid-state Marx Generator Driven Chopper for the KEK Digital Accelerator", *Proceedings of the 14th International Conference on Ion Source*, Giardini-Naxos, Sicily, Italy, September (2011).

[7] L.M. Redondo, J. Fernando Silva, H. Canacsinh, N. Ferrao, C. Mendes, R. Soares, J. Schipper, and A. Fowler, " Solid-State Marx Based Two-Switch Voltage Modulator for On-Line Isotope Mass Separator Accelerator at the European Organization for Nuclear Research", *Rev. Sci. Instr.* **81**,074703 (2010).

[8] K. Takayama and R. Briggs (*Eds.*), Induction Accelerators, Springer, ISBN 9783642139161.

[9] http://www.linear.com/designtools/software/

[10] T. Adachi, T. Arai, **K. W. Leo**, K. Takayama, and A. Tokuchi, "A Solid-State Marx Generator Driven Einzel Lens Chopper", *Rev. Sci. Instrum.* **82**, 083305 (2011).

[11] R. Becker, and W. B. Herrmannsfeldt, "IGUN- A Program for the Simulation of Positive Ion Extraction Including Magnetic Fields", *Rev. Sci. Instrum.* **63**, 2756 (1992).

5. Beam Transport

5.1 200kV High Voltage Platform

The ECRIS and related components are embedded inside a High Voltage Platform (HVP), which is insulated from the ground by six ceramic stands. A Cockcroft-Walton high-voltage power supply provides high voltage of ~200 kV for the HVP [1].

The ECRIS, microwave devices, gas injection system, turbo molecular pumps, high-voltage power supply for extraction, the Einzel lens and the Marx generator are installed inside the HVP as shown in Fig. 5.1a. An ion beam is extracted from the ECRIS by the extraction electrode (~10 kV) and accelerated by the HVP voltage (~190 kV). The HVP voltage is shared among three electrodes of the post-acceleration column. Voltage applied to each electrode is optimized by taking account of the transverse focusing action [1].

Voltage drop of the HVP occurs due to the beam loading. Large voltage drop causes a large momentum spread in the beam pulse. Therefore, the beam loading effect to the HVP voltage was simulated by using an equivalent circuit shown in Fig. 5.1b [1]. Capacitance C_1 is inserted to stabilize the voltage and C_2 is a stray capacitance. The C_2 value was estimated by using the simulation code for electrostatic problem, Femtet. Simulation result is shown in Fig. 5.1c, where an ion beam pulse with duration of 5 ms and 5 mA peak is assumed to be extracted from the HVP at a repetition of 10 Hz. As shown in the Fig. 5.1b, voltage drop is caused by the beam loading at a repetition of 10 Hz and the extent of the drop saturates after a few cycles. It was found that C_1 larger than 30 nF can stabilize the voltage within the voltage drop of 0.2% during the beam extraction.

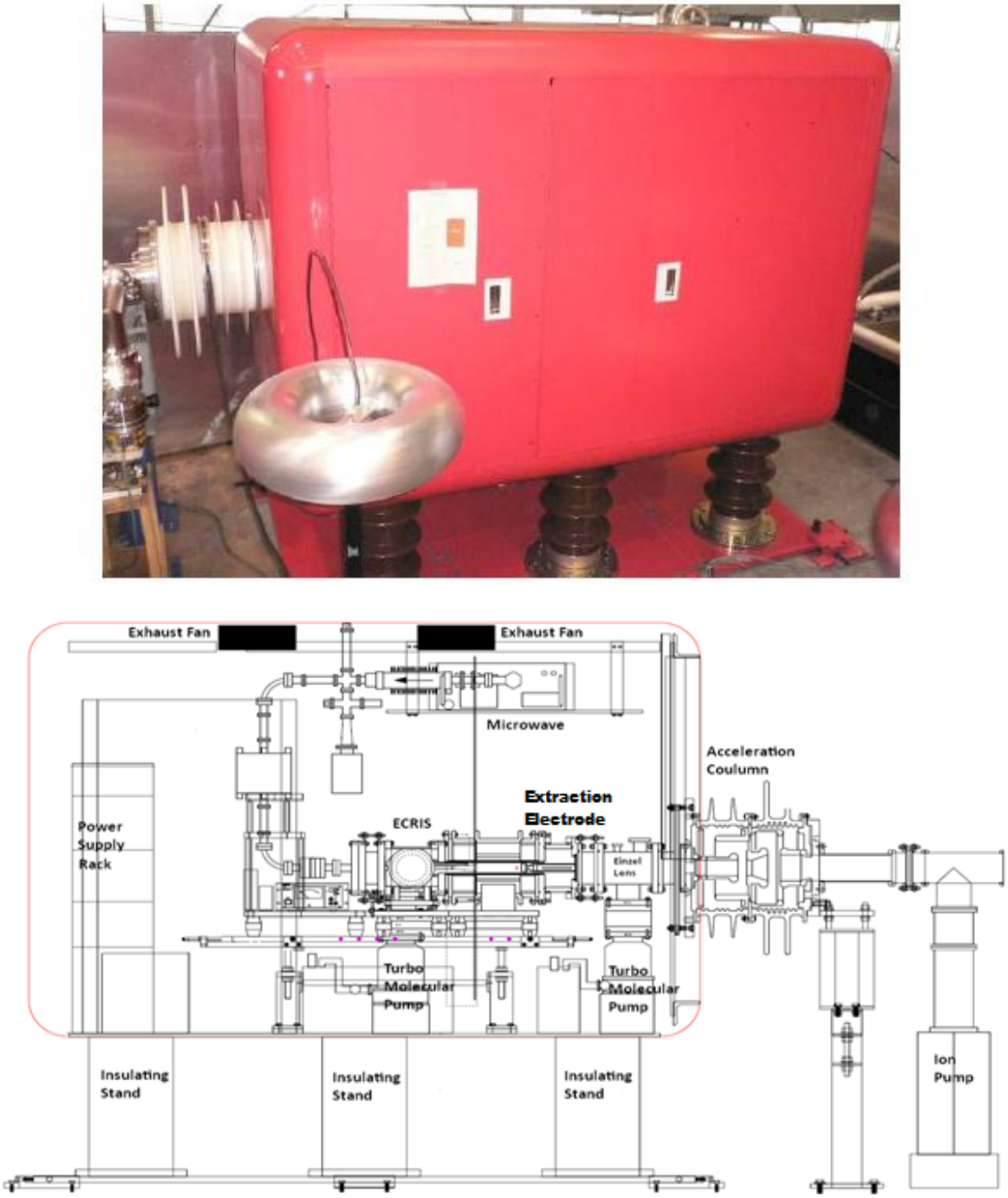

Figure 5.1a: A photograph of the HVP with an acceleration column and a diagram of its inner layout

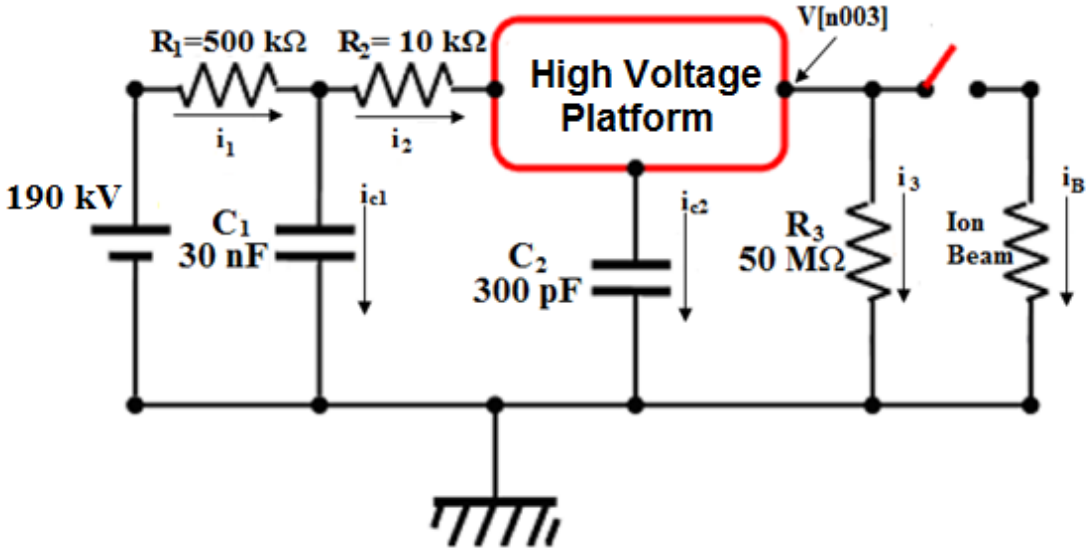

Figure 5.1b: Equivalent circuit of the HVP. R_1 and R_2 are the resistances of the feeder line. R_3 is the resistance of the ceramic chamber of the post-acceleration column. R_B is the resistance seen by the beam current. C_1 is a capacitance inserted to stabilize the voltage. C_2 is the stray capacitance of the HVP

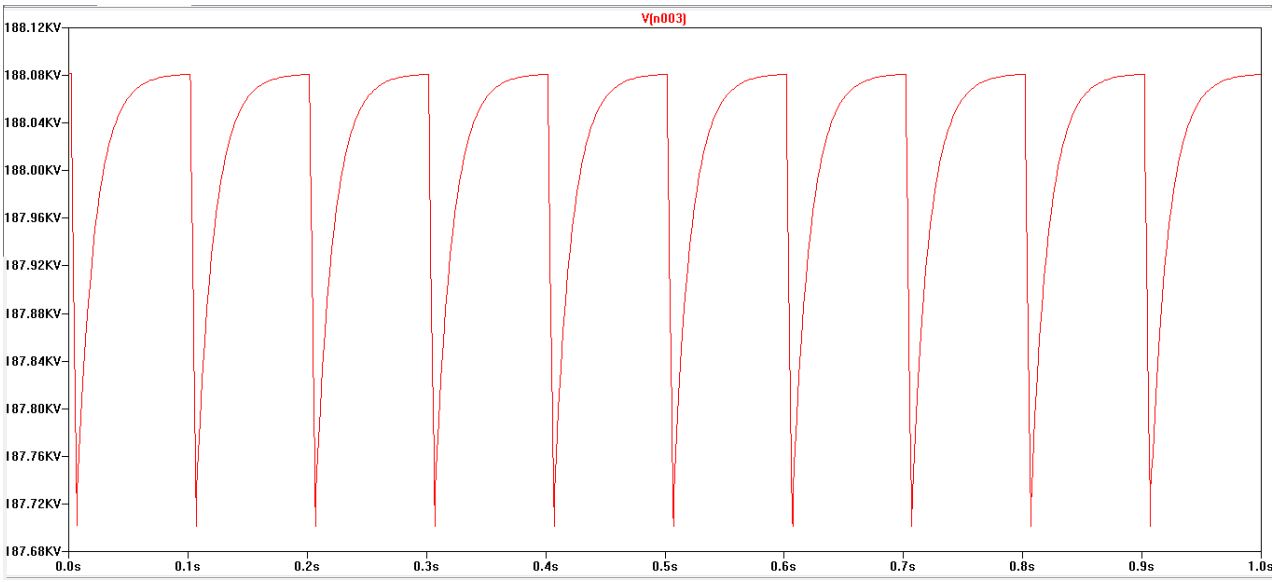

Figure 5.1c: Simulation result of the beam loading effect

5.1.1 Cockcroft-Walton Generator

A Cockcroft-Walton high voltage power supply (CW), which is fabricated by SPELLMAN High Voltage Electronics Co., supplies high voltage of 200 kV to the HVP

[2]. The CW is a multi-stage high voltage generator, whose principle is based on a multiplier ladder network. Such a network comprises multiple pair of capacitor and diode to generate high voltage by summing up the voltage of each pair, as shown in Fig. 5.1.1a.

A schematic view of the typical CW high voltage generator is shown in Fig. 5.1.1b [3]. An AC voltage is rectified by an input filter circuit at first. Then, the rectified voltage is converted to the AC voltage with higher frequency by an inverter and supplied to the high voltage multiplier through a transformer with appropriate step-up ratio. Finally, the AC voltage is rectified by the multiplier network, and the resultant high DC voltage is supplied to a load.

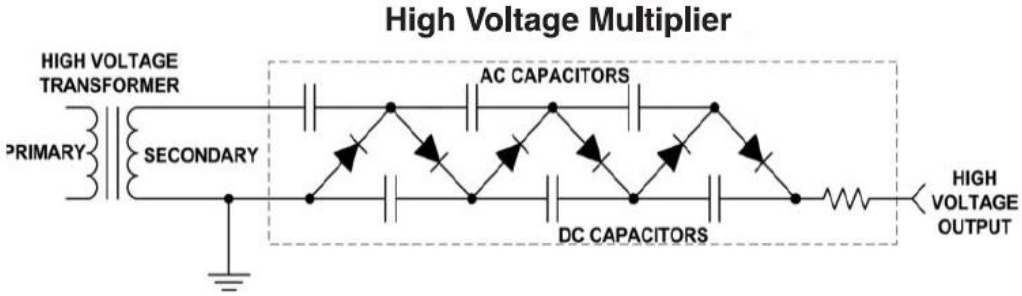

Figures 5.1.1a: Three stages high voltage multiplier [3]

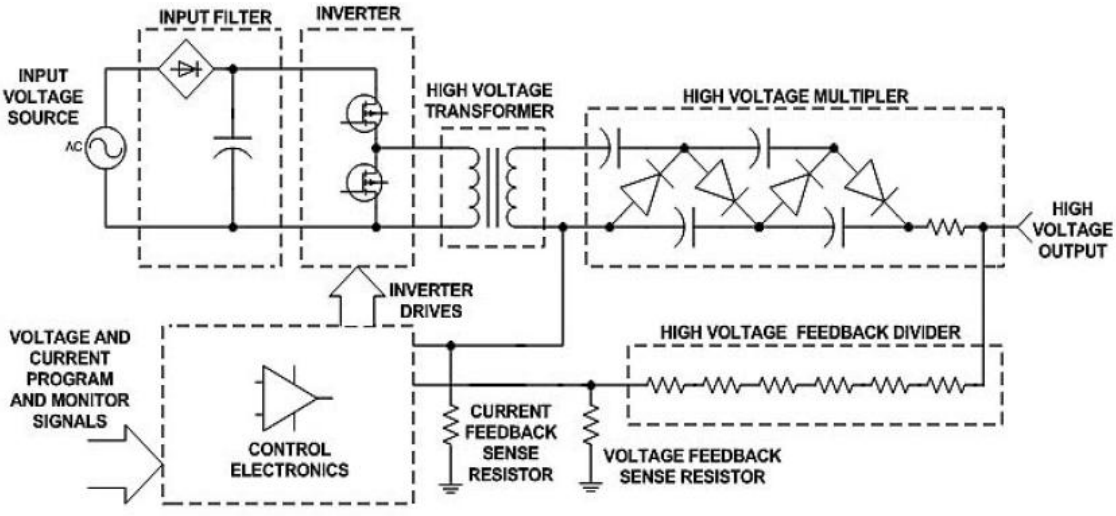

Figures 5.1.1b: Circuit diagram of a CW high voltage power supply [3]

5.1.2 Post-Acceleration Column

The post-acceleration column is shown in Fig. 5.1.2a. Right side of the acceleration column is connected to the body of the HVP and the other side is connected to the vacuum chamber that is grounded. Three electrodes are assembled inside the ceramic chamber as shown in Fig. 5.1.2a.These electrodes are biased with 190 kV for the first electrode, 105 kV for the second electrode and 0 V for the third electrode. Such a voltage configuration was optimized from stand point of the transverse focusing action by using the IGUN code [4].

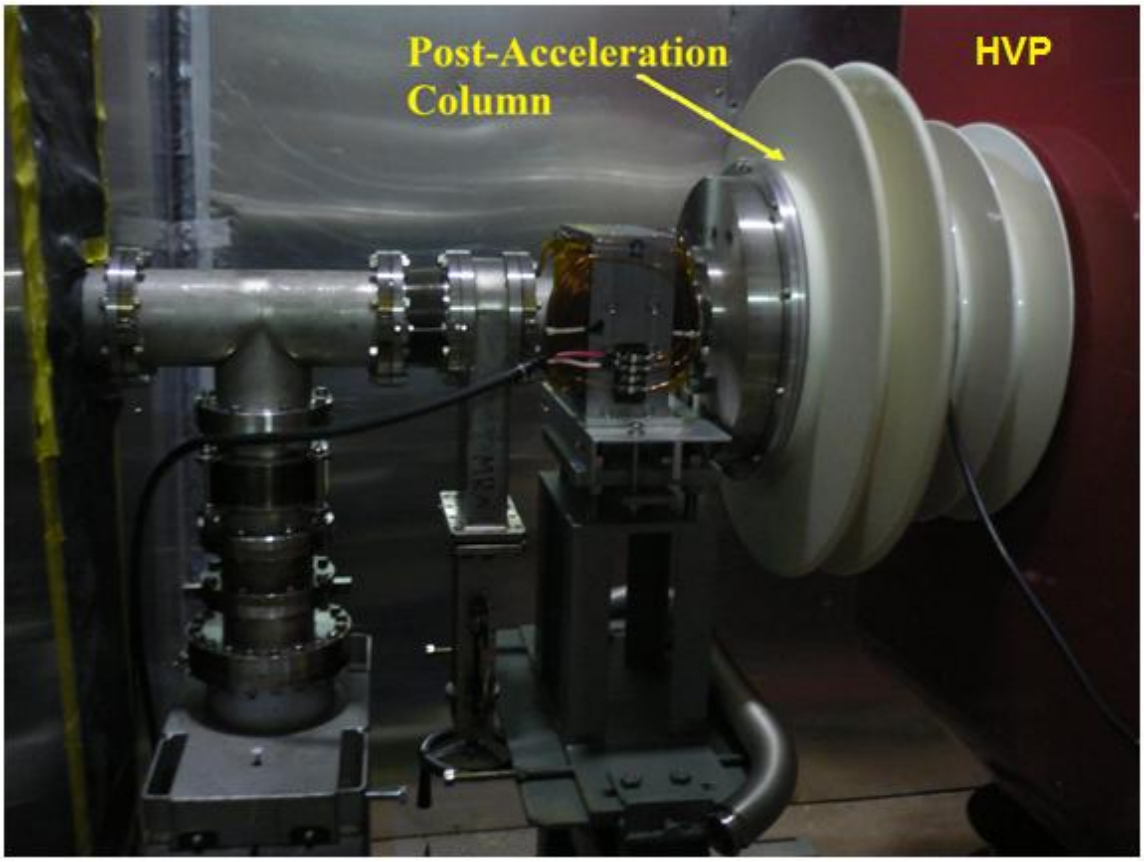

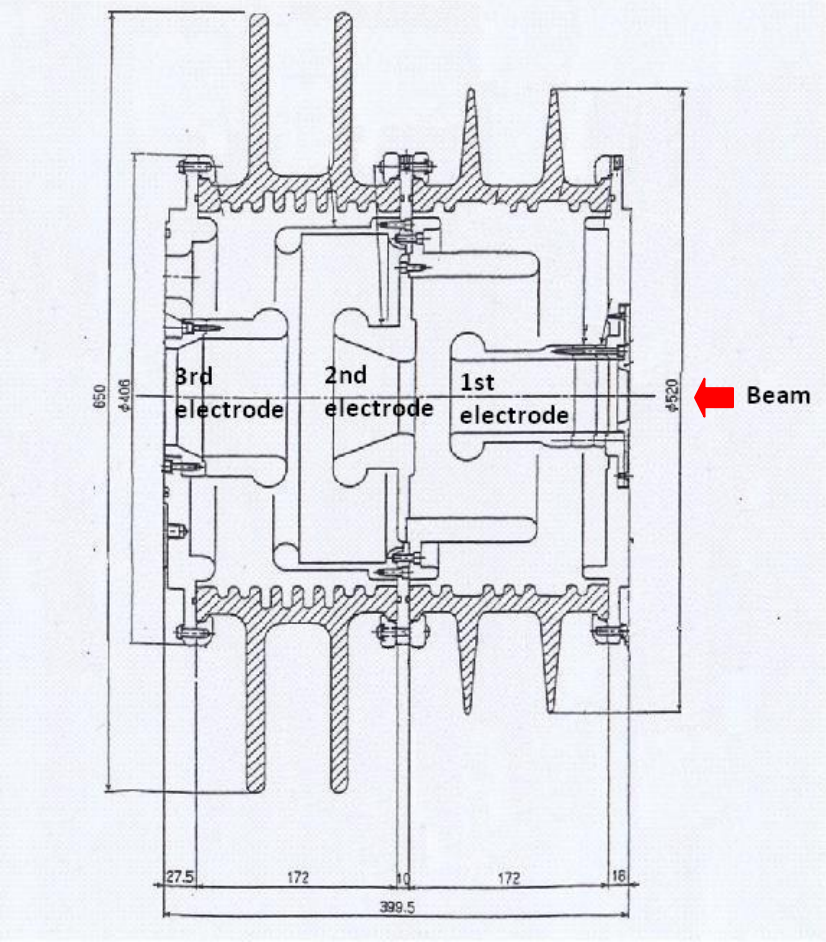

Figures 5.1.2a: A photograph of the post-acceleration column and its side cross section

5.1.3 Power Supply Distribution

The main AC power is supplied directly from the mains of 200 V to an isolation transformer, which distributes the power into two transformers located inside the HVP. One transformer steps down the voltage to 100 V and distributes it to apparatuses with the rating of 100 V. The other transformer directly supplies the 200 V to the remaining apparatuses. Typical apparatuses inside the HVP are as follows:

1. Turbo molecular pump (100ACV) – 3 units
2. Vacuum gauge (100ACV)– 2 units
3. Power supply for microwave system (200ACV)- 1 unit

4. Power supply for Marx generator (100ACV) – 1 unit
5. Power supply for extraction electrode (100ACV) – 1 unit
6. PLC control system (100ACV) – 2 units

5.2 Analyzer Magnet

5.2.1 Overview

An analyzer magnet BM1 is located just after the post-acceleration column as shown in Fig. 5.2.1a.This magnet selects the required ion and guides it to the LEBT.

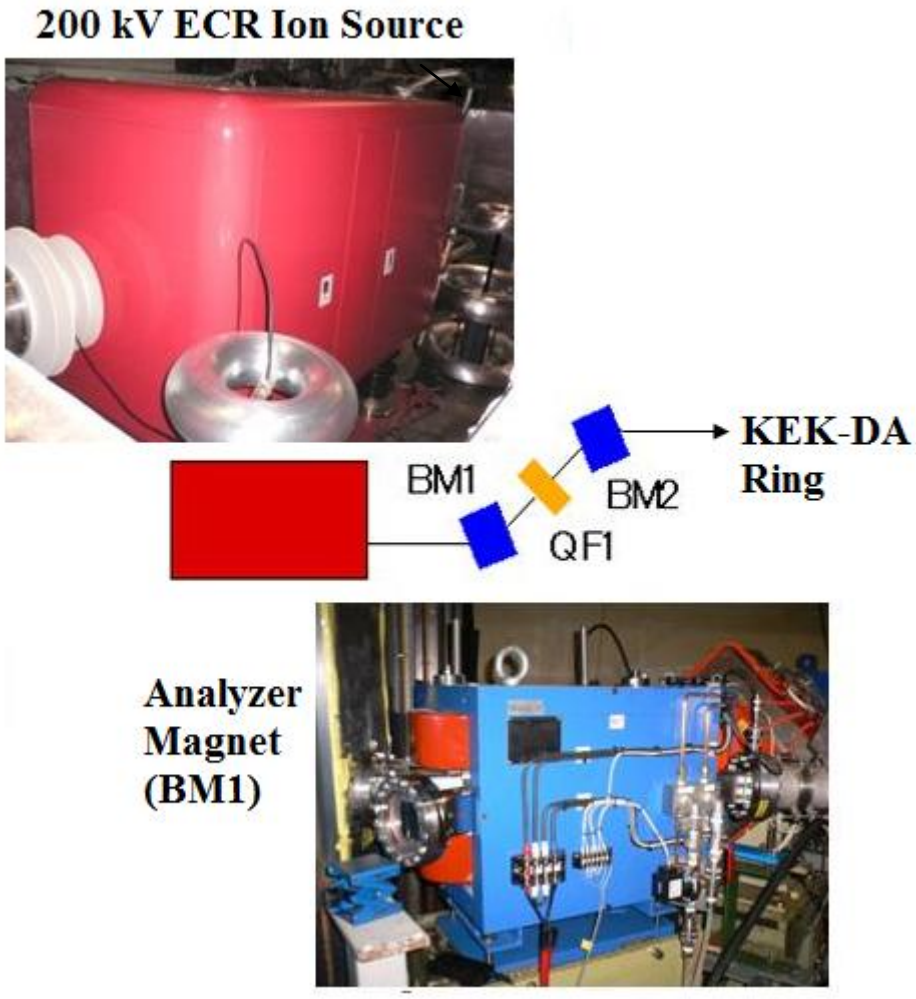

Figure 5.2.1a: Plan and photograph of the LEBT around the HVP

This magnet was manufactured by NEC Tokin Company and its specification is listed in Table 5.1.

Table 5.1: Specification of the analyzer magnet

Parameters	Figures
Magnet pole gap	70mm
Bending radius	605.9mm
Bending angle	45°
Number of coil turns	380
Edge angle @ injection	10~20°
Edge angle @ extraction	10~20°
Maximum voltage	40 V
Maximum current	60A
DC resistance in 20°C	0-52Ω
Required water flow rate	12.3 L/min
Total Weight	650 Kg

(*The bending radius was estimated by using the results of the field measurement as described later.)

A plan of the analyzer magnet is shown in Fig. 5.2.1b.

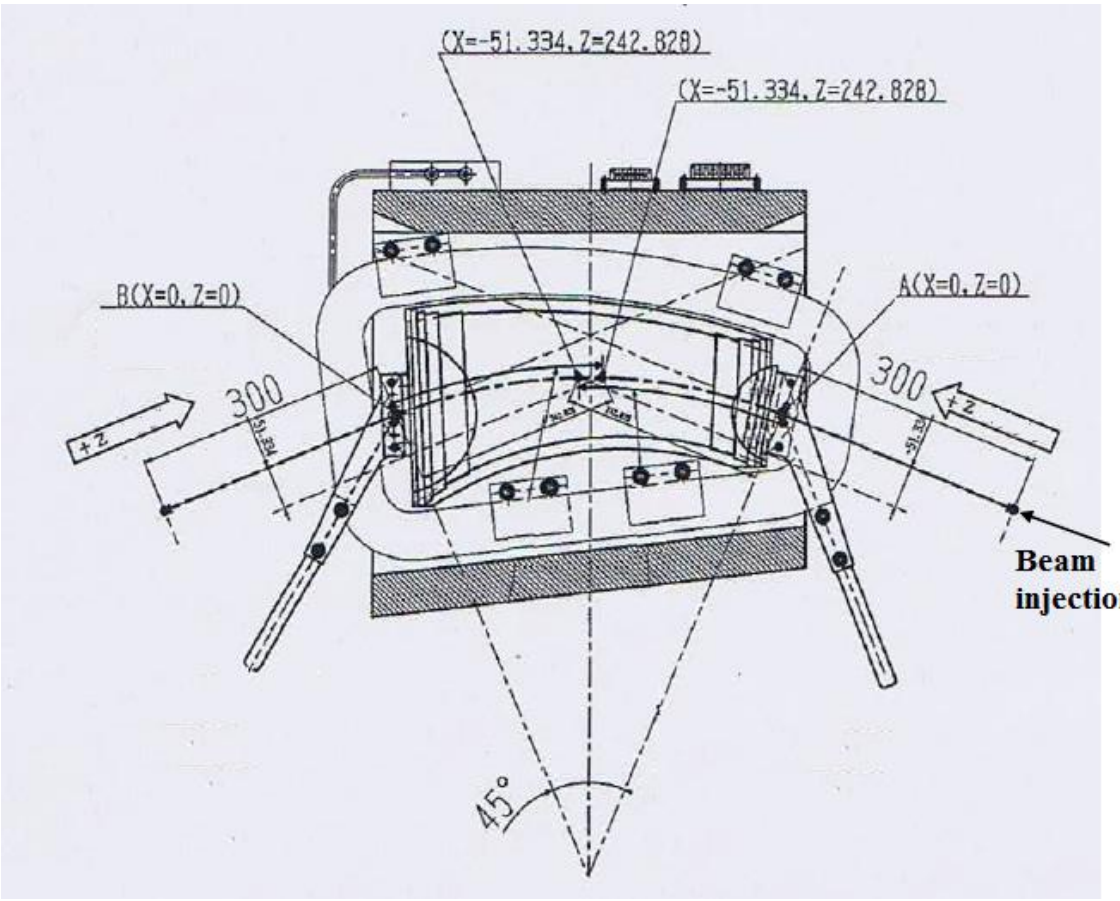

Figure 5.2.1b: Plan of the analyzer magnet

5.2.2 Field Measurement

In order to estimate the desired excitation current or magnetic field for a specific ion, the magnetic field at the magnet center was measured with the excitation current range from 0 to 60 A. The result is shown in Fig. 5.2.2a. By using this result, current dependence of the magnetic field was obtained as:

$$B = 66.4732 \times I \qquad (5.1)$$

Here, B and I are magnetic field density in gauss unit and excitation current in ampere, respectively.

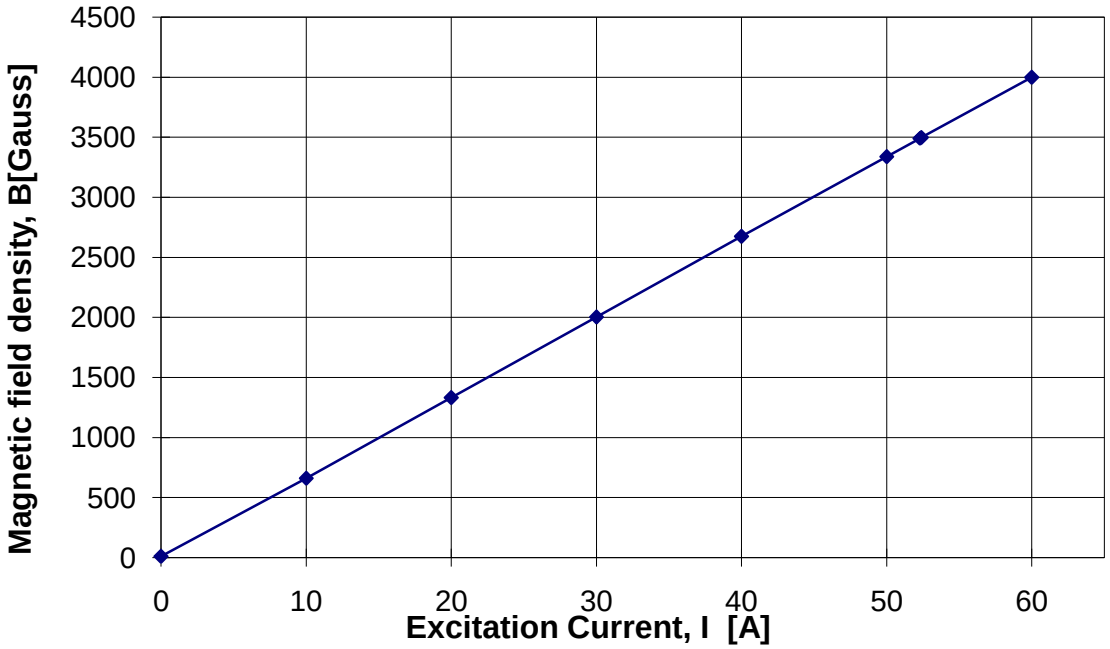

Figure 5.2.2a: Current dependence of the magnetic field at the center of the magnet

Since the magnetic field along the magnet central axis was measured by NEC Tokin Company as shown in Fig. 5.2.2b, the effective length was estimated in terms of the following formula:

$$l_{eff} = \frac{1}{B(0)} \int_{-\infty}^{\infty} B(z)dz \tag{5.2}$$

The result is given as:

$$l_{eff} = 0.4759m \tag{5.3}$$

The bending radius ρ is evaluated by assuming the bending angle to be $\pi/4$. The result is listed in the Table 5.1.

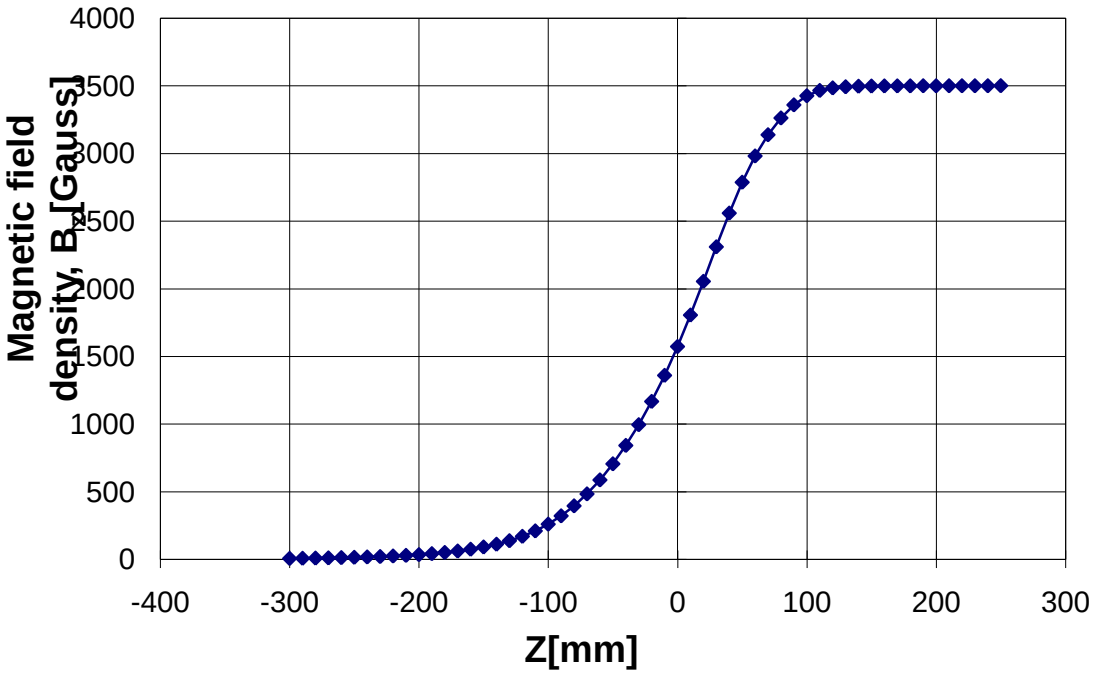

Figure 5.2.2b: z dependence of the magnetic field density along the magnet central axis

5.2.3 Excitation Current and Ion Species

In the KEK-DA, an ion is extracted from the extraction electrode with voltage V_1 (10 kV) and accelerated with V_2 (190 kV) at the post-acceleration column [1]. Hence, the total acceleration voltage is 200 kV. According to the energy conservation law, kinetic energy of an ion with the mass number A and the charge number Z is expressed as:

$$\frac{p^2}{2Am_N} = ZeV \tag{5.4}$$

Hence,

$$p = \sqrt{2Am_N ZeV} \tag{5.5}$$

According to the balance between the centrifugal force and the Lorentz force,

$$B = \frac{\sqrt{2Am_N ZeV}}{Ze\rho} = \frac{1}{\rho}\sqrt{\frac{2Am_N V}{Ze}} \tag{5.6}$$

Here, B is equivalent to the $B(0)$ in Eq. (5.2).

Here, symbols in the formula are defined as follows:

m_N : atomic mass unit,

V : acceleration voltage,

e : electron charge,

A : ion mass number,

Z : ion charge number and

ρ : bending radius.

The required excitation currents for various ions accelerated with the voltage of 200 kV are listed in Table 5.2. From Eq. (5.6), we notice that with the fixed acceleration voltage the required magnetic field is mainly dependent on the ratio of the ($\sqrt{Z}/A$). Therefore, the required excitation current for the analyzer magnet should be higher as ion charge state becomes higher.

Table 5.2: Required excitation currents for various ions

Required magnetic field of BM1 , B(0) [Gauss]	Required excitation current of BM1, I [A]	Ar (A=40)	Neon (A=20)	Oxygen (A=16)	He (A=4)
6744.66	101.46	1+			
4769.20	71.75	2+	1+		
3894.03	58.58	3+			
3372.33	50.73	4+	2+		
3016.30	45.38	5+		2+	
2753.50	41.42	6+	3+		
2549.24	38.35	7+			
2384.60	35.87	8+	4+		
2248.22	33.82	9+			
2132.85	32.09	10+	5+	4+	1+
2033.42	30.59	11+			
1947.00	29.29	12+	6+		
1870.56	28.14	13+			
1802.75	27.12	14+	7+		
1741.60	26.20	15+		6+	

1686.43	25.37	16+			
1508.28	22.69	----------	10+	8+	2+

5.3 LEBT

5.3.1 Lattice Parameters

A low-energy beam transport (LEBT) line guides an ion beam extracted from the ECR ion source to the DA ring. The LEBT is divided into two regions, which are called as Regions I and II as shown in Fig. 5.3.1a. Region I comprises axial symmetric devices, such as the Einzel lens located just after the extraction electrode, the 190 kV post-acceleration column with the inner focusing electrodes and the beam drift space up to the entrance of the analyzer magnet (BM1) [1].

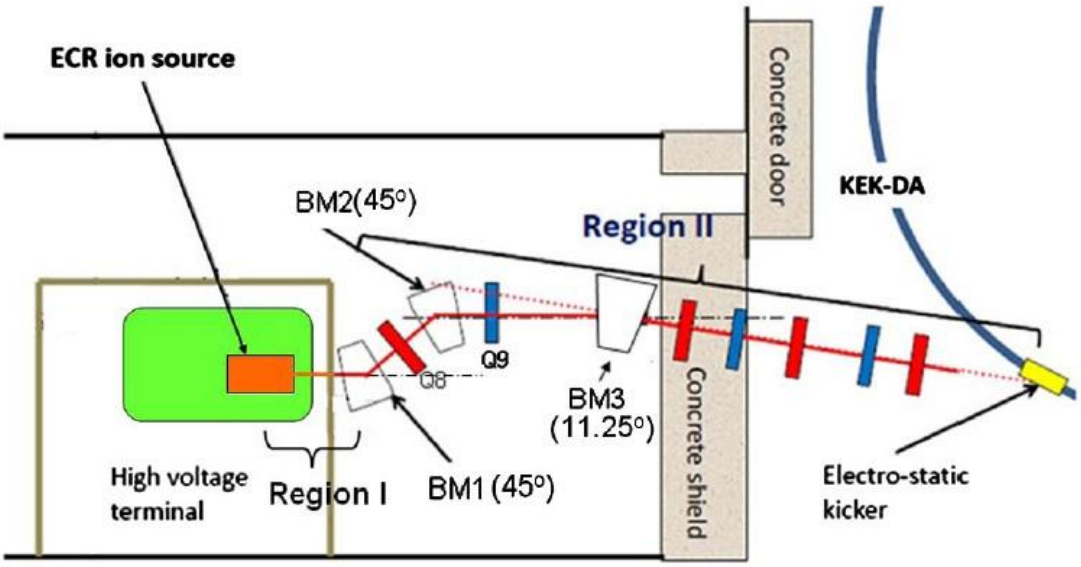

Figure 5.3.1a: LEBT line from ECRIS to KEK-DA ring [1]

In this region, the space-charge limited ion current and beam envelope are estimated using the IGUN code, assuming the experimentally obtained current fractions of He^{1+} and He^{2+}.Region II is remaining region from the entrance of the analyzer magnet to the entrance of the electrostatic injection kicker.The magnet configuration and parameters of the LEBT lattice are shown in Fig. 5.3.1b and Table 5.3. And the twiss parameters along the LEBT are shown in Fig. 5.3.1c. The lattice parameters, which is presently used, were

determined by inversely transporting the twiss parameters at the injection point (s1) of the DA ring to the entrance of the BM1 (s2), since there was no information about the beam parameters extracted from the ECRIS. Therefore, the lattice parameters must be optimized by using actual beam parameters carefully to avoid a beam loss in future.

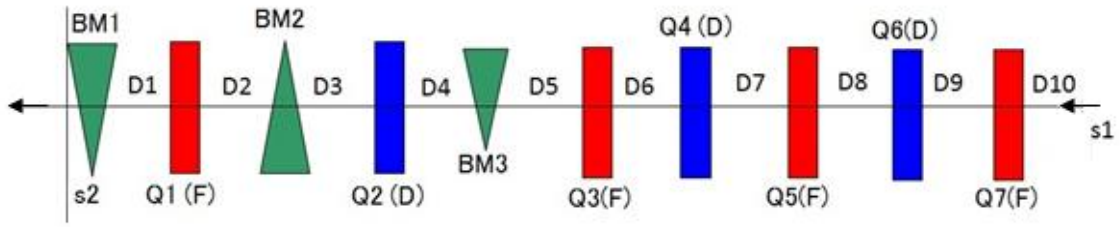

Figure 5.3.1b: Lattice of the LEBT

Table 5.3: LEBT Lattice Parameters

Drift space	Length [m]
D1	0.50
D2	0.475
D3	0.750
D4	1.18
D5	2.356
D6	0.412
D7	1.030
D8	1.043
D9	0.406
D10	3.573

Qmagnet	K-value [m^{-2}]
Q1 (F)	0.4588
Q2 (D)	1.3800
Q3 (F)	2.5955
Q4 (D)	2.3735
Q5 (F)	0.9763
Q6 (D)	2.3735
Q7 (F)	2.5955

Bending magnet	Bending angle [°]	Edge angle [°]	Curvature radius [m]
BM1	45	20	0.6
BM2	45	11.7	0.6
BM3	11.25	------	3.12

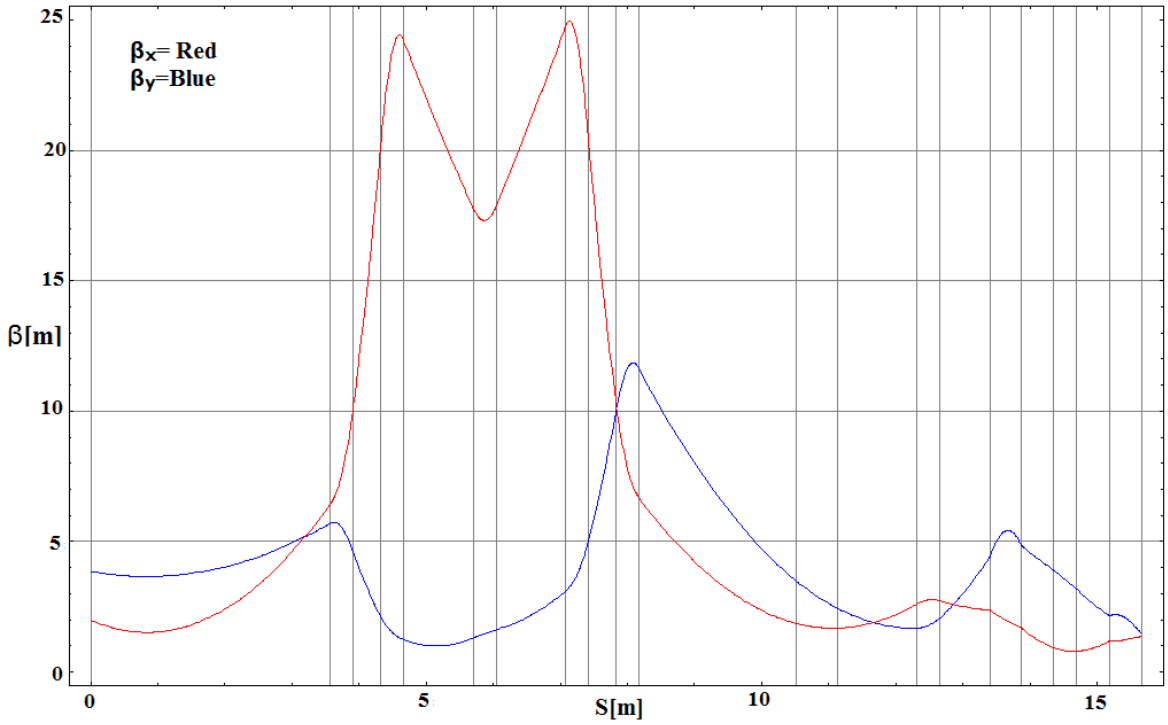

Figure 5.3.1c: Twiss parameters along the LEBT

References

[1] T. Iwashita, T. Adachi, K. Takayama, T. Arai, Y. Arakida, M. Hashimoto, E. Kadokura, M. Kawai, T. Kawakubo, Tomio Kubo, K. Koyama, H. Nakanishi, K. Okazaki, K. Okamura, H. Someya, A. Takagi, A. Tokuchi, **K. W. Leo**, and M. Wake, "KEK Digital Accelerator", *Phys. Rev. AB-ST* **14**, 071301(2011).

[2] http://www.spellmanhv.com/

[3] High Voltage reference manual from Spellman High Voltage Electronics Corporation

[4] R. Becker, and W. B. Herrmannsfeldt, "IGUN- A Program for the Simulation of Positive Ion Extraction including Magnetic Fields", *Rev. Sci. Instrum.***63**, 2756 (1992).

6. Transient Beam Motion Induced by Einzel Lens Chopper Mechanism

6.1 Introduction

The chopped beam is injected to the DA ring through the LEBT. Fig. 6.1a shows an un-accelerated circulating beam bunch signal observed by an electrostatic (ES) bunch monitor (the yellow trace). It is obvious that the bunch signal has characteristic peaks at the front and end of the pulse. It has been suspected that this may reflect any specific longitudinal beam dynamics caused in the chopper region. For the purpose to manifest what happens in the chopper region, a simple simulation code has been developed by using Visual C++, since IGUN code cannot treat the particle motion in the time-varying electro-magnetic fields.

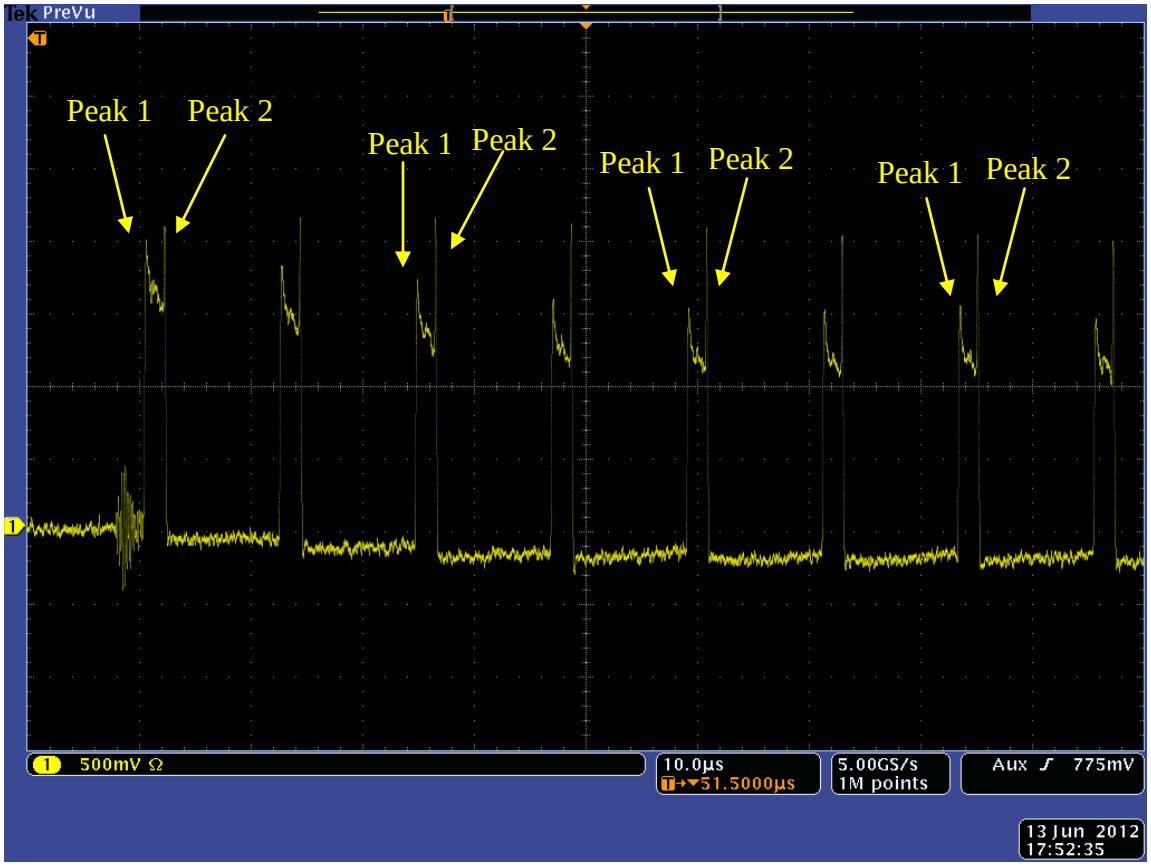

Figure 6.1a: Circulating beam signal observed by ES monitor in the DA ring

6.2 Simulation Procedure

The simulation procedure is described by the flow chart shown in Fig. 6.2a. This simulation is started from the initial plane located at the position of the extraction electrode. At first, the position and momentum of macro-particles are generated assuming a uniform distribution in the x-y plane and the Maxwell-Boltzmann distribution in the momentum space [1], as described in Appendix 4. Then, the particle is transported to downstream, which is divided into three regions: Einzel lens region, post-acceleration column region, and LEBT region as shown in Fig. 6.2b. The first two regions have the axis-symmetry, while the last region is a normal beam transport line consisting of bending magnets and quadrupole magnets. In all regions, a particle goes outside the transverse aperture, which is determined by a vacuum duct size, is rejected to estimate the transmission efficiency. The detail of each region will be described in the following sections.

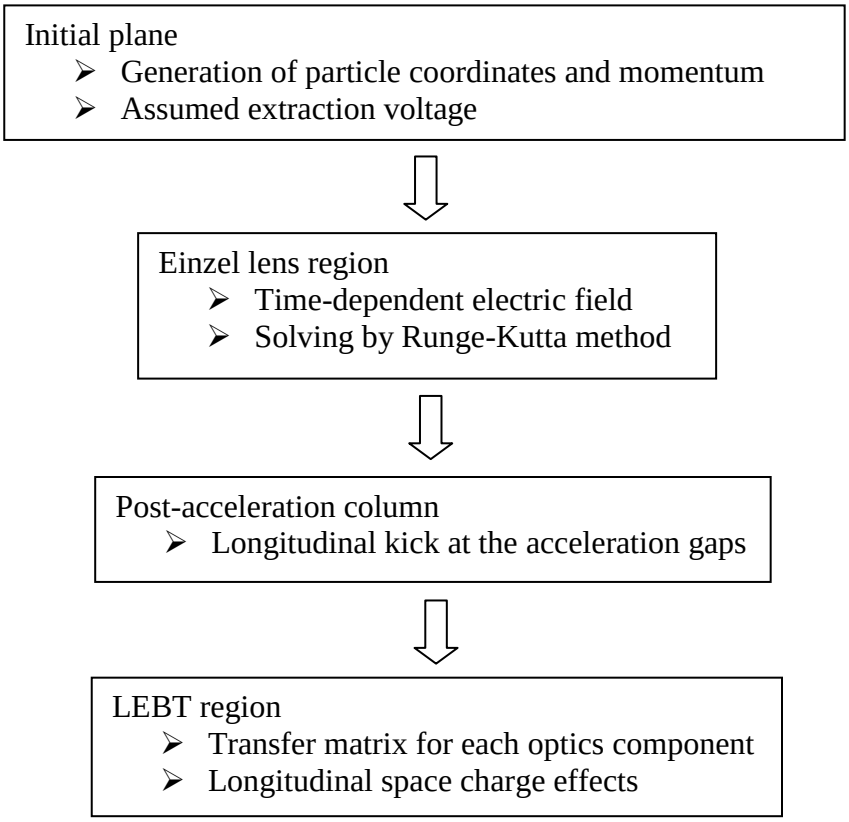

Figure 6.2a: Flow chart of the simulation procedure [1]

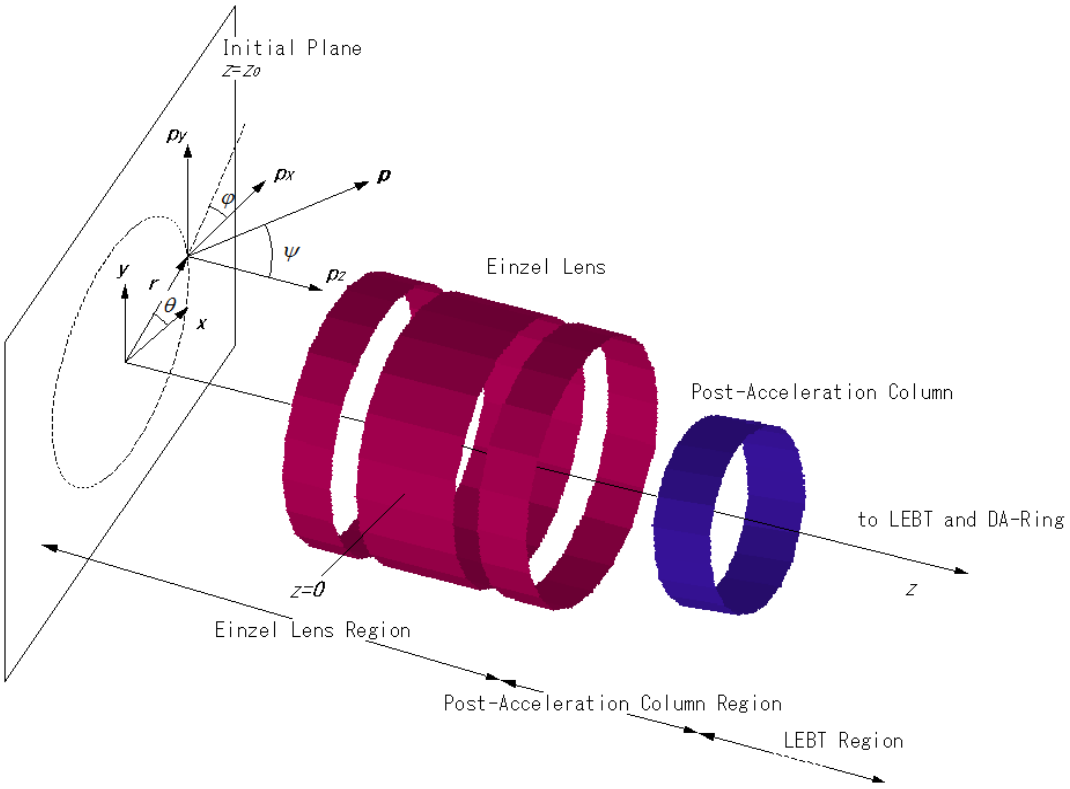

Figure 6.2b: Schematic of the various simulation regions [1]

6.2.1 Initial Condition

In the initial plane, an axis-symmetric uniform distribution with a radius of r_{max} in the x-y plane [1] is generated by the following formula:

$$r = r_{max} \cdot \sqrt{u_1} \tag{6.1}$$

$$\theta = 2\pi . u_2 \tag{6.2}$$

$$x = r \cos\theta \tag{6.3}$$

$$y = r \sin\theta \tag{6.4}$$

Here,

u_1 and u_2 = Uniform random numbers within the range from 0 to 1

In addition, a momentum obeying the Maxwell-Boltzmann distribution in the momentum space is generated by the following:

$$p = \sqrt{-2mkT.ln(1-u_3)} \tag{6.5}$$

$$\psi = cos^{-1}(1-2u_4) \tag{6.6}$$

$$\varphi = 2\pi.u_5 \tag{6.7}$$

$$p_x = p\,sin\,\psi\,cos\,\varphi \tag{6.8}$$

$$p_y = p\,sin\,\psi\,sin\,\varphi \tag{6.9}$$

$$p_z = p\,cos\,\psi \tag{6.10}$$

Here,

u_3 , u_4 and u_5 = Uniform random numbers within the range from 0 to 1

T = Plasma temperature, m = Ion mass, k = Boltzmann constant

ψ = Polar angle and φ = Azimuthal angle in the momentum space

Since the initial plane is located at the extraction electrode, a constant energy of ZV_{ext} is added to particle energy in z-component [1]. Therefore, particle momentum in z-component is modified according to the following formula:

$$p_{z,new} = \sqrt{{p_z}^2 + 2ZV_{ext}E_{tot} + Z^2{V_{ext}}^2} \tag{6.11}$$

$$E_{tot} = \sqrt{p^2 + m^2} \tag{6.12}$$

Here,

E_{total} = Relativistic total energy, V_{ext} = Extraction voltage (10 kV)

Momentum unit is eV/c and ion mass unit is eV

(Note: x and y components of the momentum are unchanged)

Since the electric field is time dependent, the initial time is generated between t_{min} and t_{max} by a random number u_6:

$$t = t_{min} + (t_{max} - t_{min}).u_6 \tag{6.13}$$

6.2.2 Einzel Lens Region

The Einzel lens region is defined from the initial plane to the location where the electric field of the lens is considered to be sufficiently low. In this region, the particle is affected by the axial symmetric electric filed which is formulated in the following section. By taking account of the definition of the coordinate system used for field formulation, the origin of the z coordinate is set at the center of the middle electrode of the Einzel lens. By using cylindrical coordinate system, the equation of motion is given by:

$$Am\frac{dv_r}{dt} = ZeE_r \tag{6.14}$$

$$Am\frac{dv_z}{dt} = ZeE_z \tag{6.15}$$

Here,

$A =$ Atomic mass number , $m =$ Atomic mass unit, $Z =$ Ion charge state

$v_r =$ Ion veloctity in r direction, $v_z =$ Ion veloctity in z direction

$E_r =$ Electric field in r direction and $E_z =$ Electric field in z direction

The Eq. (6.14) and (6.15) are solved by using the Runge-Kutta algorithm [2].

6.2.2.1 Formulation of electric field in Einzel lens

In this simulation, static field treatment is used for formulation of the time dependent field. We consider that this approach is available for our case because of the following reason:

As shown in Fig. 4.4.2b, the rising and falling times of the voltage pulse for beam chop are ~ 100 ns. It corresponds to the frequency of 10 MHz and characteristic wavelength is

30 m. On the other hand, the length of the Einzel lens is 110 mm. The characteristic wavelength size is larger than the Einzel lens length. Therefore, the static treatment is available in our case.

The time dependent electric field can be expressed by:

$$\boldsymbol{E}(t) = \boldsymbol{E_{static}}(r, z).T(t) \qquad (6.16)$$

Here, $\boldsymbol{E}_{static}$ is a static electric field and *T(t)* is a normalized waveform of the chopping voltage.

According to Appendix 5, electric field for r component is given by

$$\boldsymbol{E_r} = \frac{\phi_0}{\pi}\int_0^{\infty}\frac{I_1(x\tilde{r})}{I_0(x)}\frac{\{\cos x\,(\tilde{z}+\tilde{b}) + \cos x(\tilde{z}-\tilde{b}) - \cos x(\tilde{z}+\tilde{a}) - \cos x(\tilde{z}-\tilde{a})\}}{x(b-a)}dx$$

Electric field for z component is given by,

$$\boldsymbol{E_z} = \frac{\phi_0}{\pi}\int_0^{\infty}\frac{I_0(x\tilde{r})}{I_0(x)}\frac{\{\sin x\,(\tilde{z}+\tilde{a}) + \sin x(\tilde{z}-\tilde{a}) - \sin x(\tilde{z}+\tilde{b}) - \sin x(\tilde{z}-b)\}}{x(b-a)}dx$$

Here,

$$I_0, \mathrm{I}_1 = \text{Modified Bessel function,}$$

$$\phi_0 = \text{Potential at the middle}$$

$$\tilde{r} = \frac{r}{r_0}, \tilde{z} = \frac{z}{r_0}, \tilde{a} = \frac{a}{r_0}\ and\ \tilde{b} = \frac{b}{r_0}\ \text{(Appendix 5)}$$

6.2.2.2 Formulation of the potential in the middle electrode of Einzel lens

As expressed in (6.16), the potential is time dependent. Therefore, a time profile $\emptyset(t) = \emptyset_0 T(t)$ was prepared according to a line chart approximation from the measured output voltage signal of the Marx generator as shown in Fig. 6.2.2.2a.

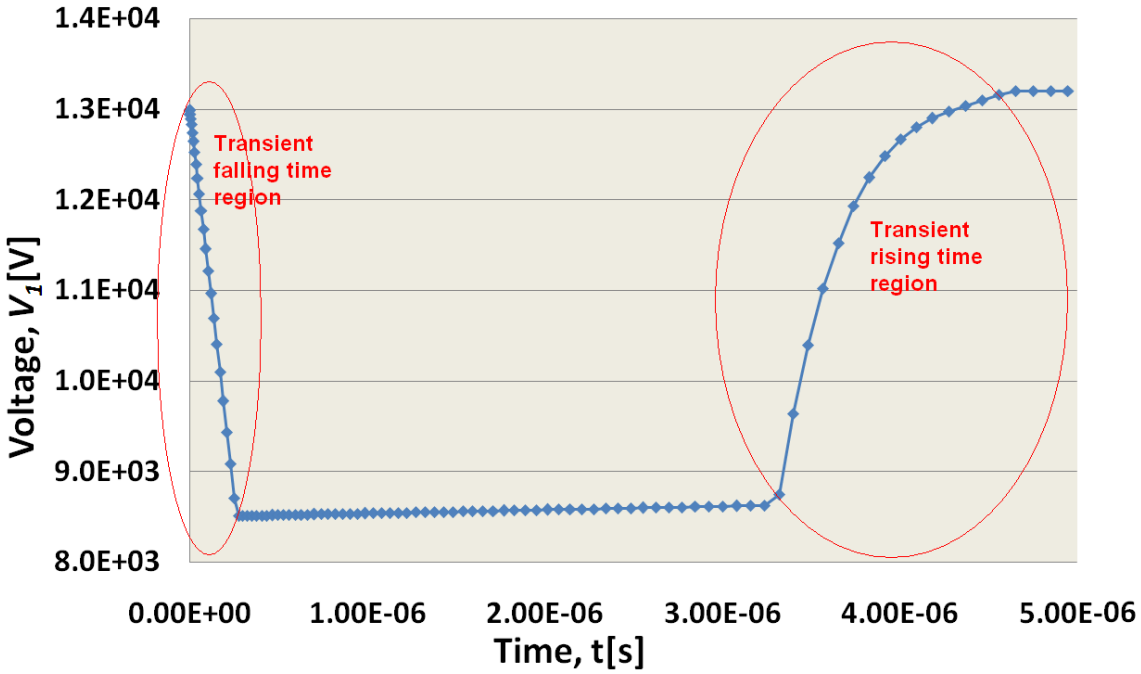

Figure 6.2.2.2a: Waveform of the chopping voltage applied to the middle electrode of the Einzel lens

The time profile is divided into four time regions and polynomial fit was carried out for each time region [1]. The results are shown below:

For $0 \leq t < 2.6X10^{-7}$s,

$$\emptyset(t) = (-1.296 \times 10^{10}) \times t + 1.30 \times 10^{4}; \quad (6.17)$$

For $2.6X10^{-7} \leq t < 3.26X10^{-6}$s,

$$\emptyset(t) = (3.8926 \times 10^{7}) \times t + 8500.0; \quad (6.18)$$

For $3.26X10^{-6} \leq t < 4.62X10^{-6}$s,

$$\emptyset(t) = (-3.558 \times 10^{32}) \times t^5 + (5.886 \times 10^{27}) \times t^4 - (3.375 \times 10^{22}) \times t^3 + (6.460 \times 10^{16}) \times t^2 + (5.357 \times 10^{10}) \times t - 217700; \quad (6.19)$$

For $t < 0$ and $t > 4.62X10^{-6}$s,

$$\emptyset(t) = 13200; \quad (6.20)$$

By using the above formulation, the time dependent electric field is evaluated numerically. Some particles are repelled and others pass through the Einzel lens. Those survival particles propagate to the post-acceleration column region.

6.2.3 Post-Acceleration Region

The post-acceleration column region comprises a drift space with the length of L and the acceleration electrode with the voltage of V_{acc} [1]. In this simulation the acceleration electrode is treated as a thin element. At the exit of the post-acceleration column region, the space coordinate and momentum are expressed as:

$$x_{out} = x_{in} + x'_{in}.L \tag{6.21}$$

$$y_{out} = y_{in} + y'_{in}.L \tag{6.22}$$

$$x'_{in} = p_{x,in}/p_{z,in} \tag{6.23}$$

$$y'_{in} = p_{y,in}/p_{z,in} \tag{6.24}$$

$$p_{x,out} = p_{x,in} \tag{6.25}$$

$$p_{y,out} = p_{y,in} \tag{6.26}$$

$$p_{z,out} = \sqrt{{p_{z,in}}^2 + 2ZV_{acc}E_{total} + Z^2{V_{acc}}^2} \tag{6.27}$$

$$E_{total} = \sqrt{{p_{x,in}}^2 + {p_{y,in}}^2 + {p_{z,in}}^2 + m^2} \tag{6.28}$$

$$t_{out} = t_{in} + \frac{L}{v_z} \tag{6.29}$$

$$v_z = \frac{cp_{z,in}}{E_{total}} \tag{6.30}$$

$$p_0 = \sqrt{(ZV_{acct})^2 + 2mZV_{acct}} \tag{6.31}$$

$$x'_{out} = p_{x,out}/p_{z,out} \tag{6.32}$$

$$y'_{out} = p_{y,out}/p_{z,out} \tag{6.33}$$

(Note: V_{acct}=200 kV and V_{acc}=190 kV)

Here suffixes "in" and "out" denote the parameters at the entrance and the exit of the post-acceleration column region, respectively. Mass and energy are expressed in eV unit and momentum is expressed in eV/c unit. The parameter p_0 denotes the nominal momentum for $\Delta p/p$ evaluation.

6.2.4 LEBT Region

The LEBT region comprises various beam optics components, such as bending magnet, quadrupole magnet and etc. Individual optics component is related with the transfer matrices in x and y direction [1]. In addition, the experimental results imply that a longitudinal space charge effect may not be neglected. At the entrance of the LEBT, phase space parameters $(x, x', y, y', \Delta p/p)$ are given by:

$$x = x_{out} \tag{6.34}$$

$$y = y_{out} \tag{6.35}$$

$$x' = p_{x,iout}/p_{z,out} \tag{6.36}$$

$$y' = p_{y,iout}/p_{z,out} \tag{6.37}$$

$$p_x = p_{x,iout} \tag{6.38}$$

$$p_y = p_{y,iout} \tag{6.39}$$

$$p_s = p_{z,out} \tag{6.40}$$

$$t = t_{out} \tag{6.41}$$

$$\nu_s = \frac{cp_s}{\sqrt{{p_x}^2 + {p_y}^2 + {p_s}^2 + m^2}} \tag{6.42}$$

$$\frac{\Delta p}{p} = \frac{p_s}{p_0} - 1 \tag{6.43}$$

Here, a parameter with a suffix "out" denotes the particle at the exit of the post-acceleration column region and s-components is replaced by z-component from now on. A longitudinal space charge is taken account at the first optics element as given below:

$$ZV_{sp} \approx -\frac{g_0}{4\pi\varepsilon_0\gamma^2}\frac{\partial\lambda(s)}{\partial s}L \tag{6.44}$$

$$\gamma = \frac{\sqrt{{p_x}^2 + {p_y}^2 + {p_s}^2 + m^2}}{m} \tag{6.45}$$

Here,

$ZV_{sp} =$ Kinetic energy given by a longitudinal space charge throuh the elemnet length of L

$L =$ Element length , $\lambda =$ Line density of the beam charge and $g_0 =$ Geometrical factor

The detail of the longitudinal space charge effect is described in Appendix 6. The line density is estimated by the following procedure.

Average time <t> is evaluated among all survival particles. Then, longitudinal position (s-direction) of each particle is estimated by the following formula as:

$$s^i = {\nu_i}^i\left(\langle t\rangle - t^i\right), \text{ i=1~ number of generated particles} \tag{6.46}$$

Here, the upper suffix is used as the particle identifier. If the s^i's are sorted into a histogram, a snap shot of the line density $\lambda(s)$ is obtained. But an additional smoothing procedure is required to correct a statistical fluctuation, which gives a large error when a derivative along the beam passage is performed.

By using a transfer matrix evaluation, the resultant beam parameters at the exit of the first element can be expressed by:

$$\begin{bmatrix} x \\ x' \\ \Delta p/p \end{bmatrix}_{exit} = M_x \begin{bmatrix} x \\ x' \\ \Delta p/p \end{bmatrix}_{in} \tag{6.47}$$

$$\begin{bmatrix} y \\ y' \\ \Delta p/p \end{bmatrix}_{exit} = M_y \begin{bmatrix} y \\ y' \\ \Delta p/p \end{bmatrix}_{in} \tag{6.48}$$

$$p_{x,exit} = p_{s,exit} \cdot x'_{exit} \tag{6.49}$$

$$p_{y,exit} = p_{s,exit} \cdot y'_{exit} \tag{6.50}$$

$$p_{s,exit} = \sqrt{{p_{s,in}}^2 + 2ZV_{sp}E_{total} + \left(ZV_{sp}\right)^2} \tag{6.51}$$

$$E_{total} = \sqrt{{p_{x,in}}^2 + {p_{y,in}}^2 + {p_{s,in}}^2 + m^2} \tag{6.52}$$

$$t_{exit} = t_{in} + \frac{L}{\nu_s} \tag{6.53}$$

$$\nu_s = \frac{cp_{s,in}}{\sqrt{{p_{x,in}}^2 + {p_{y,in}}^2 + {p_{s,in}}^2 + m^2}} \tag{6.54}$$

$$\frac{\Delta p}{p} = \frac{p_{s,exit}}{p_0} - 1 \tag{6.55}$$

$$x'_{exit} = p_{x,exit}/p_{s,exit} \tag{6.56}$$

$$y'_{exit} = p_{y,exit}/p_{s,exit} \tag{6.57}$$

If the parameters at the exit of the element are used as the input parameters for the next element, successive evaluation can be performed.

6.3 KEK-DA Ring Region

The KEK-DA ring consists of 8 sector ring magnets and 8 straight sections, which can be treated by using the same procedure performed in the LEBT region. If we prepare a transfer matrix for one section, one turn evaluation can be performed by multiplying the transfer matrix by 8 times.

6.4 Simulation Results

6.4.1 Phase Space Distribution in the Initial Plane

At the extraction electrode of the plasma chamber, 50000 macro particles of He^{1+} are generated. Transverse coordinate of each particle is randomly given by assuming a circular beam with uniform distribution of 3.5 mm in radius [1]. A particle momentum is generated according to the Maxwell-Boltzmann distribution with temperature of 5 eV [1]. After momentum generation, only the z component of the momentum is modified by considering the additional voltage of 10 kV [1]. A time between -2.0 μs and 5.0 μs is randomly assigned to each particle [1]. Initial distribution of the transverse coordinate and momentum distribution are shown in Fig. 6.4.1a and Fig. 6.4 1b.

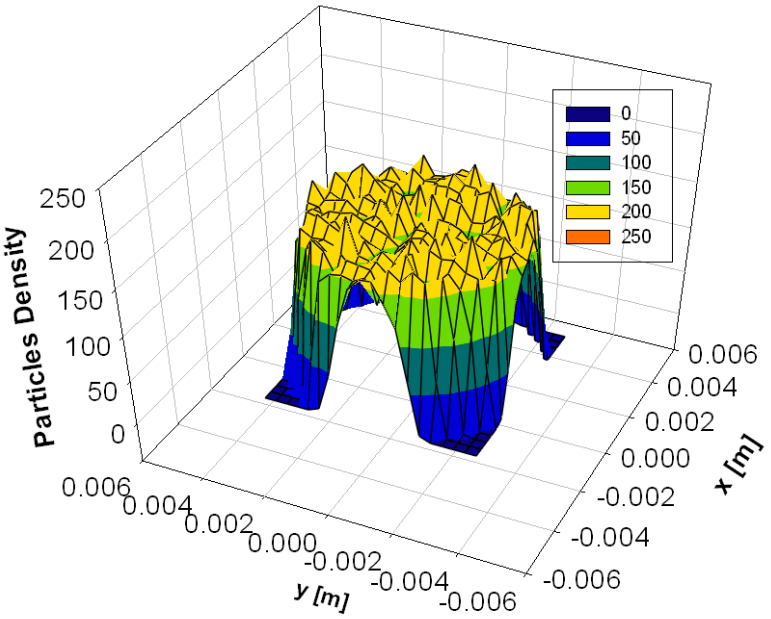

Figure 6.4.1a: Initial distribution of the transverse coordinate

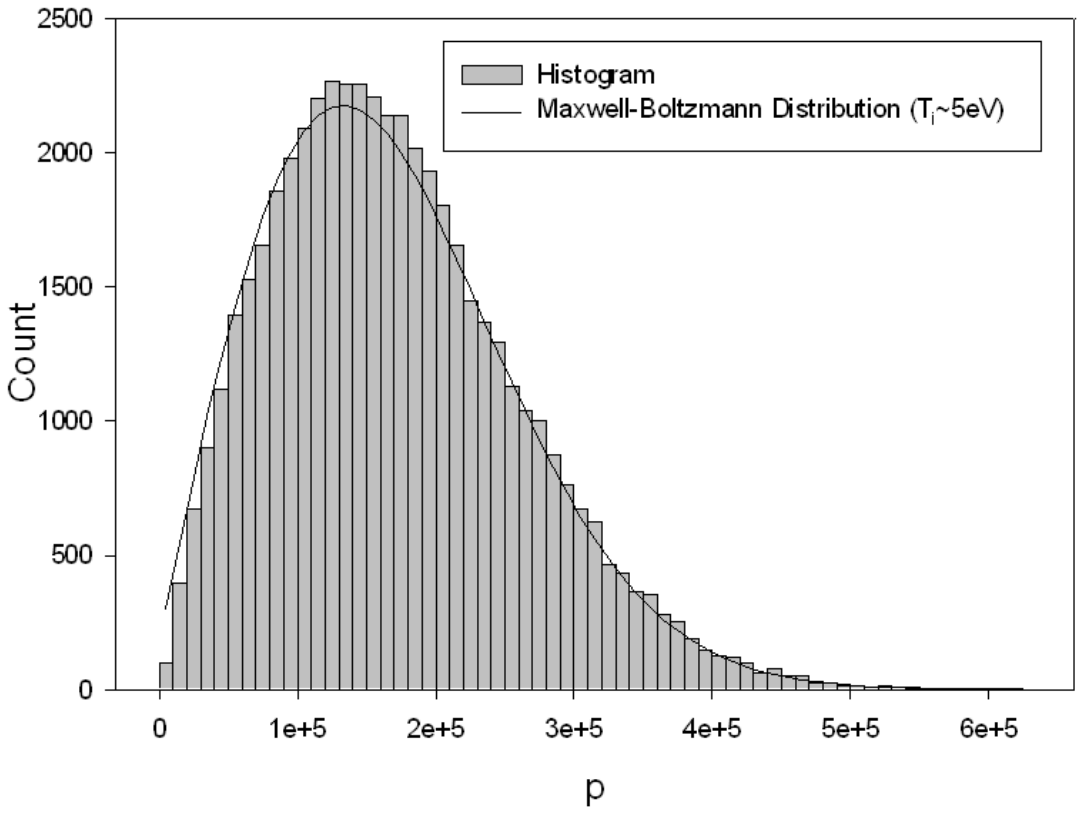

Figure 6.4.1b: Initial momentum distribution and the Maxwell Boltzmann distribution

6.4.2 Phase Space Distribution in the Einzel Lens Region

The generated particles enter the Einzel lens region. According to the time dependent voltage applied to the middle electrode of the Einzel lens, some portions of the particles pass through the Einzel Lens and others are reflected back. Phase space and transverse coordinate distributions of the surviving particles at the exit of Einzel lens or entrance of the post-acceleration column are shown in the Fig. 6.4.2a. Also, time dependent momentum deviation is shown in Fig. 6.4.2b. Since this region is axial symmetric, phase space distributions for horizontal and vertical motions are same.

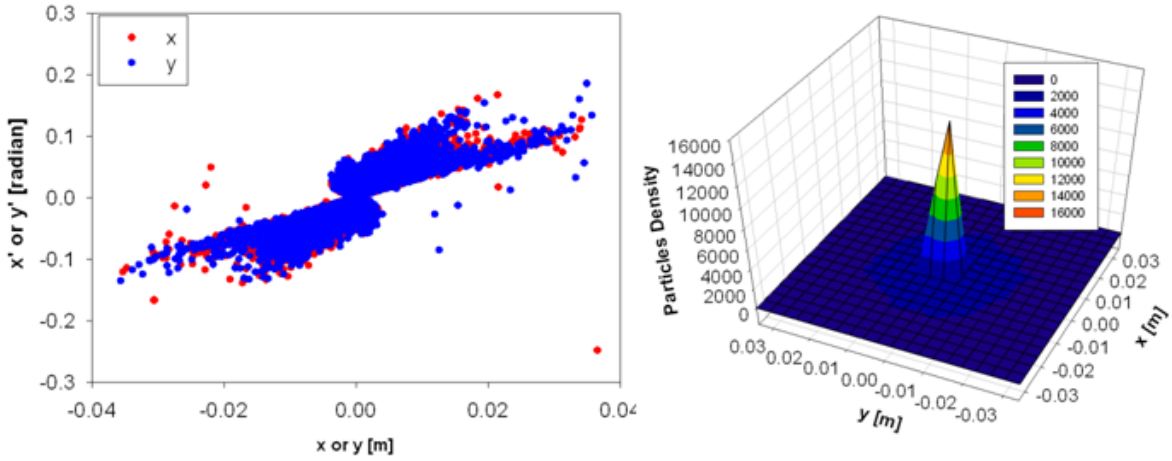

Figure 6.4.2a: Phase space (left) and transverse coordinate (right) distribution at the exit of Einzel lens (Entrance of Post-acceleration column)

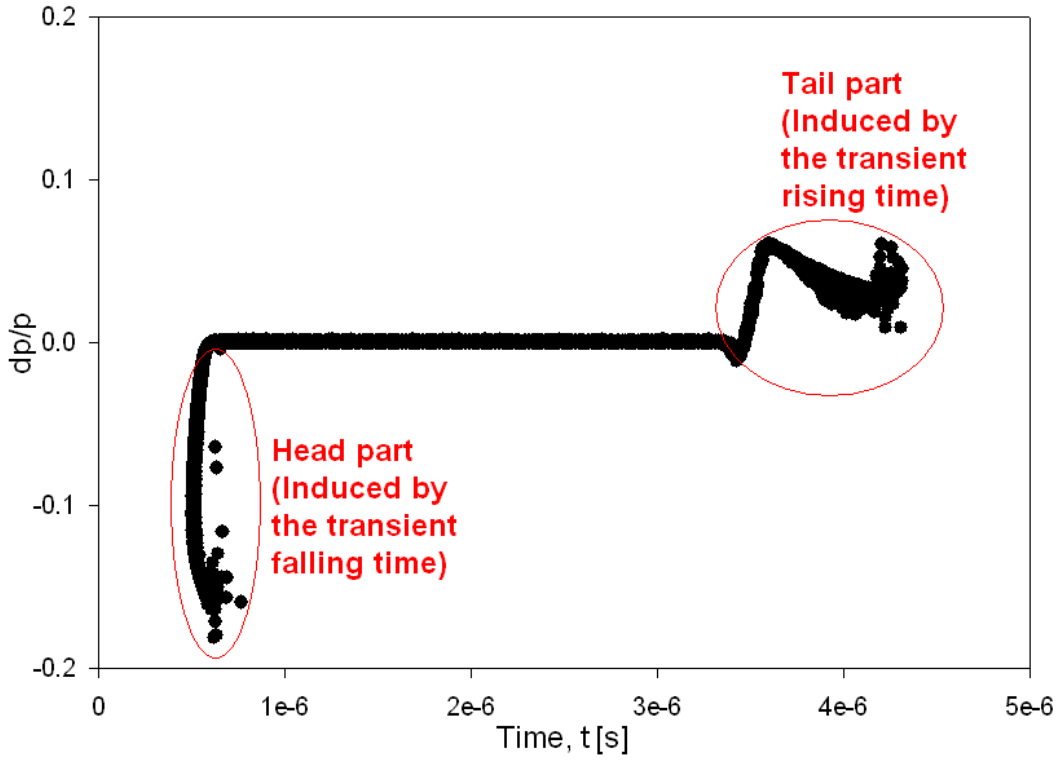

Figure 6.4.2b: Time dependent momentum deviation at the end of Einzel lens region (Entrance of Post-acceleration column) [1] .Here, the parts indicated by the circles correspond to the parts shown in. 6.2.2.2a.

6.4.3 Phase Space Distribution in the Post-Acceleration Region

At this region, the helium particles are accelerated with additional energy of V_1 eV with voltage of V_1 =190 kV. The z-component of the momentum is modified with this extra voltage. Phase space plots and transverse distributions at the exit of this region are shown in Fig. 6.4.3a. Also time dependent momentum deviation is shown in Fig. 6.4.3b.

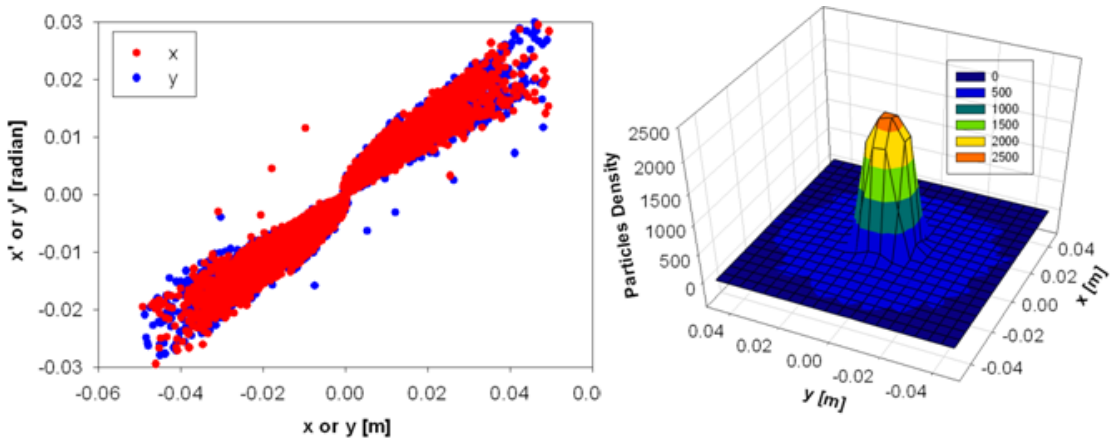

Figure 6.4.3a: Phase space (left) and transverse coordinate (right) distribution at the end of the post-acceleration column (Entrance of LEBT)

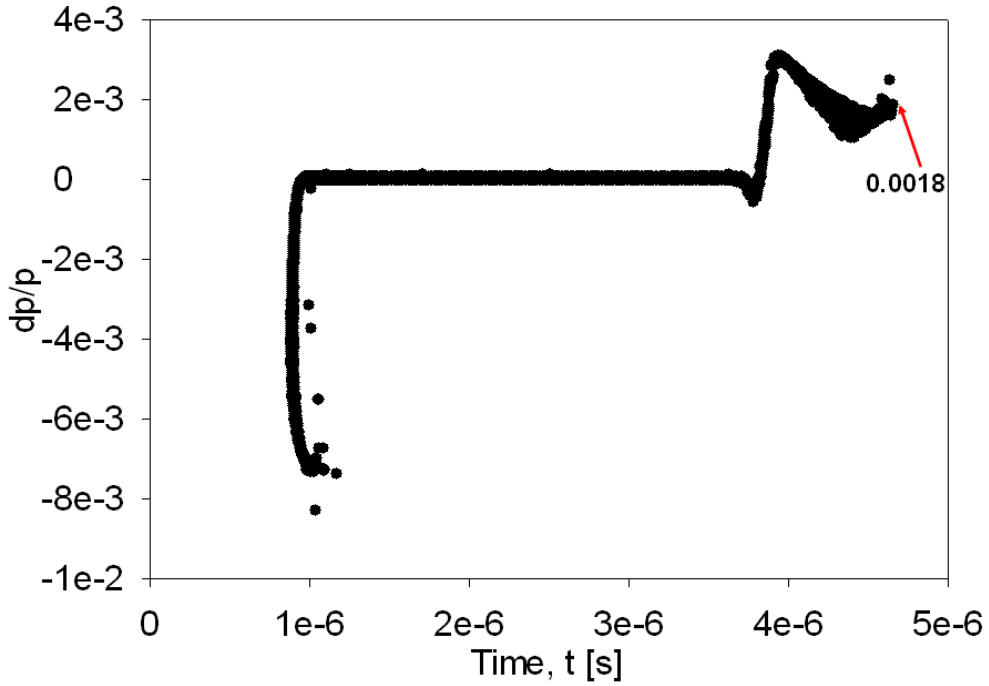

Figure 6.4.3b: Time dependent momentum deviation at the end of post-acceleration column region (Entrance of LEBT) [1]

Since this region is also axial symmetric, phase space distributions for horizontal and vertical motion is same. Figure 6.4.3b clearly shows that momentum deviations are still present after the post-acceleration column region. However, the magnitudes of the deviations have been reduced due to the dominant acceleration voltage as given by Eq. (6.61) which is consistent with our prediction according to Fig. 6.4.2.b.

$$E = mc^2 + T \tag{6.58}$$

Here, E = Total energy and T = kinetic energy.

Where $mc^2 >> T$, thus the momentum deviation can be expressed as:

$$\left(\frac{\Delta p}{p}\right) = \frac{1}{\beta^2}\left(\frac{\Delta E}{E}\right) \tag{6.59}$$

Where, $\beta = v/c$. v= particles velocity and c=light velocity.

From energy conservation law,

$$v^2 = \frac{2ZeV}{Am} \tag{6.60}$$

From (6.58), (6.59) and (6.60) with $mc^2 >> T$,

$$\left(\frac{\Delta p}{p}\right)_{AC} = \left(\frac{\Delta p}{p}\right)_{EL}\left(\frac{V_{ext}}{V_{tot}}\right) \tag{6.61}$$

Here, the indices *EL* and *AC* indicate the Einzel lens region and the post-acceleration column region, respectively. V_{ext} and V_{tot} denote the extraction voltage (10 kV) and the total acceleration voltage (200 kV), respectively.

6.4.4 Phase Space Distribution in the LEBT Region

At this region, the particles pass through 10 optics components as shown in Fig. 6.4.4a. The phase space distributions and transverse coordinate distribution at the exit of first LEBT component and exit of LEBT are plotted from Fig. 6.4.4b to 6.4.4d. Also, the time dependent momentum deviation at the end of LEBT is shown in Fig. 6.4.4e.

In this region, focusing action for horizontal and vertical motion is different. Therefore, phase space distribution for each direction becomes different as the particles pass through the LEBT region.

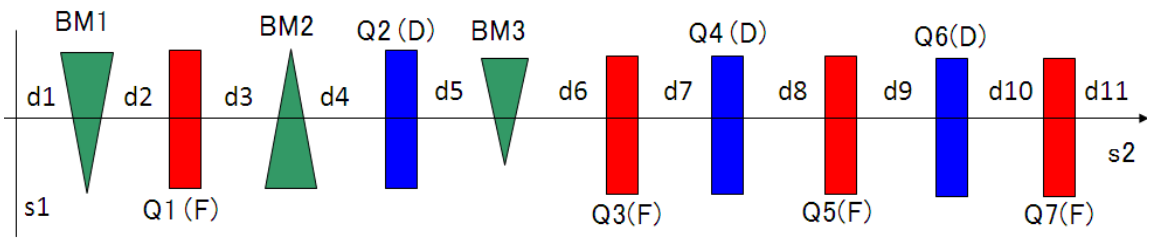

Fig. 6.4.4a: Lattice components of the LEBT

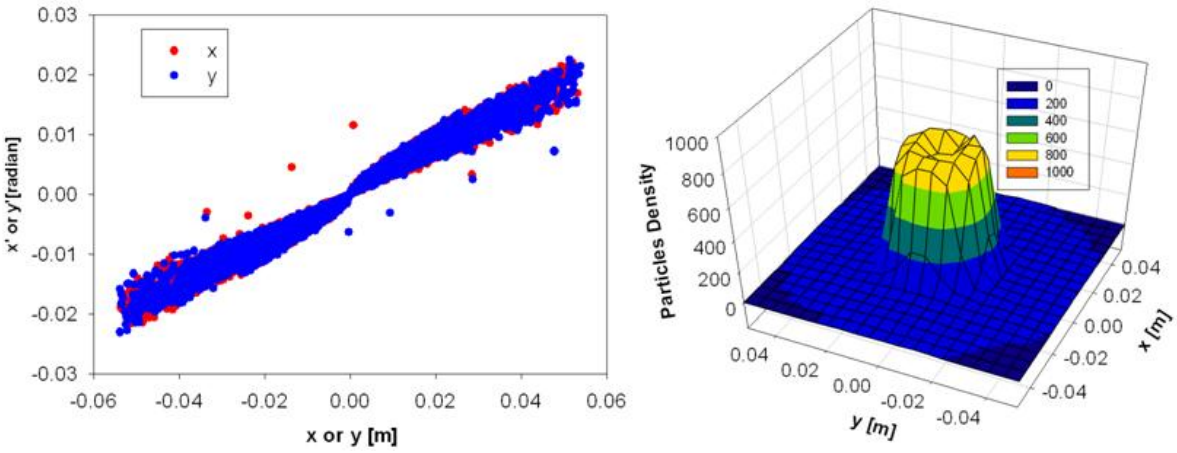

Figure 6.4.4b: Phase space (left) and transverse coordinate (right) distribution at the end of d1

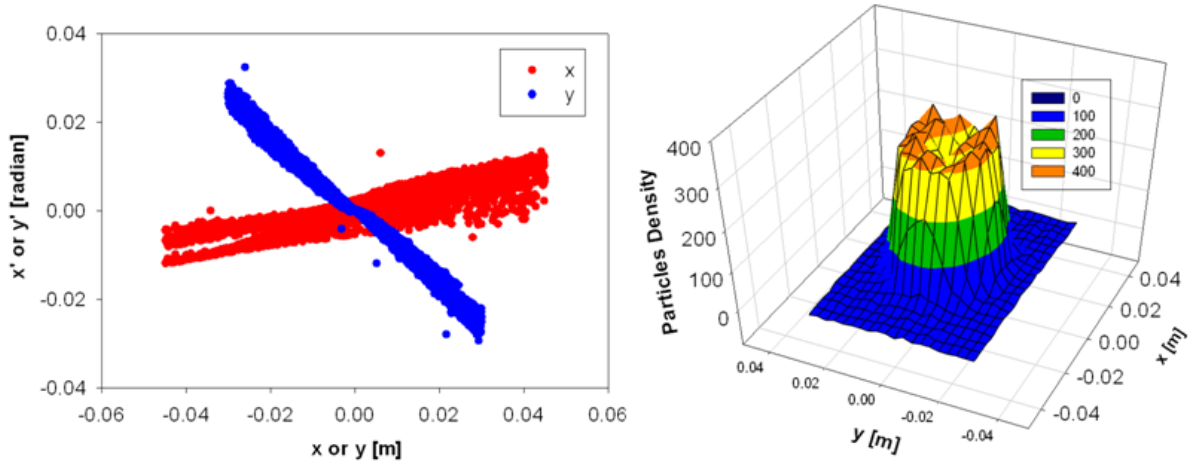

Figure 6.4.4c: Phase space (left) and transverse coordinate (right) distribution at the end of BM2

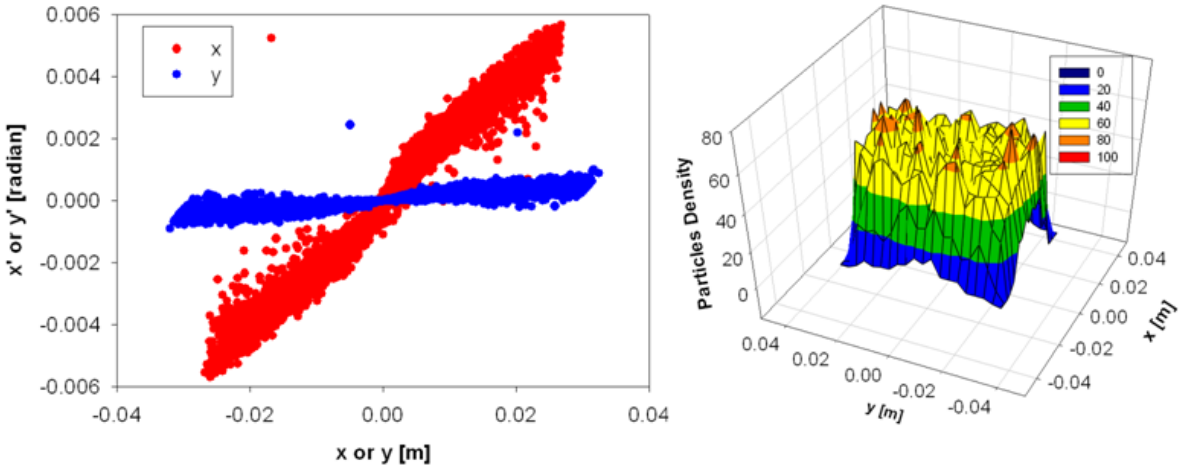

Figure 6.4.4d: Phase space (left) and transverse coordinate (right) distribution at the end of LEBT

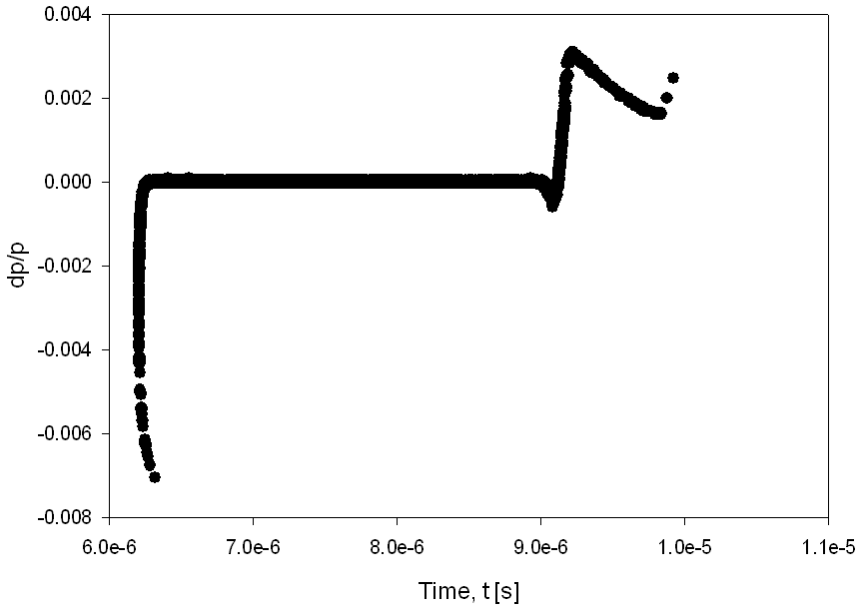

Figure 6.4.4e: Time dependent momentum deviation at the end of LEBT

Surviving particle number for each region is counted during the simulation, so that the transmission efficiency for each region can be estimated. The result is shown in Fig. 6.4.4f.

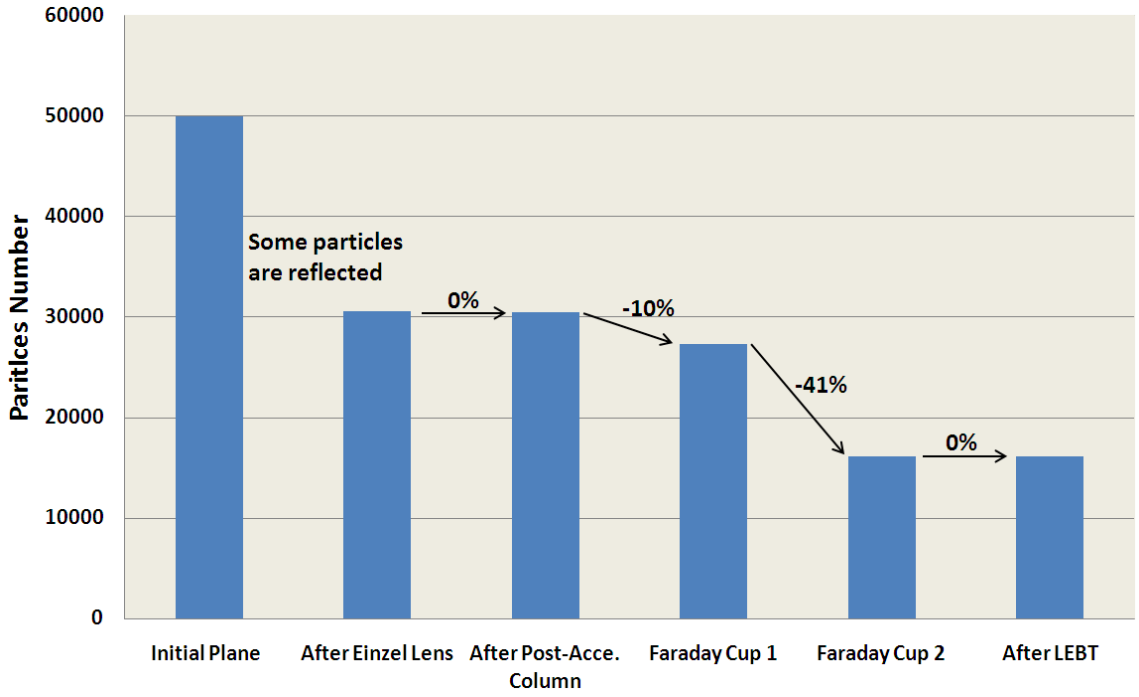

Figure 6.4.4f: Surviving particle number from initial plane to exit of Einzel lens, from exit of Einzel lens to exit of post-acceleration column and from entrance of LEBT to exit of LEBT

According to the simulation result, the LEBT transmission efficiency is ~59% and most of the particles are lost within Q3(F) and d7. On the other hand, measurement result by using two Faraday cups of FC1 and FC2 is ~80 %. There are some ambiguities relating to the optics of the LEBT, such as transverse focusing effect in the post-acceleration column, remnant field of the LEBT quadrupole magnets, transverse aperture, initial particle distribution, etc. If such ambiguities are taken into account, discrepancy between the simulation result and the measurement is not inconsistent. Thus in the transverse direction, we can say that the simulation result is qualitatively reproduced.

6.4.4.1 Evolution of the beam profile in the LEBT

Beam pulse profiles at the entrance and the exit of the LEBT are evaluated by sorting the time assigned to each particle. The results are shown in Fig. 6.4.4.1a.

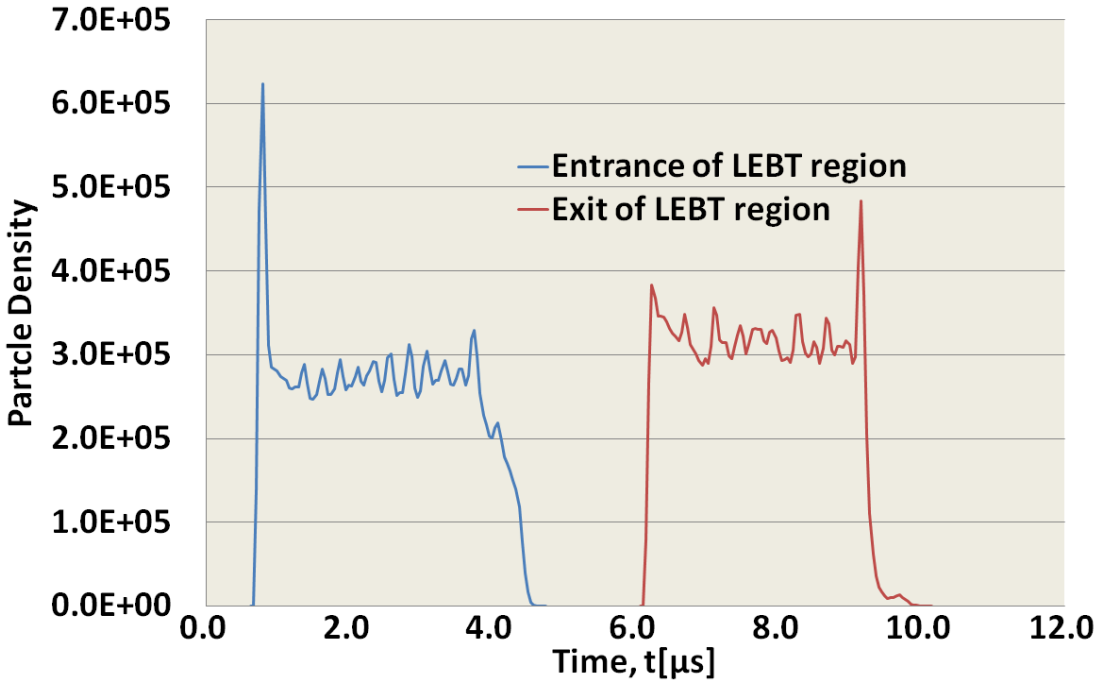

Figure 6.4.4.1a: Beam pulse profile evolution from entrance of LEBT to exit of LEBT [1]

This figure shows that the head peak and the tail peak of the beam profile change after propagating through the LEBT. This seems to imply that the head particles move slower but the tail particles move faster. A possible speculation is that this phenomenon originates from a velocity modulation generated when the particles pass through the Einzel lens region as shown in Fig. 6.4.41b. The particle velocity is mainly dependent of the voltage of the middle electrode of the Einzel lens. As shown in the Fig. 6.4.2b and 6.4.3b, a profile in the momentum deviation through a bunch strongly depends on time to leave the Einzel lens region. Those figures clearly show that the particles (head peak) which arrive early have the relatively lower momentum and the particles (tail peak) which arrive later have relatively higher momentum. At least we can state that the velocity modulation occurs within the Einzel lens region [1].

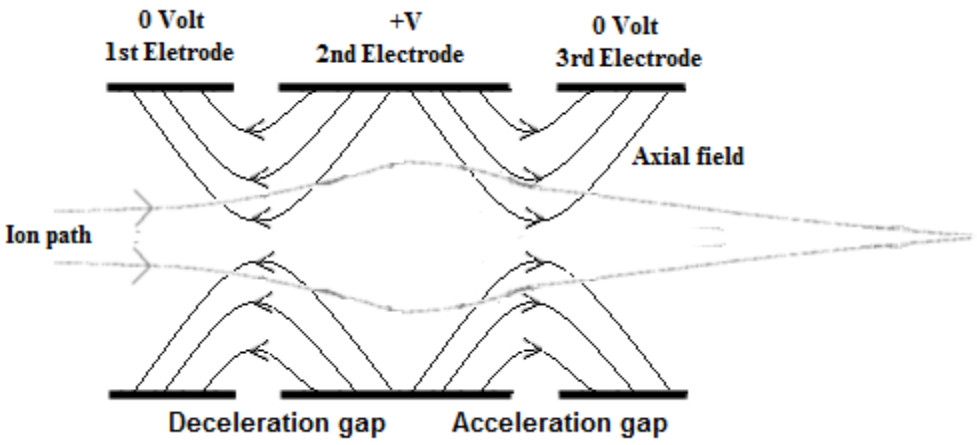

Figure 6.4.4.1b: Electric field lines and beam envelope in the Einzel lens region

In order to explain why this velocity modulation is caused, we will carefully investigate the longitudinal beam dynamics in Einzel lens region. In an ideal case with a static middle electrode potential, the particles should leave the Einzel lens region with its initial velocity. In a real situation, the voltage of Einzel lens middle electrode changes in time as shown in Fig. 6.4.4.1c, which can be denoted as early, intermediate and late regions [1].

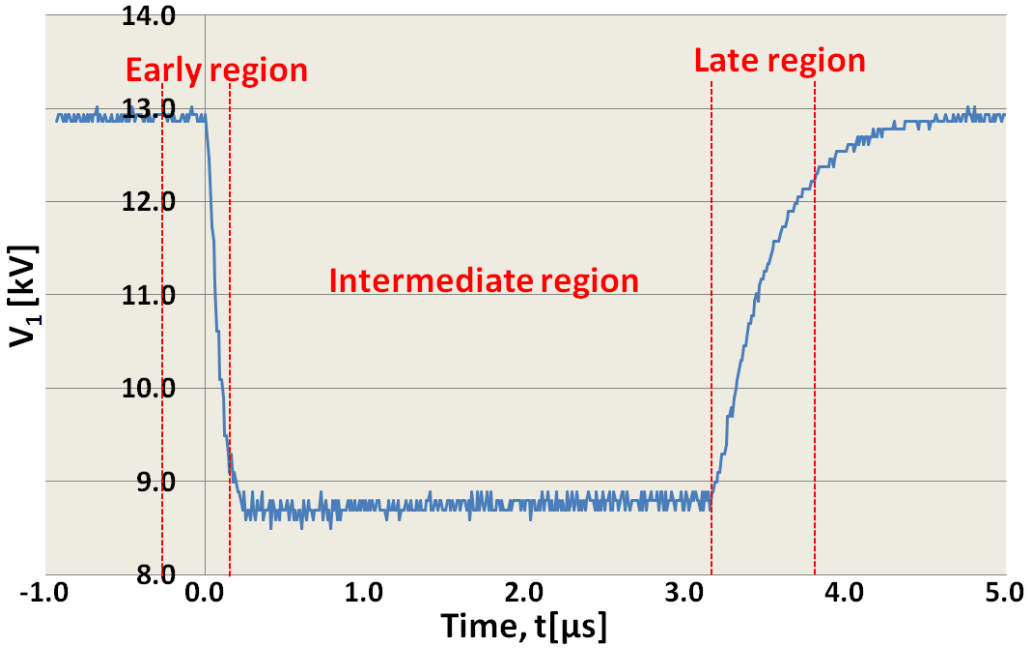

Figure 6.4.4.1c: Profile of the voltage applied to the middle electrode of the Einzel lens [1]

Let suppose that a test particle arrives at the deceleration gap when the middle electrode potential $V(t_1)=V_1$ and then this particle arrives at the acceleration gap beyond the middle electrode region when $V(t_2)=V_2$, where $t_2>t_1$. For the test particles which arrive at the deceleration gap in the early region, $V_1>V_2$. As a result, their velocity decreases from their initial value and their momentum deviation becomes negative [1]. For the test particles arrive at the deceleration gap in the intermediate region, $V_1=V_2$,, where the deceleration effect is equal to the acceleration effect and then the particle velocity remains unchanged [1]. For the test particles which arrive at the deceleration gap in the late region, $V_1<V_2$, where their particle velocity increase because the deceleration effect is much smaller than the acceleration effect and then their momentum deviation become positive [1]. In order to confirm this speculation, a number of particles generated between -2.0 to 5.0 μs are simulated and their tracks on the z-v_z phase space are shown in Fig. 6.4.4.1d.

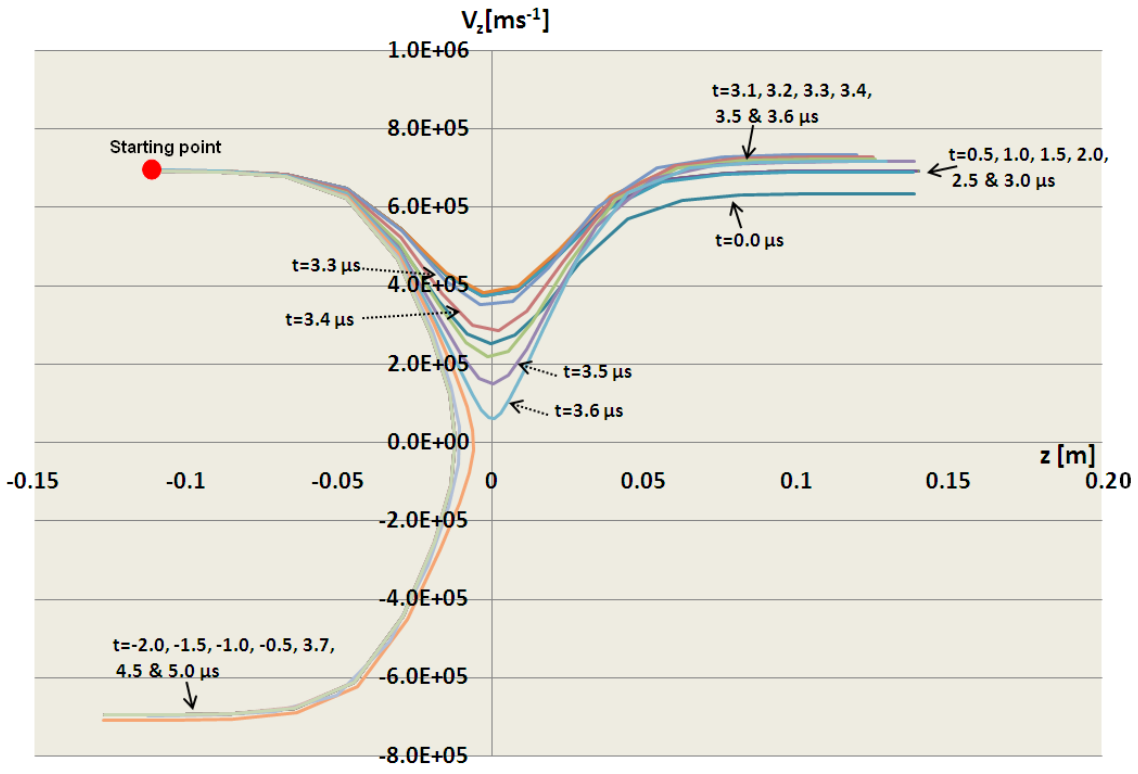

Figure 6.4.4.1d: Trajectories in z-v_z space for various particles injected at different timing [1]

In this figure, we can realize the strong time dependence of their tracks. Results can be summarized as follows:

1) In the time regions of $t \leq -0.5$ μs and $t \geq 3.7$ μs, a particle is reflected.
2) Around t=0 μs, a particle velocity is decreased.
3) In the time regions of $0.5\ \mu s \leq t \leq 3.0$ μs, a particle velocity is unchanged.
4) In the time regions of $3.1\ \mu s \leq t \leq 3.6$ μs, a particle velocity is increased.

Consequently we have identified that the strong velocity modulation is induced in the chopper region. This modulation still survives beyond the post-acceleration column region as shown in Fig. 6.4.3b.

After propagation of a chopped beam with this velocity profile through the LEBT, we can expect the orbital evolution of the bunch profile. The head peak with a relatively lower momentum should move relatively slowly; meanwhile, the tail peak with a relatively higher momentum moves relatively fast [1]. Eventually, the pulse tends to be somewhat bunched. The heights of bunch head and tail have decreases and increases, respectively. We can say that this phenomenon is so-called drift compression [1]. This characteristic still remains in the ring region, and will be discussed in chapter 8.

References

[1] **K. W. Leo**, T. Adachi, T. Arai, and K. Takayama, "Einzel Lens Chopper and Behavior of the Chopped Beam in the KEK Digital Accelerator", submitted to *Phys. Rev. AB-ST (2012).*

[2] Andi Klein and Alexander Godunov, Introductory Computational Physics, Cambridge University Press (2006) ISBN 9780521828628.

7. Beam Emittance Measurement

7.1 Overview

The experimental part of this work is focus on the measurement of the quality (beam emittance) of helium ion species extracted from the KEK-DA ECRIS. The experiment was carried out mainly at the KEK-DA complex [1].

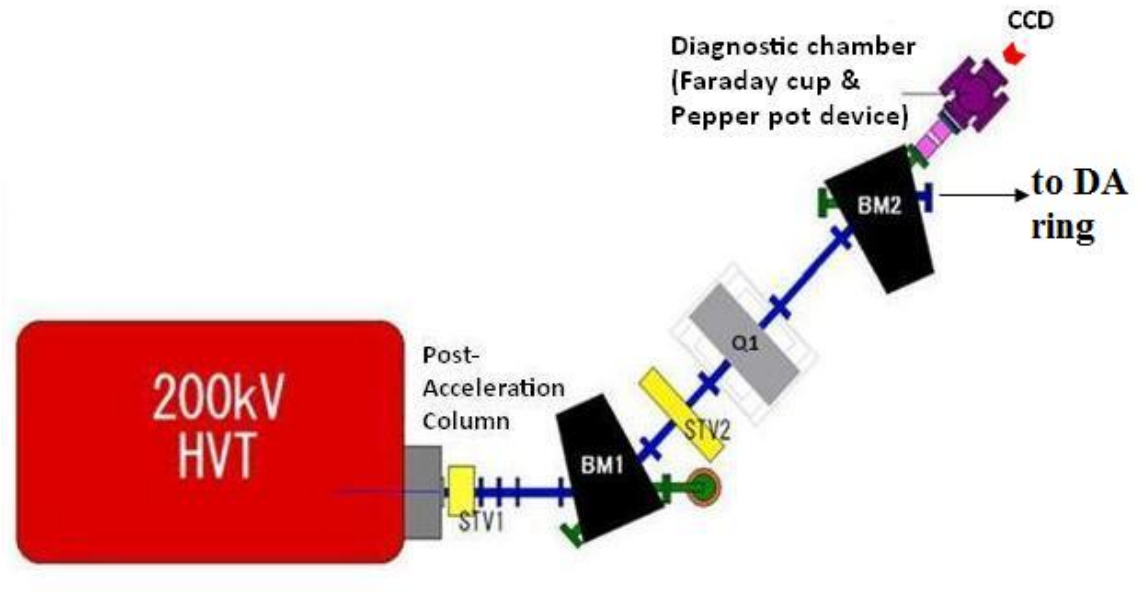

Figure 7.1a: Experimental setup

The experimental setup is shown in Fig. 7.1a. After acceleration of 200 kV (Extraction voltage: 10 kV and post-acceleration voltage: 190 kV), a beam of selected ion species by the analyzer magnet BM1 is guided to downstream. Usually, the beam is transported to the DA ring by the bending magnet BM2. In this experiment, the ion beam is injected into a diagnostic chamber by setting the current of BM2 to be zero. Fig. 7.1b shows the diagnostic chamber seen from the downstream. In the diagnostic chamber, a Faraday cup and a pepper pot device are installed to measure the beam current and emittance, respectively. Each device is switched manually by adjusting a corresponding supporting rod. For beam emittance measurement, a CCD camera is located at the end of the experimental beam line to capture pepper pot images.

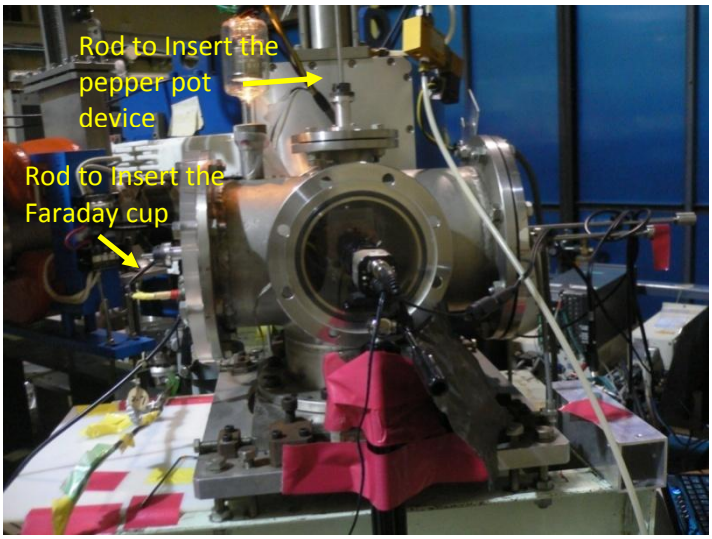

Figure 7.1b: Diagnostic chamber where a Faraday cup and a pepper pot device are installed

7.2 Beam Emittance Measurement

7.2.1 Emittance Definition

An area in two dimensional phase space of (x, x') or (y, y') occupied by the beam is characterized by transverse emittance [2] which is called as emittance in the following section. Unit of the emittance is described as *m.rad*. As the angle unit of radian is a dimension less ratio, some people use *m* instead. Emittance is conserved if particle motion is subjected only by consecutive forces, such as time-independent electric and magnetic fields [Appendix 7].

7.2.2 The Courant-Snyder Ellipse and the Twiss Parameters

Beam motion can be described in a transverse phase space by the Courant-Snyder ellipse defined by [3]:

$$\gamma x^2 + 2\alpha x x' + \beta x'^2 = \varepsilon$$

Here, $\beta, \alpha \; and \; \gamma$ are twiss parameters. The emittance or Courant-Snyder invariance is denoted by ε, which is equal to the ellipse area divided by π. Such an ellipse is shown in Fig. 7.2.2a.

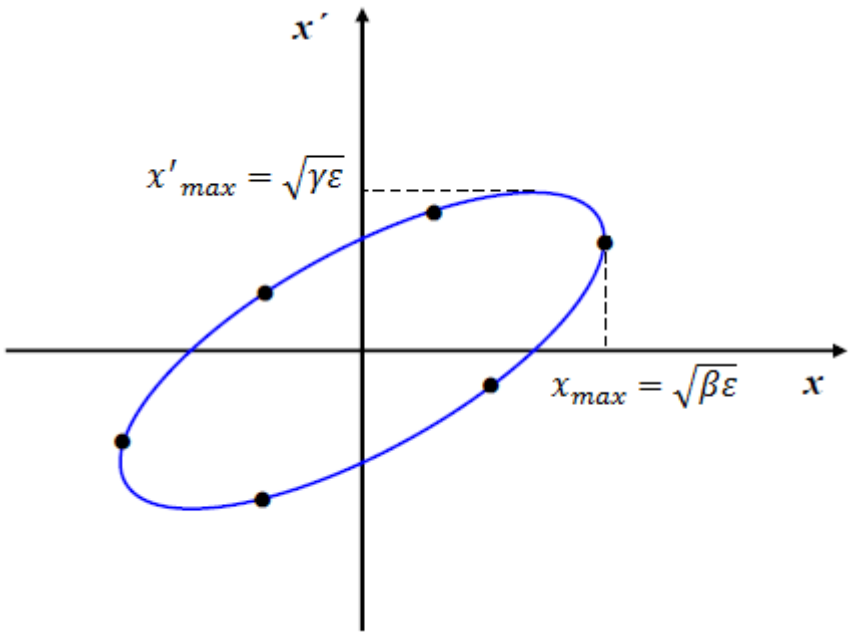

Figure 7.2.2a: Courant-Snyder ellipse

As shown in the figure, beam half width can be obtained by: $x_{max} = \sqrt{\beta\varepsilon}$

7.2.3 Pepper Pot Type Emittance Monitor

A pepper pot is often used for emittance measurement of a low energy ion beam. It consists of three main components summarized below:

a) Pepper pot mask

It contains a regular array of identical small holes which split anion beam into beamlets.

b) Screen

It is located at the downstream of the pepper pot mask with some distance. A scintillating material is used as the screen so that the images of the beamlets created on the screen can be easily observed as light spots.

c) Image capture device

Light spots on the screen are observed by an image capture device, such as a CCD camera.

7.2.3.1 Principle of the pepper pot type emittance measurement

Suppose that the incident beam is split into N beamlets by N holes on the pepper pot mask as shown in Fig. 7.2.3.1a. The beamlets create N spots on the screen located apart from the mask with a distance *d*. Since the hole size is very small (0.5 mm), finite size of each spot is considered to be caused by a spread of the beam deflection at the corresponding hole coordinate. Hence, phase space coordinates are given by [4]:

$$\left[x, x' = \frac{X - x}{d}\right]$$

$$\left[y, y' = \frac{Y - y}{d}\right]$$

Here, (x, y) and (X, Y) are the coordinate of the hole on the mask and the coordinate included in the corresponding spot on the screen, respectively.

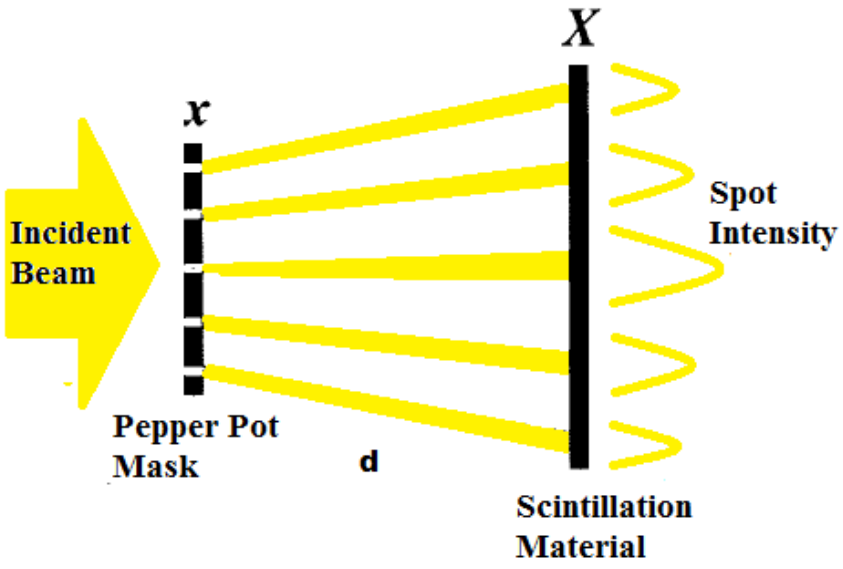

Figure 7.2.3.1a: Typical setup pepper pot monitor (Incident beam comes from the left and hits the pepper pot mask. x is the coordinate on the pepper pot mask and X is the screen coordinate. d is the distance between the pepper pot mask and the screen)

As shown in Fig. 7.2.3.1b, if the pepper pot image is given by the holes aligned with (m x n) array, we can prepare a set of the beam information on beam density distribution in the phase space by the following form:

$$\left(x_j, x'_{jh} = \frac{X_{jh} - x_j}{d}, I_{ih}\right), j = 1 \rightarrow m$$

$$and\ h = 1 \rightarrow horizotal\ pixel\ number\ at\ j - th\ peak$$

$$\left(y_k, y'_{kv} = \frac{Y_{jh} - y_j}{d}, I_{kv}\right), k = 1 \rightarrow n$$

$$and\ v = 1 \rightarrow vertical\ pixel\ number\ at\ k - th\ peak$$

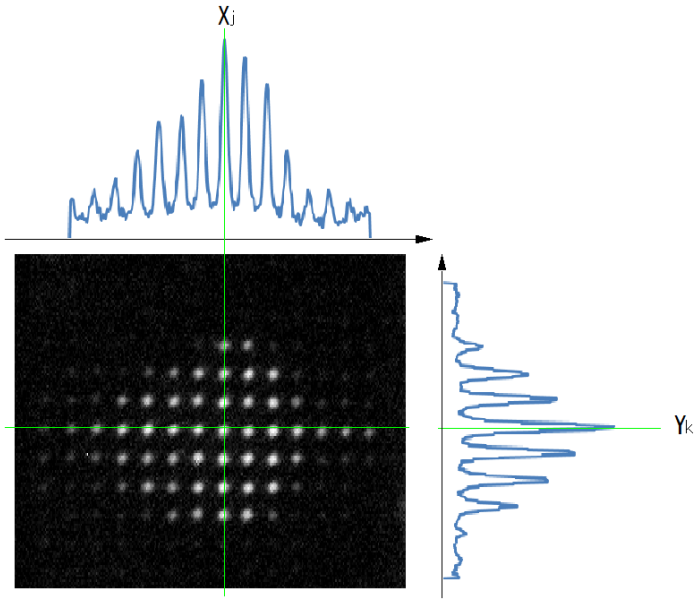

Figure 7.2.3.1b: Projection of the pepper pot image onto the horizontal and vertical plane

Here, the hole position on the mask is identified by a column j and a row k and h or v identifies the pixel coordinate along the horizontal or vertical direction included in the common spot image on the screen. I_{jh} denotes the projection of the light brightness onto the horizontal plane and I_{kv} the projection onto the vertical plane. Projection of the spot image gives a range of many peaks superposed by background. Each peak region, which

is a projection of one spot image, is defined by surrounding two bottoms as indicated by arrows in the following figure.

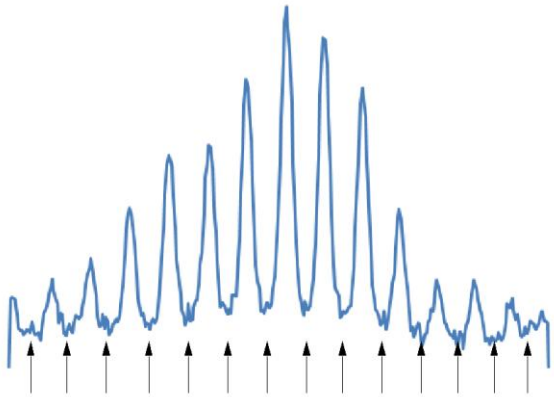

Figure 7.2.3.1c: Peak projection

Bottom position is detected as a zero-crossing point with positive slope of the differentiated distribution, which is beforehand smoothed not to detect unexpected bottom. An example is shown below.

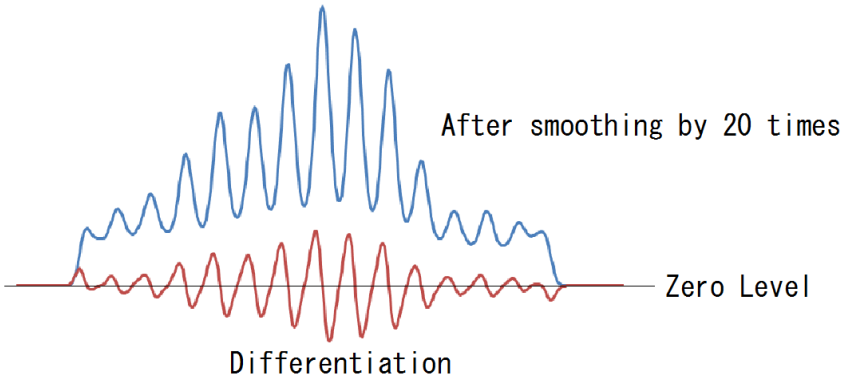

Figure 7.2.3.1d: Projection with smoothing and differential

Finally, gaussian fitting is performed for each peak to estimate a linear background. In the following figure, circles denote the measured distribution and fitting results are shown by the lines. The color distinguishes the peak region.

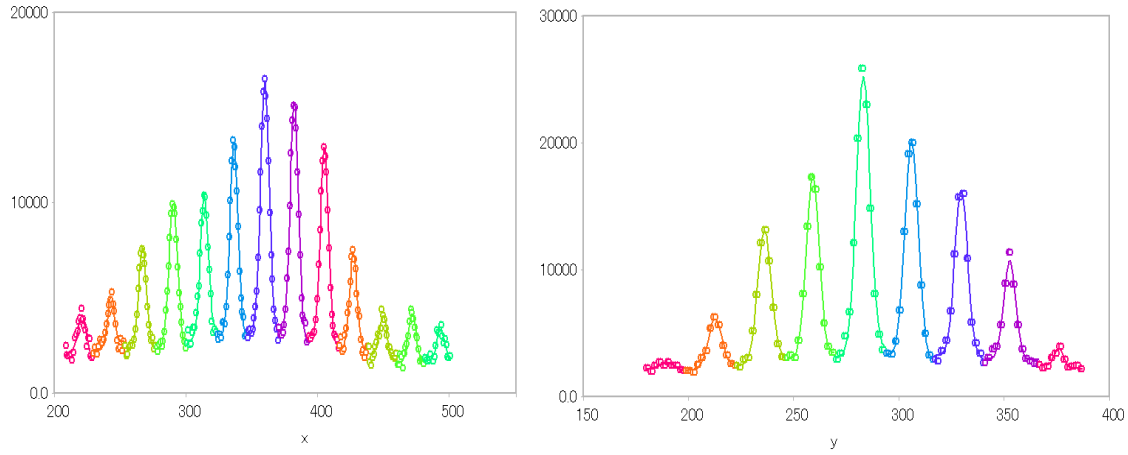

Figure 7.2.3.1e: Projection distributions of the pepper pot image onto the horizontal (left) and the vertical (right) planes

Finally, the phase space distribution is obtained by subtracting the estimated background from the light brightness. Statistical parameters can be derived from the resultant phase space distribution by using the following formula:

$$\langle x \rangle = \frac{1}{\sum_{j,h} I_{jh}} \sum_{i,h} I_{jh} x_j \qquad \langle y \rangle = \frac{1}{\sum_{k,v} I_{kv}} \sum_{k,v} I_{kv} y_k$$

$$\langle x^2 \rangle = \frac{1}{\sum_{j,h} I_{jh}} \sum_{i,h} I_{jh} \left(x_j - \langle x \rangle\right)^2 \qquad \langle y^2 \rangle = \frac{1}{\sum_{k,v} I_{kv}} \sum_{k,v} I_{kv} (y_k - \langle y \rangle)^2$$

$$\langle x' \rangle = \frac{1}{\sum_{j,h} I_{jh}} \sum_{i,h} I_{jh} {x'}_j \qquad \langle y' \rangle = \frac{1}{\sum_{k,v} I_{kv}} \sum_{k,v} I_{jh} {y'}_k$$

$$\langle {x'}^2 \rangle = \frac{1}{\sum_{j,h} I_{jh}} \sum_{i,h} I_{jh} \left({x'}_j - \langle x' \rangle\right)^2 \qquad \langle {y'}^2 \rangle = \frac{1}{\sum_{k,v} I_{kv}} \sum_{k,v} I_{kv} \left({y'}_k - \langle y' \rangle\right)^2$$

$$\langle x x' \rangle = \frac{1}{\sum_{j,h} I_{jh}} \sum_{i,h} I_{jh} \left(x_j - \langle x \rangle\right)\left({x'}_j - \langle x' \rangle\right) \qquad \langle y y' \rangle = \frac{1}{\sum_{k,v} I_{kv}} \sum_{k,v} I_{kv} (y_k - \langle y \rangle)\left({y'}_k - \langle y' \rangle\right)$$

The rms emittance and twiss parameters are defined by:

$$\boldsymbol{\varepsilon_x} = \sqrt{\langle x^2\rangle\langle x'^2\rangle - \langle xx'\rangle^2} \qquad \boldsymbol{\varepsilon_y} = \sqrt{\langle y^2\rangle\langle y'^2\rangle - \langle yy'\rangle^2}$$

$$\beta_x = \frac{\langle x^2\rangle}{\varepsilon_x} \qquad \beta_y = \frac{\langle y^2\rangle}{\varepsilon_y}$$

$$\alpha_x = -\frac{\langle xx'\rangle}{\varepsilon_x} \qquad \alpha_y = -\frac{\langle yy'\rangle}{\varepsilon_y}$$

$$\gamma_x = -\frac{\langle x'^2\rangle}{\varepsilon_x} \qquad \gamma_y = \frac{\langle y'^2\rangle}{\varepsilon_y}$$

7.2.3.2 Experimental procedure

As shown in Fig. 7.2.3.2a, a lot of holes are aligned on the circular mask (left view) and a transparent CsI scintillating crystal is used as a screen (right view).Before capturing the pepper pot image, the hole image on the screen must be taken so as to prepare a reference coordinate system. At first, we took the hole image by lighting the mask from the upstream. Unfortunately, clear spot image could not be obtained due to refraction by the crystal as shown in Fig. 7.2.3.2b. In order to avoid such a refractive effect, we took the hole image by rotating the pepper pot 180 degree and utilizing scintillation light induced by a beam. As described below, we obtained good image by using this setup. Thus, we used two setups of the pepper pot to measure beam emittance, such as normal setup and rotate setup.

Therefore, the reference coordinate determination must be performed by using the rotate setup and beam emittance measurement are performed by the normal setup. In addition, a shutter (metal plate with 1 hole) is used to determine the coordinate shift which might be caused by 180 degree rotation.

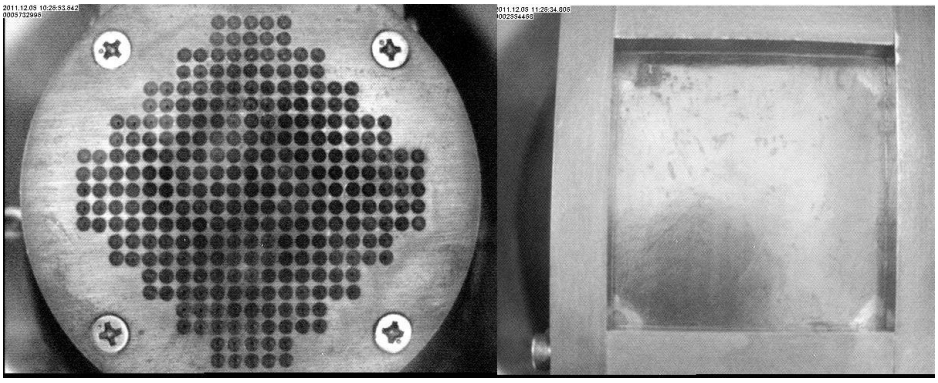

Figure 7.2.3.2a: Photograph of the pepper pot monitor (Left: seen from the upstream and Right: seen from the downstream)

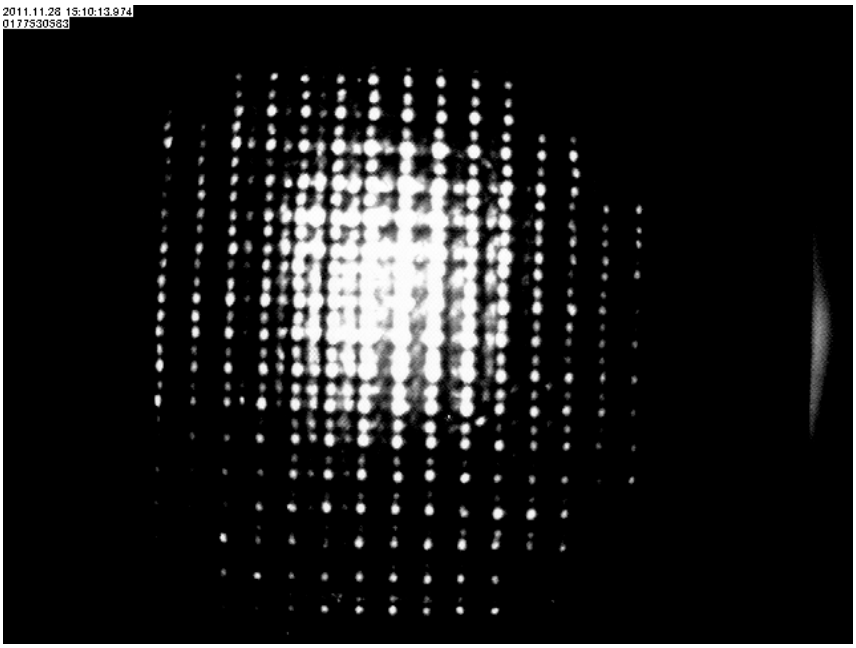

Figure 7.2.3.2b: Pepper pot coordinate image with normal setup

The experimental procedure is described below:

a) At first the pepper pot is set at the rotate setup. Since the pepper pot mask must perpendicular to the beam, the supporting rod is adjusted according to the reference mark (yellow arrow) generated by the laser marking tool as shown in Fig. 7.2.3.2c.

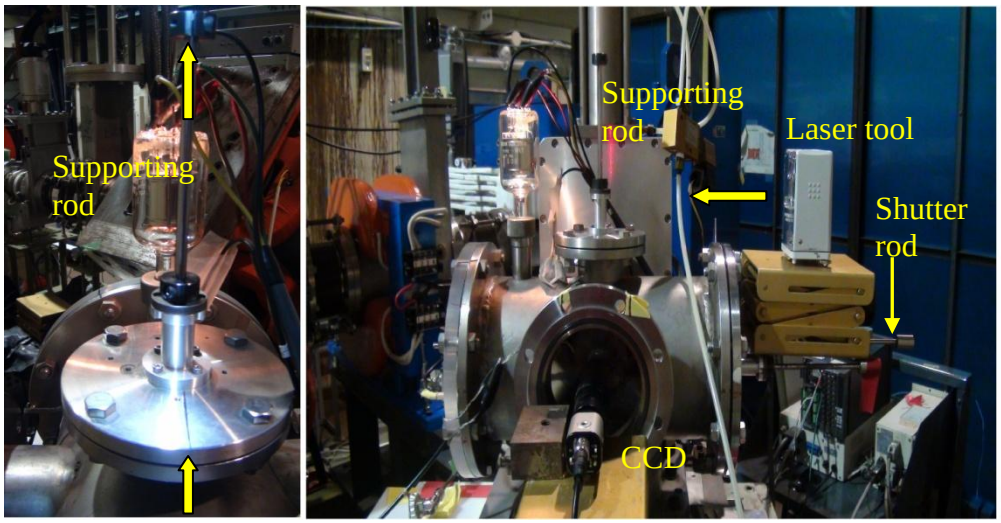

Figure 7.2.3.2c: Alignment according to the reference given by the laser marker tool mark

b) A clear image is obtained by adjusting the zoom, iris and focus functionality of the CCD as shown in Fig. 7.2.3.2d. In addition, a natural density filter is used to reduce the beam intensity which might cause the saturation of the captured image. During the beam emittance experiment, the zoom, focus and iris setting must be fixed.

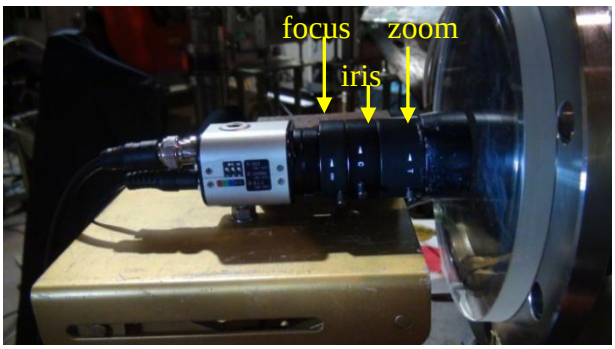

Figure 7.2.3.2d: CCD camera and its imaging options

c) By using the video recording program “VCE Express Application” or “Pepper pot” program, we can analyze the center position of the pepper pot mask with the rotate condition. Ensure that the center hole is located at the center with the pixel coordinate of (320, 240) as shown in Fig. 7.2.3.2e. If the center hole is not located at the center, try to adjust the supporting holder of the camera horizontally and vertically as shown in Fig. 7.2.3.2f.

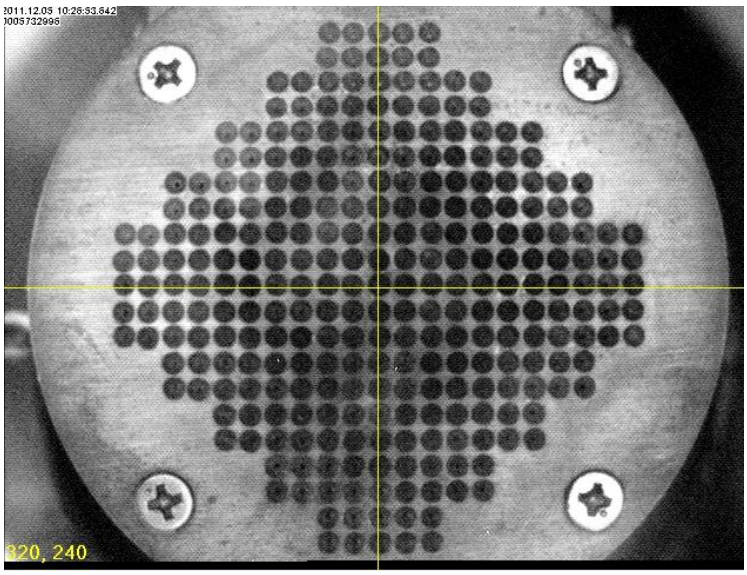

Figure 7.2.3.2e: Center hole confirmation by the pepper pot program

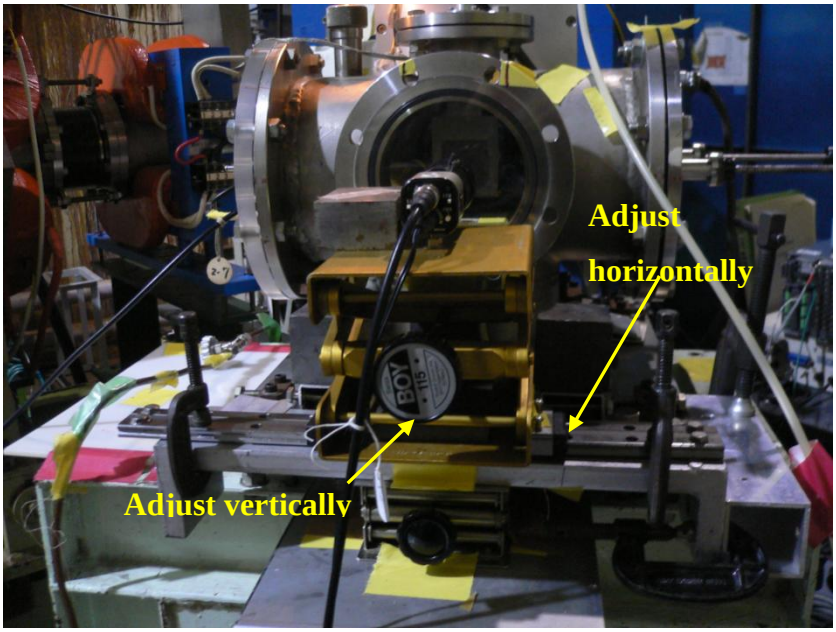

Figure 7.2.3.2f: Horizontal and vertical adjustment of the CCD camera

d) After camera adjustment, the conditions for image capture must be optimized as shown in Fig. 7.2.3.2g:
   - Input channel: S-video
   - Input video signal: Video Standard: NTSC

- De—Interlacing: Duplicate field
- Color settings: Color
- Output: RGB
- Image format: BMP: Best
- Save folder: Specified by the user
- Capture event occurs: continuous

When the ‘Start Capture” button is clicked, an image is recorded in the save folder specified by a user.

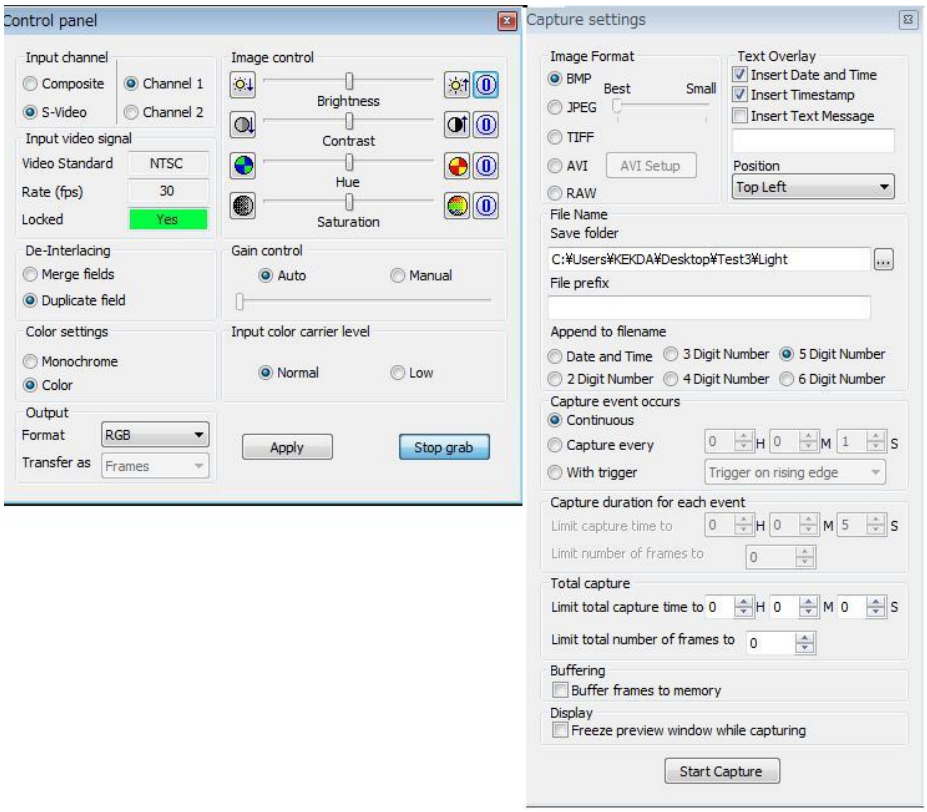

Figure 7.2.3.2g: Control panel and capture setting of the VCE express application

e) With the rotate setup, beam is delivered for determine the pixel coordinate system of the pepper pot mask as shown in Fig. 7.2.3.2h.

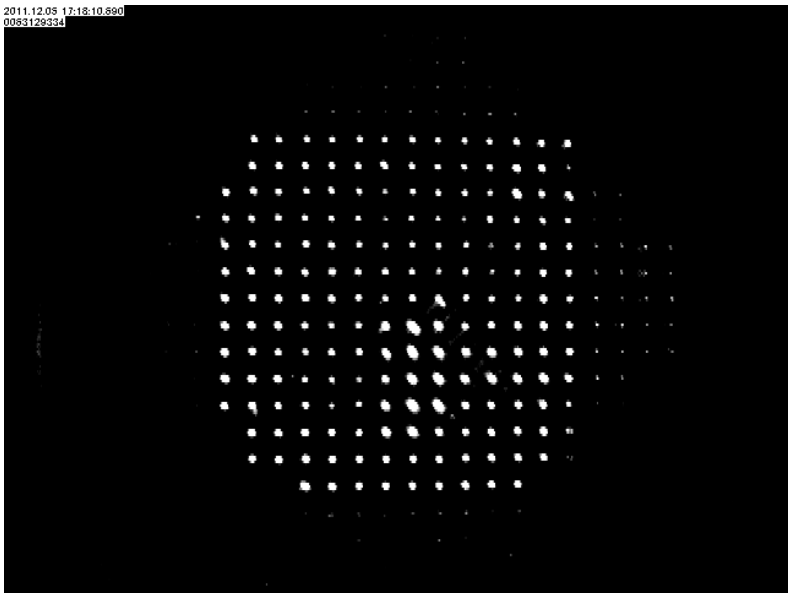

Figure 7.2.3.2h: Pepper pot mask coordinate image in the rotate condition

f) With the rotate setup again, a shutter is inserted in front of the pepper pot. A shutter with one hole located at the center can be used to determine the shift position. Then beam is delivered and the image with one hole beam spot is captured as shown in Fig. Fig. 7.2.3.2i.

g) After the measurements, the pepper pot mask is rotated to the normal setup with the shutter as shown in Fig. 7.2.3.2c. After the rotation, the alignment is checked by the laser marking tool again as shown in Fig. 7.2.3.2c.

h) With the normal setup, the beam is delivered again and the image with one hole beam spot is captured as shown in Fig. 7.2.3.2i.

Figure 7.2.3.2i: Image with shutter, Left: Rotate setup; Right: Normal setup

i) With the normal setup again, the shutter is pulled out by a shutter rod. Beam is delivered to obtain a pepper pot image for emittance measurement. Before image capturing, we must check image saturation effect as shown in Fig. 7.2.3.2j. Therefore, the natural density filter must be optimized carefully.

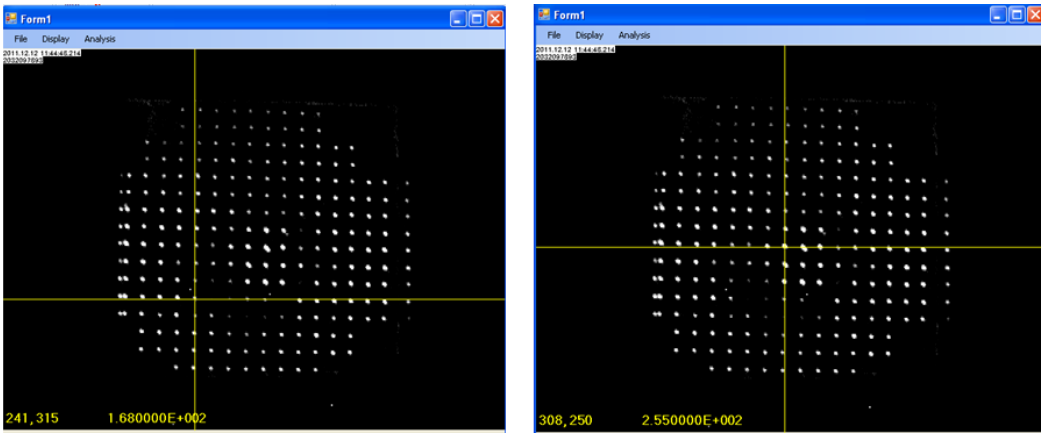

Figure 7.2.3.2j: Left: Without saturation at the reference point, Right: With saturation (255) with at reference Point

7.2.4 Pepper Pot Device for KEK-DA

Specifications of the pepper pot used for the emittance measurement in the KEK-DA are:

a) Pepper pot mask
   - The pepper pot mask used for the proton synchrotron has been reused in this experiment. Its specification is shown in Table 7.2 and Fig. 7.2.4a.

a) Screen/Scintillation material
   - Cesium Iodide ,CsI (Tl) [5]

b) Image capture devices
   - WAT-250D CCD color camera and frame grabber card [6]

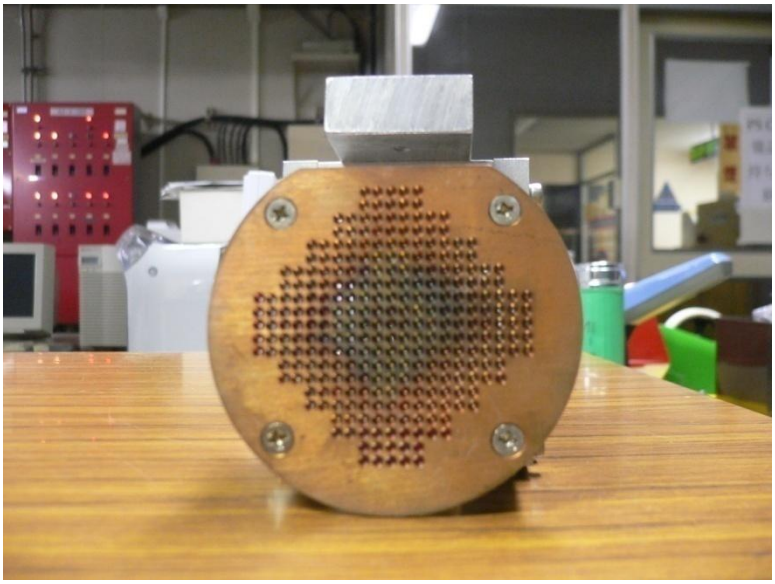

Figure 7.2.4a: Front view of the pepper pot mask

Table 7.2: Specification of the KEK-DA pepper pot mask

Specification	Figure
The diameter of the holes (Top)	2.5mm
The diameter of the holes (Bottom)	0.5mm
Thickness of the hole mask	2mm
The distance between the holes	2.6mm
The distance between the hole mask and the screen plane, d	36.8mm

7.2.5 Experimental Results

The emittance measurement was performed with the different excitation current of quadrupole magnet for He^{1+} and He^{2+}. Pepper pot image and the resultant emittance distribution for typical case with quadrupole current 2 Ampere is shown in the following section.

7.2.5.1 Result of He^{1+} ion species

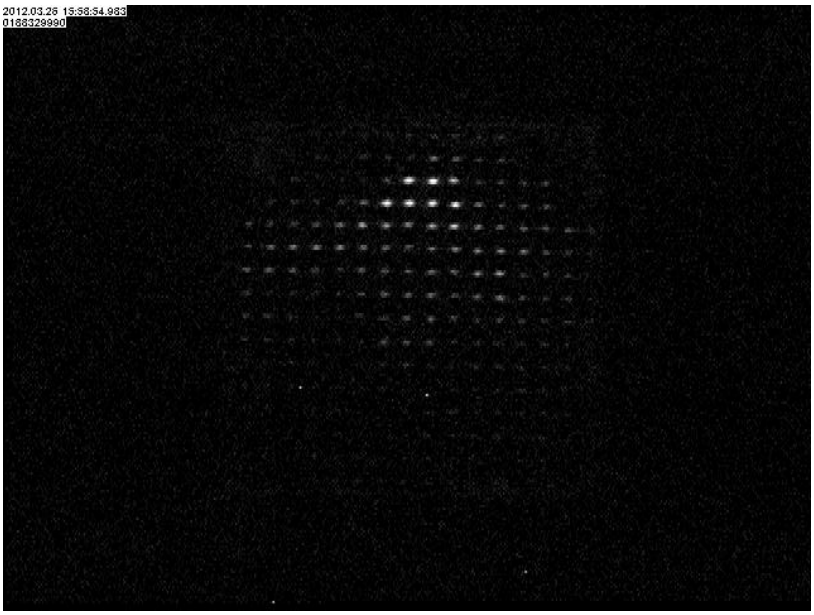

Figure 7.2.5.1a: He^{1+} pepper pot image with Q1=2A

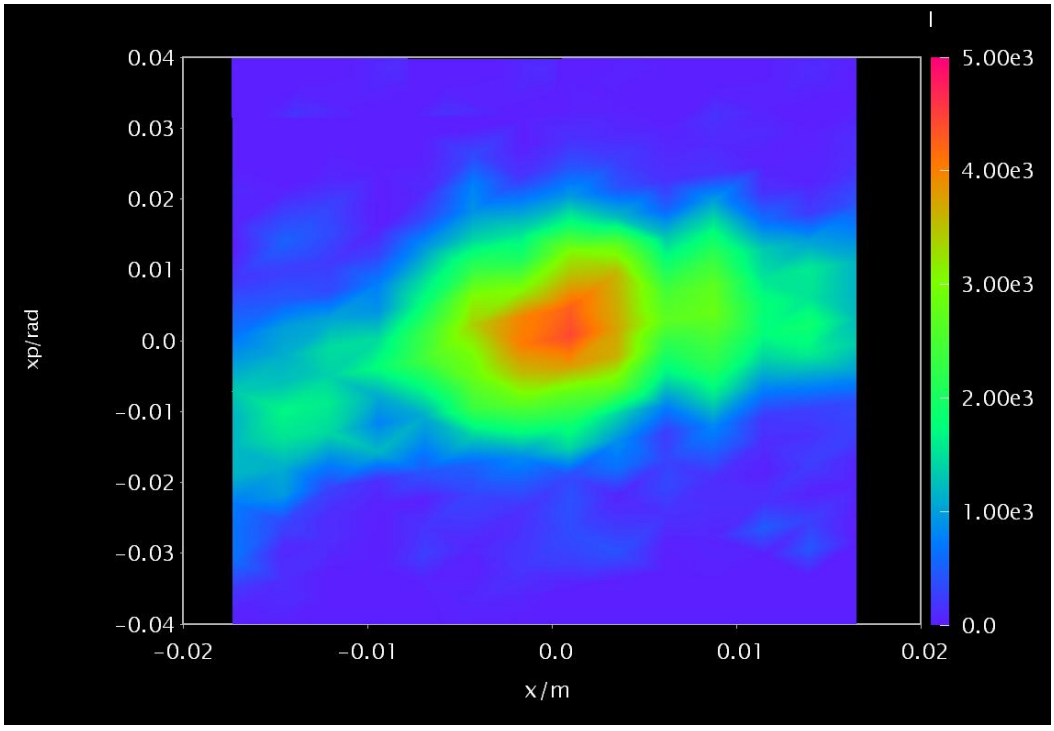

Figure 7.2.5.1b: He^{1+} phase space plot in horizontal-axis with Q1=2A

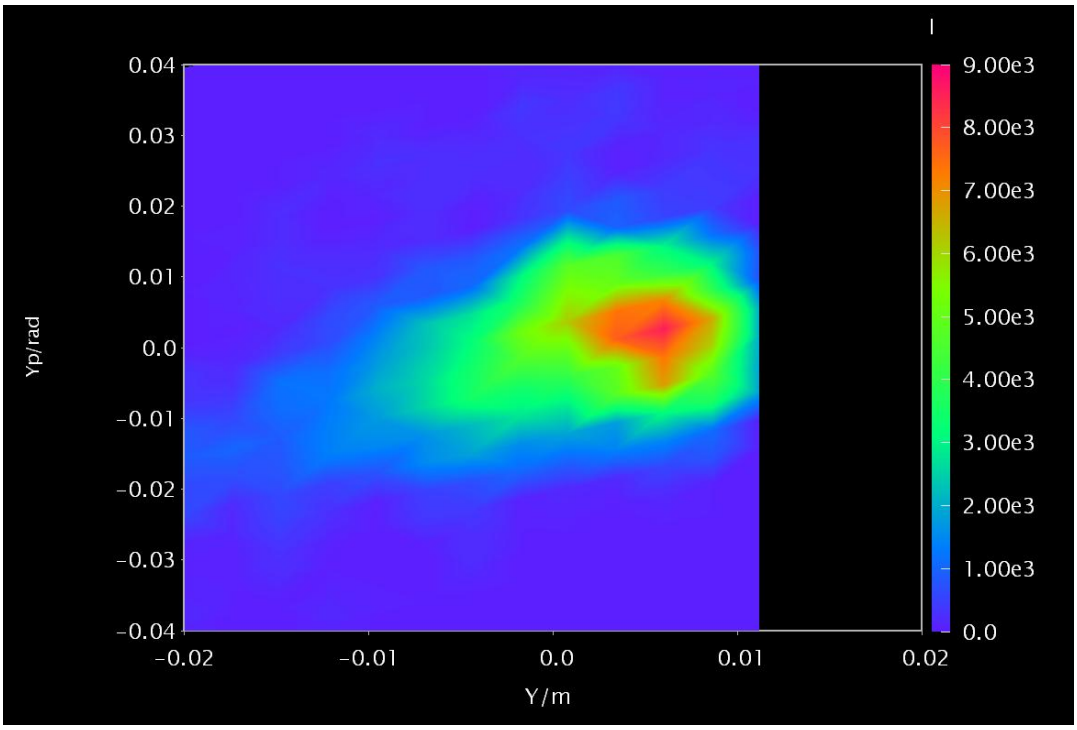

Figure 7.2.5.1c: He^{1+} phase space plot in vertical-axis with Q1=2A

7.2.5.2 Result of He^{2+} ion species

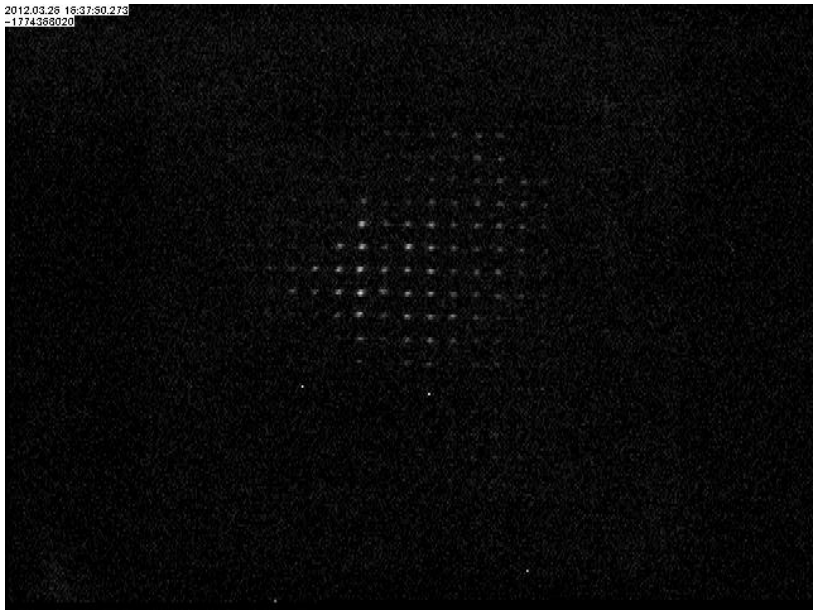

Figure 7.2.5.2a: He^{2+} pepper pot image with Q1=2A

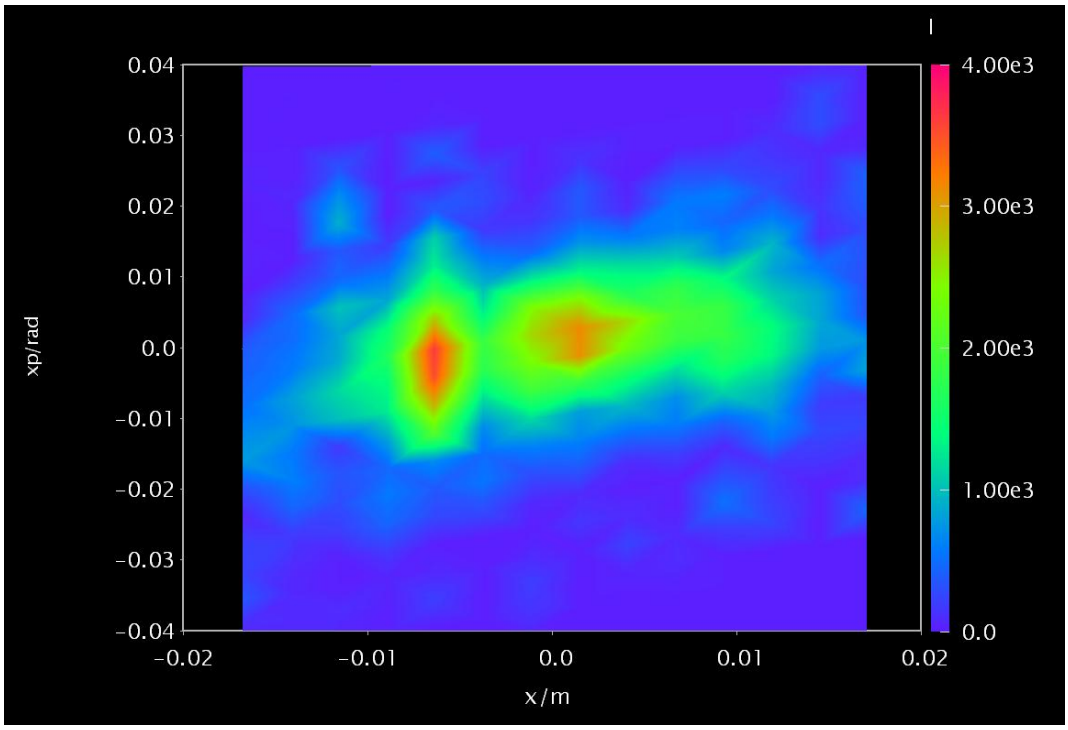

Figure 7.2.5.2b: He^{2+} phase space plot in horizontal-axis with Q1=2A

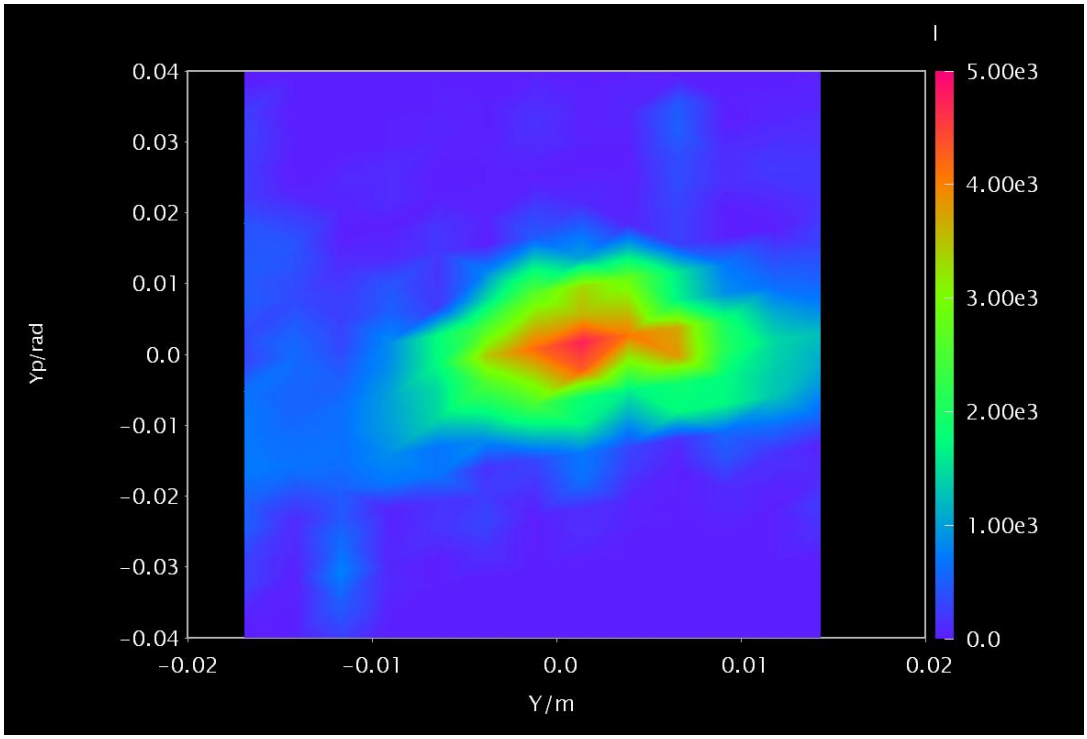

Figure 7.2.5.2c: He^{2+} phase space plot in vertical-axis with Q1=2A

7.2.5.3 Summary of the emittance measurement

Emittances of He^{1+} and He^{2+} for various quadrupole conditions are evaluated in terms of the formula given in section 7.2.3.1. The results are summarized in Table 7.3 and Table 7.4.

Table 7.3: Emittance of He^{1+} for various quadrupole conditions

Quadrupole Excitation Current, I[A]	Horizontal rms emittance, ε_x[μmrad]	Vertical rms emittance, ε_y[μmrad]
0	103	72
1	102	75
2	95	74

Table 7.4: Emittance of He^{2+} for various quadrupole conditions

Quadrupole Excitation Current, I[A]	Horizontal rms emittance, ε_x[μmrad]	Vertical rms emittance, ε_y[μmrad]
0	117	76
1	94	80
2	96	85

As shown in the tables, the rms emittance of He^{1+} and He^{2+} are ~100 μmrad for horizontal and ~75 μmrad vertical motions, respectively.

7.3 Discussion

In the emittance measurement, the un-chopped ion beam of 5 ms has been utilized. Because the chopped ion beam with a duration of ~μs cannot be observed due to our camera specification which has the limitation of its captured rate ~30 Hz. Therefore, the emittance measurements need to be performed with the un-chopped ion beam. There are two experimental results of the emittance measurement: one is the result of the pepper pot measurement at the test bench and the other is measured in the DA ring. The latter will be described below. These experimental results are compared with simulation, assuming He^{1+}as a beam particle. The pepper pot result is simulated by IGUN code, and

the result in the ring is simulated by IGUN code and own-developed code (Einzel lens simulation) which has been described in chapter 6.

7.3.1 Comparison with the IGUN Simulation

In this evaluation, the IGUN code is used to treat the beam dynamics in the axis-symmetry region from orifice/cathode to post-acceleration column. IGUN code based on the Langmuir-Child law [7] can provide the beam current, phase space plot and emittance information by referring to the experimentally obtained fractional ratios of ion beams (He^{1+} and He^{2+}), assumed plasma density and temperature. The output from the IGUN code at the entrance of post-acceleration column is treated by a self-developed program to manipulate the phase space plot from (r, r') to (x, x') and (y, y'). By using the new phase space plot data in horizontal and vertical directions and according to the formula given in section 7.2.3.1, the simulated horizontal and vertical rms emittance have been obtained as shown in table 7.5.

Table 7.5: Experimental and simulation emittance of He^{1+}

Method	Horizontal rms emittance, ε_x[μmrad]	Vertical rms emittance, ε_y[μmrad]
Experiment	~100	~75
Simulation	~103	~104

As shown in Table 7.5, rms beam emittance of He^{1+} in horizontal direction is consistent for both cases. But the vertical direction is a little different, it caused by the different horizontal and vertical aperture sizes of our bending magnet ducts as ~74 mm and ~60 mm, respectively. Therefore, more beam will loss at the vertical direction and the observed experimental vertical emittance is expected to be much smaller than the horizontal emittance.

7.3.2 Emittance in the DA Ring- Measurement and the Chopped Beam Simulation

A luminescence material, which is installed in the S1 region of the KEK-DA ring, is used to capture a chopped beam profile as shown in Fig. 7.3.2a. This plate is arranged in 45 degree perpendicular with the incident beam and with the observation point /window.

Therefore, beam profile can be captured by a camera placed through the window, as shown in Fig. 7.3.2b.

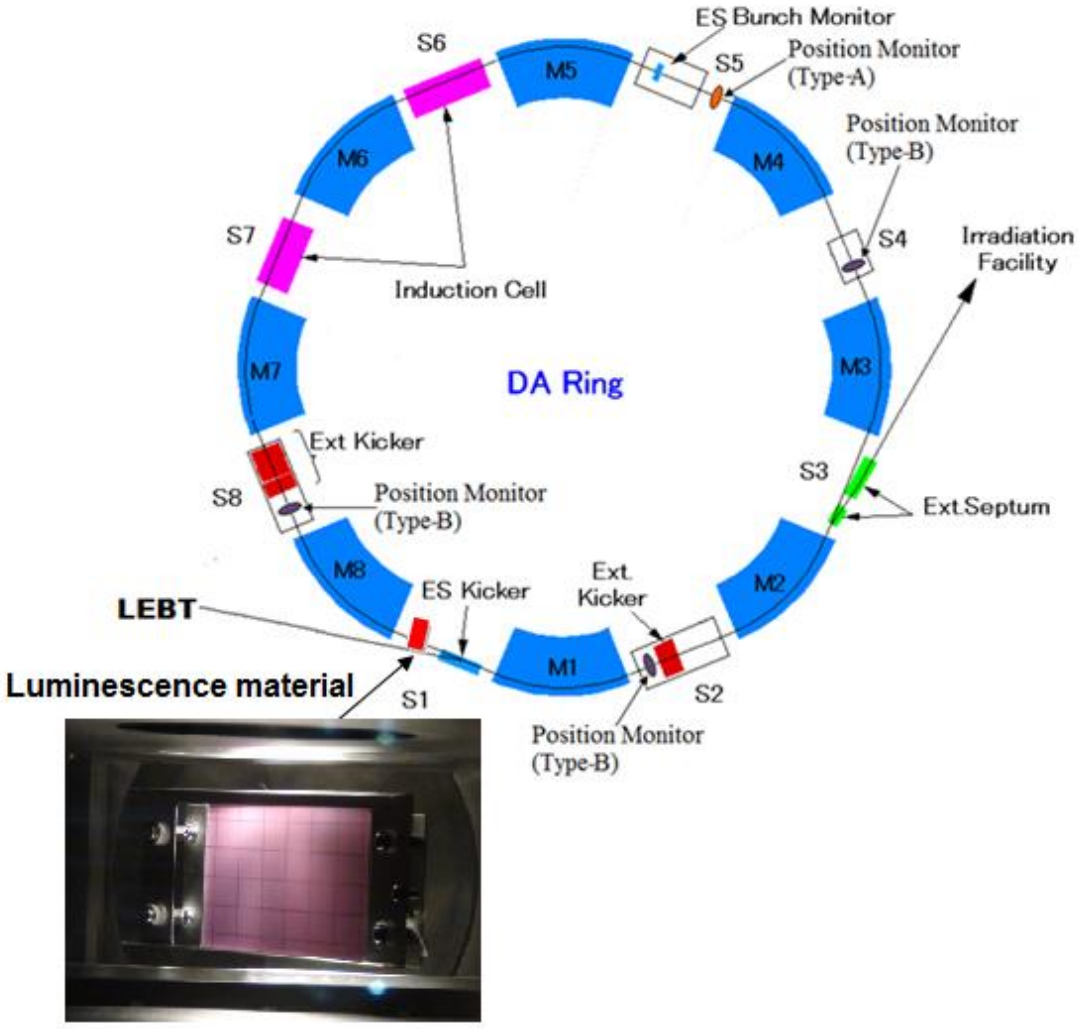

Figure 7.3.2a: A luminescence profile monitor and its location in the ring

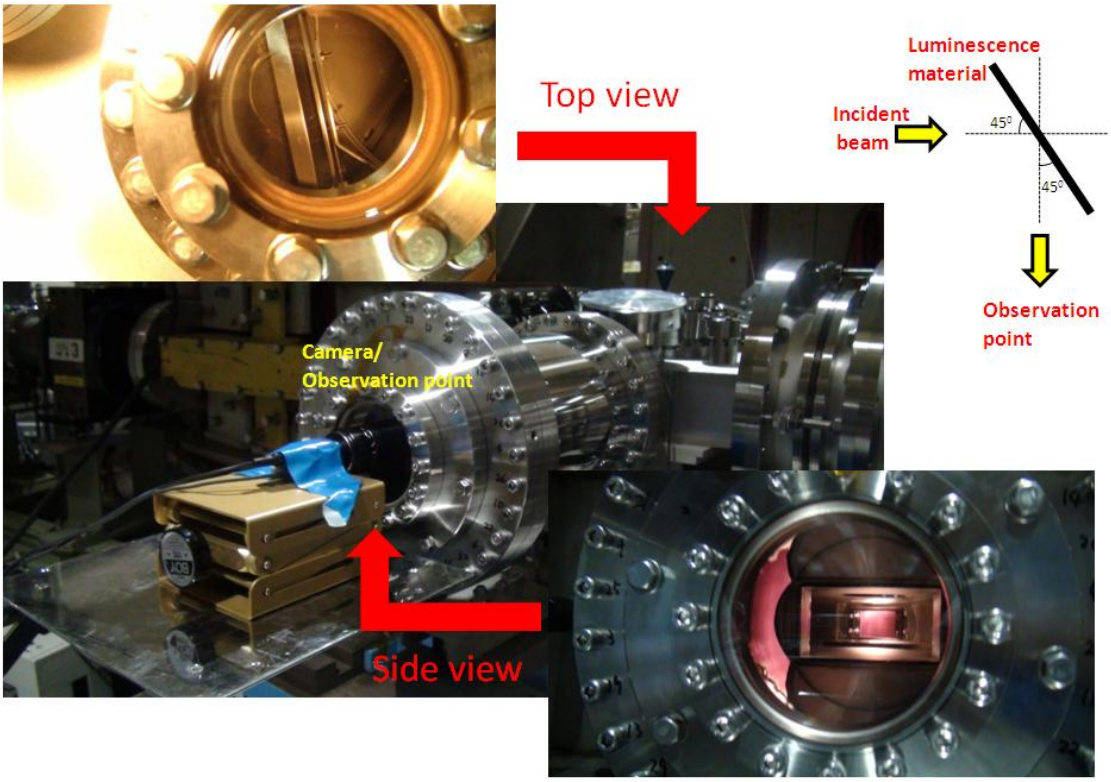

Figure 7.3.2b: Luminescence profile monitor setup

A chopped beam profile was captured as shown in Fig. 7.3.2c. By analysis of the beam profile on the luminescence profile monitor, the rms beam half width can be obtained by using the gaussian fitting as shown in Fig. 7.3.2d. As shown in Fig. 7.2.2a, the beam half width can be obtained as $x_{max}= \sqrt{\beta\varepsilon}$. According to the design value of the beta (β) function at the luminescence material position as β_x=3.6115 m and β_y=1.9218 m, the horizontal and vertical rms emittances have been obtained as shown in Table 7.6.

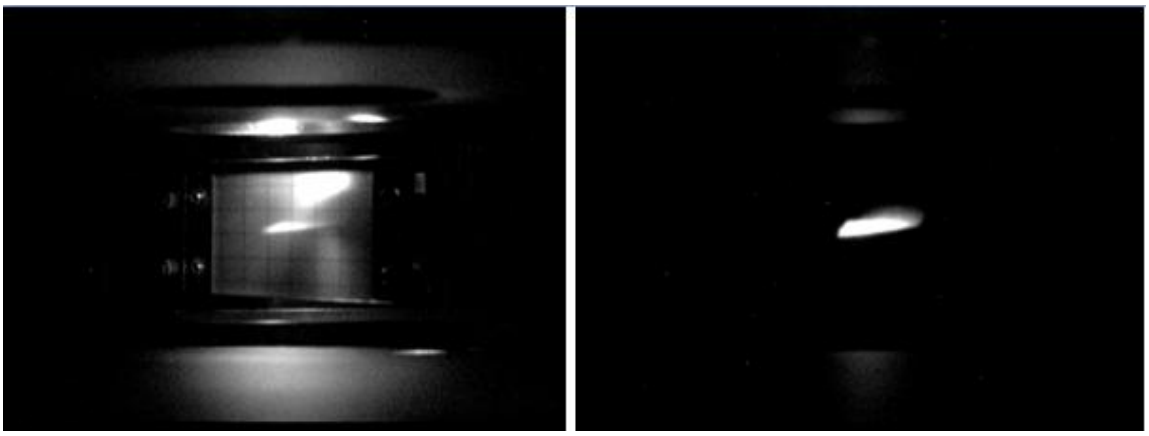

Figure 7.3.2c: Beam profile observed at the luminescence profile monitor (Right: Original background, left: Dark background)

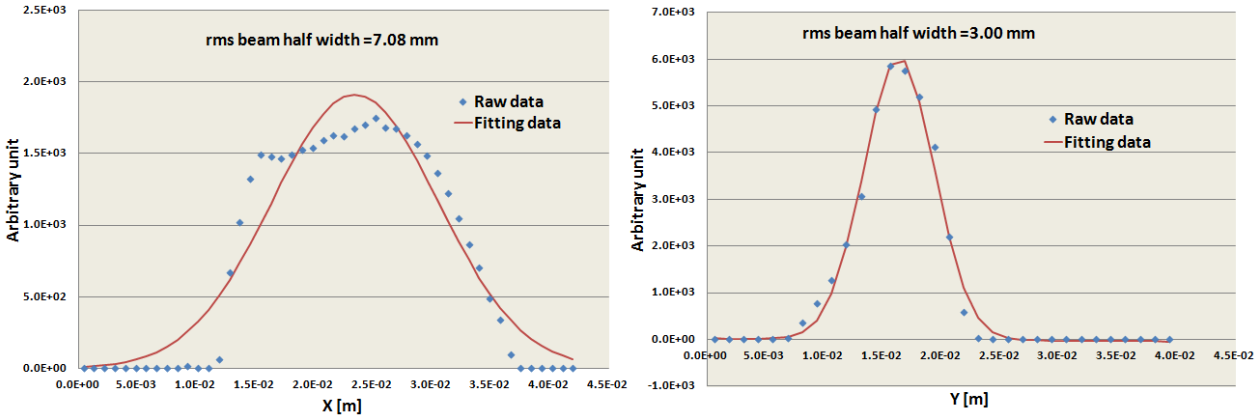

Figure 7.3.2d: Beam profile with gaussian fitting (Right: horizontal direction, left: vertical direction)

Table 7.6: Experimental and simulation emittance of the chopped He^{1+} observed at the ring

Method	Horizontal rms emittance, ε_x[μmrad]	Vertical rms emittance, ε_y[μmrad]
Experiment	~13.9	~4.7
IGUN simulation	~9.7	~3.0
Einzel lens simulation	~6.2	~3.0

The experimental result for horizontal emittance is larger than the results of two simulations. This might be caused by the transverse space charge effect which is not included in both simulation codes. In addition, since the Einzel lens simulation does not includes the transverse focusing effect in the post-acceleration column, the horizontal emittance is

smaller than the experiment by a factor 2. On the other hand, both simulation results are consistent with the experimental result for vertical emittance. Such result might be caused by the beam loss due to the small vacuum duct size in the vertical direction. In addition, the horizontal emitatnce is much larger than the vertical emittance. This phenomenon might be explained by the different vacuum duct sizes in the horizontal and vertical directions as ~ 0.08 to 0.14 m and 0.02 to 0.06m, respectively. This vacuum duct is very small especially in the vertical direction, therefore the horizontal emittance is much larger than the vertical emittance which has been obtained from our measurement and simulation results. From this evaluation, we noticed that the transverse space charge effect cannot be neglected when we consider beam emittance blow-up.

References

[1] T. Adachi, T. Arai, **K. W. Leo**, K. Takayama and A. Tokuchi, "A Solid-State Marx Generator Driven Einzel Lens Chopper", *Rev. Sci. Instrum*. **82**, 083305 (2011).

[2] Martin Stockli, Measuring and Analyzing Transverse Emittance of Charged Particle Beams, Beam Instrumentation Workshop 2006.

[3] Alexander Wu Chao and Maury Tigner, Handbook of Accelerator Physics and Engineering, World Scientific.

[4] M. Zhang, "Emittance Formula for Slits and Pepper-.pot Measurement", FERMILAB-TM-1998.

[5] http://www.neotron.co.jp/crystal/12/Csl.html

[6] http://www.imperx.com/frame-grabbers/vce-express

[7] R. Becker, and W. B. Herrmannsfeldt, "IGUN- A Program for the Simulation of Positive Ion Extraction Including Magnetic Fields", *Rev. Sci. Instrum.* **63**, 2756 (1992).

8. Chopped Beam in the Ring

8.1 Overview

In this section, a behavior of a chopped beam without acceleration is discussed. An ion beam from the ion source is chopped by the Einzel lens chopper and injected into the KEK-DA ring through the LEBT as shown in Fig. 8.1a. The injected beam circulates in the ring under a constant magnetic field, and the beam bunch signal is observed by an electrostatic (ES) bunch monitor installed in S5.

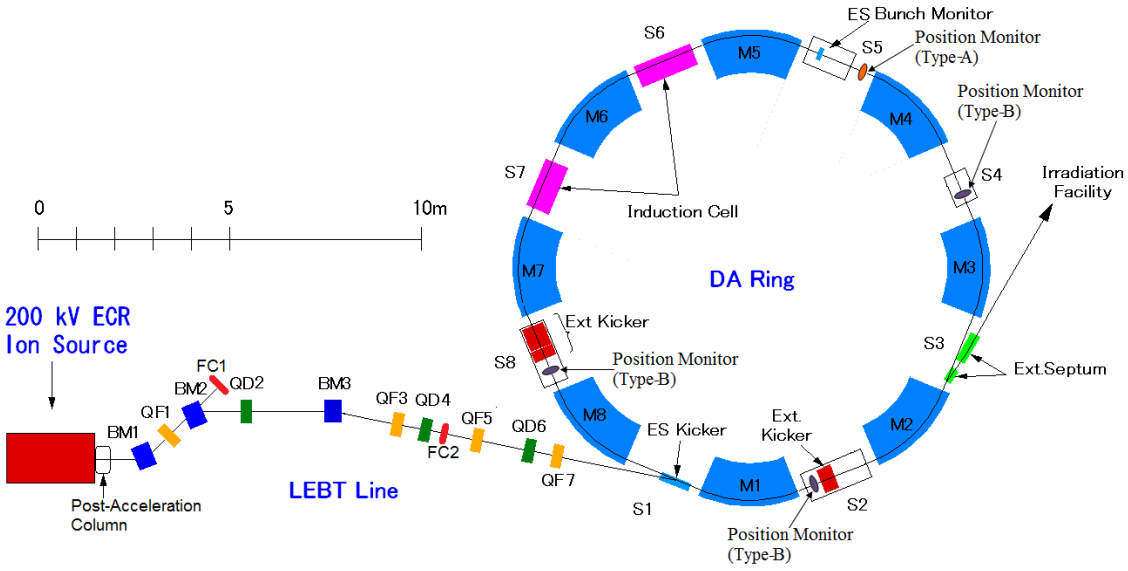

Figure 8.1a: A plan view of the digital accelerator complex

8.2 Comparison of Experimental Results with Simulation

A bunch signal from the ES monitor was captured by an oscilloscope as shown in Fig. 8.2a. The captured signal is partitioned turn by turn and each segment is aligned vertically, so that a so-called mountain view is obtained.

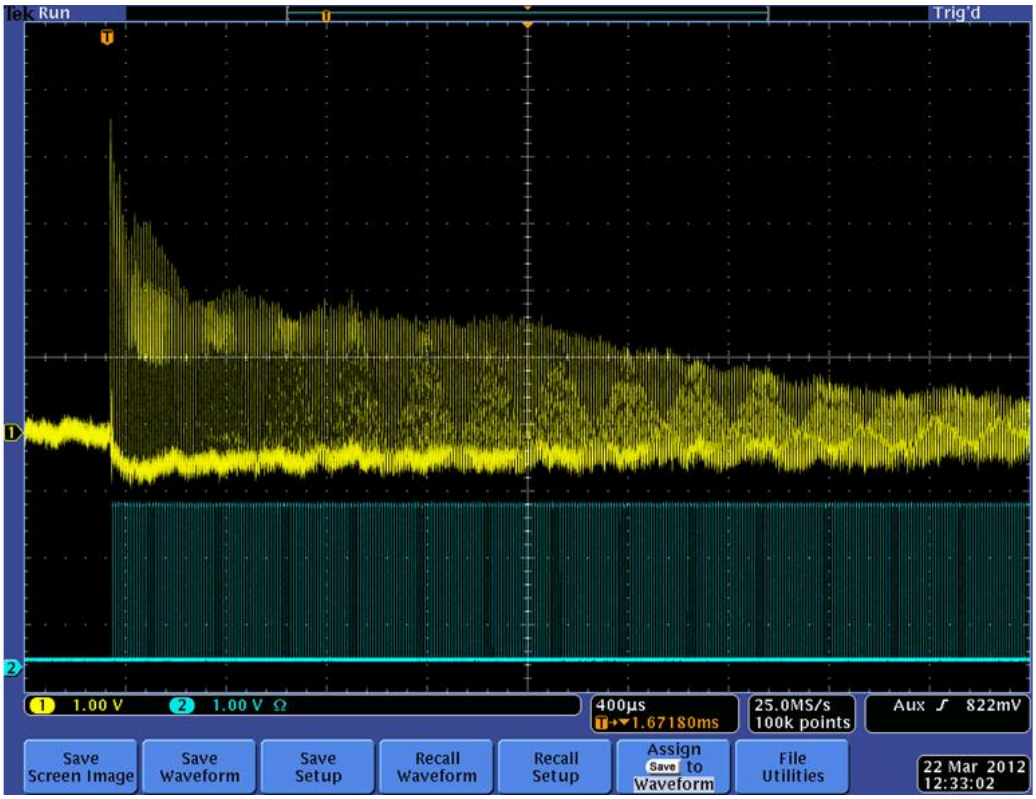

Figure 8.2a: Beam bunch signal

Two typical mountain views observed in cases of medium ion beam current (~50 µA) and high beam current (~100 µA) are plotted in Fig. 8.2b and 8.2d respectively. Here, the horizontal axis is a time within a period (corresponding to beam pulse length) and the vertical axis is the time after injection. In addition, the simulations for both cases were performed by using the own developed code as discussed in chapter 6 and the results are plotted in 8.2c and 8.2e for beam current with 50 µA and 100 µA.

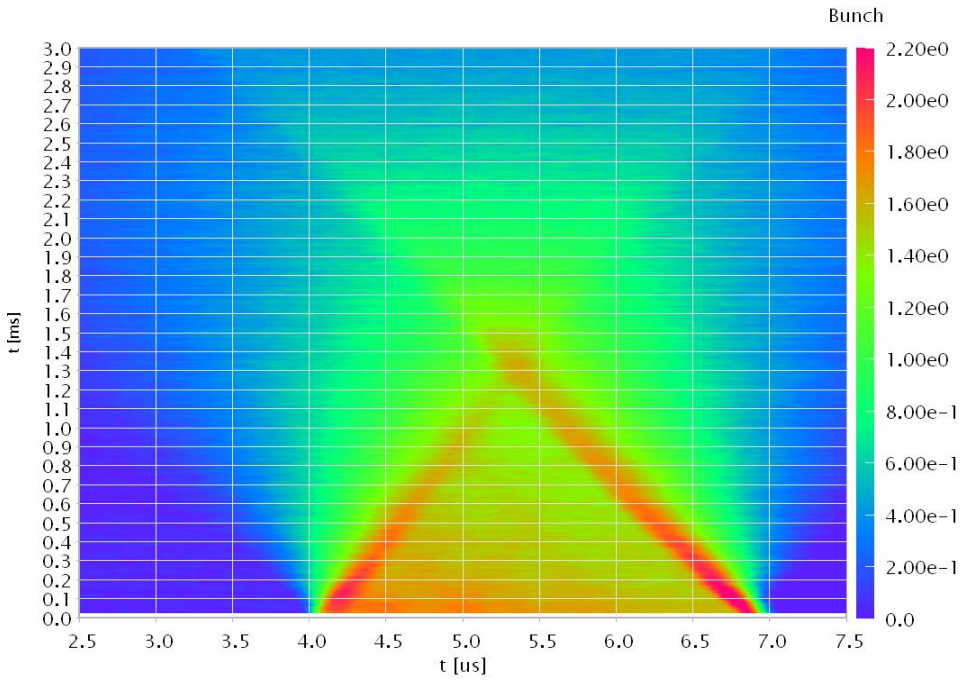

Figure 8.2b Mountain view of the ~50 µA beam bunch observed experimentally

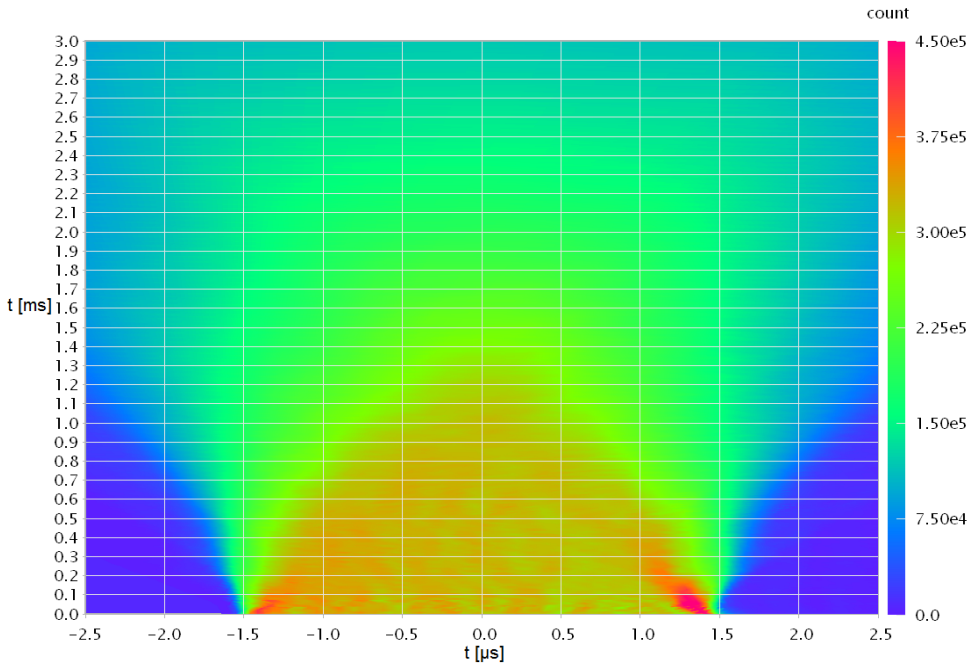

Figure 8.2c: Mountain view of the 50 µA simulated beam bunch

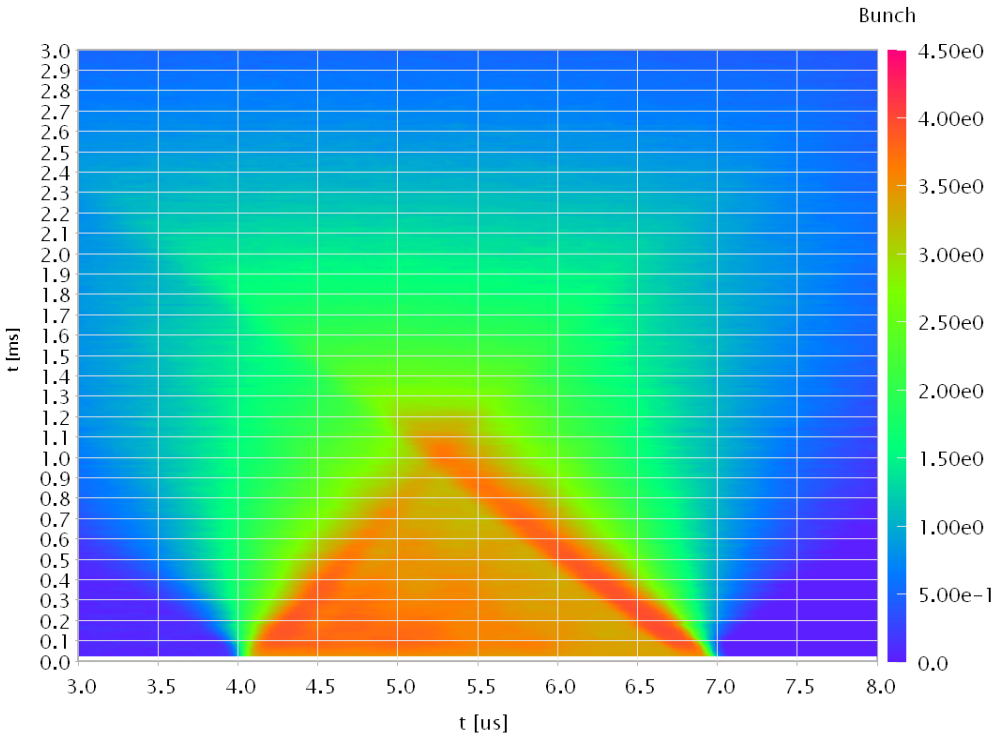

Figure 8.2d: Mountain view of the 100 µA beam bunch observed experimentally

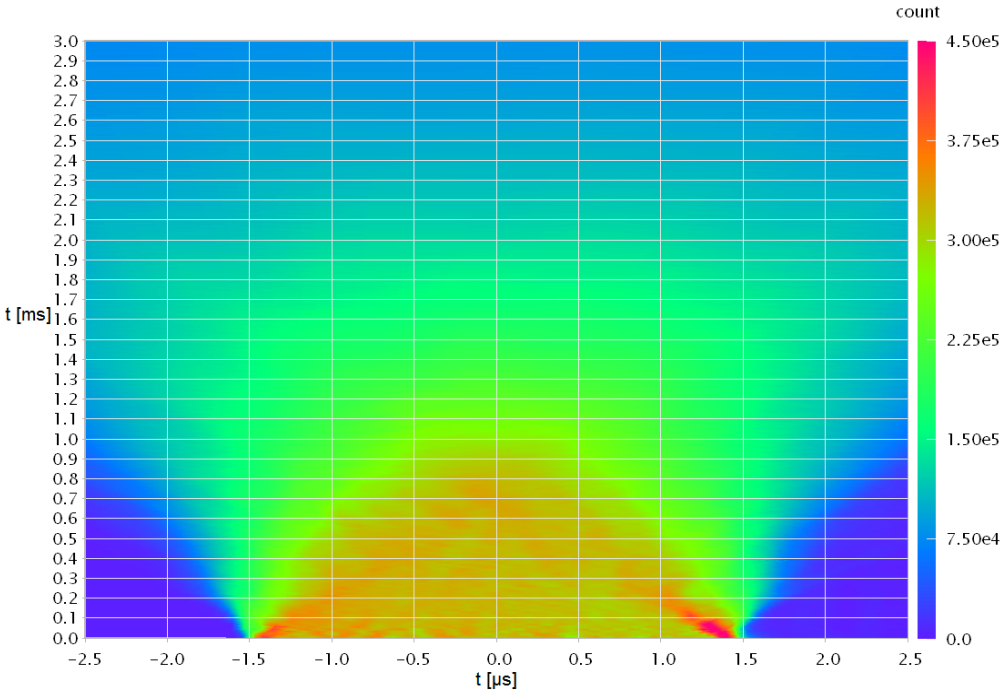

Figure 8.2e: Mountain view of the 100 µA simulated beam bunch

In this experiment, behaviour of the chopped beam was investigated while the beam was circulating freely in the ring. We expect that such a free drift with a long distance may clarify apparently-hidden nature of the chopped beam.

Major intrinsic characteristic of the Einzel lens chopper is momentum modulation at the bunch head and tail, as discussed in the chapter 6. Certainly, we can identify clearly that the bunch head is moving from left to right and bunch tail is moving from right to left in both experimental and simulation results. This phenomenon has been observed at the LEBT region with the comparison between the bunch profile at the entrance and exit of LEBT which can be called as "drift compression". In addition, a beam diffusion or spread is also observed in the experimental and simulation results. Owing to the beam motion in the ring with a long distance, the space charge effect is clearly seen: the particles are diffused outside from the bunch in time.

These characteristics can be explained in relation to the momentum deviation of the chopped pulse, which can be divided into two categories as shown in Fig. 8.2f. The parts indicated with black arrows originate from the plasma formation mechanism in the ECRIS and are known as "intrinsic momentum spread". The red arrows indicate the "transient momentum deviation" induced by the Einzel lens chopper [1].

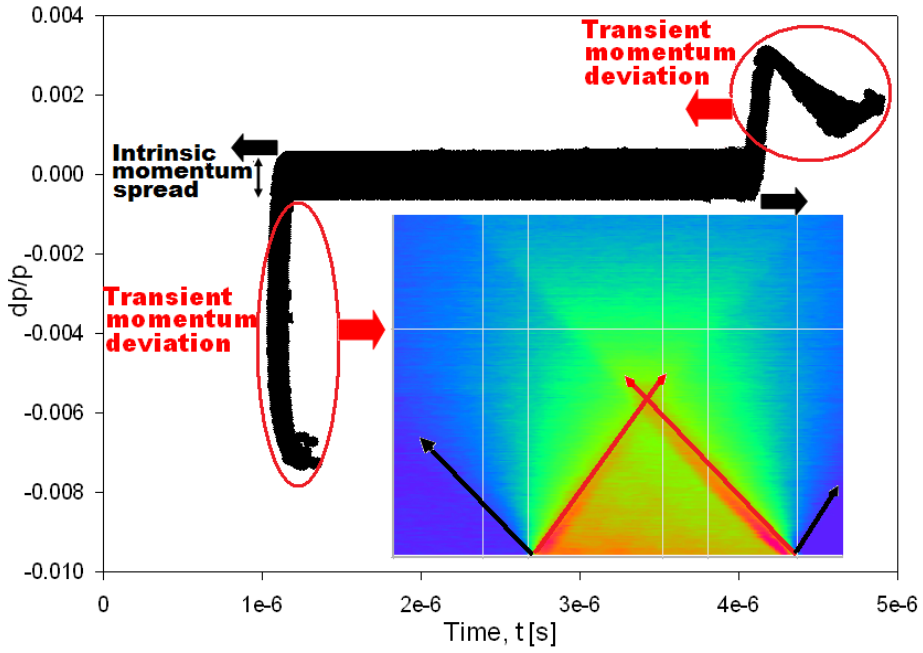

Figure 8.2f: Example of a mountain view with its momentum characteristics [1]

The drift of the ion with momentum error of $\Delta p/p$ in the time plane can be estimated in term of the following formula as:

$$\Delta T = T\eta\left(\frac{\Delta p}{p}\right) \tag{8.1}$$

where T is the revolution period of the on-momentum particle ($\Delta p/p = 0$) and η ($= 1/\gamma_T^2 - 1/\gamma^2$) is the slippage factor of the KEK-DA ring. Since η = -0.81 for He^{1+} at 200 keV, the drift is bound to the left for particles with $\Delta p/p > 0$ and to the right for particles with $\Delta p/p < 0$. The momentum error is easily evaluated by substituting ΔT as obtained from the mountain views in the time-turn plane into Eq. (8.1). If there is nothing to modify the momentum in the ring, the evaluated momentum error should reflect the momentum information of the injected beam [1].

Thus, it is expected that a beam with intrinsic momentum spread diffuses from the pulse head and tail as indicated with the black arrows in Fig. 8.2f. In contrast, a beam with transient momentum deviation drifts in the opposite direction, forming a cross in the time-turn plane, as indicated in the same figure. However, this does not hold in the presence of any perturbations, such as the longitudinal space-charge effect, in which case the extent of the diffusion and the location of the crossing point may change.

The previous section presents typical experimental and simulation results for two ion beam currents. Taking into account the above speculation and the observed results, we can estimate the maximum momentum deviation. Using the following equation,

$$\left(\frac{\Delta p}{p}\right) = \frac{\Delta T}{nT\eta} \tag{8.2}$$

where *n* is the number of turns after injection, we can estimate the maximum momentum deviation. For the lower half of the intrinsic momentum spread,

$$\left(\frac{\Delta p}{p}\right) = \frac{0.23\ \mu s}{(0.5\ ms) \times (-0.81)} = -5.7 \times 10^{-4}$$

for the lower beam current (Fig. 8.2b) and

$$\left(\frac{\Delta p}{p}\right) = \frac{0.26\ \mu s}{(0.5\ ms) \times (-0.81)} = -6.4 \times 10^{-4}$$

for the higher beam current (Fig. 8.2d), respectively.

Here, it should be noted that the upper half was not estimated due to the unclear diffusion in the pulse head part. The difference between beam currents can be attributed to the longitudinal space-charge effect. In fact, the simulation results, according to which

$$\left(\frac{\Delta p}{p}\right) = \frac{0.21\ \mu s}{(0.5\ ms) \times (-0.81)} = -5.2 \times 10^{-4}$$

for the lower beam current (Fig. 8.2c) and

$$\left(\frac{\Delta p}{p}\right) = \frac{0.27\ \mu s}{(0.5\ ms) \times (-0.81)} = -6.6 \times 10^{-4}$$

for the higher beam current (Fig. 8.2e), appear to strongly support this hypothesis.

Nevertheless, the calculated values are somewhat different, which might be caused by the initial momentum distribution at the plasma region.

Another major concern is the transient momentum deviation induced by the Einzel lens, as shown in Fig. 6.4.2b. The experimental results shown in Fig. 8.2b indicate the maximum momentum deviation at the tail part:

$$\left(\frac{\Delta p}{p}\right) = \sim\frac{-0.74\ \mu s}{(0.5\ ms) \times (-0.81)} = \sim 1.8 \times 10^{-3}$$

This momentum deviation is consistent with our predictions, as shown in Fig. 6.4.3b. Therefore, we can state that the longitudinal motion can be quantitatively reproduced in our simulation.

Another notable characteristic of the mountain view is the crossing of the two portions located at the bunch head and tail immediately after injection. The timing of the crossing seems to depend on the beam current. For instance, in the case of 50 μA, the crossing timing is ~1.3 ms after injection; in the case of 100 μA, the crossing timing is ~1.0 ms after injection. For comparison of such a behavior, simulations for two cases of ion beam currents have been performed and these timings are reproduced fairly closely by the simulation results in both cases [1]. This result implies that the crossing time depends on the space charge effect. With the contribution of the space charge effect, the particles located at the both edges of the bunch are pushed out from the bunch. For the higher ion beam current, the longitudinal space-charge effect or the longitudinal electric field in the bunch head/tail is substantially stronger [1]. As a result, a fraction of the particles located at the edges of the bunch accelerate or decelerate and diffuse notably faster with larger $\Delta p/p$, consistent with the simulation results shown in Figs. 8.2c and 8.2e.

For conclusion, the peaks at the head and tail of the chopped beam are contributed by the intrinsic characteristic of the Einzel lens chopper which has been confirmed in this study. In addition, the crossing timing is contributed by a space charge effect and the intrinsic characteristic of the Einzel lens chopper which has been confirmed with two different cases of ion beam currents [1].

References

[1] **K. W. Leo**, T. Adachi, T. Arai, and K. Takayama, "Einzel Lens Chopper and Behavior of the Chopped Beam in the KEK Digital Accelerator", submitted to *Phys. Rev. AB-ST (2012).*

9. Conclusion

9.1 Overview

An electron cyclotron resonance ion sources is one of the promising ion sources for various highly charged state ion production. It has been widely used as an ion source for cyclotrons or heavy ion synchrotrons. In its application for the KEK-DA specific performances have been required. The demand originates from the essential aspects of the digital accelerator: (1) an ion source has to be mounted in a high voltage platform and (2) 1 turn injection into the ring. Namely an ion bunch must be generated in the high voltage platform with a pulse length of order of revolution time period. Under this situation, a novel Einzel lens chopper combined with the permanent magnet ECRIS was developed.

The chopped ion beam is guided to the ring through the LEBT and it has been accelerated. In this Thesis, a full feature of this noble permanent ECRIS with the Einzel lens longitudinal chopper has been summarized. The present outcomes may be summarized in two categories. This chopper has demonstrated its capability without any failure and trouble during beam commissioning.

9.2 From Accelerator Engineering Point of View

All accelerator components except for the DA ring itself are strongly related to this Thesis. Two of most important components are the ECRIS and longitudinal chopper. Both devices must be operated in an engineering level. In order to realize the stable operation of these devices and to secure the quality of delivered beams, the following engineering subjects have been carried out as Thesis task and established as a standard machine/beam tuning method for the KEK-DA injector.

a. Beam current measurement
   - Optimization of the KEK-DA ECRIS parameters such as gas flow rate, microwave power and microwave pulse duration.
   - Calibration of the Faraday cup device.

b. Beam emittance measurement
    - Pepper pot device setting and installation.
    - Establish the experimental procedure.
    - Establish the data analysis procedure.
c. Development of an Einzel lens chopper
    - Installation of the Marx generator.
    - Measurement of the Marx generator voltage profile.
    - Optimization of the required voltage for beam blocking and beam chopping by the observed beam current.
    - Evaluation of the Einzel lens chopper performances with different timings and time durations.
d. Optimization of the LEBT parameters
    - Optimization of the excitation current for each lattice components to minimize the beam loss through LEBT before injection.
    - Power supply stability measurement.

The operational performances of the integration between an ECRIS and an Einzel lens chopper as mentioned above have been well established. Owing to their stable operation and good performance, the beam commissioning which is still under progress can be performed as scheduled.

9.3 From Accelerator Physics Point of View

Focusing on beam physics in the pulse mode operating ECRIS and Einzel lens longitudinal chopper, outcomes are summarized as follows. The former is characterized by transient phenomena where the plasma density including multi-charge state ions builds up to achieve the saturation. The Einzel lens chopper is the first demonstration in the world as a longitudinal chopper and its physical aspect has been well manifested. It is characterized by another transient phenomenon, where the head and tail of chopped beam pulse are affected by the rising and falling behaviors of the chopper voltage profile in a finite time period.

a. Physics of Einzel lens longitudinal chopper
   - Measurement voltage profiles are consistent with the simulation profiles.
   - Optimization of the required voltage for beam blocking and beam chopping by using the IGUN code.
   - Reconstruction of the chopped beam profile from the Faraday cup signal by taking account of its response.
   - Study of the transient beam motion induced by the Einzel lens chopper. It turned out that velocity modulation at pulse head and tail induces beam profile modulation in time.
   - Simulation results in the longitudinal motion could be quantitatively compared with the measurement results.

b. Practical application of inverse problem
   - Practical procedure in which a beam pulse profile is reconstructed from observed signals from a Faraday Cup has been established by applying the inverse problem.

9.4 Prospective View

For further improvement of the KEK-DA performance with higher intensity and higher acceleration energy for higher charge state ions production and the next generation of Digital Accelerator to minimize the beam loss with shorten LEBT construction.

- Necessity of high charge-state ions and further optimization of ECRIS parameters

- Many techniques are available to improve the performances of the KEK-DA ECRIS. For instance, the double frequency heating, wall coating and mixing gas technique which should be very helpful for the highly charged ion production.
- The orifice diameter optimization with the extraction gap is an essential part to be carried out in future. With these improvements, KEK-DA ECRIS will be able to provide the highly charged state ion for Argon (proposed scheme) with the required beam intensity.

- More generalization of the solid-state Marx generator driven Einzel lens longitudinal chopper, such as longer pulse, higher rep-rate, and sequential chopping for various applications

- Einzel lens chopper should be able to work for various ions species which must be performed in future works: for instance, Oxygen, Neon and Argon species.
- The Einzel lens chopper should be applicable for various pulse durations from microsecond to millisecond. The pulse duration can be varied by the modification of the capacitance of the Marx generator.

An Einzel lens chopper with flexible chopping pulse duration could be a useful and attractive tool for the accelerator community.

- More compact injection scheme (shorten LEBT)

The present KEK DA was constructed, based on the existing 40 MeV proton beam line. In principle, the ion beam can be directly injected into the ring after momentum separation and charge state separation. Beam transport through a shorten beam line should be easy. This must be employed in a future digital accelerator.

Appendix 1

Ion Sources

1.1 Introduction

An ion source is an essential component in any ion accelerator. Various applications of ion beams require a certain level of beam quantity (current) and quality (emittance). In this chapter, existing ion sources such as Plasmatron ion source, Penning ion source, vacuum arc ion source, electron beam ion source/trap, laser ion source and electron cyclotron resonance ion source are briefly summarized with their historical review, typical design, working principle and advantages and disadvantages.

1.2 Plasmatron Ion Source

1.2.1 Historical Review

Two types of plasmatron ion sources are classified as unoplasma and duoplasmatron ion source. The unoplasma ion source was developed by V. Ardenne in 1948 [1] for plasma density improvement by the electron bombardment with ion beam inside the ion source as shown in Fig. 1.2.1a. The duoplasmatron ion source was developed by V. Ardenne in 1956 [1] with electron bombardment and an aid of axial magnetic field compression inside the ion source as shown in Fig. 1.2.1b.

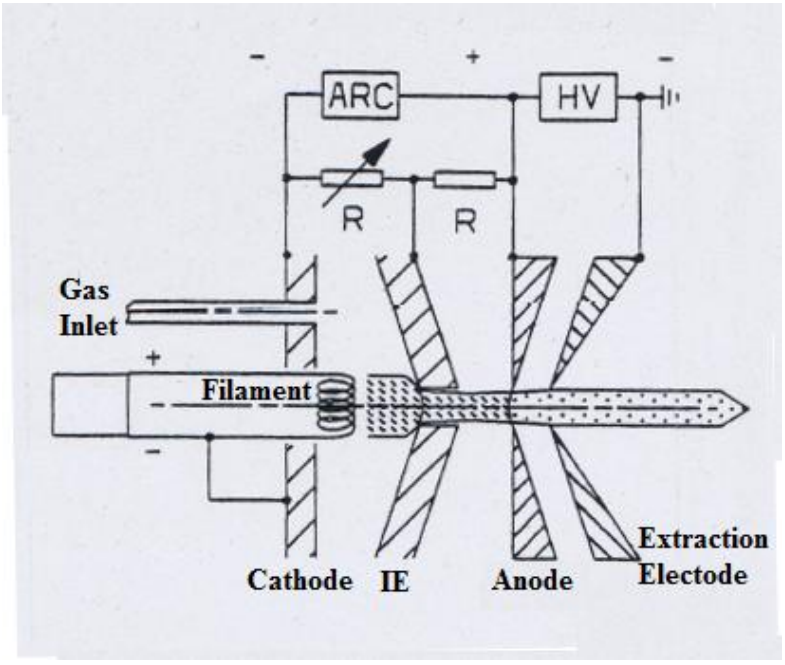

Figure 1.2.1a: Schematic view of unoplasma ion source (IE= Intermediate electrode) [1]

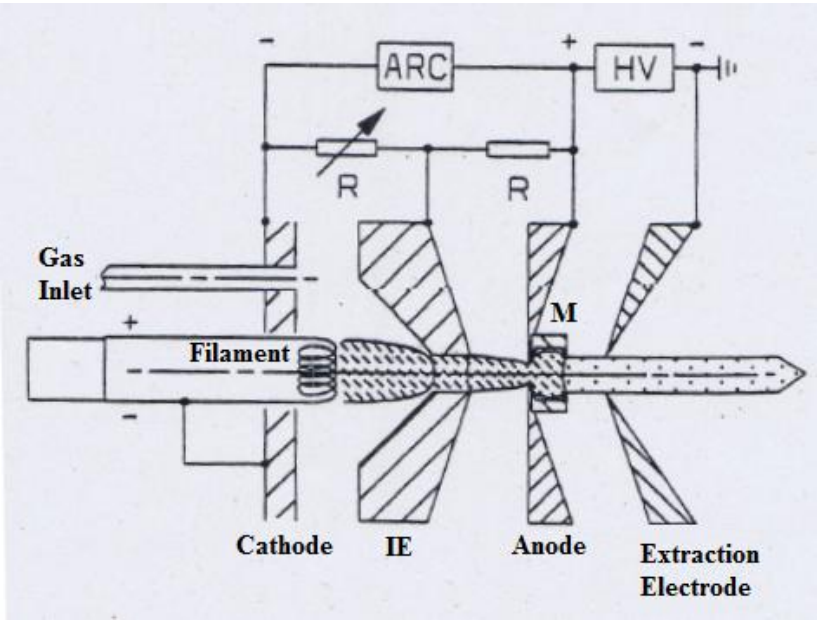

Figure 1.2.1b: Schematic view of duoplasma ion source [1]

(IE =Intermediate electrode, M=Cylindrical magnetic region)

1.2.2 Working Principle

In general, the plasmatron ion source consists of a gas inlet and a set of cathode and anode for electron bombardment. In addition, an intermediate electrode (IE) is located between cathode and anode [1]. For plasmatron ion source which consists of two plasma regions: first region between cathode and the IE and second region between the IE and the anode. At beginning, the electrons are emitted from a heated filament (cathode) and its emission is controlled by the IE potential which must be well-optimized. These electrons collide with gas atoms injected from the gas inlet and ionize them. Therefore, a low density cathode plasma is generated between the cathode and IE in the first plasma region. Furthermore, the high density plasma between the IE and the anode are generated in the second plasma region as shown in Fig. 1.2.1b. Finally the ions are extracted through the extraction electrode. For the duoplasmatron ion source configuration, an additional axial magnetic field region located at the anode is utilized to improve the ionization efficiency which the electrons are spiral along the magnetic flux density field line inside this magnetic region. Basically, the cathode plasma is compressed by a double layer into the IE channel and then further compressed by an axial magnetic field to produce very high density plasma [1].

1.3 Penning Ion Source

1.3.1 Historical Review

The Penning discharge was first studied by L. R. Maxwell in 1931[2]. The Penning ion source name, PIG, come from F. M. Penning who invented the Penning or Philips Ionization vacuum Gauge in 1937 [1]. In 1940s, Penning ion sources were first utilized as internal sources in a cyclotron [3, 4]. After that, they were utilized by linear accelerators as their ion sources in ~1956 [5].

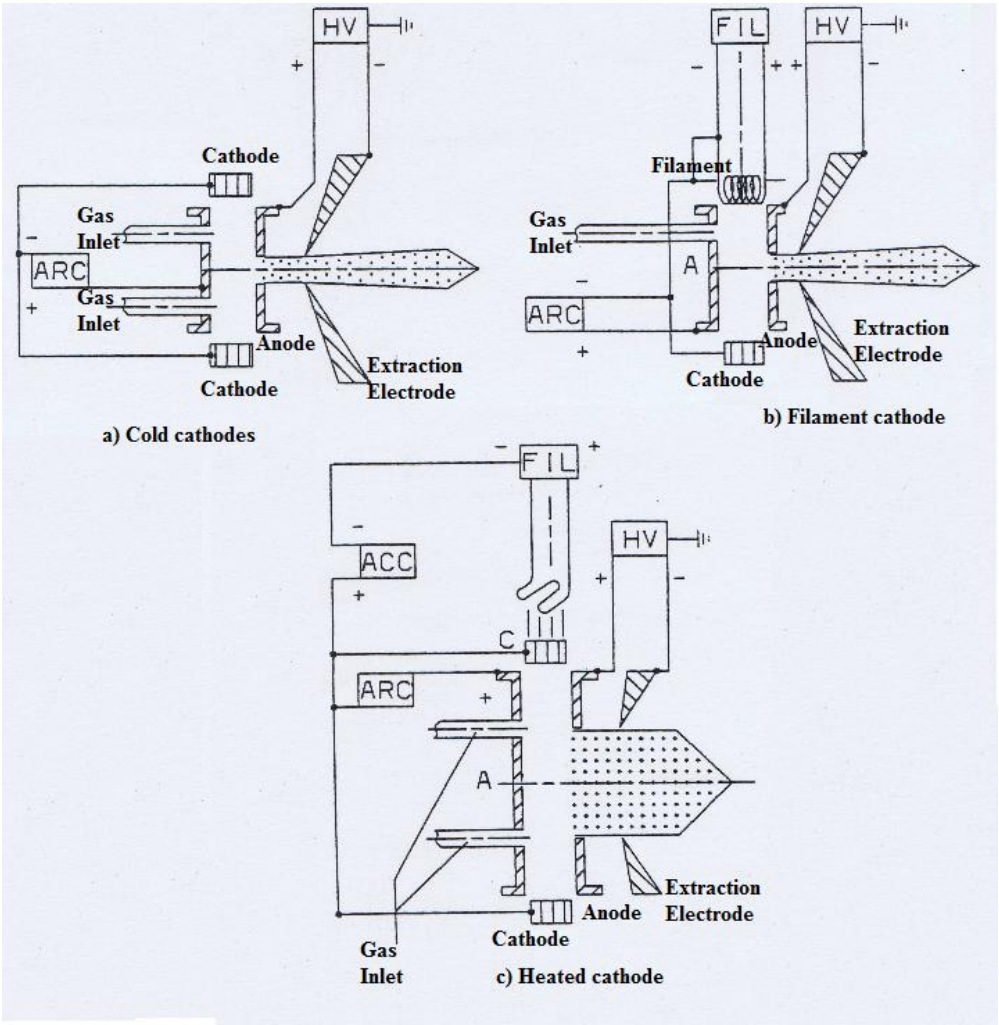

Figure 1.3.2a: Schematic view of Pennig ion source [1]

1.3.2 Working Principle

The Penning ion source as shown in Fig. 1.3.2a consists of a hallow cylinder anode with one cathode located at both end. Electrons are oscillated and confined by a strong axial, the oscillated between anode and cathode will improve the ionization efficiency [1]. A gas is

injected into the discharge through the anode close to the cathode to ease the ignition of the arc and the electrons are colliding with the atom gas [1]. Plasma is produced and ions are extracted by the extraction electrode.

1.4 Vacuum Arc Ion Source

1.4.1 Historical review

Vacuum arcs were studied by many people since 1920s with focus on the high-power switches and vacuum tubes [1]. The first reliable metal vapor vacuum arc (MEVVA) ion developed at Lawrence Berkeley Laboratory by Brown in the early 1980s [6], Humphries, Jr. and Picraux [1]. Furthermore, a multicathode ion source was introduced by Brown in 1987 [1] to extend the ion source lifetime and its flexibility operation. Later, a DC operation of MEVVA was constructed by Brown in 1991 [1].

1.4.2 Working principle

As shown in Fig. 1.4.2a, arc plasma is generated by the high voltage spark and maintained between cathode spots and the anode [1]. Material is vaporized from the cathode spots for ionization. The arc plasma parameter is dependent on the ionization behavior of the cathode spots. The cathode spots occur randomly with a lifetime of a few microseconds [1]. Basically, the arc has to be pulsed operation to limit the power dissipation at the cathode. However, a DC operation of a vacuum arc ion source is also available with a large and well cooled cathode configuration [1].

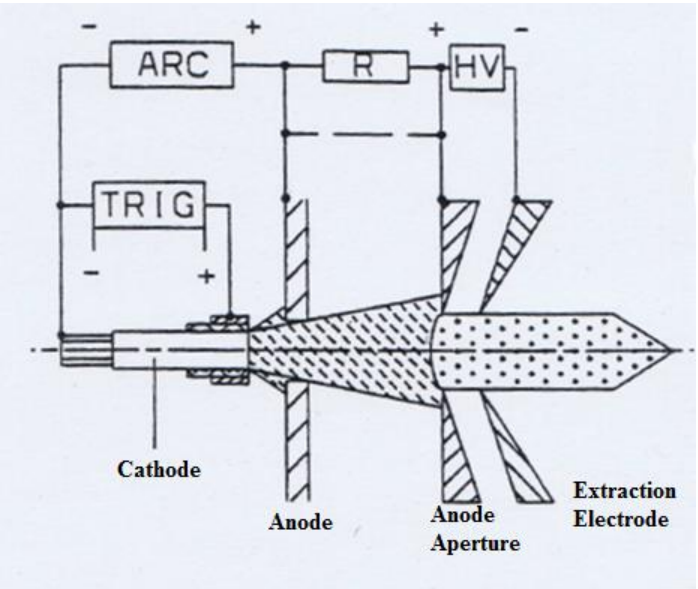

Figure 1.4.2a: Schematic view of Vacuum Arc ion source [1]

1.5 Electron Beam Ion Source (EBIS) /Trap (EBIT)

1.5.1 Historical Review

EBIS was invented by Donets in 1965 [1]. Later in 1969, he reported the production of Au^{19+} [1], using a baked-out vacuum tube inside a normal conducting solenoid. Then, he developed cryogenic versions KPYON-I to –III with his co-workers, where the electrodes inside a superconducting solenoid were kept at 4.2 K. KRYON-I injected successfully with bare nuclei of C, N and O into Dubna Synchrophasotron for 2 years [7], which KRYON-II was the first EBIS to produce bare ions of Ne, Ar, Kr and Xe [8].

EBIT was started from the Berkeley EBIS. Litvin, Vella and Sessler [9] had concluded that a long electron beam tends to instabilities and as a way out, a short electron beam ion trap was proposed. One having a Helmholtz coil top allow for radial access for spectroscopy was built and operated successfully [10].

1.5.2 Working Principle

The schematic view of the EBIS/EBIT is shown in Fig. 1.5.2a. At the beginning, electrons beam is produced and focused by the magnetic field of a solenoid. The electron beam passes through the cylindrical electrodes which form a space charge with a radial potential for ions trapped and confined axially by the potentials applied to the cylindrical electrodes surrounding the beam. Gas atoms are trapped and ionized by the electron impact ionization inside the electron beam and undergo stepwise ionization [1]. Then the ions are extracted axially by change of the axial potential distribution. When the potential of the exit barrier is lowered or the central trap potential is raised or ions gain sufficient energy, they will escape axially over the lower exit barrier [11].

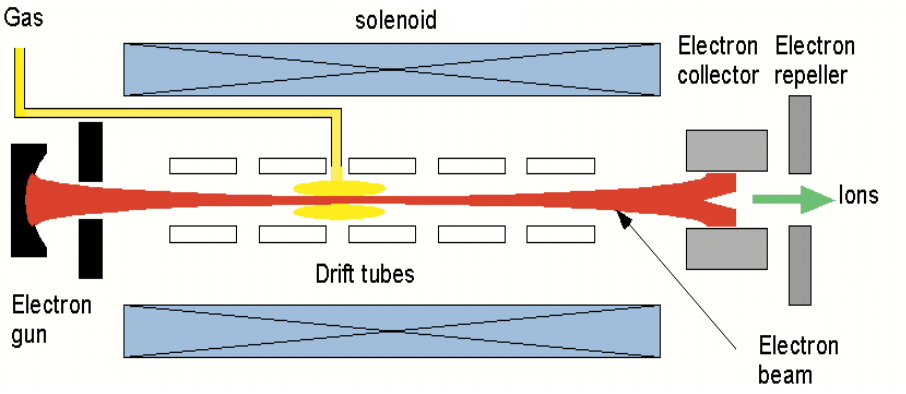

Figure 1.5.2a: Schematic view of EBIS/EBIT ion source [12]

1.6 Laser Ion Source

1.6.1 Historical review

In 1969, an ion source for accelerators produced by a laser were proposed and made independently by Peacock and Pease and Byckovsky *et al.* [1]. Highly charged ions of various materials with high expansion energy (several keV per ion) have been produced by neodymium glass lasers [1, 13]. Anan'in reported the first operation of laser ion source based on the Nd-glass laser for a cyclotron [14]. In 1984, a laser ion source was utilized as an ion source for the 10 GeV synchrotron at HINR (Dubna) [1]. In the 21st century, new schemes of laser ion source were reported by several laboratories. For examples, a direct extraction scheme from the ions source was reported by M. Nakajima [15] and direct injection scheme was proposed by M. Okamura [16].

1.6.2 Working principle

Plasma is generated when a laser beam is focused by a mirror system or lens on a solid target as shown in Fig. 1.6.2a. When a focused laser hit the target, the target is ionized and particles are evaporated. During the evaporation process, the plasma electrons are generated and heated up by the laser radiation to the temperature up to several hundreds eV [1]. The ionization process occurred by the collision between electrons and ions. During the evaporation and ionization process, the ions are expanding by the drift space between the target and the extraction electrode plane, which this expansion can be defined as ion pulse duration [1].

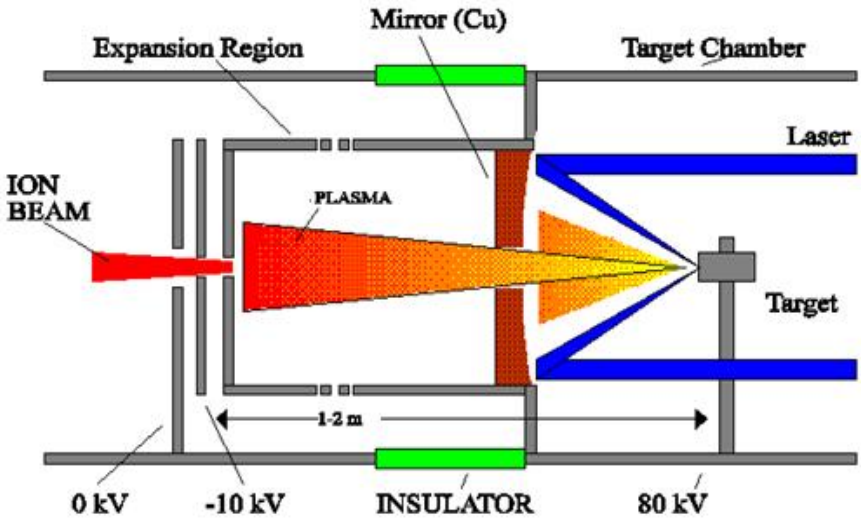

Figure 1.6.2a: Schematic view of laser ion source [17]

1.7 Electron Cyclotron Resonance Ion Source

1.7.1 Historical review

Electron cyclotron resonance ion sources (ECRIS) were first proposed by R. Geller in 1965 [18] and K. Postma in 1970 [19]. In 1971, Geller and co-workers reported on the first operational ECRIS. This ECRIS, called as MAFIOS, it can deliver a moderate charge-state ions as from a PIG ion source because ion lifetime in the plasma was short (~10^{-4}s) [1]. Other group studied similar devices as well [20]. Later in 1975, a new ECRIS design using two-stage arrangement called as SuperMAFIOS was reported [21]. The first stage was a MAFIOS which the generated plasma was guided into the second stage with a hexapole field for additional radial confinement apart from the axial mirror field. The ion lifetime was improved (~10^{-2}s) with this configuration and a very high charge states could be detected, but its power consumption of 3 MW was unacceptable for accelerator applications [22]. Although so, the SuperMAFIOS configuration is the basic of all ECRIS for multiply charged ion production with the utilization of the axial and radial magnetic field. This changed with the introduction of strong rare earth permanent magnets for the hexapole construction [1]. Geller cooperated with the cyclotron laboratories in Louvain La Neuve and Karlsruhe built the MiniMAFIOS source, which just 100 kW is needed for the mirror field coil [1]. Several hundred ECRIS have been constructed after the first prototype of ECRIS was developed. Nowadays, the conventional type of ECRIS (permanent magnet ECRIS) with lower resonance magnetic field have evolved into the superconducting magnets type of ECRIS [23].

1.7.2 Working principle

An ECRIS consist of a plasma chamber, a set of the axial confinement magnet, a radial confinement magnet, microwave injection, gas inlet and extraction system as shown in Fig. 1.7.2a. The ECRIS operation principle can be described in Fig. 1.7.2a, a gas and a microwave power are injected into the plasma chamber. The free electrons with the gyrate motion in the plasma chamber will gain the energy if their gyration frequency ω_{ce} is equals to the microwave frequency ω_{RF}. This is called as cyclotron frequency which can be deduced as [19]:

$$\omega_{ce} = \omega_{RF} = \left(\frac{e}{m_e}\right) B_{res}$$

Hence, B_{res}, e and m_e denote the resonance magnetic field density, charge and mass of the electron.

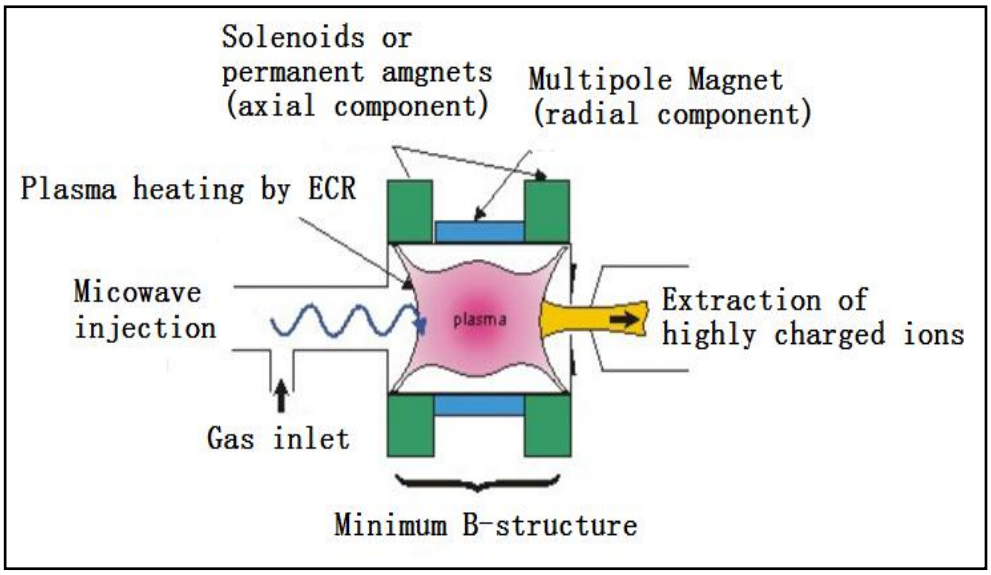

Figure 1.7.2a Schematic view of ECRIS

The energetic electrons are trapped into a plasma region by the mirror field from the ring magnet and the radial field from the hexapole magnet. The trapped electrons collide with the neutral atoms and ions as well. Therefore, the ions are produced inside the plasma chamber. The ions inside the plasma are extracted by an electrode system.

1.7.3 Permanent magnet type of ECRIS

A permanent type of ECIS is a compact ECRSI with a permanent magnet material which have been employed for the axial magnetic confinement (Ring magnet) and radial magnetic confinement (Hexapole magnet). The materials used for the permanent magnet usually are made from CoSm or NdFe [1]. This type of ECRIS can reduce the power consumption and the cooling system for the magnet system. Therefore, this type of ECRIS is suited to be embedded into the High Voltage Platform for accelerator applications. However, due to the limitation of the rare earth magnetic property, the ECRIS is operating at the lower frequency compare with the superconducting magnet type of ECRIS.

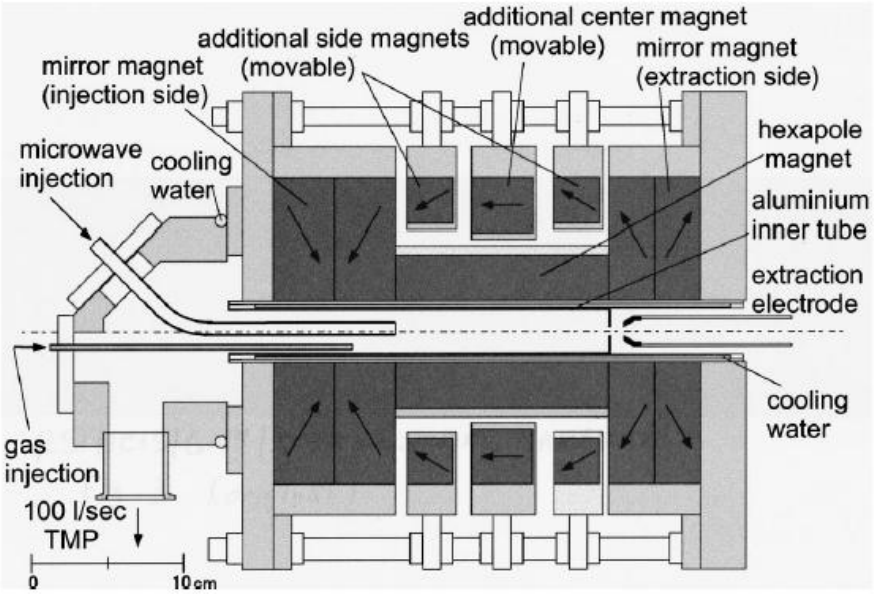

Fig. 1.7.3a: Permanent type ECRIS of Cyclotron and Radioisotope Center, Tohoku University with moveable side magnet [24]

1.7.4 Superconducting magnet type of ECRIS

The latest ECRIS generation is a superconducting magnet type of ECRIS [23]. Its magnetic structure is employed with the superconducting material. Therefore, these magnetic parameters allow this ECRIS to operate in the higher electron heating frequency with the better performance to produce the higher charged ions. But the superconducting magnet needs a complicated cooling system. The Fig. 1.7.4a shows the superconducting magnet type of ECRIS (SECRAL) which can be operated at 18/28 GHz [25].

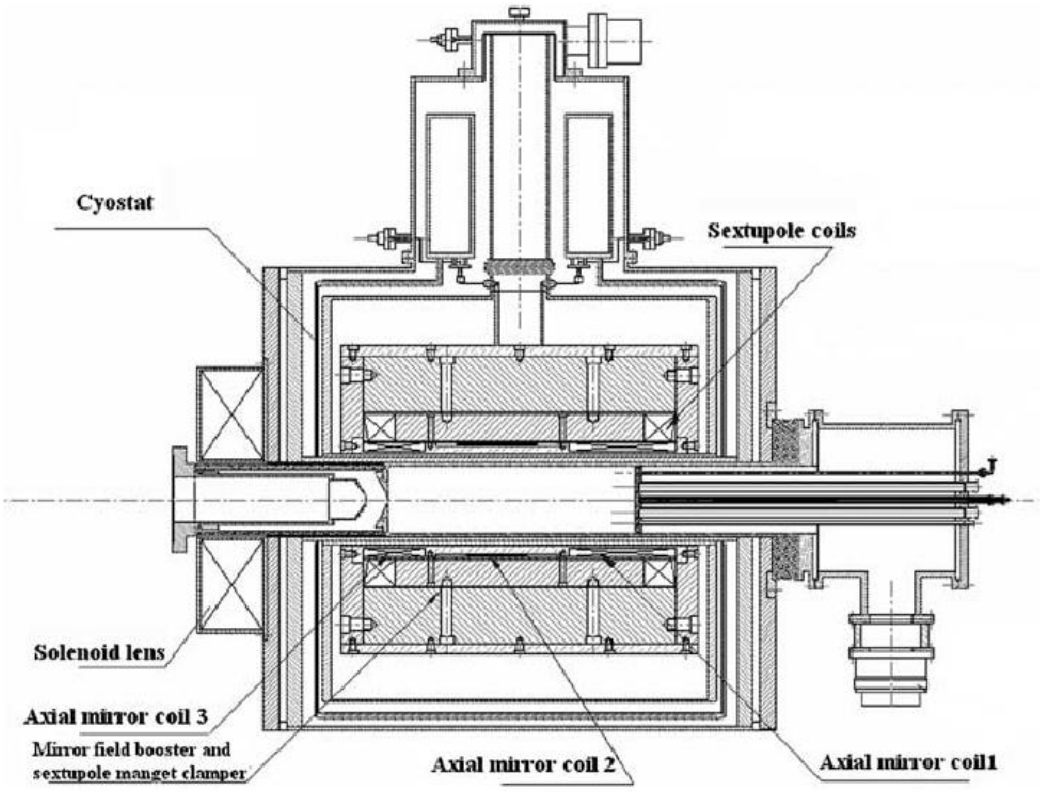

Figure 1.7.4a Schematic view of IMP SECRAL [25]

1.7.5 ECRIS with supporting techniques

1.7.5.1 Introduction

Since the development of the ECRIS, many laboratories have been carried out with many techniques to improve their ECRIS performances for higher multi-charged ions production. Basically, the requirements for higher charge state ions production with ECR ion sources can be summarized as follows [18, 26]:

i. The electron density, n_e must be adequate to produce the higher charge state ions.
ii. The electron energy, E_e must be sufficient enough for atoms or ions ionization to the desired charge state.
iii. The confinement time, τ_{conf} of the ions must be long enough to achieve the higher charge state.

The probability for higher charge state production can be assumed to be proportional to n_e and E_e. The following methods are commonly used to improve the performance of the ECR ion sources. Common techniques which have been employed in the worldwide ECRIS society will be discussed.

1.7.5.2 Double frequency heating

The higher charge-state ion intensity can be improved by using multiple frequencies heating, in which additionally resonance surfaces for electron heating are created [27, 28]. This technique has been applied by many laboratories to improve their ECR ion sources performance such as Argonne national Laboratory (ANL) [29, 30], RIKEN [31] and IMP [32]. At University of Jyväskylä (JYFL), double frequency heating with a tunable TWT amplifier was utilized and the increasing in beam current was observed as shown in Fig. 1.7.5.2a [33].

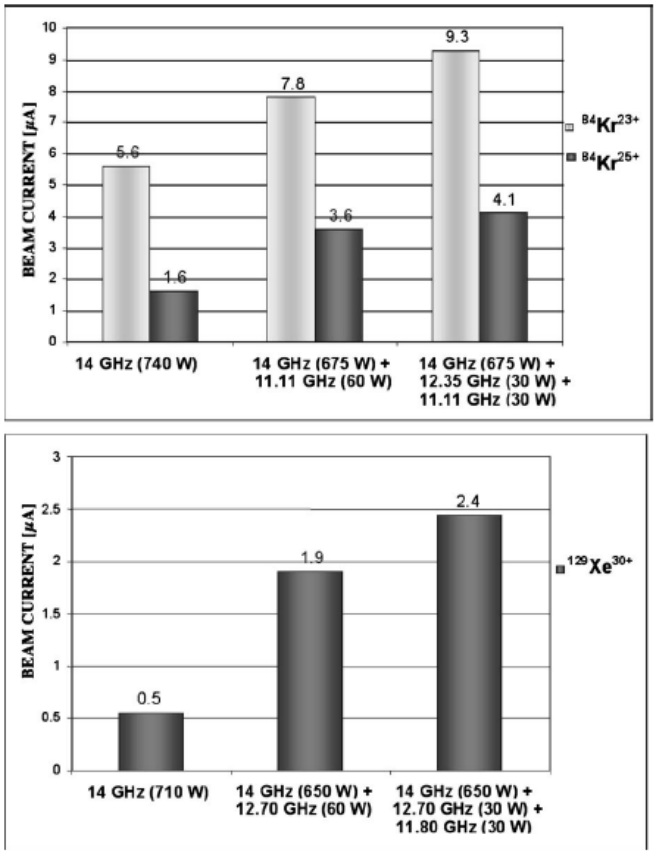

Figure 1 .7.5.2a: The improvement of Krypton and Xenon ion beam currents with multiple frequencies technique at JYFL [33]

Assuming an appropriate frequency gap between employed frequencies, the performance of the ECR ion sources improved by double frequency heating has been observed in several experiments:

i. The charge state distribution (CSD) is shifted towards to higher charge state [29].
ii. The production times of highly charge state ions decrease by introducing the secondary frequency [34].

1.7.5.3 Biased disk technique

Biased electrodes technique is used in most modern ECR ion sources now both in continuous and in pulsed mode of operation [31, 35] as shown in the schematic view of Fig. 1.7.5.3a. It was observed that with a hundred voltage of a biased electrode located at the end of the injection end of the plasma chamber, the beam intensity of the higher charges state ions can be increased significantly. Many experiments have been performed to realize the advantages of the biased electrode technique such as biased disk position experiment [36], test a biased electrode with the different sizes and shapes [37] and test with the different biased voltages [38].

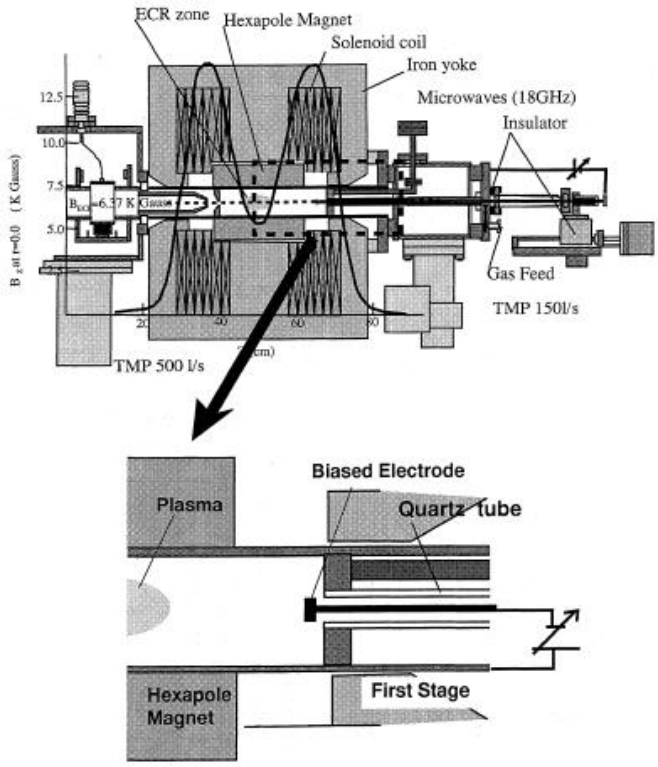

Figure 1.7.5.3a: Schematic view of RIIKEN 18 GHz ECRIS with biased electrode [31]

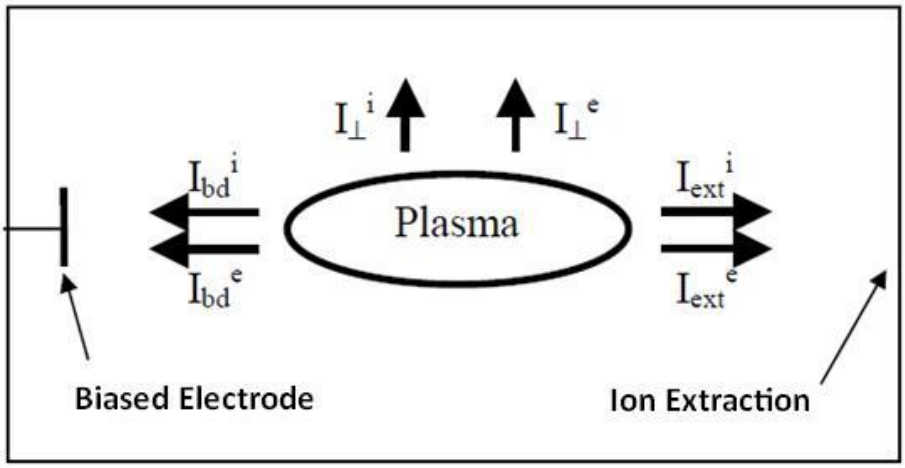

$$I_{\perp}^{i} + I_{bd}^{i} + I_{ext}^{i} + I_{\perp}^{e} + I_{bd}^{e} + I_{ext}^{e} = 0$$

Figure 1.7.5.3b: Simon short-circuits currents in the ECRIS plasma chamber. (Note: Arrow shows the particles flux) [39]

In generally, the effect of the biased electrode can be explained by a "Simon Short Circuit Currents" [39] diagram as shown in Fig. 1.7.5.3b. Which the equation shown as in Fig. 1.7.5.3b expressed the balance equation of the currents due to the electron and ion losses. The drain current of the extracted beam current is included in the extraction end current of I_{ext}. By applying the biased voltage to the electrode, the electron flux at the injection end of the source can be decreased due to the electrons repelled, therefore the electrons density inside the ECR plasma are increasing. However, in order to satisfy the balance equation as shown in Fig. 1.7.5.3b the ion fluxes (mainly in the radial direction: $I_{\perp}^{i}$) out to the plasma have to be decreased. Consequently, the ECR ion source performance can be improved due to the electrons density increment and the increment of the ions' confinement time as well.

1.7.5.4 Mixing gas technique

The remarkable effect can be obtained with the gas mixing technique was discovered by Drentje [40]. Presently, this technique has been utilized by many laboratories to produce the higher charges state ions [41, 42]. By adding a lighter gas (excluding hydrogen) into the plasma with a heavier gas, the intensities of the higher charge state ions of the heavier gas can be increased significantly. Since the discovery of this technique, various explanations were suggested, such as:

a) A dilution effect lowering the mean ion charge state, which the electron loss rate will be reduced and the electron density is increased [3].

b) Ion cooling phenomena from the mass effect in ion-ion collisions; the low mass/low charge ions of the added gas transport energy from the heavy ions out from the plasma due to their lower confinement [43,44].

c) Increment of the electron density due to the better ionization efficiency with the added gas [45].

At University of Jyväskylä (JYFL), the effect of gas mixing on the production efficiency of argon ion beams was measured with the following gases: helium (He), nitrogen (N_2), oxygen (O_2), neon (Ne) and krypton (Kr) as shown in Fig. 1.7.5.4a [46]. From this measurement result, we can find out that the added gas for the main gas of argon species is oxygen which has been utilized by SuSI ion source [46] and SECRAL [47].

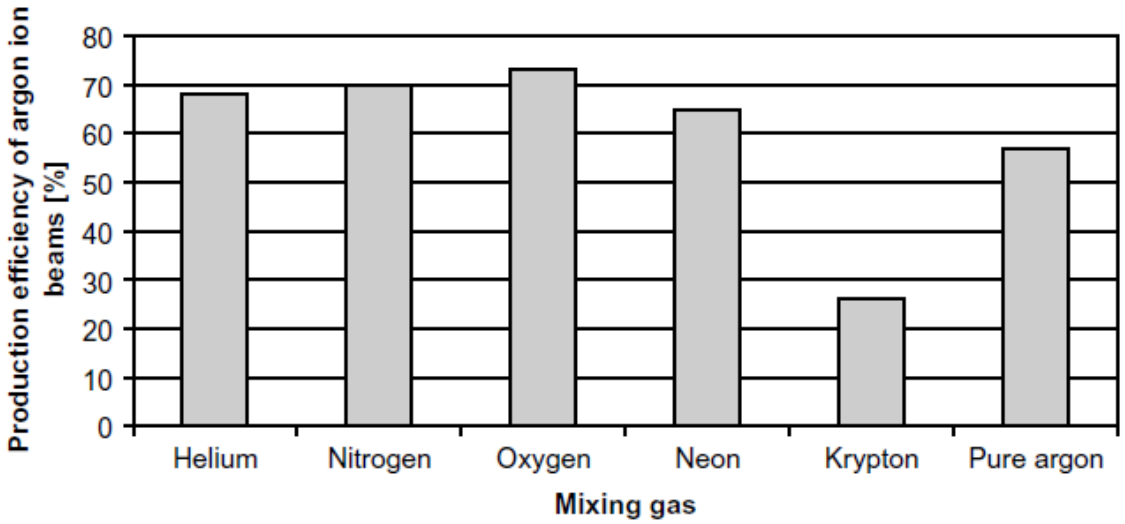

Figures 1.7.5.4a: The production efficiencies of argon ion beams obtained with different mixing gases [46]

1.7.5.5 Wall coating

The property of plasma chamber can improve the ECRIS performance significantly based on the secondary emission coefficient of the material [3]. The RIKEN group coated their plasma chamber with the aluminium oxide and the remarkable results were obtained for the high charge state ions production as shown in Fig. 1.7.5.5a [49, 50]. This can be explained by the two explanations as below:

a) The secondary electron emission coefficient of the plasma chamber with the silicon oxide layer is higher. Therefore, the electron density is increased due to the cold electrons emission from the wall of the plasma chamber.

b) The modification of the plasma potential due to the insulating properties of the silicon oxide layer.

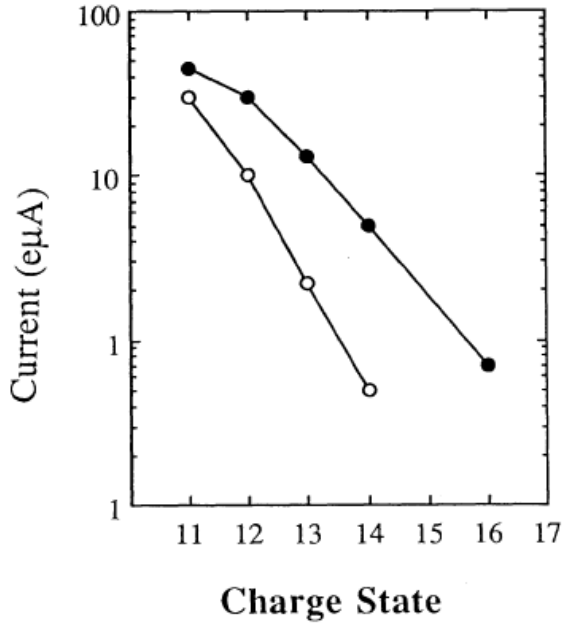

Figure 1.7.5.5a: Beam intensity of argon ions as a function of charge state. Open and closed circles are the beam intensities before and after producing Al ions (Aluminium oxide coating) [50]

Nowadays, most of the modern ECRIS plasma chambers are made from the aluminium or stainless steel instead of copper. The secondary electron emission coefficient, δ with the impact electron energies of the elements, E_{pmax} is shown in Table 1.1 [51].

Table 1.1: Secondary electron emission coefficient with the optimal electron impact energies for several elements

Compound/Element	Al	Cu	MgO	SiO_2	Al_2O_3
δ_{max}	1.0	1.3	3-15	2.1- 4	2-9
E_{pmax} (eV)	300	600	400-1500	400	------

1.8 Summary

Various ion sources are available in the world. Individual ion sources, they have their own advantages and disadvantages as summarized in Table 1.2 [1]. Our requirements to the ion source are: stable production of multi-charged ions, good beam quantity (higher beam current) and quality (small beam emittance), low repetition rate with μ-pulse length, compact size to be embedded into a high voltage terminal with low power consumption. With the comparison among those ion sources, EBIS/EBIT and ECRIS are the compatible ion sources which fulfill the requirement of the KEK-DA ion source. But within the cost and simplicity construction factors consideration, ECRIS is much cheaper and with much simple construction compared with EBIS/EBIT [1]. In addition, the related x-band microwave

components are available in the group. Therefore, an ECRIS has been selected presently as an ion source for KEK-DA.

Table 1.2: Comparison of the ion sources performances

Ion Sources	Beam current	Beam emittance	Repetition rate	Pulse length	Highly-charged ions	Long term operation Stability
Plasmatron	●	●	●	●	△	△
Penning	●	△	●	●	●	△
Vacuum Arc	●	△	△	△	△	△
EBIS and EBIT	●	●	●	●	●	●
Laser	●	●	△	△	△	●
ECRIS	●	●	●	●	●	●

Remarks:

△ = poor △ = Moderate △ = Good(Metal ions) ● = Good

References

[1] Bernhard Wolf (Eds), Handbook of Ion sources, CRC Press (1995) ISBN 0849325021.

[2] L. R. Maxwell, "The Production of an Intense Beam of Hydrogen Positive Ions", *Rev. Sci. Instrum*, **2**, 129 (1931).

[3] A. T. Finkelstein, "A High Efficiency Ion Source", *Rev. Sci. Instrum*, **11**, 94 (1940).

[4] M. S. Livingston, M. G. Holloway ,and C. P. Baker, "A Capillary Ion Source for Cyclotron", *Rev. Sci. Instrum.* **10**, 63 (1939).

[5] C. E. Anderson , and K. W. Ehlers, "Ion Source for the Production of Multiply Charged heavy Ions", *Rev. Sci. Instrum.* **27**, 809 (1956).

[6] K. W. Ehlers , and K. N. Leung, "Characteristics of the Berkeley Multicusp Ion Source", *Rev. Sci. Instrum.* **50**, 1353 (1979).

[7] E. D. Donets, "Review of the JINR Electron Beam Ion Sources", *IEEE Trans. Nucl. Sci.*, NS-23, 897 (1976).

[8] E. D. Donets, "Electron Beam Ion Sources and Associated Physics at JINR", *Nucl. Instrum. Methods* **B9,** 522-525 (1985).

[9] C. Litvin, M. C. Vella , and A. Sessler, " Linear Electrostatic Instability of the Electron Beam Ion Source", *Nucl. Instrum. Methods* **198,** 189-192 (1982).

[10] M. A. Levine *et al*., " use of an Electron Beam Ion Trap in the Study of Highly Charged Ions", The *Nucl. Instrum. Methods* **B43,** 431-440 (1989).

[11] Martin P. Stockli , and C. L. Cocke , " The Physics of Electron Beam Ion Sources", *Nucl. Instrum. Methods* **B56/57,** 239-245 (1991).

[12] http://www.msl.se/crysis/ebis.gif

[13] G. F. Tonon, "Laser Sources for Multiply- Charged Heavy Ions", *IEEE Trans. Nucl. Sci. 19*, 172 (1972).

[14] O. B. Anan'in, Yu. A. Bykovskii, Yu. P. Kozyrev, and A. S. Tsybin, "Acceleration of Laser-Plasma Ions in a Cyclotron", *JETP-Letters*, **17**, No. 9, 460-463 (1973).

[15] M. Nakajima, N. Kobayashi, and K. Horioka, "Direct Extraction of Ions from Expanding Laser Ablation Plasma", *Technical Research Report NIFS-PROC-61*, 149, National Institute for Fusion Science, Toki, Japan, (2005).

[16] M. Okamura, T. Katayama, R.A. Jameson, T. Takeuchi, T. Hattori and H. Kashiwagi, "Scheme for Direct Plasma Injection into an RFQ Linac", Laser and Particle Beams (2002), 20: pp 451-454.

[17] http://scrivens.web.cern.ch/scrivens/lis/reports/pragspie/largepic/img00003.gif

[18] H. Postma, "*Multiply* Charged Heavy Ions Produced by Energetic Plasma", *Phys. Lett.* **31A**, 196-19 (1970).

[19] R. Geller, Electron Cyclotron Resonance Ion Sources and ECR Plasma, Institute of Physics Publishing, London (1996), ISBN 0740301074.

[20] H. Tamagawa, I. Alexeff, C. M. Jones , and P. D. Miller, " Use of the Hot-Electron Mirror Machine INTEREM as a High-Z Ion Source", *IEEE Trans. Nucl. Sci.* NS-23, 994-998 (1876).

[21] P. Briand, R. Geller, B. Jacquot, C. Jacquot ,and A. Theiss, " Production and Abundance measurements of Multicharged Xenon Ions in ECR Produced Plasmas", *Nucl. Instrum. Methods* **127,** 441-443 (1975).

[22] R. Geller, "Electron Cyclotron Resonance (E.V./R) Multiply Charged Ion Sources", *IEEE Trans. Nucl. Sci.* 26, 2120-2127 (1979).

[23] C. M. Lyneis, D. LEitner, D. S. Todd, G. Sabbi, S. Prestemon, S. Caspi ,and P. Ferracin, " Fourth Generation Electron Cyclotron Resonance Ion Sources (Invited)", *Rev. Sci. Instrum*. **79**, 02A321 (2008).

[24] A. Yamazaki, N. Fujita, E. Tanaka, and T. Shinozuka, T. Yokoi, T. Ozawa and H. Tanaka, " Design of an All-Permanent-Magnet ECR Ion Source at the Cyclotron and Radioisotope Center", *Rev. Sci. Instrum*. **73**, 589 (2002).

[25] L. T. Sun, H. W. Zhao, Z. M. Zhang, B. Wei, X. Z. Zhang, X. H. Guo ,X. W. Ma, Y Cao, W. Hw ,and H. Y. Zhao," Brief Review of Multiple Charge State ECR Ion Sources in Lanzhou", *Nucl. Instrum. Methods* B **235,** 524-529 (2005).

[26] A. G. Drentje, "Techniques and mechanisms applied in electron Cyclotron Resonance Sources for Highly Charged Ions", *Rev. Sci. Instrum.* **74**, 2631 (2003).

[27] Z.Q. Xie , and C.M. Lyneis, "Two Frequency Plasma Heating in a High Charge State Electron Cyclotron Resonance Ion Source", *Rev. Sci. Instrum.* **66**, 4218 (1995).

[28] G. D. Alton , F. W. Meyer, Y. Liuy, J. R. Beebe, and D. Turcker , " Enhancing the performances of Traditional Electron Cyclotron Resonance Ion Sources with Multiple-Discrete-Frequency Microwave radiation", *Rev. Sci. Instrum.* 69, 2305 (1998).

[29] R.C. Vondrasek, R.H. Scott, and R.C. Pardo, "Magnetic Field Ugrade of Argonne National Laboratory 14 GHz ECR Ion Source", *Rev. Sci. Instrum.* **66**, 4218 (1995).

[30] R. Vondrasek, R. Scott, and R. Pardo, "ECRIS Operation with Multiple Frequencies", *Rev. Sci. Instrum.* **75**, 1532 (2004).

[31] T. Nagakawa. M. Kidera, Y. Higurashi, J. Ohonishi, A. Goto *et al*, "New Superconducting Electron Cyclotron Resonance Ion Source for RIKEN RI Beam Factory Project", *Rev. Sci. Instrum.* **79,** 02A327 (2008).

[32] L. T. Sun, H. W. Zhao, W. Lu, X. Z. Zhang, Y.C. Feng *et al.*, "Production of Highly Charged Ion Beams with SECRAL", *Rev. Sci. Instrum.* **81**, 02A318 (2010).

[33] H. Koivisto, P. Suominen, O. Tarvainen, and A. Virtanen, "Electron Cyclotron Resonance Ion Source Realted Development Work for Heavy-Ion Irradiation Tests", *Rev. Sci. Instrum.* **77**, 03A316 (2006).

[34] R.C.Vondrasek, R.H. Scott, and R.C. Pardo, "ECRIS Operation with Multiple Frequencies", *Rev. Sci. Instrum.* **77**, 03A337 (2006).

[35] H. W. Zhao, L. T. Sun, X. Z. Zhang, Z. M. Zhang, X. H. Guo *et al*.," Advanced Superconducting Electron Cyclotron Resonance Ion Source SECRAL: Design, Construction, and the First Test Result", *Rev. Sci. Instrum.* **77**. 03A333 (2006).

[36] T. Nakagawa, Y. Higurashi, J. Ohnishi, M. Tamura *et al.*, "First Results from the New RIKEN Superconducting Electron Cyclotron Resonance Ion Source (Invited)", *Rev. Sci. Instrum.* **81**, 02A320 (2010).

[37] S. Biri *et al.*, "Highly Charged Ion Production Using an Electrode in Biased and Floating Modes", *Proceedings of the 14th International Workshop on ECR Ion Sources*, Geneva, p. 81 (1999).

[38] S. Gammino, J. Sibring, and A. G. Drentje, "Experiment with a Biased Disk at the K.V.I. ECRIS", *Rev. Sci. Instrum.* **63**, 2872 (1992).

[39] A. G. Drentje, U. Wolters, A. Nadzeyka, D. Meyer and K. Wiesemann, "Simon Short Circuit Effect in ECRIS", *Rev. Sci. Instrum.*, 73, 516 (2002).

[40] A. G. Drentje, "The ECR Ion Source and Associated Equipment at the KVI", *Nucl. Instrum. Methods Phys.* Res. B **9**, 526 (1985).

[41] C. Lyneis, D. Leitner, M. Leitner, C. Taylor, and S. Abbott, " The third Generation Superconducting 28 GHz electron Cyclotron Resonance Ion Sources VENUS (Invited)", *Rev. Sci. Instrum.*, **81**, 02A201 (2010).

[42] H. W. Zhao, L. T. Sun, W. Lu,X. Z. Zhang, X. H. Guo *et al.* , " New Development of Advanced Superconducting Electron Cyclotron Resonance Ion Source SECRAL (Invited)", *Rev. Sci. Instrum.*, **81**, 02A202 (2010).

[43] G. D. Shirkhov, "A Classical Model of Ion Confinement and losses in ECR Ion Sources", *Plasma Sources Sci. Technol.* **2**, 250 (1993).

[44] Z. Q. Xie, and C. M. Lyneis, "Plasma Potentials and Performance of the Advanced Electron Cyclotron Resonance Ion Source", *Rev. Sci. Instrum.* **65**, 2947 (1994).

[45] M. Delaunay, "Influence of Ionization Cross Sections on the Gas Mixing Effect for the Production of Ar^{9+} Ions in a CAPRICE ECR Source", *Rev. Sci. Instrum.* ***63***, 2861 (1992).

[46] O. Tarvainen, P. Suominen, and H. Koivisto, " Effect of the Gas Mixing Technique on the Production of Ion Beams Extracted from An Electron Cyclotron Resonance Ion Source", *Nucl. Instrum. Methods Phys. Res. B* **217**, 136-142 (2004).

[47] L. T. Sun, J. Brandon, D. Cole, M. Doleans, D. Morris, G. Machicoane, E. Pozdeyev, T. Ropponen, L. Tobos, " Intense Beam Production with SUSI", *19th International Workshop on ECR Ion Sources 2010*, Grenoble, France, Pg. 4 (2010).

[48] H.W. Zhao, W. Lu, L.T. Sun, X.H. Guo, X.Z. Zhang, Y. Cao, H. Y. Zhao, Y.C. Feng, J. Y. Li, D. Z. Xie, " SECRAL status and First Beam Test at 24 GHz", *19th International Workshop on ECR Ion Sources 2010*, Grenoble, France, Pg. 1 (2010).

[49] T. Nakagawa, T. Kurita, M. Kidera, M. Imanaka, Y. Higurashi *et al.*, " Intense Beam Production from RIKEN 18 GHz ECRIS and Liquid He free SC-ECRISs", *Rev. Sci. Instrum.* **73**, 513 (2002).

[50] T. Nakagawa, “Effect of Coating on the Plasma Chamber Wall in RIKEN Electron Cyclotron Resonance Ion Source”, *Japanese Journal of Applied Physics*, Vol. **30**, No. 5B, 930-932 (1991).

[51] Handbook of Chemistry and Physics, 81st Edition, Edited by David. R. Lide, CRC Press, Inc. (2000).

Appendix 2

Electron Cyclotron Resonance Ion Source

2.1 Introduction

The history of the ECRIS started from late 1960s, when the Geller Group developed the Electron Cyclotron Resonance Ion Source (ECRIS) for fusion plasma research [1]. After demonstration of the first ECRIS prototype, several hundred ECRIS have been constructed. These ECRIS have been used for heavy ion accelerators and atomic physics researches such as, RIKEN SC-ECRIS in the Institute of Physical and Chemical Research (RIKEN) for the RIKEN cyclotron [2], VENUS ECRIS in Lawrence Berkeley National Laboratory for rare isotope accelerator [3], SECRAL ESCRIS in Institute of Modern Physics (IMP) for cyclotron [4]. In 1987 Geller and co-workers discovered the semi-empirical laws for ECRIS called as "scaling laws" [5], which predicted the performance of an ECRIS by their parameters. After a few ten years, semi-empirical rules were review by other ECRIS laboratories [6, 7]. According to the old and new scaling laws, the important parameters are microwave frequency and mirror ratio as below.

$$q_{opt} \propto log\, B^{1.5} \tag{2.1}$$

$$q_{opt} \propto \log \omega^{3.5} \tag{2.2}$$

$$q_{opt} \propto P^{1/3} \tag{2.3}$$

$$I_q \propto \omega^2 \mathrm{M}^{\mathrm{a}} \ \ (\mathrm{a} = 0.5\sim1) \tag{2.4}$$

Here,

$q_{opt} =$ Charge state giving maximun current, $B = \left(\frac{B_{max} + B_{min}}{2}\right)$

$\omega =$ Microwave angular frequency, $M =$ Atomic mass number and

$I_q = C$urrent of ions with charge state q

Therefore the ECRIS is moving forward from the conventional ECRIS to the superconducting ECRIS. The superconducting ECRIS in the worldwide laboratories [7] is shown in Table. 2.1.

Table 2.1: 3rd Generation of SC-ECR ion sources (Φ=Plasma chamber diameter)

	VENUS	SECRAL	SUSI	RIKEN SC-ECR	MS-ECRIS
f (GHz)	28	18-24	18-24	28	28
B_{inj} (T)	4.0	3.7	3.6	3.8	4.5
B_{rad} (T)	2.1	2.0	2.0	2.1	2.7
Φ(mm)	150	118-126	100	150	180

2.2 Operating Principle of ECRIS

As shown in Fig. 2.2a, a typical ECRIS consists of a plasma chamber in vacuum, microwaves system for heating electrons, a set of magnet to provide a magnetic mirror field for plasma confinement in the axial direction, a hexapole magnet for the radial plasma confinement and an extraction electrode for ion extraction [1, 8]. Gas and microwaves are injected into the plasma chamber. In general, injected microwaves interact with free electrons performing cyclotron motions. In order to gain energy through microwaves, the Larmor frequency of a free electron must be equal to the frequency of microwaves [1, 8]. Ions are ionized in the plasma chamber through step-by-step ionization process which is a dominant process. There the energy of electrons must be higher than the ionization potential of desired charge-state of ion. Ions produced in the ECR plasma are extracted and accelerated with the aid of the extraction voltage across the gap between the plasma chamber and an ion extraction electrode. The details of the physical processes in an ECRIS are described in the next sections.

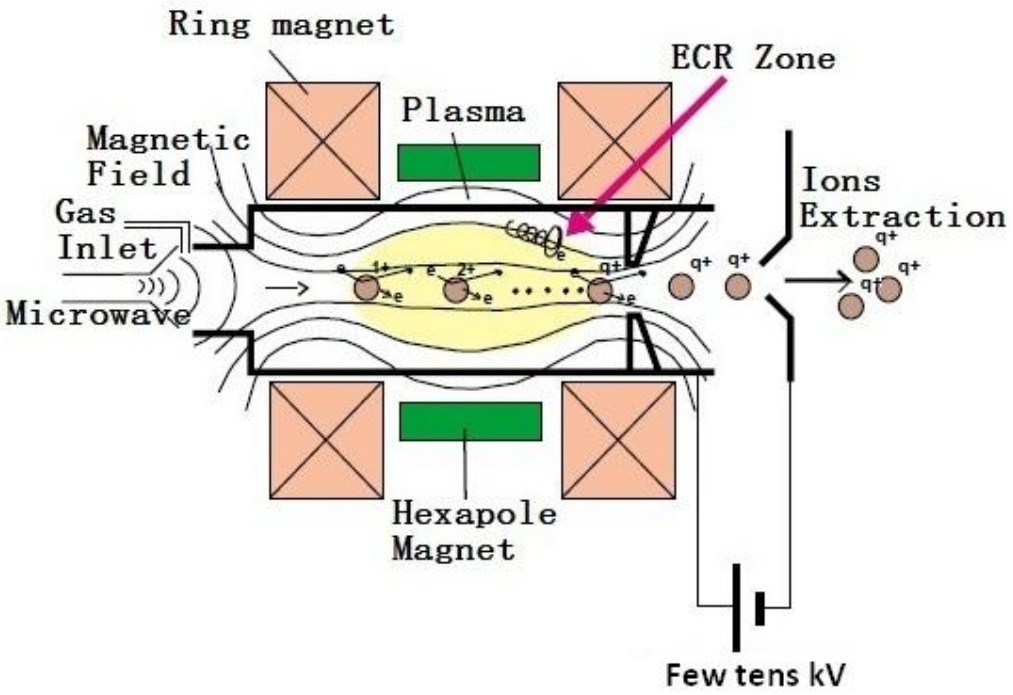

Fig. 2.2a: Schematic view of an ECRIS

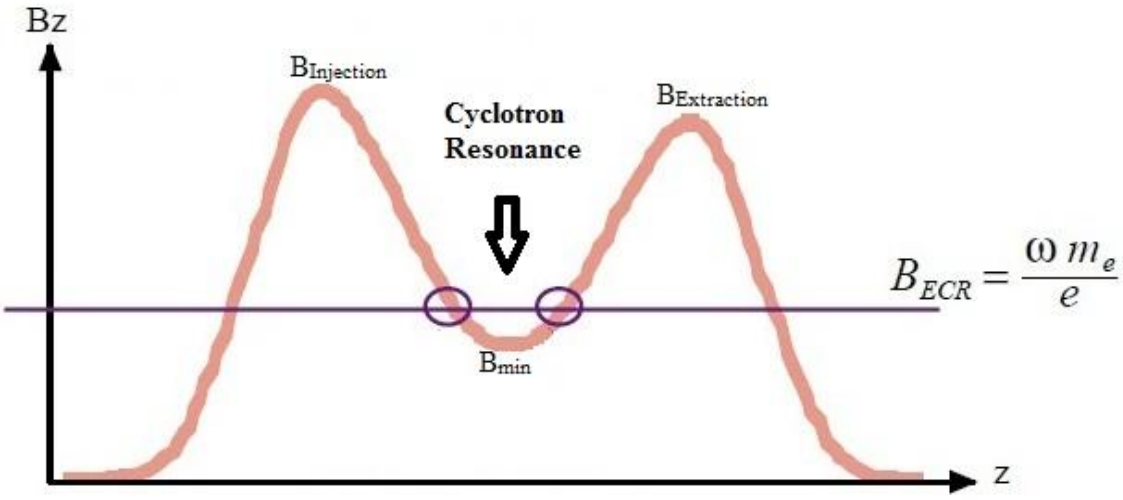

Figure 2.2b: Axial magnetic field profile on the central axis

2.2.1 ECR Heating by Microwaves

In the magnetic fields, electrons rotate around the magnetic flux lines with a particular frequency. When the rotating frequency of the electrons is equal to the frequency of microwaves supplied into the plasma chamber,

$$f_e = \frac{eB_{ECR}}{2\pi m_e} = f_{rf} \tag{2.5}$$

where,

$f_e =$ ECR frequency, $B =$ ECR magnetic flux density

$f_{rf} =$ Microwave frequency, $m_e =$ Eletron mass and $e =$ electron charge,

Electron Cyclotron Resonance (ECR) heating can occur [1, 8, 9, 10].

The ECRIS magnetic fields are designed so that there are closed, equal magnetic field surfaces surrounding the plasma region indicated by two circles as shown in Fig. 2.2b. On this surface, the electron cyclotron frequency is equal to the microwave frequency. This surface is called the ECR surface. If the electric field of the microwaves is in the same phase as the electron gyration motion, the microwave energy can be efficiently transferred to kinetic energy of the electron. After sufficient electron heating the atoms and ions can be ionized through collision [1, 8, 9].

2.2.2 Magnetic Confinement

The plasma confinement in an ECRIS is archived by a superposition of an axial and radial magnetic field [1, 8]. The confinement of electrons is essential for the ECRIS to produce an intense beam of highly charged heavy ions. A higher electron temperature and density given by a well confined plasma leads to the higher efficiency of ionization and production of highly charged ions. The reason why a hexapole magnet must be utilized additionally will be discussed at the next section.

2.2.2.1 Magnetic mirror confinement

Characteristic of the magnetic confinement of the ECRIS can be described as the magnetic mirror field effect. Consider slowly varying field along the Z direction as shown in Fig. 2.2.2.1a.

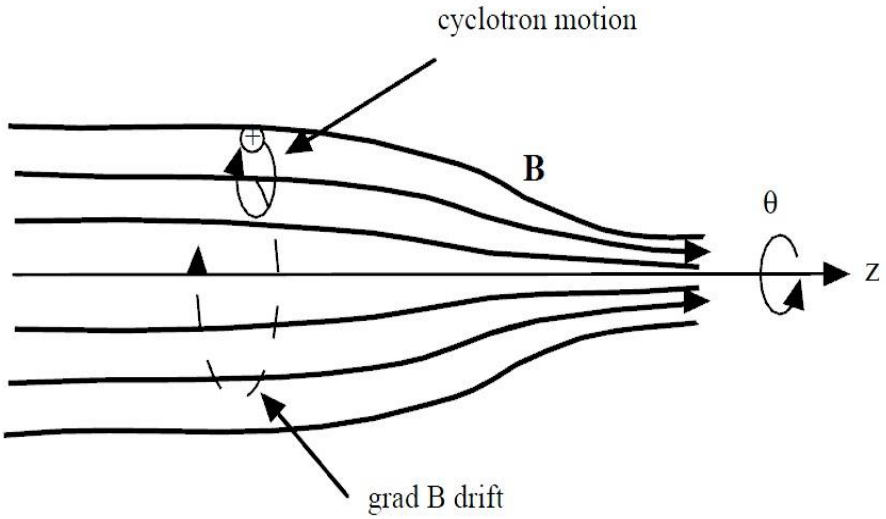

Figure 2.2.2.1a: Particle drift in the magnetic field

Equation motion in the cylindrical coordinate system,

$$\frac{\mathrm{d}v_\mathrm{r}}{\mathrm{dt}} - v_\theta \frac{\mathrm{d}\theta}{dt} = \frac{\mathrm{q}}{\mathrm{m}}\, v_\theta \mathrm{B_z} \tag{2.6}$$

$$\frac{\mathrm{d}v_\theta}{\mathrm{dt}} + v_\mathrm{r} \frac{\mathrm{d}\theta}{dt} = \frac{\mathrm{q}}{\mathrm{m}}\, (v_z \mathrm{B_r} - v_r \mathrm{B_z}) \tag{2.7}$$

$$\frac{\mathrm{d}v_\mathrm{z}}{\mathrm{dt}} = -\frac{\mathrm{q}}{\mathrm{m}}\, v_\theta \mathrm{B_r} \tag{2.8}$$

Assuming that the field is axisymmetric,

$$\mathrm{B_\theta} = 0 \text{ and } \frac{\partial}{\partial \theta} = 0 \tag{2.9}$$

Assuming that v_θ=constant during gyration and v_r=0,

From (2.6),

$$\frac{\mathrm{d}\theta}{dt} = -\frac{\mathrm{q}}{\mathrm{m}}\, \mathrm{B_z} \tag{2.10}$$

$$v_\theta = r_L \frac{\mathrm{d}\theta}{dt} = -r_L \frac{\mathrm{q}}{\mathrm{m}}\, \mathrm{B_z} \tag{2.11}$$

From (2.8) and (2.11),

$$\frac{\mathrm{d}v_\mathrm{z}}{\mathrm{dt}} = \left(\frac{\mathrm{q}}{\mathrm{m}}\right)^2 r_L \mathrm{B_z B_r} \tag{2.12}$$

From the 2nd Maxwell equation, the magnetic field in the cylindrical coordinate system satisfies the following equation,

$$\boldsymbol{\nabla . B} = 0$$

$$\frac{1}{\mathrm{r}}\frac{\partial}{\partial r}(rB_r)+\frac{1}{\mathrm{r}}\frac{\partial \mathrm{B}_\theta}{\partial \theta}+\frac{\partial B_z}{\partial z}=0 \tag{2.13}$$

From the (2.9) and (2.13),

$$\frac{1}{\mathrm{r}}\frac{\partial}{\partial r}(rB_r)+\frac{\partial B_z}{\partial z}=0 \tag{2.14}$$

Assuming that $\partial B_z/\partial z$ for small $r = constant$, integral of (2.14) by r gives,

$$rB_r=-\int_0^{r_L} r\frac{\partial B_z}{\partial z}dr \cong -\frac{1}{2}{r_L}^2\left[\frac{\partial B_z}{\partial z}\right] \tag{2.15}$$

$$B_r=-\frac{1}{2}r_L\left[\frac{\partial B_z}{\partial z}\right] \tag{2.16}$$

From (2.16) and (2.12),

$$\frac{\mathrm{d}v_\mathrm{z}}{\mathrm{dt}}=\left(\frac{\mathrm{q}}{\mathrm{m}}\right)^2 r_L \mathrm{B_z}\left(-\frac{1}{2}r\frac{\partial B_z}{\partial z}\right)$$

$$\frac{\mathrm{d}v_\mathrm{z}}{\mathrm{dt}}=-\left(\frac{\mathrm{q}}{\mathrm{m}}\right)^2 \frac{{r_L}^2}{2} B_z\left(\frac{\partial B_z}{\partial z}\right) \tag{2.17}$$

Multiply the (2.11) with (2.11),

$${v_\theta}^2={r_L}^2\left(\frac{\mathrm{q}}{\mathrm{m}}\right)^2 {\mathrm{B_z}}^2 \tag{2.18}$$

From (2.18) and (2.17),

$$\frac{\mathrm{d}v_\mathrm{z}}{\mathrm{dt}}=-\frac{v_\theta}{2\mathrm{B_z}}\left(\frac{\partial B_z}{\partial z}\right) \tag{2.19}$$

Multiply both sides of (2.19) with m,

$$\mathrm{m}\frac{\mathrm{d}v_\mathrm{z}}{\mathrm{dt}}=-\frac{\mathrm{m}v_\theta}{2\mathrm{B_z}}\left(\frac{\partial B_z}{\partial z}\right) \tag{2.20}$$

Gyration of particles can be defined as:

$$\mathrm{m}\frac{\mathrm{d}v_\mathrm{z}}{\mathrm{dt}}=-\mu\left(\frac{\partial B_z}{\partial z}\right) \tag{2.21}$$

And μ =magnetic moment of the gyration particle.

From now, consider as the Cartesian coordinate system,

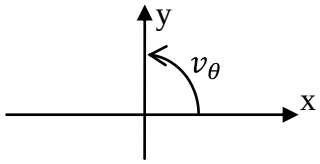

$$x = r_L \cos\dot{\theta}t \tag{2.22}$$

$$y = r_L \sin\dot{\theta}t \tag{2.23}$$

$$\omega \equiv -\dot{\theta} = \frac{qB_z}{m} \tag{2.24}$$

From (2.24), (2.22) and (2.23),

$$x = r_L \cos(-\omega t) \tag{2.25}$$

$$y = r_L \sin(-\omega t) \tag{2.26}$$

Differential (2.25) and (2.26) respect with t,

$$v_x = -\omega r_L \sin(-\omega t) = v_\theta \sin(\omega t) \tag{2.27}$$

$$v_y = \omega r_L \cos(-\omega t) = v_\theta \cos(\omega t) \tag{2.28}$$

And, $v_\theta = -\omega r_L$

For field change in y-direction,

With assumption that $\frac{dB}{dt} = 0$ and $\frac{dB}{dy} = b = \text{constant}$

$$B = B_0 + by \tag{2.29}$$

From (2.26) and (2.29),

$$B = B_0 - br_L \sin(\omega t) \tag{2.30}$$

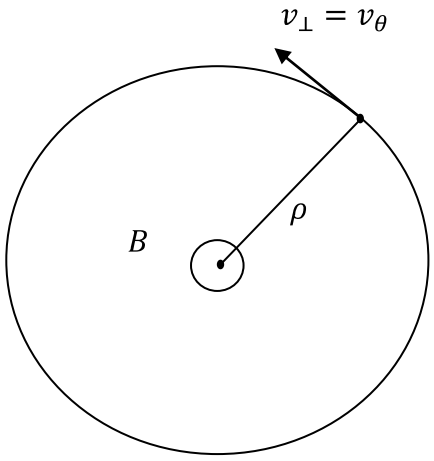

Unit vector,

$$\frac{\boldsymbol{B}}{|\boldsymbol{B}|} = \frac{\boldsymbol{v}_\perp \times \boldsymbol{\rho}}{|\boldsymbol{v}_\perp \times \boldsymbol{\rho}|} = \frac{\boldsymbol{v}_\perp \times \boldsymbol{\rho}}{|\boldsymbol{v}_\perp||\boldsymbol{\rho}| \sin\emptyset} = \frac{\boldsymbol{v}_\perp \times \boldsymbol{\rho}}{\rho^2 \omega} \tag{2.31}$$

And $\emptyset = 90°$.

Multiply (2.29) with $\boldsymbol{v}_\perp$,

$$\boldsymbol{v}_{\perp} \times \frac{\boldsymbol{B}}{B} = \frac{\boldsymbol{v}_{\perp} \times (\boldsymbol{v}_{\perp} \times \boldsymbol{\rho})}{\rho^2 \omega} = \frac{\boldsymbol{v}_{\perp}(\boldsymbol{v}_{\perp}.\boldsymbol{\rho}) - \boldsymbol{\rho}({v_{\perp}}^2)}{\rho^2 \omega} \tag{2.32}$$

$$\boldsymbol{v}_{\perp} \times \frac{\boldsymbol{B}}{B} = \frac{-\boldsymbol{\rho}{v_{\perp}}^2}{\rho^2 \omega} = -\boldsymbol{\rho}\omega \tag{2.33}$$

$$\boldsymbol{\rho} = -\frac{1}{\omega}\boldsymbol{v}_{\perp} \times \frac{\boldsymbol{B}}{B} = -\frac{m}{qB^2}(\boldsymbol{v}_{\perp} \times \boldsymbol{B}) \tag{2.34}$$

For Cartesian coordinate, $B_x = 0, B_y = 0, B_z = B$

$$(\boldsymbol{v}_{\perp} \times \boldsymbol{B}) = \big(v_y B\big)\hat{\boldsymbol{x}} - (v_x B)\hat{\boldsymbol{y}} \tag{2.35}$$

For x-direction, from (2.34) and (2.35),

$$\rho_x = -\frac{m}{qB^2}\big(v_y B\big) = -\frac{mv_y}{qB} \tag{2.36}$$

For y-direction, from (2.34) and (2.35),

$$\rho_y = -\frac{m}{qB^2}(-v_x B) = \frac{mv_x}{qB} \tag{2.37}$$

From (2.36), differential both sides respect with t,

$$\Delta\,\rho_x = \frac{m\Delta B}{qB^2}\,v_y \tag{2.38}$$

From (2.37), differential both sides respect with t,

$$\Delta\,\rho_y = -\frac{m\Delta B}{qB^2}\,v_x \tag{2.39}$$

Substitute (2.28) to (2.38),

$$\Delta\,\rho_x = \frac{m\Delta B}{qB^2}\,v_{\perp}\cos(\omega t) \tag{2.40}$$

$$\frac{d\rho_x}{dt} = \frac{m}{qB^2}\frac{dB}{dt}\,v_{\perp}\cos(\omega t) \tag{2.41}$$

Substitute (2.27) to (2.39),

$$\Delta\,\rho_y = -\frac{m\Delta B}{qB^2}\,v_{\perp}\sin(\omega t) \tag{2.42}$$

$$\frac{d\rho_y}{dt} = -\frac{m}{qB^2}\frac{dB}{dt}\,v_{\perp}\sin(\omega t) \tag{2.43}$$

From (2.30), differential respect with t,

$$\frac{dB}{dt} = -\mathrm{b}r_L\omega\cos(\omega\mathrm{t}) \tag{2.44}$$

Substitute (2.44) to (2.41),

$$\frac{d\rho_x}{dt} = -\frac{mv_\perp}{qB^2}\mathrm{b}r_L\omega\cos^2(\omega\mathrm{t}) \tag{2.45}$$

$$\frac{d\rho_x}{dt} = \frac{m{v_\perp}^2}{qB^2}\mathrm{b}\cos^2(\omega\mathrm{t}) \tag{2.46}$$

Substitute (2.44) to (2.43),

$$\frac{d\rho_y}{dt} = \frac{mv_\perp}{qB^2}\mathrm{b}r_L\omega\sin(\omega\mathrm{t})\cos(\omega\mathrm{t}) \tag{2.47}$$

$$\frac{d\rho_y}{dt} = -\frac{m{v_\perp}^2}{qB^2}\mathrm{b}\sin(\omega\mathrm{t})\cos(\omega\mathrm{t}) \tag{2.48}$$

Average of $\frac{d\rho_x}{dt}$,

$$\langle\frac{d\rho_x}{dt}\rangle = \frac{1}{T}\int_0^T \frac{d\rho_x}{dt}\,dt = \frac{1}{T}\left(\frac{m{v_\perp}^2}{qB^2}\mathrm{b}\int_0^T \cos^2(\omega\mathrm{t})\,dt\right)$$

$$\langle\frac{d\rho_x}{dt}\rangle = \langle v_\mathrm{x}\rangle = \frac{\mu}{qB}\mathrm{b} \tag{2.49}$$

Average of $\frac{d\rho_y}{dt}$,

$$\langle\frac{d\rho_y}{dt}\rangle = \frac{1}{T}\int_0^T \frac{d\rho_x}{dt}\,dt = \frac{1}{T}\left(-\frac{m{v_\perp}^2}{qB^2}\mathrm{b}\int_0^T \sin(\omega\mathrm{t})\cos(\omega\mathrm{t})\,dt\right)$$

$$\langle\frac{d\rho_x}{dt}\rangle = 0 \tag{2.50}$$

For y-direction, equation of motion,

$$\mathrm{m}\frac{\mathrm{d}\langle v_\mathrm{y}\rangle}{\mathrm{dt}} = -\,\mathrm{q}\langle v_\mathrm{x}\rangle\,\mathrm{B} = -\,\mathrm{q}\left(\frac{\mu}{qB}\mathrm{b}\right)\mathrm{B} = -\mu\frac{dB}{dy} \tag{2.51}$$

For field change in x-direction,

With assumption that $\frac{\mathrm{dB}}{\mathrm{dt}} = 0$ and $\frac{\mathrm{dB}}{\mathrm{dx}} = \mathrm{b} = \mathrm{constant}$

$$B = B_0 + \mathrm{bx} \tag{2.52}$$

From (2.52) and (2.25),

$$B = B_0 + \mathrm{b}r_L \cos(\omega \mathrm{t}) \tag{2.53}$$

From (2.53), differential respect with t,

$$\frac{dB}{dt} = -\mathrm{b}r_L \omega \sin(\omega \mathrm{t}) \tag{2.54}$$

Substitute (2.54) to (2.41),

$$\frac{d\rho_x}{dt} = -\frac{mv_\perp}{qB^2}\mathrm{b}r_L \omega \sin(\omega \mathrm{t})\cos(\omega \mathrm{t}) \tag{2.55}$$

$$\frac{d\rho_x}{dt} = \frac{m{v_\perp}^2}{qB^2}\mathrm{b}\sin(\omega \mathrm{t})\cos(\omega \mathrm{t}) \tag{2.56}$$

Substitute (2.54) to (2.43),

$$\frac{d\rho_y}{dt} = \frac{mv_\perp}{qB^2}\mathrm{b}r_L \omega \sin^2(\omega \mathrm{t}) \tag{2.57}$$

$$\frac{d\rho_y}{dt} = -\frac{m{v_\perp}^2}{qB^2}\mathrm{b}\sin^2(\omega \mathrm{t}) \tag{2.58}$$

Average of $\frac{d\rho_x}{dt}$,

$$\left\langle \frac{d\rho_x}{dt} \right\rangle = \frac{1}{T}\int_0^T \frac{d\rho_x}{dt}\,dt = \frac{1}{T}\left(\frac{m{v_\perp}^2}{qB^2}\mathrm{b}\int_0^T \sin(\omega \mathrm{t})\cos(\omega \mathrm{t})\,dt\right)$$

$$\left\langle \frac{d\rho_x}{dt} \right\rangle = 0 \tag{2.59}$$

Average of $\frac{d\rho_y}{dt}$,

$$\left\langle \frac{d\rho_y}{dt} \right\rangle = \frac{1}{T}\int_0^T \frac{d\rho_x}{dt}\,dt = \frac{1}{T}\left(-\frac{m{v_\perp}^2}{qB^2}\mathrm{b}\int_0^T \sin^2(\omega \mathrm{t})\,dt\right)$$

$$\left\langle \frac{d\rho_y}{dt} \right\rangle = \langle v_\mathrm{y} \rangle = -\frac{\mu}{qB}\mathrm{b} \tag{2.60}$$

For x-direction, equation of motion,

$$\mathrm{m}\frac{\mathrm{d}\langle v_{\mathrm{x}}\rangle}{\mathrm{dt}} = \mathrm{q}\langle v_{\mathrm{y}}\rangle \mathrm{B} = -\mu\frac{dB}{dx} \tag{2.61}$$

Therefore,

$$\mathrm{m}\frac{\mathrm{d}v_{\mathrm{x}}}{\mathrm{dt}} = -\mu\frac{dB}{dx} \tag{2.62}$$

$$\mathrm{m}\frac{\mathrm{d}v_{\mathrm{y}}}{\mathrm{dt}} = -\mu\frac{dB}{dy} \tag{2.63}$$

From (2.21),

$$\mathrm{m}\frac{\mathrm{d}v_{\mathrm{z}}}{\mathrm{dt}} = -\mu\frac{dB}{dz}$$

In general solution,

$$\mathrm{m}\frac{\mathrm{d}\boldsymbol{v}}{\mathrm{dt}} = -\mu\nabla\boldsymbol{B} \tag{2.64}$$

And $\dot{\boldsymbol{v}} = \ddot{\boldsymbol{S}}$, from (2.64)

Gyration at the center can be defined as

$$\mathrm{m}\ddot{\boldsymbol{S}} = -\mu\nabla\boldsymbol{B} \tag{2.65}$$

Therefore, Characteristic of the magnetic confinement of the ECRIS can be described as the magnetic mirror field effect. In general, the motion of the gyration center is dominated by the drift force written at,

$$\boldsymbol{F}_{\parallel} = -\mu\left(\frac{\partial B}{\partial \boldsymbol{s}}\right) = -\mu\nabla_{\parallel}\boldsymbol{B} \tag{2.66}$$

where $d\boldsymbol{s}$ is a line element along $\boldsymbol{B}$. The above equation means that the forces affect the charged particle from stronger $\boldsymbol{B}$ to weaker $\boldsymbol{B}$.

The magnetic moment of gyrating particle is defined by

$$\mu = \frac{1}{2}\frac{m{v_{\perp}}^2}{B} \tag{2.67}$$

It is known that the above magnetic moment μ is a constant of motion as described below

$$\therefore\ \frac{d\mu}{dt} = 0 \tag{2.68}$$

2.2.2.1.1 Invariant of μ

There is an important law saying that μ remains invariant during the particle motion as shown below.

$$m\frac{dv_{\parallel}}{dt} = -\mu\frac{\partial B}{\partial s}$$

Multiplying by $v_{\parallel}$ on the both sides,

$$mv_{\parallel}\frac{dv_{\parallel}}{dt} = -\mu\frac{\partial B}{\partial s}\frac{ds}{dt}$$

$$\frac{d}{dt}\left(\frac{1}{2}m{v_{\parallel}}^2\right) = -\mu\frac{\partial B}{\partial t} \tag{2.69}$$

The magnetic moment of gyrating particle is defined by

$$\mu = \frac{1}{2}\frac{m{v_{\perp}}^2}{B} \tag{2.70}$$

According to the energy conservation law and (2.79),

$$\frac{d}{dt}\left(\frac{1}{2}m{v_{\parallel}}^2 + \frac{1}{2}m{v_{\perp}}^2\right) = \frac{d}{dt}\left(\frac{1}{2}m{v_{\parallel}}^2 + \mu B\right) = 0 \tag{2.71}$$

From (2.69) and (2.71), we can proof that the μ is invariant as:

$$-\mu\frac{dB}{dt} + \frac{d}{dt}(\mu B) = 0$$

$$-\mu\frac{dB}{dt} + \mu\frac{dB}{dt} + B\frac{d\mu}{dt} = 0$$

As a particle moves into a stronger field region in the course of its thermal motion, it sees an increasing *B*. Therefore,$v_{\perp}$ must increase in order to keep μ constant. On the other hand, $v_{\parallel}$ must decrease according to the energy conservation law. The $v_{\parallel}$ becomes zero at the location where *B* is enough high, and the force $\boldsymbol{F}_{\parallel}$ reflects the particle back to the weaker field region. As the result, a plasma electron can be trapped in non-uniform field which is formed by a simple pair of coils as shown in Fig. 2.2.2.1.1a.

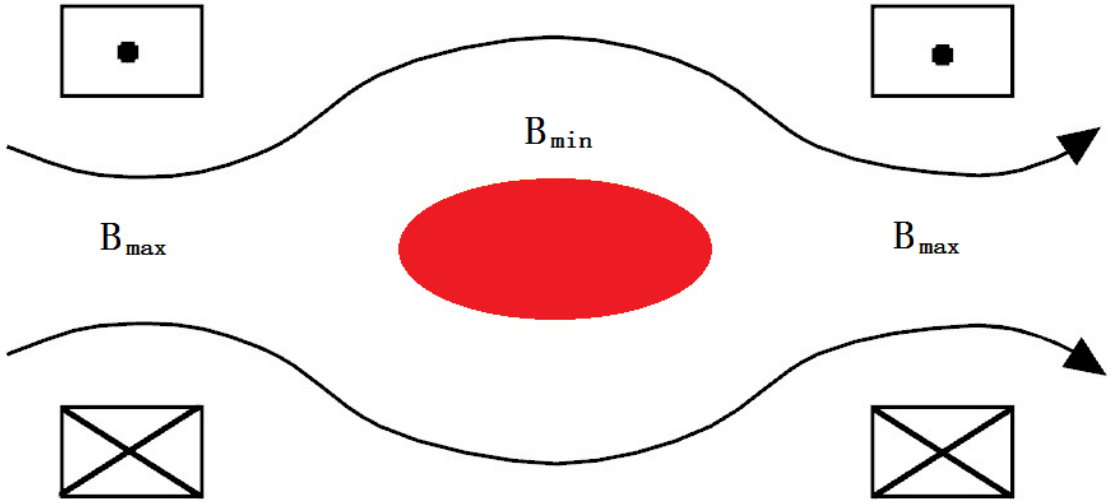

Figure 2.2.2.1.1a: Plasma trapped at the magnetic mirrors

However, trapping is not perfect. For instance, a particle with $v_\perp = 0$ will have not a magnetic moment and will not feel any force along $\boldsymbol{B}$. A particle with small $v_\perp/v_\parallel$ at the midplane where $B = B_{min}$ will escape if the maximum field B_{max} is not large enough.

As a matter of fact, a particle with $v_\perp = v_{\perp 0}$ and $v_\parallel = v_{\parallel \mathbf{0}}$ at the midplane will have $v_\perp = v'_\perp$ and $v_\parallel = 0$ at its turning point. The magnetic field at the turning point is B'.

The invariance of μ yields,

$$\frac{1}{2}\frac{m{v_{\perp 0}}^2}{B_{min}} = \frac{1}{2}\frac{m{v'_\perp}^2}{B'} \tag{2.72}$$

The energy conservation law requires,

$$\frac{1}{2}m{v_{\perp 0}}^2 + \frac{1}{2}m{v_{\parallel 0}}^2 = \frac{1}{2}m{v'_\perp}^2$$

$$\therefore \quad {v'_\perp}^2 = {v_{\perp 0}}^2 + {v_{\parallel 0}}^2 = {v_0}^2 \tag{2.73}$$

From the (2.72) and (2.73),

$$\frac{B_{min}}{B'} = \frac{{v_{\perp 0}}^2}{{v'_\perp}^2} = \frac{{v_{\perp 0}}^2}{{v_0}^2} \equiv \sin^2\theta \tag{2.74}$$

where θ is called the pitch angle of the orbit in the midplane (weak-field region).

The above equation means that a particle with smaller θ will reflect in the regions of B' higher than B_{min}, and in the case where B' exceeds B_{max} due to too small θ, the particle is

reflected at all. Replacing B' by B_{max} in the equation (2.74), the smallest θ of a confined particle is obtained in the following equation,

$$sin^2\,\theta_m = \frac{B_{min}}{B_{max}} = \frac{1}{R_m} \tag{2.75}$$

Here, R_m is called the "mirror ratio".

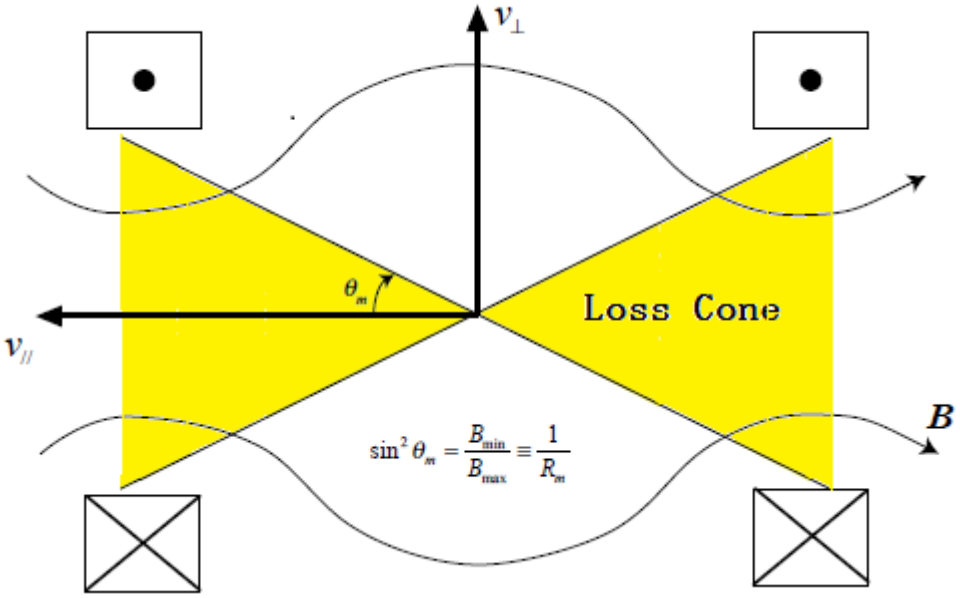

Figure 2.2.2.1.1b: Loss cone in a velocity space

Equation (2.75) defines the boundary of a region in the velocity space in the shape of a cone, which is called as a 'loss cone' as shown is Fig. 2.2.2.1.1b. Particles lying within the loss cone (yellow region) are not confined. Note that the loss cone is independent of charge and mass. If there occurs no collision, particles outside the loss cone are well confined. When a particle is scattered by-collision into the loss cone, it is lost. For better plasma confinement, we need to reduce the probability that particles escape into the loss cone. Therefore, a higher mirror ratio is desirable.

2.2.3 Ionization Process

In a standard ECRIS, the charge multiplication of an ion is caused by a three dominant processes as [1, 9]:

a) Electron impact ionization,
b) Charge exchange with neutrals (even ions) and
c) Diffusion or transport of ions

The probability of highly charged ion production by a single electron impact falls off rapidly with increasing charge state of the ion. Therefore, the only efficient way to obtain a reasonable yield of highly charged ions is successive ionization. The multi-ionization processes for the temporal evolution of ion species in the plasma can be described by rate equations [3, 11] as:

$$\frac{dn_q}{dt} = n_{q-1}n_e < \sigma_{q-1\to q}{}^{ionis} v >_e + n_0 n_{q+1} < \sigma_{q+1\to q}{}^{ex} v >_i - n_q n_e < \sigma_{q\to q+1}{}^{ionis} v >_e - n_0 n_q < \sigma_{q\to q-1}{}^{ex} v >_i - \frac{n_q}{\tau_q} \quad (2.76)$$

Here,

n_q = Ion density of charge state q

n_e = Electron density

$\sigma_{q-1\to q}{}^{ionis}$ = The cross section for the eletron impact inonization from charge state $q-1$ to q

n_0 = Neural atom density

$\sigma_{q+1\to q}{}^{ex}$ = The charge exchange cross section: probability for an ion with charge state $q+1$ to capture an electron from a neutral atom and to be reduce to charge state q

$\frac{n_q}{\tau_q}$ =An empirical term to take account the time of confinement τ_q of an ion in the plasma

$< >_e$ =Mean electron velocity

$< >_i$ = Mean ion velocity

The positive terms in the sum are associated with creation of ions with charge state q, while the negative terms correspond to ion destruction. The first four terms stand for the creation term of charge state q through ionization of charge state ($q-1$), charge exchange of charge state ($q+1$) with neutrals, the loss term thorough ionization towards to charge state ($q+1$) and charge exchange with neutrals of charge state q respectively. The last term corresponds to diffusion outside the plasma.

2.2.3.1 Electron impact ionization

When an energetic electron crosses an atom or a charged ion, it can kick out a shell electron orbiting around the nucleus as:

$$e^- + A^{i+} \to e^- + e^- + A^{(i+1)+}$$

This is the main process to ionize atoms. This reaction is possible above a threshold energy P_i corresponding to the binding energy of the i^{th} electron in the atom. The ionization cross section σ can be estimated using the Lotz formula [12] written by

$$\sigma_{i\to i+1} \sim \frac{ln\left(\frac{T_e}{P_{i+1}}\right)}{T_e P_{i+1}}$$

where,

$T_e =$ Energy of the eletron and

$P_{i+1} =$ Binding energy of the electron at $(i+1)$th subshell

Fig. 2.2.3.1a [13] shows the experimental data of the cross section with T_e for hydrogen. One can see that a maximum of ionisation probability is given at $T_e \sim$ 2-3 P_{i+1}.

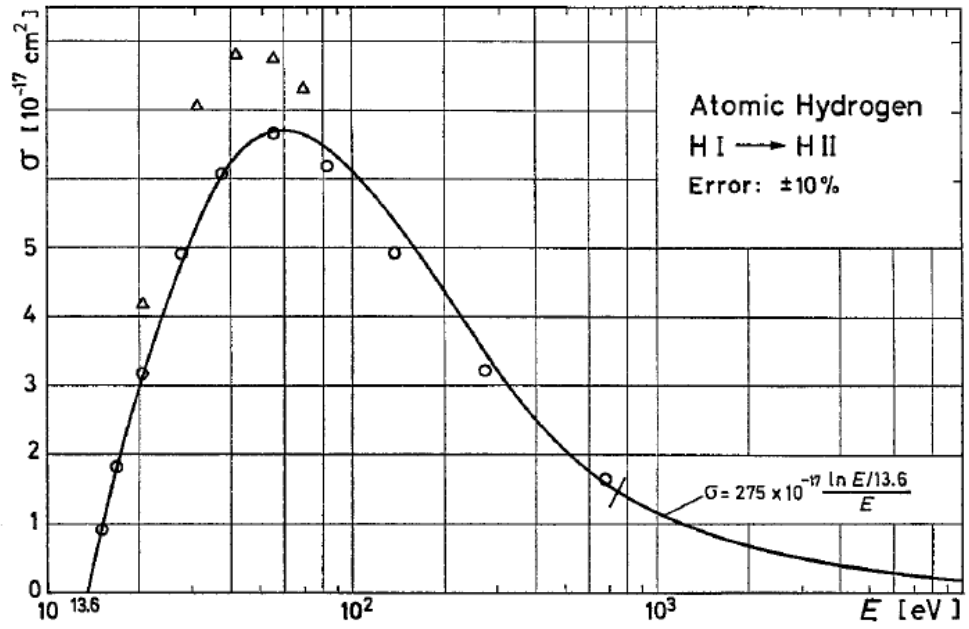

Figure 2.2.3.1a: Example of the electron impact cross section with the electron energy for hydrogen [13]

It is important to note that the electron impact cross section decreases with the increment of the charge-state of the ion. Furthermore, the energy required to ionize high charge state ions increases with the charge-state, following the increment of binding energy of the inner shell electrons. The binding energy is plotted in Fig. 2.2.3.1b [1] as a function of the atom charge state Z.

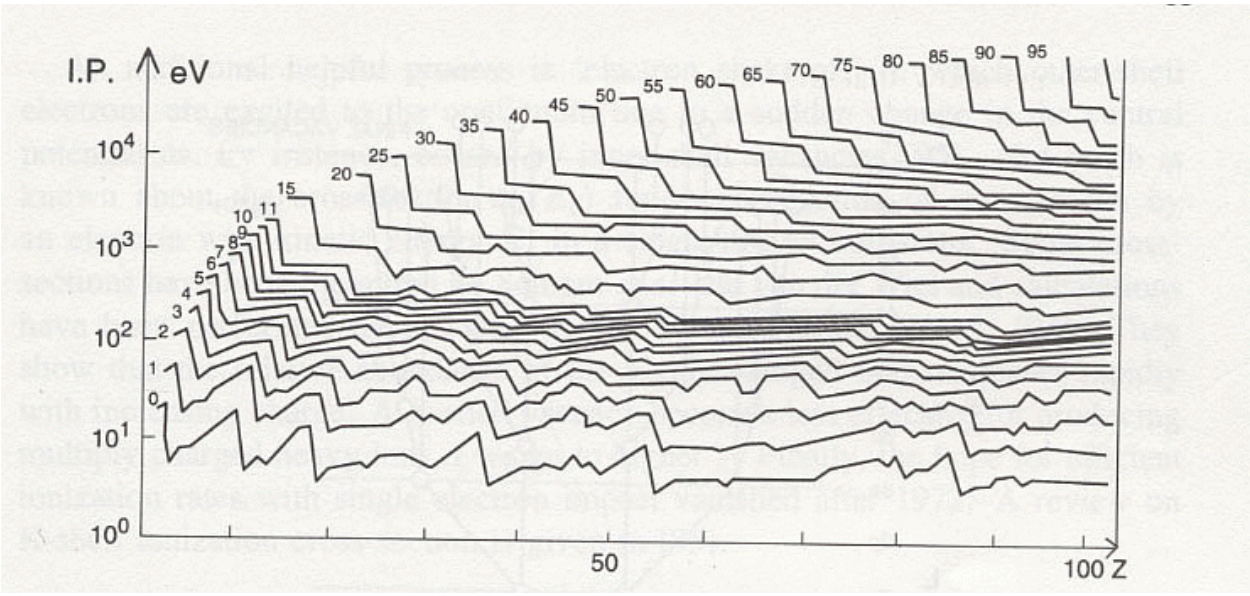

Figure 2.2.3.1b: Ionization potentials of elements [1]

2.2.4.1 Charge exchange

When an atom passes close to an ion, an electron of the atom is attracted by the ion electric field and finally captured by the ion. This phenomenon often balances electron impact ionisation in a plasma.

$$A^0 + B^{i+} \rightarrow A^{1+} + B^{(i-1)+}$$

The cross section associated with charge exchange is very large and this phenomenon is dominant at high pressure in partially ionized plasmas. Several semi-empirical formulas can be used to estimate the charge exchange process. For instance, from Ref. 14:

$$\sigma_{ce(i \rightarrow i-1)} \approx 1.43 \times 10^{-12} . i^{1.17} . {I_0}^{-2.76} [cm^2]$$

Where,

$I_0 =$ Ionization potential of the atom in eV and

$i =$ Initial ion charge state of i

2.2.4 Ion Extraction

In the previous sections, I had described how the multi-charged ions are produced in the ECRIS plasma. Now let have a look: how ions are extracted toward the accelerator.

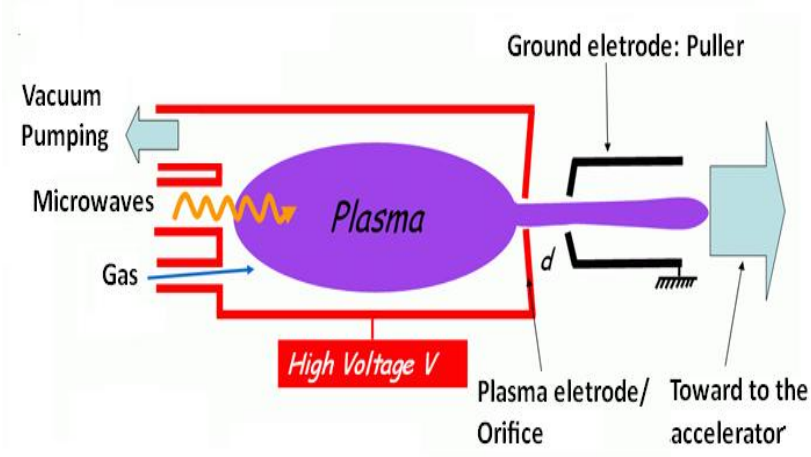

Figure 2.2.4a: Ion extraction in an ECRIS

On the extraction side of Fig. 2.2.4a, the plasma chamber is closed by the plasma electrode, where a small circular hole with a diameter of few mm is open. The whole plasma chamber is set to a high voltage, typically in the range few tens kV. In front of the plasma electrode is placed a ground electrode, frequently named as a "puller". Therefore, an electric field is induced between two electrodes, separated by a distance *d*. The electric field extracts ions from the edge of the plasma.

2.2.4.1 Langmuir-Child law

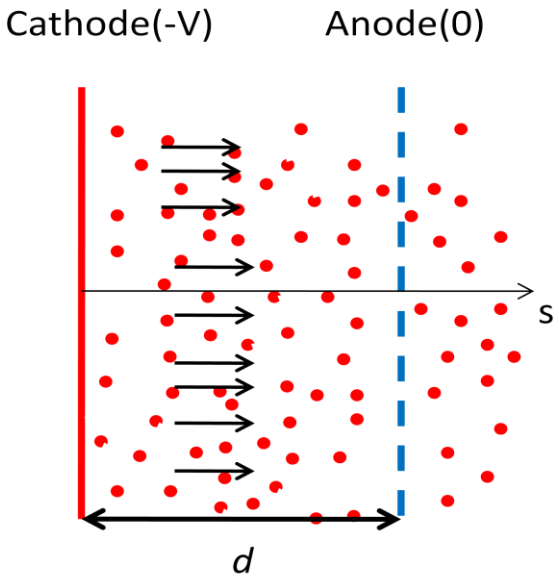

Figure 2.2.4.1a: Particles are extracted between the electrodes with a distance of d

The well-known Langmuir-Child law suggested that when the extracted ions current increases, the concentration of ion charge around the extraction electrode becomes non-negligible and create electric fields that disrupt the externally applied primary electric fields [10]. The Langmuir-Child law gives the maximum current or so-called space-charge limited current that can be extracted by the external electric fields before the ion induced electric fields totally compensate the primary external electric fields. According to the Langmuir-Child law, ion current density can be expressed by:

Here,

$$J = \ Current\ density, v = \ \text{Particle velocity}, n = Particle\ density,$$

$$\phi = Potential\ and\ E = Electric\ field$$

$$J = qnv$$

For electron charge, $(q = -e)$

$$J = -env \tag{2.77}$$

$$E = -\frac{d\phi}{dx}$$

$$m\frac{dv}{dt} = -e\mathrm{E}$$

$$mv\frac{dv}{dx} = -e\mathrm{E}$$

$$m\frac{d}{dx}\left(\frac{1}{2}v^2\right) = e\frac{d\phi}{dx} \tag{2.78}$$

By integration of (2.78) with $x = 0\ and\ \phi = -V$

$$v = \sqrt{\frac{2e}{m}[\phi + V]} \tag{2.79}$$

From Poisson equation,

$$\frac{d^2\phi}{dx^2} = -\frac{\rho}{\epsilon_0} = \frac{en}{\epsilon_0} \tag{2.80}$$

Substitute (2.79) to (2.77),

$$en = J\sqrt{\frac{m}{2e[\phi + V]}} \tag{2.81}$$

Substitute (2.81) to (2.80),

$$\frac{d^2\phi}{dx^2} = \frac{J}{\epsilon_0}\sqrt{\frac{m}{2e[\phi + V]}} \tag{2.82}$$

In general, J depends on x, but becomes constant at space charge limit. At the space charge limit, charge density becomes constant. ->dρ/dt=0 Hence, J becomes x-independent from the equation of continuity.

From (2.82) multiply by $d\phi/dx$,

$$\frac{d^2\phi}{dx^2} \times \frac{d\phi}{dx} = \frac{J}{\epsilon_0}\sqrt{\frac{m}{2e[\phi + V]}} \times \frac{d\phi}{dx}$$

$$\frac{d}{dx}\left[\frac{1}{2}\left[\frac{d\phi}{dx}\right]^2\right] = \frac{J}{\epsilon_0}\sqrt{\frac{m}{2e}} \times \frac{d}{dx}\left[\frac{(\phi + V)^{1/2}}{\frac{1}{2}}\right] \tag{2.83}$$

From (2.83), as given with $x = 0$, $\phi(0) = -V and\ \phi(\mathrm{d}) = 0$,

$$\left[\frac{1}{2}\left[\frac{d\phi}{dx}\right]^2\right]_0^{\phi} = \frac{2J}{\epsilon_0}\sqrt{\frac{m}{2e}} \times \left[(\phi + V)^{1/2}\right]_0^{\phi}$$

$$\left[\frac{d\phi}{dx}\right]^2 - \left[\frac{d\phi(0)}{dx}\right]^2 = \frac{4J}{\epsilon_0}\sqrt{\frac{m}{2e}} \times \left[(\phi + V)^{1/2} - (\phi(0) + V)^{1/2}\right]$$

$$\left[\frac{d\phi}{dx}\right]^2 - \left[\frac{d\phi(0)}{dx}\right]^2 = \frac{4J}{\epsilon_0}\sqrt{\frac{m}{2e}} \times \left[(\phi + V)^{1/2}\right] \tag{2.84}$$

And for the space-charge limitation condition, $\mathrm{E} = 0\ and\ \ d\phi(0)/dx = 0$,

From (2.84),

$$\left[\frac{d\phi}{dx}\right]^2 = \frac{4J}{\epsilon_0}\sqrt{\frac{m}{2e}} \times \left[(\phi + V)^{1/2}\right]$$

$$\left[\frac{d\phi}{dx}\right] = 2\sqrt{\frac{J}{\epsilon_0}}\left(\frac{m}{2e}\right)^{1/4} \times (\phi + V)^{1/4}$$

$$\left[\frac{d\phi}{(\phi+V)^{1/4}}\right] = 2\sqrt{\frac{J}{\epsilon_0}}\left(\frac{m}{2e}\right)^{1/4} dx$$

$$\int_{-V}^{0} \frac{d\phi}{(\phi+V)} = 2\sqrt{\frac{J}{\epsilon_0}}\left(\frac{m}{2e}\right)^{1/4} \int_{0}^{d} dx$$

$$\left[\frac{4}{3}(V)^{3/4}\right] = 2\sqrt{\frac{J}{\epsilon_0}}\left(\frac{m}{2e}\right)^{1/4} d$$

Space-charge limited current can be express as :

$$J = \left[\frac{4}{9}\epsilon_0\left(\frac{2e}{m}\right)^{1/2}\left(\frac{V^{3/2}}{d^2}\right)\right] \quad (2.85)$$

where,

$m_N =$ Atomic mass unit, $V =$ Extraction voltage, $e =$ electron charge,

$A =$ Ion mass number, $\epsilon_0 =$ Permitivity of vacuum and $d =$ Extraction gap

This formulation is only available for single charge state ion.

References

[1] R. Geller, Electron Cyclotron Resonance Ion Sources and ECR Plasma, Institute of Physics Publishing, London (1996), ISBN 0740301074.

[2] T. Nakagawa, J. Arje, Y. Miyazawa, M. Hemmi, T. Chiba, N. Inab, M. Kase, T. Kageyamaa, 0. Kamigaito, A. Gotoa, M.G. Niimura, Y. Yanoa, *Nucl. Inst. Meth. In Phys. Research A* **396** (1997) p.9-12.

[3] D. Leitner , C.M. Lyneis, S.R. Abbott, D. Collins, R.D. Dwinell, M.L. Galloway, M. Leitner, D.S. Todd, *Nucl. Inst. Meth. In Phys. Research B* **235** (2005) p.486-493.

[4] L T Sun, H W Zhao, X H Guo, X Z Zhang, Z M Zhang, P Yuan, W L Zhan, B W Wei, X H Cai, J Y Li, Y C Feng, W He, Y Cao, M T Song, X X Li, H Wang, B H Ma, W Lu and T Jin, Journal of Physics: Conference Series 58 (2007) 435–438.

[5] S. Gammino, G. Ciavola, and L. Celona, D. Hitz, A. Girard, and G. Melin, Rev. Sci. Instrum. **72**, 11 (2001).

[6] A. G. Drentje, Rev. Sci. Instrum. **74**, 5 (2003).

[7] H. W. Zhao, *Proceeding of IPAC10*, May 23rd-28th, 2010 Kyoto, Japan, MOZMH02 (2010).

[8] Francis F. Chen, Introduction to Plasma Physics and Controlled Fusion Volume 1: Plasma Physics (1984) Plenum Press, New York, ISBN 0-306-41332-9.

[9] G. Melin, A. G. Drentje, A. Girard, and D. Hitz, J. Appl. Phys., **86,** 9 (1999).

[10] I.G. Brown, The Physics and Technology of Ion Sources (2nd Edition), John Wiley & Sons, (2004), ISBN 3-527-40410-4.

Appendix 3

Faraday Cup Model

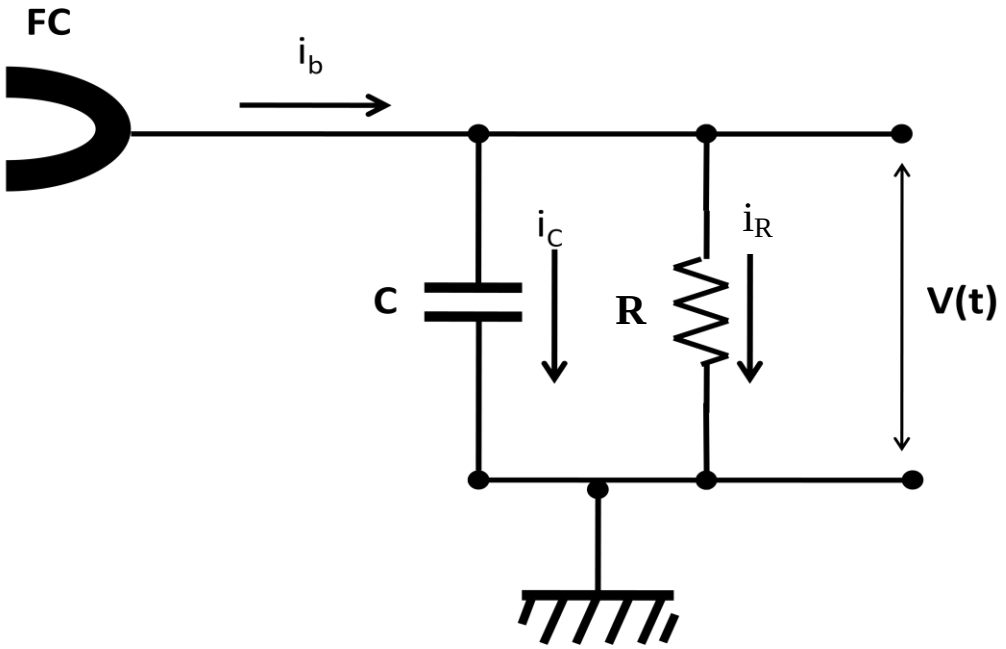

Figure 3.1: FC measurement circuit

Here,

$$c = \ Stary\ capacitor\ (173pF), R = Calibarationresistor(1\ k\Omega),$$

$$i_b = Ion\ beam\ current, i_c = Current\ flow\ through\ capacitor$$

$$and\ \ i_R = Current\ flow\ through\ resistor$$

The equivalent circuit of ion beam current measurement with FC as shown in Fig. 3.1:

$$i_b = i_c + i_R \tag{3.1}$$

$$Q = CV\ and\ i_c = \frac{dQ}{dt} = C\frac{dV_c}{dt} \tag{3.2}$$

From (3.2),

$$V_c = \frac{1}{C}\int_0^t i_c dt \tag{3.3}$$

$$V_R = i_R R \tag{3.4}$$

$$V(t) = V_R = V_c \tag{3.5}$$

Substitute (3.3) and (3.4) into (3.5),

$$i_R R = \frac{1}{C}\int_0^t i_c dt \tag{3.7}$$

Substitute (3.1) into (3.6),

$$i_R R = \frac{1}{C}\int_0^t (i_b - i_R) dt \tag{3.7}$$

Differential both side with respect with t,

$$\frac{di_R}{dt} = \frac{1}{RC}(i_b - i_R) \tag{3.8}$$

$$\frac{di_R}{dt} + \frac{i_R}{RC} = \frac{i_b}{RC} \tag{3.9}$$

Try to solve the 1st order inhomogeneous differential equation:

Assume the right side is 0,

$$\frac{di_R}{dt} + \frac{i_R}{RC} = 0 \tag{3.10}$$

$$\frac{di_R}{i_R} = -\frac{1}{RC} dt \tag{3.11}$$

$$[\ln i_R]_A^{i_R} = -\frac{t}{RC} \tag{3.12}$$

$$i_R = Ae^{-t/RC} \tag{3.13}$$

Here,

A $= Assumed\ to\ be\ dependent\ on\ time$

Differential (3.13),

$$\frac{di_R}{dt} = \frac{dA}{dt}\left(e^{-t/RC}\right) - \frac{A}{RC}\left(e^{-t/RC}\right) \tag{3.14}$$

Substitute (3.13) and (3.14) into (3.9),

$$\frac{dA}{dt}\left(e^{-t/RC}\right) - \frac{A}{RC}\left(e^{-t/RC}\right) + \frac{A}{RC}e^{-t/RC} = \frac{i_b}{RC} \tag{3.15}$$

$$\frac{dA}{dt}\left(e^{-t/RC}\right) = \frac{i_b}{RC} \tag{3.16}$$

$$A = \int_0^t \frac{i_b}{RC}\left(e^{t/RC}\right) dt \tag{3.17}$$

Substitute (3.17) into (3.13),

$$i_R = \left\{\int_0^t \frac{i_b}{RC}\left(e^{t'/RC}\right) dt'\right\}\left\{e^{-t/RC}\right\} \tag{3.18}$$

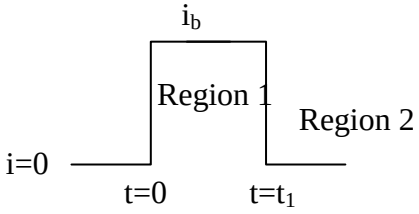

From (3.18) and refer to the figure as above:

For $t<t_1$, i_b=Constant (Region 1)

$$i_R = \left\{\int_0^t \frac{i_b}{RC}\left(e^{t'/RC}\right) dt'\right\}\left\{e^{-t/RC}\right\} \tag{3.19}$$

$$i_{R1}(t) = i_b(1 - e^{-t/RC}) \tag{3.20}$$

For $t>t_1$, i_b=0 (Region 2)

$$i_R = \left\{\int_0^t \frac{i_b}{RC}\left(e^{t'/RC}\right) dt'\right\}\left\{e^{-t/RC}\right\} \tag{3.21}$$

$$i_R = \left\{\int_0^{t1} \frac{i_b}{RC}\left(e^{t'/RC}\right) dt'\right\}\left\{e^{-t/RC}\right\} + \left\{\int_{t1}^t \frac{i_b}{RC}\left(e^{t'/RC}\right) dt'\right\}\left\{e^{-t/RC}\right\} \tag{3.22}$$

$$i_{R2}(t) = i_b(e^{t'/RC} - 1)\, e^{-t/RC} \tag{3.23}$$

Appendix 4

Initial Plane Formulation

The one-dimensional Maxwell-Boltzmann distribution,

$$f(E)dE \propto e^{(-E/kT)}dE \tag{4.1}$$

Here,

$$E = Kinetic\ energy\ , k = Boltmann's\ constant,$$
$$T = Temperature,$$
$$E = \frac{P^2}{2m} \tag{4.2}$$

$$dE = \frac{p}{m}dp \tag{4.3}$$

From (4.2) , (4.3) and (4.1),

$$e^{(-E/2kT)}dE = e^{(-p^2/2mkT)}\left(\frac{p}{m}\right)dp$$

$$f(p) \propto \left(\frac{p}{m}\right)e^{(-p^2/2mkT)} \tag{4.4}$$

$$F(p) = \int_0^p f(p)\,dp = \int_0^p \left(\frac{p}{m}\right)e^{(-p^2/2mkT)}\,dp \tag{4.5}$$
$$= \left[-kTe^{(-p^2/2mkT)}\right]_0^p = KT\left[1 - e^{(-p^2/2mkT)}\right]$$

Normalized,

$$F(\infty) = 1 \tag{4.6}$$

$$f(p) \to \mathrm{C}f(p), \qquad \mathrm{C} = some\ factor \tag{4.7}$$

$$\mathrm{C}\int_0^\infty f(p)\,dp = \mathrm{C}kT = kT\ where\ e^{-\infty} = vanish \tag{4.8}$$

Normalized integration function,

$$F(p) = 1 - e^{(-p^2/2mkT)} \tag{4.9}$$

$0 \leq u < 1$,

$$u_1 = 1 - e^{(-p^2/2mkT)} \tag{4.10}$$

$$\ln(1 - u_1) = -\frac{p^2}{2mkT} \tag{4.11}$$

$$p = \sqrt{-2mkT \ln(1 - u_1)} \tag{4.12}$$

Momentum direction,

$$\text{Solid Angle, } d\Omega = \frac{ds}{r^2} \tag{4.13}$$

$$d\Omega = d\varphi|\mathrm{d}(\cos\theta)| \text{ for polar coordinate system} \tag{4.14}$$

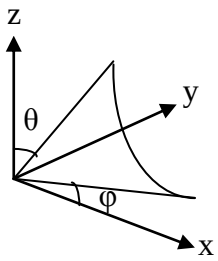

$$f(\theta, \varphi) d\varphi d\theta = 1 d\Omega \tag{4.15}$$

$$= d\varphi d(\cos\theta) \tag{4.16}$$

$$= d\varphi \sin\theta \, d\theta = 1 \tag{4.17}$$

$$\varphi = 2\pi u_1 \tag{4.18}$$

$$F(0 \le \theta < \pi) = C \int_0^{\pi} |\sin\theta \, d\theta| = 1 \tag{4.19}$$

$$[-\cos\theta]_0^{\pi} = 2C = 1, C = \frac{1}{2} \tag{4.20}$$

$$F(0 \le \theta < \theta) = C \int_0^{\theta} \sin\theta \, d\theta = u_2 \tag{4.21}$$

$$\frac{1}{2}[1 - \cos\theta] = u_2 \tag{4.22}$$

$$\theta = \cos^{-1}(1 - 2u_2) \tag{4.23}$$

Here,

$u_1, u_2, u_3 =$ Random number from 0 to 1

Appendix 5

Formulation of the Electric Field in the Einzel Lens Region

From the 1st Maxwell equation:

$$\nabla . \boldsymbol{E} = \frac{\rho}{\varepsilon} \tag{5.1}$$

Where ρ = charge density and ε=permittivity of the vacuum

According to the potential gradient as:

$$\boldsymbol{E} = -\nabla \emptyset \tag{5.2}$$

Therefore, from (5.2) and (5.1)

$$\nabla . \boldsymbol{E} = -\nabla . (\nabla \emptyset)$$

$$\nabla^2 V = -\frac{\rho}{\varepsilon} \tag{5.3}$$

(5.3) is Poisson equation. At the point in space where the charge density is zero, ρ=0;

$$\text{Laplace equation}, \nabla^2 \emptyset = 0 \tag{5.4}$$

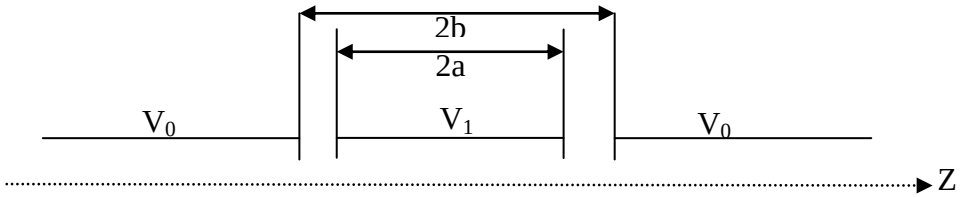

Assumed that the cylindrical is very long and axisymmetric. Laplace's equation in cylindrical coordinate can be written as:

$$\nabla^2 \emptyset = \frac{1}{r}\frac{\partial}{\partial r}\left(r\frac{\partial \emptyset}{\partial r}\right) + \frac{1}{r^2}\frac{\partial^2 \emptyset}{\partial \theta^2} + \frac{\partial \emptyset}{\partial z} = 0 \tag{5.5}$$

For azimuthal -axis, which can be assumed as axisymmetric,

$$\frac{\partial}{\partial \theta} = 0 \tag{5.6}$$

(5.6) into (5.5),

$$\nabla^2 \emptyset = \frac{1}{r}\frac{\partial}{\partial r}\left(r\frac{\partial \emptyset}{\partial r}\right) + \frac{\partial^2 \emptyset}{\partial z^2} = 0 \tag{5.7}$$

$$\nabla^2 \emptyset = \frac{1}{r}\left(\frac{\partial \emptyset}{\partial r}\right) + \frac{\partial^2 \emptyset}{\partial r^2} + \frac{\partial^2 \emptyset}{\partial z^2} = 0 \tag{5.8}$$

By using the method of separation of variables by assuming the solution for (6.7) as in the form:

$$\emptyset(r,z) = \boldsymbol{R}(r)\boldsymbol{Z}(z) \tag{5.9}$$

From (5.9), Z is independent

$$\frac{\partial \emptyset}{\partial r} = \boldsymbol{Z}(z)\frac{\partial \boldsymbol{R}(r)}{\partial r} \tag{5.10}$$

$$\frac{\partial^2 \emptyset}{\partial r^2} = \boldsymbol{Z}(z)\frac{\partial^2 \boldsymbol{R}(r)}{\partial r^2} \tag{5.11}$$

From (5.9), r is independent

$$\frac{\partial \emptyset}{\partial z} = \boldsymbol{R}(r)\frac{\partial \boldsymbol{Z}(z)}{\partial z} \tag{5.12}$$

$$\frac{\partial^2 \emptyset}{\partial z^2} = \boldsymbol{R}(r)\frac{\partial^2 \boldsymbol{Z}(z)}{\partial z^2} \tag{5.13}$$

(5.10), (5.11), (5.12) and (5.13) into (5.8),

$$\frac{1}{r}\left(\boldsymbol{Z}(z)\frac{\partial \boldsymbol{R}(r)}{\partial r}\right) + \boldsymbol{Z}(z)\frac{\partial^2 \boldsymbol{R}(r)}{\partial r^2} + \boldsymbol{R}(r)\frac{\partial^2 \boldsymbol{Z}(z)}{\partial z^2} = 0 \tag{5.14}$$

Divided (5.14) by $\boldsymbol{R}(r)\boldsymbol{Z}(z)$,

$$\frac{1}{r}\left(\frac{\mathbf{1}}{\boldsymbol{R}(r)}\frac{\partial \boldsymbol{R}(r)}{\partial r}\right) + \frac{\mathbf{1}}{\boldsymbol{R}(r)}\frac{\partial^2 \boldsymbol{R}(r)}{\partial r^2} + \frac{\mathbf{1}}{\boldsymbol{Z}(z)}\frac{\partial^2 \boldsymbol{Z}(z)}{\partial z^2} = 0 \tag{5.15}$$

Simplified by $\boldsymbol{R}(r) = R, \boldsymbol{Z}(z) = Z$,

Separating Z term from (5.15),

$$\frac{1}{r}\left(\frac{1}{R}\frac{\partial R}{\partial r}\right) + \frac{1}{R}\frac{\partial^2 R}{\partial r^2} = -\frac{1}{Z}\frac{\partial^2 Z}{\partial z^2} \tag{5.16}$$

(5.16) only can be satisfied for all values if both sides are equal to a constant as:

$$\lambda = constant$$

$$-\frac{1}{Z}\frac{\partial^2 Z}{\partial z^2} = \lambda^2 \tag{5.17}$$

Also ,

$$\frac{1}{r}\left(\frac{1}{R}\frac{\partial R}{\partial r}\right) + \frac{1}{R}\frac{\partial^2 R}{\partial r^2} = \lambda^2$$

$$\frac{r}{R}\left(\frac{1}{R}\frac{\partial R}{\partial r}\right)+\frac{r^2}{R}\frac{\partial^2 R}{\partial r^2}-\lambda^2 r^2=0 \tag{5.18}$$

Solution for (5.17) is,

$$\frac{\partial^2 Z}{\partial z^2}+z\lambda^2=0$$

$$\boldsymbol{Z}(z)=A_1 e^{i\lambda z}+A_2 e^{-i\lambda z} \tag{5.19}$$

$$Where\ A_1\ \&\ A_2\ are\ arbitrary\ constant$$

$$\sin\lambda z=\frac{e^{i\lambda z}-e^{-i\lambda z}}{2i} \tag{5.20}$$

$$\cos\lambda z=\frac{e^{i\lambda z}+e^{-i\lambda z}}{2} \tag{5.21}$$

$$\boldsymbol{Z}(z)=A_1\sin(\lambda z)+A_2\cos(\lambda z) \tag{5.22}$$

Assumed that axis-symmetry at Z=0,

$$\boldsymbol{Z}(z)=A_2\cos(\lambda z) \tag{5.23}$$

Solution for (5.18) is,

$$\frac{r}{R}\left(\frac{1}{R}\frac{\partial R}{\partial r}\right)+\frac{r^2}{R}\frac{\partial^2 R}{\partial r^2}-\lambda^2 r^2=0$$

Solution by modified Bessel function, $\mathbf{I}_0$, $\mathbf{K}_0$

In our case, $0\leq r<\infty$,

For $\mathbf{I}_0(r=0)<\infty$ and $\mathbf{K}_0(r=0)=\infty$

Therefore, R dependent on $\mathbf{I}_0$

$$\boldsymbol{R}(r)=B_1 I_0(\lambda r), B_1=constant \tag{5.24}$$

Combination of both solutions,

$$\boldsymbol{Z}(z)=A_2\cos(\lambda z)\quad \text{and}\quad \boldsymbol{R}(r)=B_1 I_0(\lambda r)$$

$$\emptyset(r,z)=C_1\cos(\lambda z)\,I_0(\lambda r)\quad ,\quad C_1=constant \tag{5.25}$$

General solution,

$$\emptyset_{general}=\int_0^\infty A(\lambda)\cos(\lambda z)\,I_0(\lambda r)\,d\lambda \tag{5.26}$$

Boundary condition,

$$At\ r = r_0, I_0(\lambda r) = constant$$

r=r_0 ——————————————————

r=0 ……

From (5.26),

$$\emptyset(r,z) = \int_0^\infty A\,(\lambda)\cos(\lambda z)\; I_0(\lambda r)d\lambda$$

With $r = r_0, I_0(\lambda r) = I_0(\lambda r_0)$

$$\emptyset(r_0,z) = \int_0^\infty A\,(\lambda)\cos(\lambda z)\; I_0(\lambda r_0)d\lambda \tag{5.27}$$

Multiply (5.27) both sides with $\int_{-\infty}^{\infty}\cos(\lambda' z)\;dz$,

$$\int_{-\infty}^{\infty}\emptyset(r_0,z)\cos(\lambda' z)\;dz = \int_{-\infty}^{\infty}\int_0^\infty A(\lambda)\;I_0(\lambda r_0)\cos\,(\lambda z)\;\cos(\lambda' z)\;d\lambda dz$$

$$\int_{-\infty}^{\infty}\emptyset(r_0,z)\cos\left(\lambda^{'} z\right)\;dz \tag{5.28}$$

$$= \int_0^\infty [A(\lambda)I_0(\lambda r_0)\int_{-\infty}^{\infty}\cos(\lambda z)\cos\left(\lambda^{'} z\right)dz]d\lambda)$$

For dz,

$$\int_{-\infty}^{\infty}\cos(\lambda z)\cos(\lambda' z)\;dz = \frac{1}{2}\int_{-\infty}^{\infty}\{\cos(\lambda+\lambda')z + \cos(\lambda-\lambda')z\}dz$$

$$\int_{-\infty}^{\infty}\cos(\lambda z)\cos\left(\lambda^{'} z\right)dz = \frac{1}{2}\left[\frac{\sin\left(\lambda+\lambda^{'}\right)}{\left(\lambda+\lambda^{'}\right)}z + \frac{\sin\left(\lambda-\lambda^{'}\right)}{\left(\lambda-\lambda^{'}\right)}z\right]_{-\infty}^{\infty} \tag{5.29}$$

(5.29) into (5.28),

$$\int_{-\infty}^{\infty}\emptyset(r_0,z)\cos(\lambda' z)\;dz = \int_0^\infty [A(\lambda)I_0(\lambda r_0)\left\{\frac{1}{2}\left[\frac{\sin(\lambda+\lambda')}{(\lambda+\lambda')}z + \frac{\sin(\lambda-\lambda')}{(\lambda-\lambda')}z\right]_{-\infty}^{\infty}\right\}d\lambda$$

$$\lim_{A\to\infty}\frac{1}{2}\left[\frac{\sin(\lambda+\lambda')}{(\lambda+\lambda')}z + \frac{\sin(\lambda-\lambda')}{(\lambda-\lambda')}z\right]_{-A}^{A} = \lim_{A\to\infty}\left[\frac{\sin(\lambda+\lambda')}{(\lambda+\lambda')}A + \frac{\sin(\lambda-\lambda')}{(\lambda-\lambda')}A\right]$$

$$= \pi\delta(\lambda+\lambda') + \pi\delta(\lambda-\lambda')$$

$$\delta = deltafunction, which\ \delta(0) = +\infty, \delta(\neq 0) = 0$$

$$\int_{-\infty}^{\infty}\delta(x)\;dx = 1$$

In our case,

$$\lambda\lambda' > 0\ , therefore\ \delta(\lambda+\lambda') = 0\ ; \lambda+\lambda' \neq 0$$

$$\int_{-\infty}^{\infty} \emptyset(r_0, z)\cos(\lambda' z)\, dz = \int_0^{\infty} \pi A(\lambda) I_0(\lambda r_0)\, \delta(\lambda - \lambda')\, d\lambda$$

$$= \pi A(\lambda') I_0(\lambda' r_0)$$

$$\text{and } \int_0^{\infty} \delta(\lambda - \lambda')\ d\lambda = 1$$

$$A(\lambda) = \frac{1}{\pi A(\lambda) I_0(\lambda r_0)} \int_{-\infty}^{\infty} \emptyset(r_0, \zeta)\cos(\lambda\zeta)\, d\zeta \tag{5.30}$$

(5.30) into (5.27),

$$\emptyset(r, z) = \frac{1}{\pi} \int_0^{\infty} \frac{I_0(\lambda r)}{I_0(\lambda r_0)} \left[\int_{-\infty}^{\infty} \emptyset(r_0, \zeta)\cos(\lambda\zeta)\, d\zeta \right] \cos\,(\lambda z) d\lambda$$

$$= \frac{1}{2\pi} \int_0^{\infty} \frac{I_0(\lambda r)}{I_0(\lambda r_0)} \left[\int_{-\infty}^{\infty} \emptyset(r_0, \zeta)\{\cos\lambda(z+\zeta) + \cos\lambda(z-\zeta)\}\, dz \right] d\lambda \tag{5.31}$$

Z refer to the some interested point and ζ from -∞ to ∞

By assumed that the boundary condition as shown in the Fig. below and r_0 is the radius of the electrode $\phi_0(r_0, z)$

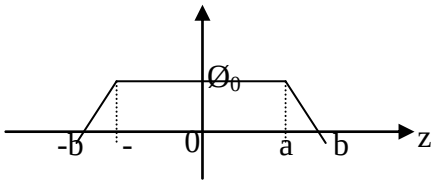

Condition 1, $-b < \zeta < -a\,, r = r_0, \emptyset(r_0, \zeta) = \frac{\phi_0}{b-a}(\zeta + b)$

With (5.31) refer to dz component

$$\emptyset(r_0, \zeta) = \int_{-b}^{-a} \frac{\phi_0}{b-a}(\zeta + b)\{\cos\lambda(z+\zeta) + \cos\lambda(z-\zeta)\}\, d\zeta \tag{5.32}$$

Condition 2, $a \le \zeta < b\ ,\ r = r_0, \emptyset(r_0, \zeta) = \frac{\phi_0}{b-a}(b - \zeta)$

With (5.31) refer to dz component

$$\emptyset(r_0, \zeta) = \int_{a}^{b} \frac{\phi_0}{b-a}(b - \zeta)\{\cos\lambda(z+\zeta) + \cos\lambda(z-\zeta)\}\, d\zeta \tag{5.33}$$

Condition 3, $-a \le \zeta < a\,, r = r_0,\ \emptyset(r_0, \zeta) = \phi_0$

With (5.31) refer to dz component

$$\emptyset(r_0, \zeta) = \int_{-a}^{-a} \phi_0\{\cos\lambda(z+\zeta) + \cos\lambda(z-\zeta)\}\, d\zeta \tag{5.34}$$

And $\zeta \le -b\ \ \&\ \ \zeta \ge b, r = r_0,$

$$\emptyset(r_0, \zeta) = 0 \tag{5.35}$$

Combination of (6.32), (6.33) , (6.34) and (6.35), the total integration from -∞ to ∞ is,

$$\emptyset(r,z) = \frac{\phi_0}{\pi}\int_0^{\infty}\frac{I_0(\lambda r)}{I_0(\lambda r_0)}\frac{\{\cos\lambda(z+a)+\cos\lambda(z-a)-\cos\lambda(z+b)-\cos\lambda(z-b)\}}{\lambda^2(b-a)}d\lambda \tag{5.36}$$

For useful numerical formulation,

$$x \equiv \lambda r_0 \;\rightarrow\; d\lambda = \frac{dx}{r_0}$$

From (5.36),

$$\emptyset(r,z) = \frac{\phi_0}{\pi}\int_0^{\infty}\frac{I_0\left(x\frac{r}{r_0}\right)}{I_0(x)}\frac{\left\{\cos x\frac{(z+a)}{r_0}+\cos x\frac{(z-a)}{r_0}-\cos x\frac{(z+b)}{r_0}-\cos x\frac{(z-b)}{r_0}\right\}}{x^2\frac{(b-a)}{r_0}}dx$$

Hence,$\tilde{r} = \frac{r}{r_0}, \tilde{z} = \frac{z}{r_0}, \tilde{a} = \frac{a}{r_0}\ and\ \tilde{b} = \frac{b}{r_0}$

$$\emptyset(r,z) = \frac{\phi_0}{\pi}\int_0^{\infty}\frac{I_0(x\tilde{r})}{I_0(x)}\frac{\{\cos x\,(\tilde{z}+\tilde{a})+\cos x(\tilde{z}-\tilde{a})-\cos x(\tilde{z}+\tilde{b})-\cos x(\tilde{z}-\tilde{b})\}}{x^2(\tilde{b}-\tilde{a})}dx$$

From (5.2),

$$\boldsymbol{E} = -\nabla\emptyset$$

$$\boldsymbol{E_r} = -\frac{\partial\emptyset(r,z)}{\partial \mathrm{r}} \text{ and } \boldsymbol{E_r} = -\frac{\partial\emptyset(r,z)}{\partial \mathrm{z}}$$

Electric field for r-axis,

$$\boldsymbol{E_r} = -\frac{\phi_0}{\pi}\int_0^{\infty}\frac{1}{I_0(x)}\frac{\partial I_0(x\tilde{r})}{\partial r}\frac{\{\cos x\,(\tilde{z}+\tilde{a})+\cos x(\tilde{z}-\tilde{a})-\cos x(\tilde{z}+\tilde{b})-\cos x(\tilde{z}-\tilde{b})\}}{x^2(\tilde{b}-\tilde{a})}dx$$

$$\frac{\partial I_0(x\tilde{r})}{\partial r} = \frac{\partial I_0(x\tilde{r})}{\partial(x\tilde{r})}\frac{\partial(x\tilde{r})}{\partial\tilde{r}}\frac{\partial\tilde{r}}{\partial r} = I_1(x\tilde{r})\left(\frac{x}{r_0}\right)$$

$$\boldsymbol{E_r} = \frac{\phi_0}{\pi}\int_0^{\infty}\frac{I_1(x\tilde{r})}{I_0(x)}\frac{\{\cos x\,(\tilde{z}+\tilde{b})+\cos x(\tilde{z}-\tilde{b})-\cos x(\tilde{z}+\tilde{a})-\cos x(\tilde{z}-\tilde{a})\}}{x(b-a)}dx$$

Electric field for z axis,

$$\boldsymbol{E_z} = \frac{\phi_0}{\pi}\int_0^{\infty}\frac{I_0(x\tilde{r})}{I_0(x)}\frac{\{\sin x\,(\tilde{z}+\tilde{a})+\sin x(\tilde{z}-\tilde{a})-\sin x(\tilde{z}+\tilde{b})-\sin x(\tilde{z}-b)\}}{x(b-a)}dx$$

The final expression for E_r and E_z can be treated numerically.

Appendix 6

Longitudinal Space Charge Effect

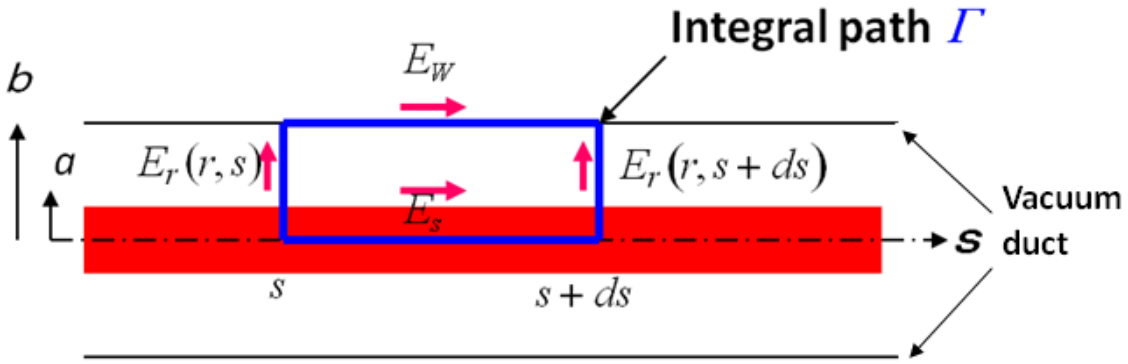

Figure 6.1: Bunch beam (red region) located in a vacuum duct

According to Gauss law,

$$\boldsymbol{\nabla}.\boldsymbol{E} = \frac{\rho}{\varepsilon_0} \tag{6.1}$$

From the divergence theorem,

$$\int \boldsymbol{E}\,.d\boldsymbol{A} = \int \frac{\rho}{\varepsilon_0} dV \tag{6.2}$$

For case r≤a,

$$d\boldsymbol{A} = 2\pi r ds \tag{6.3}$$

$$d\boldsymbol{V} = \pi r^2 ds \tag{6.4}$$

Substitute (6.3) and (6.4) into (6.2),

$$E_r = \frac{\rho}{2\varepsilon_0} r \tag{6.5}$$

For case r>a,

$$d\boldsymbol{A} = 2\pi r ds \tag{6.6}$$

$$d\boldsymbol{V} = \pi a^2 ds \tag{6.7}$$

Substitute (6.6) and (6.7) into (6.2),

$$E_r = \frac{a^2 \rho}{2\varepsilon_0 r} \tag{6.8}$$

From the 4th Maxell equation,

$$\nabla \times \boldsymbol{B} = \mu_0 \left(\boldsymbol{J} + \varepsilon_0 \frac{\partial \boldsymbol{E}}{\partial t} \right), \quad \frac{\partial \boldsymbol{E}}{\partial t} = 0 \tag{6.9}$$

$$\int \boldsymbol{B_\theta}.d\boldsymbol{l} = \int \mu_0 \boldsymbol{J}.d\boldsymbol{A} \tag{6.10}$$

$$B_\theta = \frac{\mu_0 I_B}{2\pi r} \tag{6.11}$$

For case r≤a,

$$I_B = \rho v(\pi r^2) \tag{6.12}$$

Substitute (6.12) into (6.11),

$$B_\theta = \frac{\mu_0 \rho v}{2} r \tag{6.13}$$

For case r>a,

$$I_B = \rho v(\pi a^2) \tag{6.14}$$

Substitute (6.14) into (6.11),

$$B = \frac{\mu_0 a^2 \rho v}{2r} \tag{6.15}$$

Introducing the line density to (6.5), (6.8), (6.13) and (6.15) as,

$$\lambda(s') = \int_0^a \int_0^{2\pi} \rho(r, \theta, s')\, r dr d\theta = \pi a^2 \rho(s') \tag{6.16}$$

Therefore,

For case r≤a,

$$E_r = \frac{\lambda(s') r}{2\pi \varepsilon_0 a^2} \tag{6.17}$$

$$B_\theta = \frac{\mu_0 v \lambda(s') r}{2\pi a^2} \tag{6.18}$$

For case r >a,

$$E_r = \frac{\lambda(s')}{2\pi \varepsilon_0 r} \tag{6.19}$$

$$B_\theta = \frac{\mu_0 v \lambda(s')}{2\pi r} \tag{6.20}$$

From the 2nd Maxwell equation,

$$\nabla \times \boldsymbol{E} = -\frac{\partial \boldsymbol{B}}{\partial t} \tag{6.20}$$

Integration the path as shown in Fig. 6.1 and according the stoke's theorem,

$$E_s.ds + \int_0^b E_r(r, s+ds)dr - E_w.ds - \int_0^b E_r(r,s)dr = -\frac{\partial}{\partial t}\int \boldsymbol{B}.d\boldsymbol{s} \tag{6.21}$$

From (6.17) and (6.19),

$$\begin{aligned}\int_0^b E_r(r,s)dr &= \frac{\lambda(s)}{2\pi\varepsilon_0}\left\{\int_0^a \frac{r}{a^2}dr + \int_a^b \frac{dr}{r}\right\} \\ &= \frac{\lambda(s)}{2\pi\varepsilon_0}\left[\frac{1}{2} + \ln\left(\frac{b}{a}\right)\right] \\ &= \frac{g_0\lambda(s')}{4\pi\varepsilon_0}\end{aligned} \tag{6.22}$$

Here,

$$Geometric\ factor, g_0 = 1 + 2\ln\left(\frac{b}{a}\right) \tag{6.23}$$

From (6.18) and (6.20),

$$\phi(s) = \int \boldsymbol{B}.d\boldsymbol{s} \cong ds\int_0^b B_\theta dr = ds\left(\frac{\mu_0}{2\pi}\right)\nu\lambda(s)\left\{\int_0^a \frac{r}{a^2}dr + \int_a^b \frac{dr}{r}\right\}$$

$$\phi(s) = ds\frac{\mu_0 g_0 \lambda(s')}{4\pi} \tag{6.24}$$

$$\frac{\partial\phi}{\partial t} = ds\frac{\mu_0 g_0 \nu}{4\pi}\frac{\partial\lambda(s)}{\partial t} \tag{6.25}$$

Here,

$$\frac{\partial\lambda(s')}{\partial t} = \frac{\partial\lambda(s')}{\partial s'}\left(\frac{\partial s'}{\partial t}\right) = -\nu\frac{\partial\lambda(s')}{\partial s'} \tag{6.26}$$

Thus,

$$-\frac{\partial\phi}{\partial t} = ds\frac{\mu_0 g_0 \nu^2}{4\pi}\dot{\lambda},\ \ and\ \dot{\lambda} \equiv \frac{d\lambda(s)}{ds} \tag{6.27}$$

Substitute related derivation from (6.22) and (6.27) into (6.21),

$$(E_s - E_w).ds + \frac{g_0}{4\pi\varepsilon_0}[\lambda(s+ds,t) - \lambda(s,t)] = ds\frac{\mu_0 g_0 \nu^2}{4\pi}\dot{\lambda} \tag{6.28}$$

Divided (6.28) by ds and taking a limit of ds→0,

$$E_s = E_w - \frac{g_0}{4\pi\varepsilon_0}[1 - \varepsilon_0\mu_0 v^2]\dot{\lambda}, \quad c = \frac{1}{\sqrt{\varepsilon_0\mu_0}} \tag{6.28}$$

$$c = \frac{1}{\sqrt{\varepsilon_0\mu_0}} \quad and \quad \gamma = \frac{1}{\sqrt{1 - \left(\frac{v}{c}\right)^2}} \tag{6.29}$$

Substitute (6.29) into (6.28),

$$E_s = E_w - \frac{g_0\dot{\lambda}}{4\pi\varepsilon_0\gamma^2} \tag{6.30}$$

Appendix 7

Twiss Parameters

Consider a Hill equation for equation of motion,

$$x'' + k(s)x(s) = 0 \tag{7.1}$$

Here,

$$x'' = \frac{d^2x(s)}{ds^2}\ , k(s) = Periodic\ fucntion$$

General solution for (7.1) is,

$$x(s) = A\sqrt{\beta(s)}\cos(\varphi(s) + \emptyset) \tag{7.2}$$

With,

$$\varphi' = \frac{1}{\beta(s)} \tag{7.3}$$

$$\cos(\varphi(s) + \emptyset) = \frac{x(s)}{A\sqrt{\beta(s)}} \tag{7.4}$$

Here,

$$A\ , \emptyset = Integration\ constant\ determined\ by\ initial\ condition$$

Differential (7.2) respect to s,

$$x'(s) = \frac{A}{\sqrt{\beta(s)}}\left(\frac{1}{2}\right)\beta'(s)(\cos(\varphi(s) + \emptyset) - A\sqrt{\beta(s)}\,\varphi'\sin(\varphi(s) + \emptyset) \tag{7.5}$$

$$\cos^2(\varphi(s) + \emptyset) + \sin^2(\varphi(s) + \emptyset) = 1 \tag{7.6}$$

Substitute (7.3), (7.4) and (7.6) into (7.5),

$$x'(s) = \frac{A}{\sqrt{\beta(s)}}\left(\frac{\beta'(s)}{2}\right)\left(\frac{x(s)}{A\sqrt{\beta(s)}}\right) - \frac{A\sqrt{\beta(s)}}{\beta(s)}\sqrt{1 - \cos^2(\varphi(s) + \emptyset)}$$

$$x'(s) = \frac{\beta'(s)}{2\beta(s)}x(s) - \frac{A}{\sqrt{\beta(s)}}\sqrt{1 - \left(\frac{x(s)}{A\sqrt{\beta(s)}}\right)^2}$$

Simplify $x'(s) = x, x(s) = x, \beta'(s) = \beta', \beta(s) = \beta$

$$x' - \frac{\beta'}{2\beta}x = \frac{A}{\sqrt{\beta}}\sqrt{1 - \left(\frac{x}{A\sqrt{\beta}}\right)^2} \tag{7.8}$$

Square both side,

$$x'^2 + \frac{\beta'^2}{4\beta^2}x^2 - \frac{\beta'}{\beta}xx' = \frac{A^2}{\beta} - \frac{x^2}{\beta^2} \tag{7.9}$$

$$x'^2 + \left(\frac{\beta'^2}{4\beta^2} + \frac{1}{\beta^2}\right)x^2 - \frac{\beta'}{\beta}xx' = \frac{A^2}{\beta} \tag{7.10}$$

$$\frac{\beta}{A^2}x'^2 + \left(\frac{\beta'^2}{4\beta A^2} + \frac{1}{\beta A^2}\right)x^2 - \frac{\beta'}{A^2}xx' = 1 \tag{7.11}$$

From (7.10) this equation can be expressed as ellipse in an implicit equation with an enclosed area as:

$$ax^2 + bxy + cy^2 = 1 \tag{7.12}$$

Here,

$$Area = \frac{2\pi}{\sqrt{4ac - b^2}} \tag{7.13}$$

Comparison with (7.11) and (7.12),

$$x = x \; and \; x' = y \tag{7.14}$$

$$a = \frac{\beta}{A^2} \tag{7.15}$$

$$b = -\frac{\beta'}{A^2} \tag{7.16}$$

$$c = \frac{\beta'^2}{4\beta A^2} + \frac{1}{\beta A^2} \tag{7.17}$$

Substitute (7.15) ,(7.16) and (7.17) into (7.13),

$$Area = \frac{2\pi}{\sqrt{4ac - b^2}} = \frac{2\pi}{2/A^2} = \pi A^2 \tag{7.18}$$

Introducing a new parameter,

$$\alpha = -\frac{1}{2}\beta' \tag{7.19}$$

$$\gamma = \frac{(1 + \alpha^2)}{\beta} \tag{7.20}$$

$$\pi\varepsilon = \pi A^2, A = \sqrt{\varepsilon} \tag{7.21}$$

Substitute (7.19), (7.20) and (7.21) into (7.11),

$$\beta x'^2 + \left(\frac{\beta'^2}{4\beta} + \frac{1}{\beta}\right)x^2 - \beta' x x' = A^2 \tag{7.22}$$

$$\beta x'^2 + \gamma x^2 + 2\alpha x x' = \varepsilon \tag{7.23}$$

Hence,

$$A = invariant\ and\ \varepsilon = invariant$$

By substitute $A = \sqrt{\varepsilon}$

$$x(s) = \sqrt{\varepsilon}\sqrt{\beta(s)}\cos(\varphi(s) + \emptyset) \tag{7.24}$$

$$x'(s) = -\frac{\sqrt{\varepsilon}}{\beta(s)}(\alpha(s)\cos(\varphi(s) + \emptyset) + \sin(\varphi(s) + \emptyset) \tag{7.25}$$